Among these, the RFO control is the most popular due to its simplicity. For the AFO control, there is a coupling between the slip angular velocity and the air-gap flux, and for the SFO control, there is a coupling between the $q$-axis current and the stator flux. These couplings can make the associated vector control complex. Thus in this book, we will focus only on the RFO control.

### 5.2.2 DIRECT VECTOR CONTROL BASED ON THE ROTOR FLUX

In the vector control based on the rotor flux, the rotor flux linkage is used as the reference flux. The rotor flux linkage generated by the three-phase rotor currents can be expressed as a complex vector $\boldsymbol{\lambda}_r$ as

$$\begin{aligned}\boldsymbol{\lambda}_r &= \frac{2}{3}(\lambda_{ar} + a\lambda_{br} + a^2\lambda_{cr}) \\ &= |\lambda_r| e^{j\omega_e t} = |\lambda_r| e^{j\theta_e} \quad \left(\theta_e = \int \omega_e(t)dt + \theta(0)\right)\end{aligned} \tag{5.7}$$

The rotor flux linkage vector $\boldsymbol{\lambda}_r$ rotates at the speed $\omega_e$ corresponding to the operating frequency of the stator currents (i.e., synchronous speed), and thus the position of this flux linkage vector varies over time.

For the vector control based on the rotor flux, the position of the rotor flux linkage vector should be assigned to the $d$-axis. Thus we need to use the synchronous $d-q$ reference frame rotating at the speed equal to that of the rotor flux linkage vector. By doing so, the $d$-axis is always locked at the position of the rotor flux linkage vector. As a result, the rotor flux linkage in the synchronous $d-q$ reference frame has entirely the $d$-axis component and no $q$-axis component, i.e., $\boldsymbol{\lambda}_r = \lambda_{dr}^e$, and $\lambda_{qr}^e = 0$.

In such a direct vector control, the position of the rotor flux linkage vector can be identified as follows.

The rotor flux linkage vector in the stationary reference frame as shown in Fig. 5.9 has both the $d-q$ axes components, $\lambda_{dr}^s$ and $\lambda_{qr}^s$, whose magnitudes are changed according to the position of the rotor flux linkage vector.

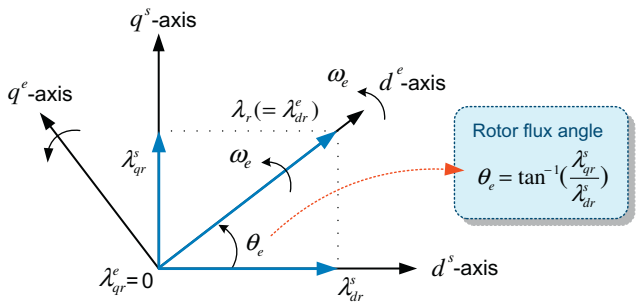



**FIGURE 5.9**

Rotor flux angle.

If these stationary $d-q$ rotor flux linkages are known, then we can obtain the rotor flux angle from the following equation.

$$\theta_e = \tan^{-1}\left(\frac{\lambda_{qr}^s}{\lambda_{dr}^s}\right) \tag{5.8}$$

Like this, the direct vector control uses the rotor flux angle calculated by using Eq. (5.8) from the stationary $d-q$ rotor flux linkages, which are obtained by detection or estimation.

Next, we are going to discuss the meaning of the $d-q$ axes stator currents in the synchronous reference frame oriented to the rotor flux linkages vector $\boldsymbol{\lambda}_r$.

#### 5.2.2.1 Relation between the d-axis stator current and the rotor flux linkage

In the rotor flux−oriented vector control, there is an intimate relation between the $d$-axis stator current $i_{ds}^e$ and the rotor flux linkage. The $d$-axis rotor voltage equation in the synchronous reference frame is

$$0 = R_r i_{dr}^e + p\lambda_{dr}^e - (\omega_e - \omega_r)\lambda_{qr}^e \tag{5.9}$$

Here, $p$ denotes a differential operator.

The necessary and sufficient condition for the rotor flux−oriented vector control is $\lambda_{dr}^e = \boldsymbol{\lambda}_r$ and, thus $\lambda_{qr}^e = 0$.

Applying $\lambda_{qr}^e = 0$ to Eq. (5.9), we can obtain the $d$-axis rotor current as

$$i_{dr}^e = -\frac{p\lambda_{dr}^e}{R_r} \tag{5.10}$$

If this rotor current is substituted into the following $d$-axis rotor flux linkage equation,

$$\lambda_{dr}^e = L_r i_{dr}^e + L_m i_{ds}^e \tag{5.11}$$

then the following relation between the $d$-axis stator currents $i_{ds}^e$ and the rotor flux linkage $\lambda_{dr}^e$ can be found.

$$\lambda_{dr}^e = \frac{R_r L_m}{R_r + L_r p} i_{ds}^e = \frac{L_m}{1 + T_r p} i_{ds}^e \quad \left(T_r = \frac{L_r}{R_r}\right) \tag{5.12}$$

From this, it can be seen that the rotor flux linkage $\boldsymbol{\lambda}_r (= \lambda_{dr}^e)$ is proportional to the $d$-axis stator current by the first-order lag with the rotor time constant $T_r$. Thus the rotor flux linkage to a sudden change in the $d$-axis current will change

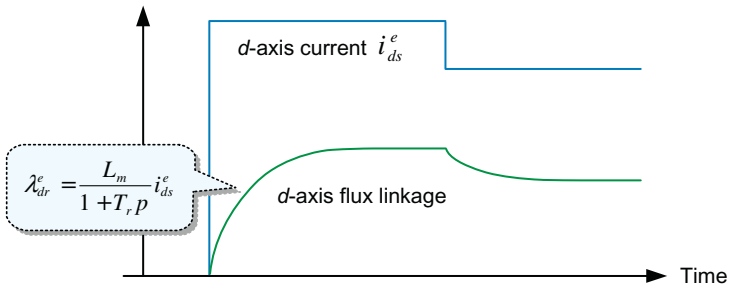



**FIGURE 5.10**

Relation between the *d*-axis stator current and the rotor flux.

exponentially with the time constant of $T_r$ as shown in Fig. 5.10. This phenomenon occurs, as can be seen from Eq. (5.10), because the variation in the rotor flux linkage by the changing in the *d*-axis stator current induces a rotor current $i_{dr}^e$ decaying with a rotor time constant $T_r$.

Although there is a time delay, the magnitude of the rotor flux linkage can be regulated by the *d*-axis stator current. Thus the *d*-axis stator current $i_{ds}^e$ can be called the *flux-producing current*.

With the *d*-axis current $i_{ds}^e$ held constant, the magnitude of the rotor flux linkage $\lambda_{dr}^e$ is directly related to $i_{ds}^e$ as

$$|\lambda_r| = \lambda_{dr}^e = L_m\, i_{ds}^e \tag{5.13}$$

Normally, the magnitude of the rotor flux linkage is kept constant for operations below the rated speed, so the *d*-axis current command is given as a constant value of $i_{ds}^{e*}(= \lambda_{dr}^{e*}/L_m)$.

Next, we will examine the relationship between the *q*-axis stator current and the output torque.

#### 5.2.2.2 Relationship between the q-axis stator current and the output torque

By applying $\lambda_{qr}^e = 0$ to Eq. (4.99), the torque equation becomes

$$T_e = \frac{3}{2}\frac{P}{2}\frac{L_m}{L_r}(\lambda_{dr}^e i_{qs}^e - \lambda_{qr}^e i_{ds}^e) = \frac{3}{2}\frac{P}{2}\frac{L_m}{L_r}\lambda_{dr}^e i_{qs}^e \tag{5.14}$$

With the rotor flux held constant, the torque equation reduces further to

$$T_e = K_T\, i_{qs}^e \quad \left(K_T = \frac{3}{2}\frac{P}{2}\frac{L_m}{L_r}\lambda_{dr}^e\right) \tag{5.15}$$

The torque is directly related to the *q*-axis stator current $i_{qs}^e$, so this current can be called the *torque-producing current*. By controlling the *q*-axis stator current

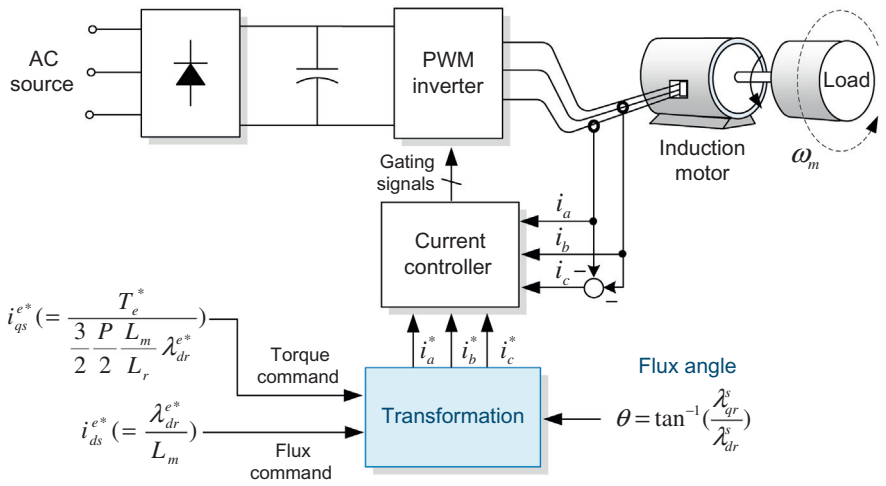



**FIGURE 5.11**

Induction motor drive system by the direct vector control.

instantaneously, the torque of an induction motor can be controlled instantaneously as in a DC motor.

By combining Eqs. (5.12) and (5.14), the torque can also be expressed in terms of the stator currents as

$$T_e = \frac{3}{2}\frac{P}{2}\frac{L_m^2}{L_r}\frac{1}{\left(1+\frac{L_r}{R_r}p\right)} i_{ds}^e\, i_{qs}^e \tag{5.16}$$

With the $d$-axis current $i_{ds}^e$ held constant, the torque is given as

$$T_e = \frac{3}{2}\frac{P}{2}\frac{L_m^2}{L_r} i_{ds}^e\, i_{qs}^e \tag{5.17}$$

### 5.2.2.3 Induction motor drive system by the direct vector control

An induction motor drive system that adapts the direct vector control based on the rotor flux is shown in Fig. 5.11.

In the direct vector control of an induction motor, the rotor flux linkage is kept constant and the torque is regulated by controlling $i_{qs}^e$. Accordingly, the $d$-axis current command $i_{ds}^{e*}$ will be given from the rotor flux command $\lambda_{dr}^{e*}$ by using Eq. (5.13) as

$$i_{ds}^{e*} = \frac{\lambda_{dr}^{e*}}{L_m} \tag{5.18}$$

The rated value of the rotor flux linkage command $\lambda_{dr}^{e*}$ depends on the rated voltage and frequency of a given motor. The ways to calculate the rated rotor flux linkage for a given motor will be described later in this section.

After applying the $d$-axis current command $i_{ds}^{e*}$ of Eq. (5.18), as shown in Fig. 5.10, a time to build up the rotor flux linkage to its final value is required. This build-up time depends on the rotor time constant $T_r$ and will be normally about $5T_r$.

After the rotor flux linkage arrives at the final value, the $q$-axis current can be applied to produce the required torque. Using Eq. (5.15), the $q$-axis current command $i_{qs}^{e*}$ can be calculated from the output torque command $T_e^*$, which may be given from a speed or torque controller, as

$$i_{qs}^{e*} = \frac{T_e^*}{K_T} \quad \left(K_T = \frac{3}{2}\frac{P}{2}\frac{L_m}{L_r}\lambda_{dr}^{e*}\right) \tag{5.19}$$

We need to regulate the stator currents of the induction motor to follow these current commands. It should be noted that these $d-q$ current commands $i_{ds}^{e*}$ and $i_{qs}^{e*}$ are variables in the synchronous reference frame. We need to know the three-phase current commands $i_{as}^*$, $i_{bs}^*$, $i_{cs}^*$ of the induction motor. To obtain these three-phase current commands, we need to transform $i_{ds}^{e*}$ and $i_{qs}^{e*}$ into $i_{as}^*$, $i_{bs}^*$, $i_{cs}^*$ by using the rotor flux angle $\theta_e$. Alternatively, after transforming these synchronous current commands into stationary current commands as

$$i_{ds}^{s*} = i_{ds}^{e*}\cos\theta_e - i_{qs}^{e*}\sin\theta_e \tag{5.20}$$

$$i_{qs}^{s*} = i_{ds}^{e*}\sin\theta_e + i_{qs}^{e*}\cos\theta_e \tag{5.21}$$

then, we can transform these stationary current commands into three-phase current commands as

$$i_{as}^* = i_{ds}^{s*} \tag{5.22}$$

$$i_{bs}^* = -\frac{1}{2}i_{ds}^{s*} + \frac{\sqrt{3}}{2}i_{qs}^{s*} \tag{5.23}$$

$$i_{cs}^* = -\frac{1}{2}i_{ds}^{s*} - \frac{\sqrt{3}}{2}i_{qs}^{s*} \tag{5.24}$$

Finally, if the stator currents of an induction motor are regulated to instantaneously follow these three-phase current commands by using a current controller, then the instantaneous torque control of an induction motor can be achieved.

On the other hand, there is a more effective control method in regulating the stator currents. In this method of using a synchronous reference frame current

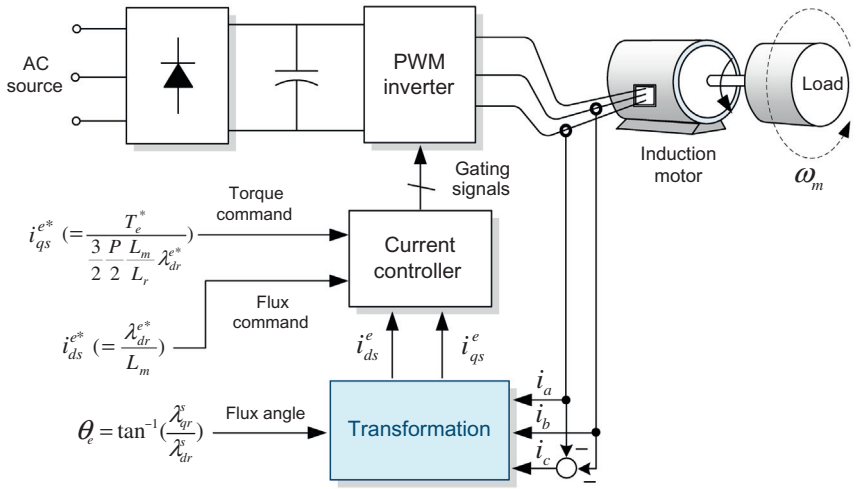



**FIGURE 5.12**

Direct vector control system with the synchronous reference current regulator.

regulator, the synchronous current commands, $i_{ds}^{e*}$ and $i_{qs}^{e*}$, are used directly instead of the three-phase current commands as shown in Fig. 5.12. In this case, the three-phase stator currents, $i_{as}$, $i_{bs}$, $i_{cs}$, of the induction motor are transformed into synchronous $dq$ currents, $i_{ds}^e$ and $i_{qs}^e$. This synchronous reference frame regulator, which will be described in detail in Chapter 6, shows an excellent current control performance. Thus, most vector control systems employ this synchronous regulator.

In this control, as it is called "Vector control", we can see that both the magnitude and the phase of the stator current vector vary according to the output torque command. As an example, Fig. 5.13 describes how the stator current command vector alters when the torque command is changed. The stator current vector of the induction motor is assumed to be $\boldsymbol{i}_s^*$ initially. If a larger torque needs to be produced, the $q$-axis current command will be increased from $i_{qs}^{e*}$ to $i_{qs1}^{e*}$, but the $d$-axis current command $i_{ds}^{e*}$ will remain the same. This requires a new stator current command vector $\boldsymbol{i}_{s1}^*$, and thus both the magnitude and the phase of the stator current vector are changed. Likewise, if the flux command is changed, both the magnitude and the phase of the stator current vector will be also changed.

Fig. 5.14 shows experimental results for the direct vector control on 5-hp, 4-pole induction motor when the speed command is changed from 500 to 1500 r/min.

The most difficult aspect of implementing the direct vector control is finding the instantaneous position of the rotor flux linkage, i.e., the rotor flux angle,

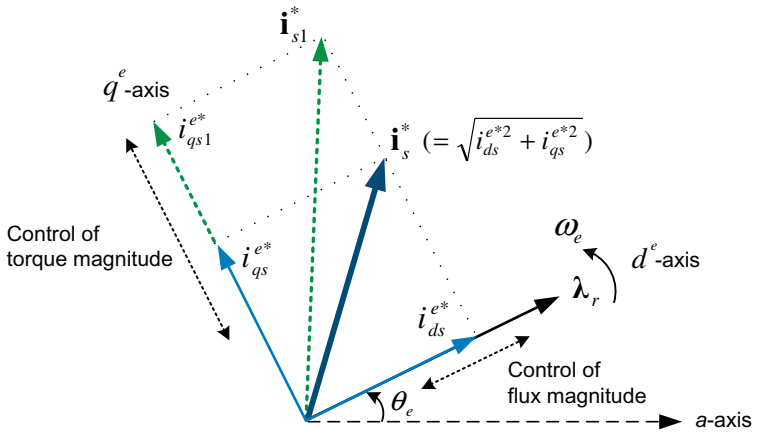



**FIGURE 5.13**

Stator $d$–$q$ current commands.

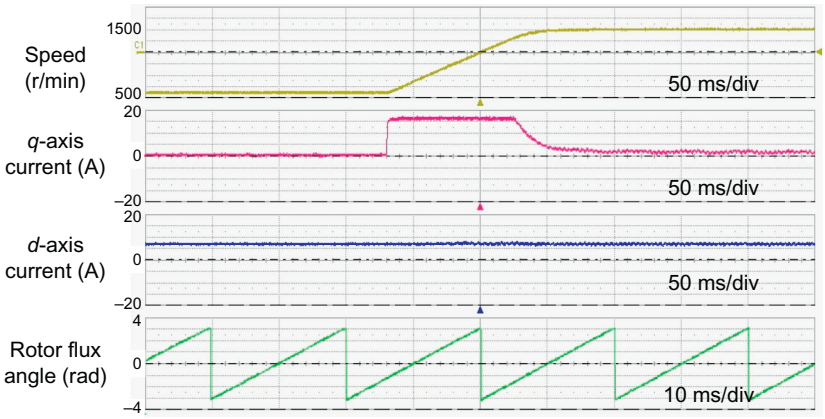



**FIGURE 5.14**

Experimental results for the direct vector control of 5-hp induction motor.

accurately. It is not an overstatement to say that the performance of the instantaneous torque control depends on the accuracy of the rotor flux angle. A way to obtain the rotor flux angle is to calculate the rotor flux linkage from the air-gap flux detected by Hall effect sensors or sensing coils, which are installed in the applied motor. However, this method is costly and is not practical. A widely used method is to estimate the rotor flux linkage from voltages and currents of the motor, which will be described in more detail in Chapter 6.

## MATLAB/SIMULINK SIMULATION: VECTOR CONTROL OF AN INDUCTION MOTOR

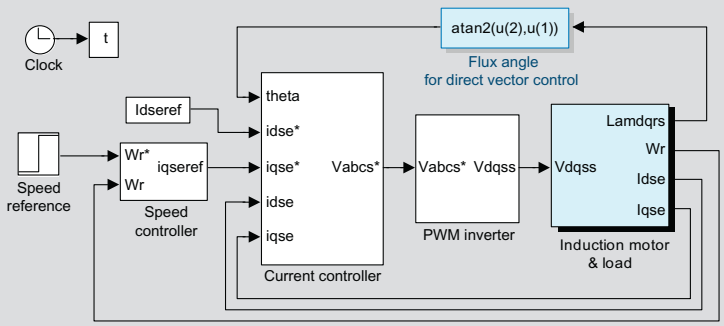
The rated values and parameters of an induction motor are as follows.

- 5-hp, 220 V, 60 Hz, 4-Pole, 1750 r/min, 12.8 A rms

$$R_s = 0.295\Omega, \quad R_r = 0.379\Omega, \quad L_m = 59 \text{ mH}, \quad L_{ls} = L_{lr} = 1.794 \text{ mH}$$

The rated $d$- and $q$-axes stator currents can be obtained as follows.

- Rated torque: $T_e = (P/2)(\text{power}/\omega_s(1-s)) = 20.35$ Nm
- Rated $d$-axis current: $I_{ds}^e \cong \dfrac{V_{ph\_peak}}{\sqrt{R_s^2 + X_s^2}} = 7.84$ A
- Rated flux linkage: $|\lambda_r| = L_m I_{ds}^e = 0.4624$ Wb
- Rated $q$-axis current: $I_{qs}^e = T_e / \left(\dfrac{3}{2}\dfrac{P}{2}\dfrac{L_m^2}{L_r} I_{ds}^e\right) = 15.12$ A
- Simulation block for the direct vector control

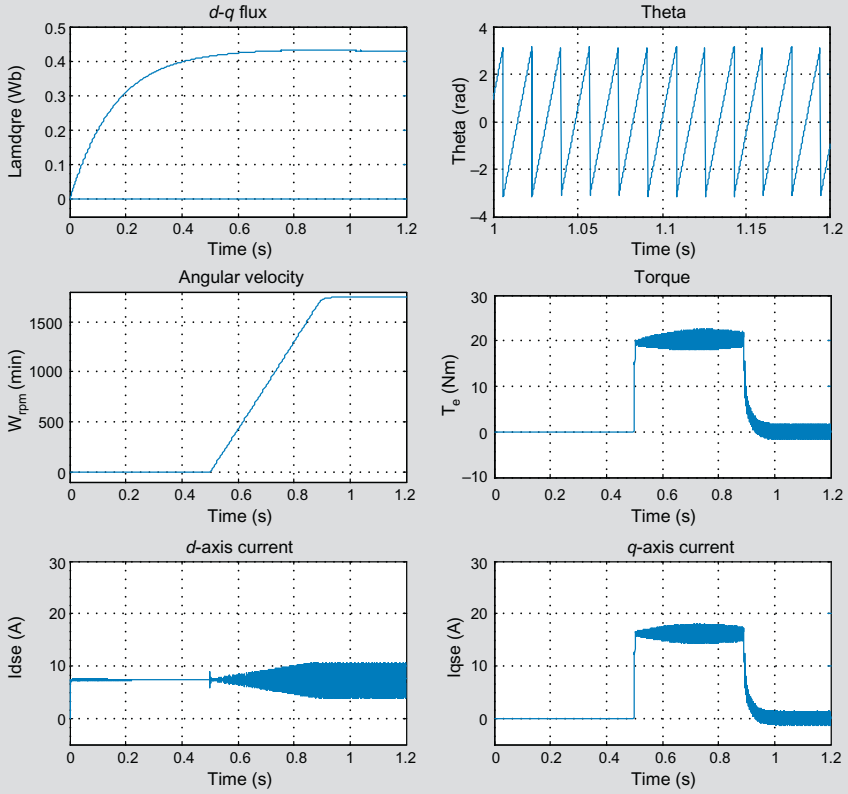



  - Flux angle: $\theta_e = \tan^{-1}(\lambda_{qr}^s / \lambda_{dr}^s)$
  - Load model: refer to Chapter 1.
  - Speed controller: refer to Chapter 2.
  - Induction motor model: refer to Chapter 4.
  - Current controller: refer to Chapter 6.
  - PWM inverter: refer to Chapter 7.
- Simulation results

  The $q$-axis current (thus torque) is applied when the rotor flux linkage builds up to the value in the steady-state condition.

(*Continued*)

**MATLAB/SIMULINK SIMULATION: VECTOR CONTROL OF AN INDUCTION MOTOR (CONTINUED)**




## 5.2.3 INDIRECT VECTOR CONTROL BASED ON THE ROTOR FLUX

As mentioned in Section 5.2.2, we need to know the accurate rotor flux linkage for obtaining the rotor flux angle in the direct vector control. However, it is not easy to obtain the rotor flux linkage accurately. The indirect vector control does not use the rotor flux linkage directly for obtaining the rotor flux angle, so it may be implemented easily.

From the steady-state equivalent circuit of an induction motor in Fig. 5.15, we can see that the slip $s$ determines how the stator current can be divided into the flux- and torque (or rotor)-producing currents. Thus we can infer from this that the desired flux and torque can be obtained by controlling the slip. The flux- and

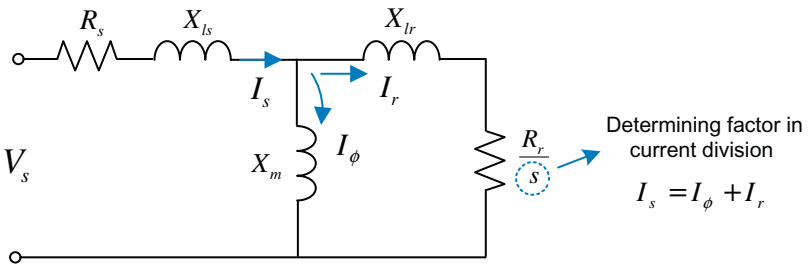



**FIGURE 5.15**

Steady-state equivalent circuit of an induction motor.

the torque-producing currents in the stated-state equivalent circuit are not equal to those in the vector control. However, similar to this concept, the principle of the indirect vector control is to control the slip so that the stator current can be divided into the desired flux- and the torque-producing components. Now we will take a closer look at the principle of the indirect vector control.

As stated in Section 5.2.2, in the vector control, since the $d$-axis is assigned to the position of the rotor flux linkage, there is no rotor flux linkage in the $q$-axis, i.e., $\lambda_{qr}^e = 0$.

Thus in the vector control, the rotor voltage equation becomes

$$v_{qr}^e = R_r i_{qr}^e + p\lambda_{qr}^e + (\omega_e - \omega_r)\lambda_{dr}^e = R_r i_{qr}^e + (\omega_e - \omega_r)\lambda_{dr}^e = 0 \tag{5.25}$$

From this, the slip angular frequency $\omega_{sl}$ required in the vector control can be derived as

$$\omega_e - \omega_r = \omega_{sl} = -\frac{R_r i_{qr}^e}{\lambda_{dr}^e} \tag{5.26}$$

Here, the rotor current can be obtained as Eq. (5.28) from the rotor flux linkage equation of Eq. (5.27).

$$\lambda_{qr}^e = L_r i_{qr}^e + L_m i_{qs}^e = 0 \tag{5.27}$$

$$i_{qr}^e = -\frac{L_m}{L_r} i_{qs}^e \tag{5.28}$$

Combining Eqs. (5.26) and (5.28) yields the requirement of the slip angular frequency for the vector control as

$$\omega_{sl} = \frac{L_m R_r}{L_r} \frac{i_{qs}^e}{\lambda_{dr}^e} \tag{5.29}$$

From Eq. (5.12), this can also be expressed in $d-q$ axes currents as

$$\omega_{sl} = \left(\frac{1}{T_r} + p\right) \frac{i_{qs}^e}{i_{ds}^e} \quad \left(T_r = \frac{L_r}{R_r}\right) \tag{5.30}$$

With the rotor flux linkage held constant, we can finally obtain the important slip requirement for the indirect vector control as

$$\omega_{sl} = \frac{1}{T_r}\frac{i_{qs}^e}{i_{ds}^e} \tag{5.31}$$

This slip relation indicates that if we want to divide the stator currents into the specific values of $d-q$ axes currents, we have to set the operating slip angular frequency of an induction motor at the value of Eq. (5.31) calculated by using the specific values. After that, using the information of the rotor velocity $\omega_r$, we can obtain the rotor flux angle as

$$\theta_e = \int \omega_e dt = \int (\omega_{sl} + \omega_r) dt \tag{5.32}$$

Like this, in the indirect vector control, instead of using the rotor flux linkage directly, the slip angular frequency is adjusted to achieve the required division of the $d-q$ axes currents.

Fig. 5.16 shows the indirect vector control system of an induction motor, where the slip angular frequency $\omega_{sl}^*$ is calculated from $d-q$ axes current commands for the required torque and flux production.

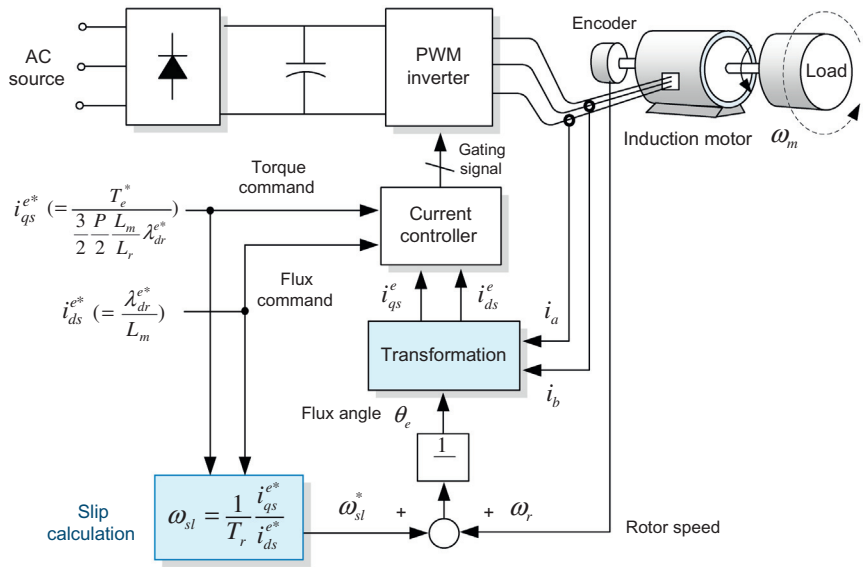



**FIGURE 5.16**

Induction motor drive system using the indirect vector control.

Since the indirect vector control uses the rotor flux angle obtained from adding the slip angular velocity to the rotor velocity, this is often called the *feedforward field-oriented control*. The indirect vector control that does not require the information of the rotor flux linkage has an advantage of easy implementation and a better performance in low-speed operations.

A drawback of the indirect vector control is that the rotor speed is required to obtain the rotor flux angle. The rotor speed is normally found using an encoder, a type of a position sensor, which will be discussed in Chapter 9. Recently the vector control that does not require an expensive position sensor, called the *sensorless control*, has received a lot of attention. In this case, however, we cannot use this simple indirect vector control technique.

In addition, the indirect vector control is also problematic in which the rotor open circuit time constant $T_r$ required in the calculation of Eq. (5.31) is sensitive to both the temperature and rotor flux level. The rotor resistance $R_r$ can easily change with temperature, and the rotor inductance $L_r$ can vary with the magnitude of the rotor flux. These variations result in an inaccurate slip angular frequency, and thus an accurate vector control cannot be achieved. Therefore in the indirect vector control, the accuracy of the torque control depends on that of these parameters. The parameters of an induction motor can be obtained by the block test and no-load test, which were described in Chapter 3. However, these tests may lack accuracy. Thus we need to use an alternative method that can obtain these parameters more accurately. For both the direct vector control and the indirect vector control, the accuracy of these parameters is important. The parameters can be obtained by off-line auto tuning method prior to the start-up or online estimation method during a normal operation [1−3].

Now we will take a close look at how an incorrect rotor time constant (by an inaccurate $R_r$) influences the indirect vector control performance.

### 5.2.4 DETUNING IN THE INDIRECT VECTOR CONTROL

The following slip relation indicates the necessary condition for dividing the stator current into the desired values of the $d$- and $q$-axes currents correctly.

$$\omega_{sl}^{*} = \frac{1}{T_r}\frac{i_{qs}^{e*}}{i_{ds}^{e*}} = \frac{R_r}{L_r}\frac{i_{qs}^{e*}}{i_{ds}^{e*}} \tag{5.33}$$

Since the value of the rotor time constant $T_r$ used in the slip calculator can vary easily during operations, the slip angular frequency is likely to be incorrect. The value of the rotor resistance especially varies with temperature. If the temperature increases by 10°C, the rotor resistance will increase about 4%. From the heat produced from copper losses, the resistance of a rotor in an enclosed space can increase more than that of a stator. Besides the temperature, the value of the

rotor resistance can vary with the operating frequency of the rotor circuit due to the skin effect.

The rotor self-inductance varies with the value of the rotor flux linkage. The rotor flux linkage remains constant for a normal operation below the rated speed, so the rotor self-inductance may remain unchanged. However, the rotor self-inductance will change for high-speed operations, which require a reduced rotor flux level for a field-weakening operation.

The variations of the parameters due to the reasons mentioned above make the value of the rotor time constant used in the slip calculator to deviate from the correct value, which is referred to as *detuning* [4]. In this detuned operation the $d$-axis will be misaligned from the true rotor flux axis due to an incorrect slip angular frequency. As a result, the actual $d-q$ axes currents will be different from their commands, and in turn, the actual rotor flux linkage and torque will be different from their commands. Moreover, the decoupling of the rotor flux linkage and torque is lost, i.e., the correct vector control cannot be achieved, so steady-state and transient torque responses will be degraded. Fig. 5.17 shows the currents and output torque for a detuned operation [5].

We will take a look at the influence of the detuned rotor resistance on the rotor flux linkage and output torque. Assuming that the rotor resistance increases due to an increase in the temperature, the rotor time constant used by the slip calculator will be larger, so the produced slip frequency will be smaller than the desired value. As a result, the $d-q$ axes set by the controller will lag behind the true axis as shown in Fig. 5.18. Hence, the actual $d$-axis current component will increase, but the actual $q$-axis current will decrease. This will cause the actual rotor flux linkage to increase but not proportionally to the increase in the $d$-axis current due to magnetic saturation. Consequently, the output torque will be reduced, and a bigger $q$-axis current command will be imposed to obtain the required output torque.

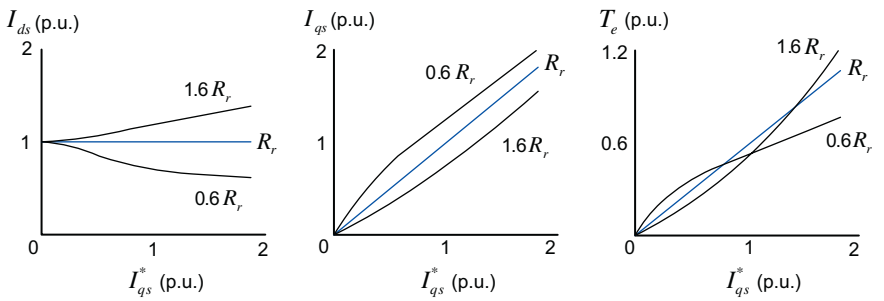



**FIGURE 5.17**

Detuning effects.

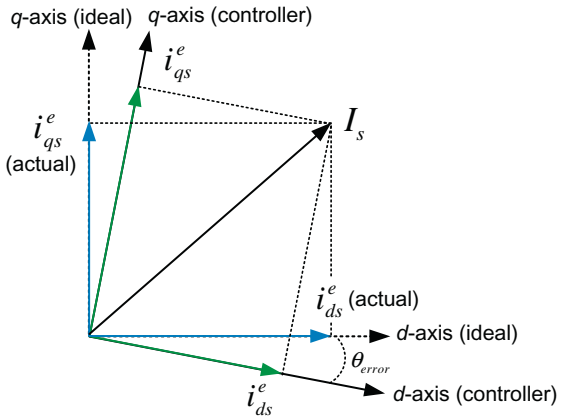



**FIGURE 5.18**

Reference frame error due to detuning effect.

On the contrary, when the rotor resistance decreases, the calculated slip frequency becomes larger than the desired value because the slip calculator uses a smaller time constant. Thus the actual $q$-axis component current increases but the actual $d$-axis current decreases. As a result of this, the actual rotor flux linkage is significantly reduced, and in turn, the output torque is reduced. In these two detuned cases the $d$-axis is misaligned from the true rotor flux axis due to the incorrect slip frequency. As a result, the distribution of the $d-q$ axes currents will be inadequate, so the induction motor will not be able to generate the desired rotor flux linkage and output torque. In addition, the detuning leads to additional motor losses and a reduction of the peak torque capability. Generally, larger high-efficiency motors with a large magnetizing inductance and a low rotor resistance are much more sensitive to detuning than small low-efficiency motors.

## 5.3 FLUX ESTIMATION OF AN INDUCTION MOTOR

As described in Section 5.2, the most important information for realizing the vector control is the position of the rotor flux linkage, i.e., the rotor flux angle for the $d-q$ axes transformation. The position of the rotor flux linkage is directly identified from the rotor position for permanent magnet synchronous motors (PMSMs). However, it is not possible to identify the position of the rotor flux linkage directly from the rotor position for induction motors, which operate with a slip with regard to the synchronous speed.

Now we will examine the ways to find the rotor flux linkage for the direct vector control. To find the rotor flux angle, the $d-q$ axes rotor flux linkages in the stationary reference frame are required as we can see from Eq. (5.8) as

$$\theta_e = \tan^{-1}\left(\frac{\lambda_{qr}^s}{\lambda_{dr}^s}\right) \tag{5.34}$$

There are two methods to obtain the stationary rotor flux linkages: one is to measure the flux linkages or the physical quantity proportional to the flux linkages, and the other one is to estimate them indirectly from the mathematical motor model. In the direct method the rotor flux linkage is obtained from the air-gap flux acquired from the Hall effect sensors or the sensing coils installed inside the stator. However, since there are some difficulties in the practical usage of the direct method, the rotor flux linkages are commonly estimated from the mathematical motor model by using the motor voltage, current, and/or speed as follows.

There are two typical open-loop observers for estimating the rotor flux linkage: one is based on the stator voltage equations, which is referred to as the *voltage model*, and the other one is based on the rotor voltage equations, which is known as the *current model*.

### 5.3.1 ROTOR FLUX LINKAGES ESTIMATION BASED ON THE STATOR VOLTAGE EQUATIONS: VOLTAGE MODEL

In this method the stator flux linkages are obtained from the stator voltage equations and, in turn, the rotor flux linkages are estimated from these stator flux linkages. This method requires information on the stator voltages and currents.

First, the stator flux linkages can be found from the integral of stator voltages as

$$v_{ds}^s = R_s i_{ds}^s + \frac{d\lambda_{ds}^s}{dt} \tag{5.35}$$

$$v_{qs}^s = R_s i_{qs}^s + \frac{d\lambda_{qs}^s}{dt} \tag{5.36}$$

$$\lambda_{ds}^s = \int \left(v_{ds}^s - R_s i_{ds}^s\right) dt = \int e_{ds}^s dt \tag{5.37}$$

$$\lambda_{qs}^s = \int \left(v_{qs}^s - R_s i_{qs}^s\right) dt = \int e_{qs}^s dt \tag{5.38}$$

where $e_{ds}^s = v_{ds}^s - R_s i_{ds}^s$ and $e_{qs}^s = v_{qs}^s - R_s i_{qs}^s$.

The rotor flux linkages can be obtained from these stator flux linkages as follows.

The $d$-axis rotor flux linkage in the stationary reference frame is given by

$$\lambda_{dr}^s = L_r i_{dr}^s + L_m i_{ds}^s \tag{5.39}$$

Here, the nonmeasurable rotor current $i_{dr}^s$ can be obtained from the $d$-axis stator flux linkage and the stator current as

$$i_{dr}^s = \frac{\lambda_{ds}^s - L_s i_{ds}^s}{L_m} \leftarrow \lambda_{ds}^s = L_s i_{ds}^s + L_m i_{dr}^s \tag{5.40}$$

Substituting this rotor current into Eq. (5.39), we can finally obtain the equation for the stationary $d$-axis rotor flux linkage as

$$\hat{\lambda}_{dr}^s = \frac{L_r}{L_m}(\lambda_{ds}^s - \sigma L_s i_{ds}^s) \tag{5.41}$$

where $\sigma = (1 - L_m^2/L_s L_r)$ is a total leakage factor.

Likewise, we can obtain the stationary $q$-axis rotor flux linkage as

$$\hat{\lambda}_{qr}^s = \frac{L_r}{L_m}(\lambda_{qs}^s - \sigma L_s i_{qs}^s) \tag{5.42}$$

Using the arctangent function of these estimated stationary $d-q$ axes rotor flux linkages, the flux angle can be calculated as

$$\hat{\theta}_e = \tan^{-1}\left(\frac{\hat{\lambda}_{qr}^s}{\hat{\lambda}_{dr}^s}\right) \tag{5.43}$$

The strength of this method is its simplicity and insensitivity to the parameter variations except for the stator resistance. However, since this method is fundamentally based on the estimation of the back-EMF $e_{dqs}^s$ its performance depends on the rotor speed. Thus this method works well in the medium- to high-speed range, in which the back-EMF becomes large enough. However, in the low-speed range with a low operation voltage, it may be easily influenced by the inaccuracy of the stator resistance, the sensor noise, and the inverter-nonlinearity effect. Thus this method based on the voltage model is normally used in high-speed regions.

To estimate the rotor flux linkage accurately with this method, it should be noted that it is necessary to offer accurate stator voltages and currents. A voltage sensor may be used to obtain the stator voltages, but it is hard to measure the actual stator voltages precisely because the motor voltages are given by the inverter as a high-frequency pulse width modulator (PWM) waveform. Thus instead of measuring the actual stator voltages, the voltage commands or the voltages reconstructed by using the DC-link voltage and the commanded PWM duty are commonly used. However, the reconstructed value may differ from the actual output voltage due to inverter-nonlinearity such as the dead-time effect, turn-on/off delay time, and voltage drop across switching devices. Though such voltage errors can be reduced by a proper compensation technique, it is not easy to obtain an accurate voltage in the low-speed range of 10% below the rated speed.

Unlike the voltages, the stator currents are directly measured by current sensors. When the measured currents include a DC offset or noise, the integration

of the back-EMF may be saturated. Thus instead of a pure integrator, a first-order, low-pass filter is commonly used. This low-pass filter can be considered as the combination of a pure integrator and a high-pass filter as

$$\lambda^s_{dqs}(s) = \left[e^s_{dqs}(s) \times \frac{s}{s+\alpha}\right] \times \frac{1}{s} = e^s_{dqs}(s) \times \frac{1}{s+\alpha} \tag{5.44}$$

However, the use of such low-pass filter can cause errors in the phase and the magnitude of the estimated flux linkages, especially in low-speed regions. The cutoff frequency of the filter in Eq. (5.44) greatly influences the errors of the flux estimator and is usually chosen as the reciprocal of the rotor time constant $T_r$.

### A DIGITAL FIRST-ORDER, LOW-PASS FILTER FOR THE FLUX ESTIMATION

Let us find out a digital first-order, low-pass filter required for the flux estimation. Here, we discuss how to transform an analog filter designed using the Laplace transform ($s$-domain) into an equivalent digital filter. The first-order, low-pass filter designed in the $s$-domain has a transfer function of:

$$y(s) = \frac{1}{s+\frac{1}{\tau}} \cdot x(s)$$

Using the bilinear transform to replace the Laplace operator $s$ with a $z$-operator, we can convert the analog first-order, low-pass filter to an equivalent digital filter as follows.

To apply the bilinear transform, we just need to replace the $s$ by $s = 2/T((1-z^{-1})/(1+z^{-1}))$, where $T$ is the sampling period.

$$y[n] = \frac{1}{\frac{2}{T}\left(\frac{1-z^{-1}}{1+z^{-1}}\right)+\frac{1}{\tau}} \cdot x[n] = \frac{1+z^{-1}}{(k_1+k_2)+(k_1-k_2)z^{-1}} \cdot x[n] \qquad \left(k_1 = \frac{2}{T}, k_2 = \frac{1}{\tau}\right)$$

$$\therefore \quad y[n] = \frac{(k_1-k_2)}{(k_1+k_2)} y[n-1] + \frac{1}{(k_1+k_2)}(x[n]+x[n-1])$$

Using the above equation, the digital filter for estimating the stator flux linkage can be given as

$$\therefore \quad \lambda^s_{dqs}[n] = \frac{(k_1-k_2)}{(k_1+k_2)} \lambda^s_{dqs}[n-1] + \frac{1}{(k_1+k_2)}(e^s_{dqs}[n] + e^s_{dqs}[n-1])$$

where $e^s_{dqs}[n] = v^s_{dqs}[n] - R_s i^s_{dqs}[n]$

## 5.3.2 ROTOR FLUX LINKAGES ESTIMATION BASED ON THE ROTOR VOLTAGE EQUATIONS: CURRENT MODEL

In this method the rotor flux linkages are obtained from the rotor voltage equations using the information on the stator currents and the rotor speed.

The rotor flux linkages can be directly obtained from the following rotor voltage equations as

$$v_{dr}^{\omega} = R_r i_{dr}^{\omega} + \frac{d\lambda_{dr}^{\omega}}{dt} - (\omega - \omega_r)\lambda_{qr}^{\omega} = 0 \tag{5.45}$$

$$v_{qr}^{\omega} = R_r i_{qr}^{\omega} + \frac{d\lambda_{qr}^{\omega}}{dt} + (\omega - \omega_r)\lambda_{dr}^{\omega} = 0 \tag{5.46}$$

Here, the nonmeasurable rotor currents can be replaced by the rotor flux linkage and the stator current as

$$i_{dr}^{\omega} = \frac{\lambda_{dr}^{\omega} - L_m i_{ds}^{\omega}}{L_r} \leftarrow \lambda_{dr}^{\omega} = L_r i_{dr}^{\omega} + L_m i_{ds}^{\omega} \tag{5.47}$$

$$i_{qr}^{\omega} = \frac{\lambda_{qr}^{\omega} - L_m i_{qs}^{\omega}}{L_r} \leftarrow \lambda_{qr}^{\omega} = L_r i_{qr}^{\omega} + L_m i_{qs}^{\omega} \tag{5.48}$$

Substituting these rotor currents into Eqs. (5.45) and (5.46), the equations of the rotor flux linkage can be found as

$$\frac{d\lambda_{dr}^{\omega}}{dt} = -\frac{R_r}{L_r}\lambda_{dr}^{\omega} + R_r\frac{L_m}{L_r}i_{ds}^{\omega} + (\omega - \omega_r)\lambda_{qr}^{\omega} \tag{5.49}$$

$$\frac{d\lambda_{qr}^{\omega}}{dt} = -\frac{R_r}{L_r}\lambda_{qr}^{\omega} + R_r\frac{L_m}{L_r}i_{qs}^{\omega} - (\omega - \omega_r)\lambda_{dr}^{\omega} \tag{5.50}$$

There is a difficulty in solving these equations due to the cross-coupling components between the axes. These undesirable cross-coupling components can be eliminated when the rotor flux linkages are estimated from the rotor reference frame ($\omega = \omega_r$) using the measured rotor speed $\omega_r$ as

$$\frac{d\lambda_{dr}^{r}}{dt} = -\frac{R_r}{L_r}\lambda_{dr}^{r} + \frac{R_r}{L_r}L_m i_{ds}^{r} \tag{5.51}$$

$$\frac{d\lambda_{qr}^{r}}{dt} = -\frac{R_r}{L_r}\lambda_{qr}^{r} + \frac{R_r}{L_r}L_m i_{qs}^{r} \tag{5.52}$$

The rotor flux linkages can be obtained from the integral of these two differential equations (5.51) and (5.52). Here, the knowledge of the stator currents in the rotor reference frame is necessary to solve these equations. These currents can be obtained by using the knowledge of the rotor speed $\omega_r$ as

$$i_{ds}^{r} = i_{ds}^{s}\cos\theta_r + i_{qs}^{s}\sin\theta_r \tag{5.53}$$

$$i_{qs}^{r} = -i_{ds}^{s}\sin\theta_r + i_{qs}^{s}\cos\theta_r \tag{5.54}$$

where $\theta_r\left(=\int \omega_r dt\right)$.

Finally, the required rotor flux linkage can be obtained by transforming Eqs. (5.51) and (5.52) back into the stationary reference frame as

$$\lambda_{dr}^{s} = \lambda_{dr}^{r}\cos\theta_r - \lambda_{qr}^{r}\sin\theta_r \tag{5.55}$$

$$\lambda_{qr}^{s} = \lambda_{qr}^{r}\sin\theta_r + \lambda_{qr}^{r}\cos\theta_r \tag{5.56}$$

Besides the knowledge of the rotor speed, this method requires the rotor resistance. Thus, the estimation performance is largely affected by the variation of the rotor resistance. Because of this, online identification and correction of the rotor resistance are essential for improving the estimation performance. In contrast to the voltage model that is advantageous for high-speed operations, this estimation method based on the current model is useful in low-speed regions because it may give an oscillatory response in high-speed regions.

### 5.3.3 COMBINED FLUX ESTIMATION METHOD

In high-speed regions where the back-EMF is large enough, the flux estimation technique based on the voltage model using an integration of the back-EMF has an advantage of accuracy and robustness to parameters variation. However, in low-speed regions where it is hard to obtain accurate information on the back-EMF, the flux estimation based on the current model using the rotor speed has an advantage over the one based on the voltage model. Therefore, it is desirable to estimate the rotor flux linkage by using the current model in low-speed regions and the voltage model in high-speed regions. For this reason, a method combining these two models was introduced to produce a good performance over the whole speed range [6]. Fig. 5.19 shows the block diagram of this combined method that estimates the rotor flux linkages gradually by using the current model in the low-speed region and the voltage model in the high-speed region.

When combining the two models, a method to alternate between these two models is important. The flux estimator in Ref. [6] uses a filter to combine the two models effectively according to the operating frequency as follows.

Fig. 5.19 can be simplified to Fig. 5.20. Here, $\lambda^s_{dqr\_cm}$ denotes the rotor flux linkage estimated by the current model, and $\lambda^s_{dqr\_vm}$ denotes the rotor flux linkage estimated by the voltage model. The gains are given by $K_p = K_1 L_r / L_m$, $K_i = K_2 L_r / L_m$.

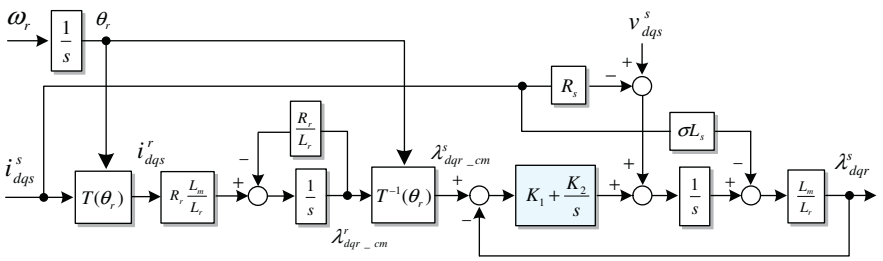



**FIGURE 5.19**

Block diagram of a combined method.

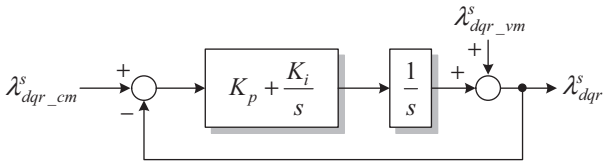



**FIGURE 5.20**

Simplified combined method.

The output of this simplified combined estimator can be expressed as

$$\lambda^s_{dqr} = \frac{s^2}{s^2 + K_p s + K_i}\lambda^s_{dqr\_vm} + \frac{K_p s + K_i}{s^2 + K_p s + K_i}\lambda^s_{dqr\_cm} \tag{5.57}$$

This consists of the sum of the second-order, high-pass filtered rotor flux linkage $\lambda^s_{dqr\_vm}$ based on the voltage model and the second-order, low-pass filtered rotor flux linkage $\lambda^s_{dqr\_cm}$ based on the current model.

This means that the final estimated flux linkage is automatically obtained from the current model in the low-frequency (low-speed) region and the voltage model in the high-frequency (high-speed) region.

In this estimator the transition frequency $\omega_c$ between the two models is commonly selected at 10 Hz. The transition frequency $\omega_c$ can be established through the gains of a proportional−integral (PI) controller as shown in Fig. 5.20. This utilizes the concept of designing the cutoff frequency for a second-order Butterworth filter as follows.

By comparing the transfer function of a second-order, high-pass Butterworth filter with the first term of Eq. (5.57), we can see that there exists the following relationship between gains and parameters of the filter as

$$G(s) = \frac{s^2}{s^2 + 2\zeta\omega_n s + \omega_n^2} \leftrightarrow \frac{s^2}{s^2 + K_p s + K_i} \tag{5.58}$$

$$K_p = 2\zeta\omega_n, \quad K_i = \omega_n^2 \tag{5.59}$$

## TYPES OF SECOND-ORDER BUTTERWORTH FILTER

The transfer functions of second-order filters are:

- High-pass filter: $G(s) = \dfrac{s^2}{s^2 + 2\zeta\omega_n s + \omega_n^2}$
- Band-pass filter: $G(s) = \dfrac{2\zeta\omega_n s}{s^2 + 2\zeta\omega_n s + \omega_n^2}$
- Low-pass filter: $G(s) = \dfrac{\omega_n^2}{s^2 + 2\zeta\omega_n s + \omega_n^2}$

where $\omega_n$ denotes an undamped natural frequency and $\zeta$ denotes a damping ratio.

In the Butterworth filter, if $\zeta = 0.707$, then $\omega_n$ becomes the bandwidth. To set the bandwidth $\omega_n$ equal to the transition frequency $\omega_c$, the PI gains are given as

$$K_p = \sqrt{2}\omega_c, \quad K_i = \omega_c^2 \tag{5.60}$$

Finally, $K_1$ and $K_2$ needed for the estimator in Fig. 5.19 are given as

$$K_1 = K_p \frac{L_m}{L_r} = \sqrt{2}\omega_c \frac{L_m}{L_r} \tag{5.61}$$

$$K_2 = K_i \frac{L_m}{L_r} = \omega_c^2 \frac{L_m}{L_r} \tag{5.62}$$

Besides the estimators mentioned here, there are several different estimation methods that use the modern control theory such as observers using the state equations [7]. The estimated rotor flux linkages can be also used for the sensorless vector control without using any position/speed sensors, which will be discussed in Chapter 9.

## 5.4 FLUX CONTROLLER OF INDUCTION MOTORS

The estimated rotor flux linkage mentioned previously is primarily used to obtain the rotor flux angle. However, this estimated rotor flux linkage may also be used for flux control to improve the stability of the torque control or to achieve the field-weakening control for high-speed operations.

From Section 5.3, we can see that the relationship between the $d$-axis stator currents $i_{ds}^e$ and the rotor flux linkage $\lambda_{dr}^e$ for the vector-controlled induction motor is given as

$$\lambda_{dr}^e = \frac{L_m}{1 + T_r p} i_{ds}^e \tag{5.63}$$

The magnitude of the rotor flux linkage can be controlled by the $d$-axis current. However, its instantaneous value is not proportional to the $d$-axis current when the $d$-axis current is changing. Thus when the magnitude of the rotor flux linkage has to be changed quickly for the field-weakening control, the rotor flux linkage needs to be controlled directly. Moreover, even when an induction motor is driven with a constant flux level, the flux control can enhance the stability of the drive system.

For the flux control, a PI controller is commonly used. Now we will take a close look at the design of such flux controller, i.e., how to select PI gains for achieving the desired control bandwidth.

### 5.4.1 PROPORTIONAL–INTEGRAL FLUX CONTROLLER

In the vector control based on the rotor flux, the magnitude of the rotor flux linkage can be controlled by the $d$-axis current $i_{ds}^{e}$, so the output of the PI flux controller has to be the $d$-axis current. The block diagram of the flux control system from Eq. (5.63) and a PI controller can be given as Fig. 5.21.

The gains of a PI flux controller can be determined in a similar way as those of a current/speed controller as was described in Chapter 2, as follows.

First, we assume that the dynamics of the $d$-axis current controller is fast enough compared to the flux change. The open-loop transfer function of the flux control system shown in Fig. 5.21 is given as

$$G_f^o(s) = \left(K_{pf} + \frac{K_{if}}{s}\right) \cdot \frac{L_m \dfrac{R_r}{L_r}}{s + \dfrac{R_r}{L_r}} = \frac{K_{pf}\left(s + \dfrac{K_{if}}{K_{pf}}\right)}{s} \cdot \frac{L_m \dfrac{R_r}{L_r}}{s + \dfrac{R_r}{L_r}} \tag{5.64}$$

Similar to the design of a current controller described in Section 2.6, if the zero of the PI controller is designed to cancel the pole of the system, i.e., $K_{if}/K_{pf} = R_r/L_r$, then the transfer function of Eq. (5.64) can be simplified as

$$G_f^o(s) = \frac{K_{pf} L_m \dfrac{R_r}{L_r}}{s} \tag{5.65}$$

The gain crossover frequency of this open-loop frequency response equals to the bandwidth of the flux control system. Hence the proportional and the integral gains to obtain the required control bandwidth $\omega_f$ can be given as

$$\text{Proportional gain:} \quad K_{pf} = \frac{L_r}{R_r L_m}\omega_f \tag{5.66}$$

$$\text{Integral gain:} \quad K_{if} = \frac{R_r}{L_r}K_{pf} = \frac{\omega_f}{L_m} \tag{5.67}$$

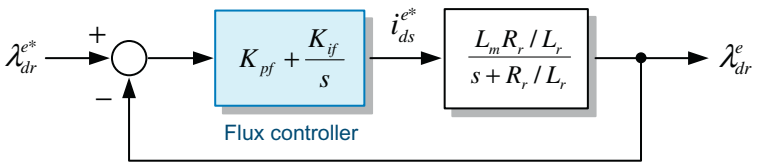



**FIGURE 5.21**

Flux control system including PI flux controller.

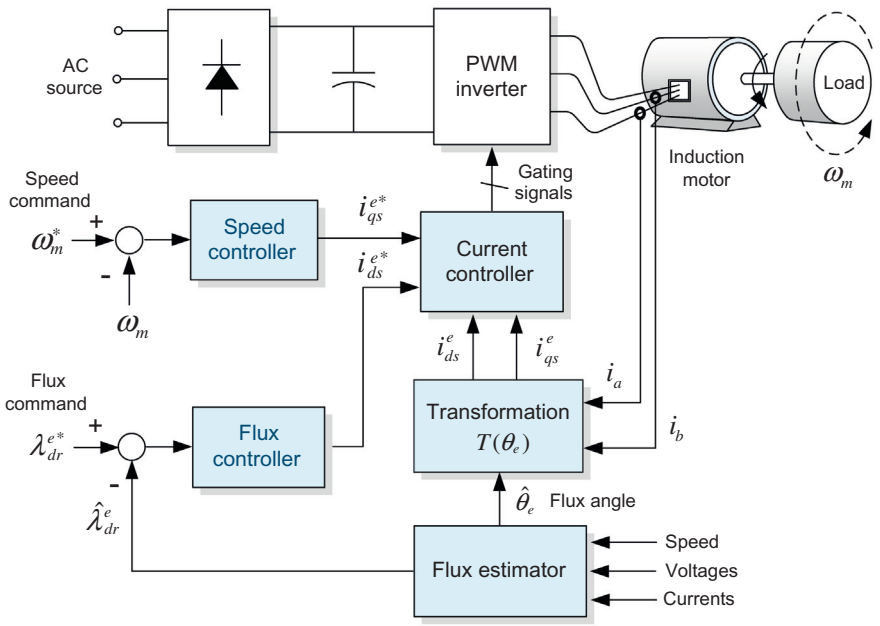



**FIGURE 5.22**

Vector control system including speed and flux controllers.

When the bandwidth of the current controller is several thousand radians per second, the bandwidth of the flux controller is designed generally within several ten to several hundred radians per second. This flux controller also needs an anti-windup control just like the speed/current controllers. The performance of the flux control can also be enhanced by the feedforward compensation using the flux command.

The diagram of the vector control system including speed and flux controllers for an induction motor is shown in Fig. 5.22. A PI controller as mentioned in Chapter 2 is commonly used for the speed control. The gain selection procedure of the PI speed controller was explained in detail in Section 2.7.

## 5.5 VECTOR CONTROL OF PERMANENT MAGNET SYNCHRONOUS MOTORS

Due to their superior performance compared to DC motors or induction motors, PMSMs have become increasingly popular in various high-performance motor drive applications. The vector control for PMSMs is relatively simple compared

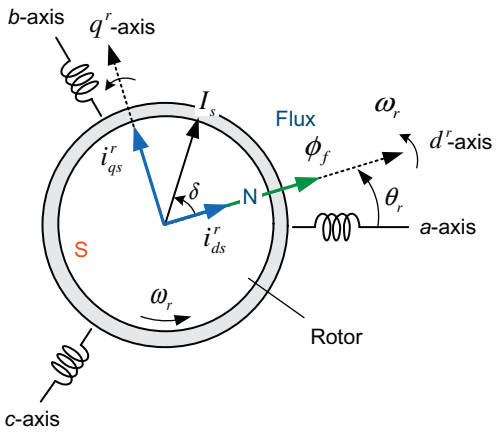



**FIGURE 5.23**

Rotor flux in a permanent magnet synchronous motor.

to that of induction motors. As shown in Fig. 5.23, this is because the rotor position itself is the position of the rotor flux, which is essential information for the vector control. Therefore, unlike for an induction motor, the complicated estimation algorithms are not required to obtain the rotor flux for the vector control of a PMSM.

As shown in Chapter 4, PMSMs can be classified into SPM and IPM types. These two types differ in the output torque expression and thus are slightly different in the way of implementing the vector control. First, we will begin with the vector control method for an SPMSM.

The three requirements for the instantaneous torque control of a DC motor can be rewritten to apply to a PMSM as follows:

1. The space angle between the field flux and the torque-producing current is always 90 degrees.
2. Both the field flux and the torque-producing current can be controlled independently.
3. The torque-producing current has to be controlled instantaneously.

Now we will take a look at how we can meet these three requirements for a PMSM. For a PMSM, the requirement 2 for the instantaneous torque control can be inherently fulfilled. In PMSMs the field flux of the rotor is produced by permanent magnets, while the torque-producing current is given by the current of stator windings. Thus the field flux and the torque-producing current can be controlled independently. In addition, the torque-producing current (i.e., the stator current) can be controlled instantaneously by the synchronous reference frame current regulator and the PWM inverter and thus can satisfy the requirement 3.

Likewise, the requirements 2 and 3 are relatively easy to fulfill for a PMSM. For the vector control of a PMSM, it is important to fulfill the requirement 1, i.e., to maintain the space angle between the field flux and the torque-producing current at 90 degrees. To achieve this, it is necessary to first transform the three-phase *abc* stator currents into two $d-q$ axes currents, just like in an induction motor. When transforming, the $d$-axis is aligned with the position of the rotor flux (i.e., the flux of the permanent magnet on the rotor) and then the $q$-axis current becomes the true torque-producing current, which is orthogonal to the rotor flux. In a PMSM, the permanent magnet flux of the rotor is rotating at the same speed as the rotor speed $\omega_r$ as shown in Fig. 5.23. Thus, we have to make the $d-q$ axes rotate at the rotor speed $\omega_r$. This implies that we need to use the transformation of the stator currents into the *rotor reference frame* ($d^r - q^r$ axis). Such transformation requires the rotor position $\theta_r$, i.e., the position of the permanent magnet. This can be obtained from the position sensors such as a resolver or an absolute encoder, which will be discussed in Chapter 9. Unlike in induction motors, it should be noted that the absolute initial position of the rotor flux is needed for the start-up of a PMSM, so an absolute type position sensor has to be used. However, instead of costly absolute type position sensors, an incremental encoder accompanied by an extra initial position detection method is often used.

### 5.5.1 VECTOR CONTROL OF A SURFACE-MOUNTED PERMANENT MAGNET SYNCHRONOUS MOTOR

In the vector control of an SPMSM, the stator currents are transformed into the rotor reference frame ($d^r - q^r$ axis) where the $d$-axis is assigned as the rotor flux position $\theta_r$ as shown in Fig. 5.24.

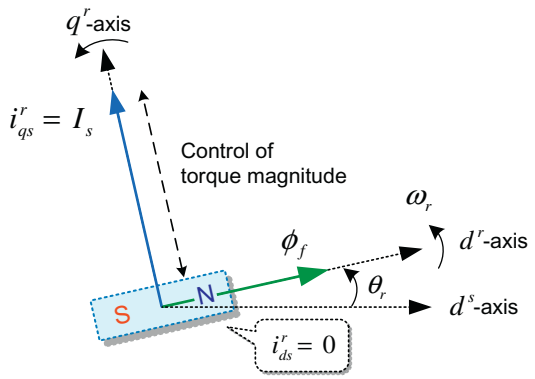



**FIGURE 5.24**

$d-q$ currents in the vector control of an SPMSM.

Here, it is important to note that an SPMSM does not require any $d$-axis current to produce the flux unlike an induction motor. Moreover, the $d$-axis current does not contribute to the torque production, which is proportional to only the $q$-axis component of the stator current. This can be seen from the following torque expression of an SPMSM.

$$T_e = \frac{P}{2}\frac{3}{2}\phi_f i_{qs}^r \tag{5.68}$$

Therefore, it is desirable to assign all the stator currents to the $q$-axis current to make a full use of the allowed motor current. In other words, in the vector control of an SPMSM, all the stator current $I_s$ is used as the $q$-axis current $i_{qs}^r$, while the $d$-axis current is zero.

Consequently, the necessary condition for the maximum torque per ampere (MTPA) in the vector control of an SPMSM is $i_{ds}^r = 0$. In such condition, if we can control the $q$-axis current $i_{qs}^r$ instantaneously, then the torque of the SPMSM can be controlled instantaneously like in the DC motors. The diagram of the vector control system for an SPMSM is shown in Fig. 5.25.

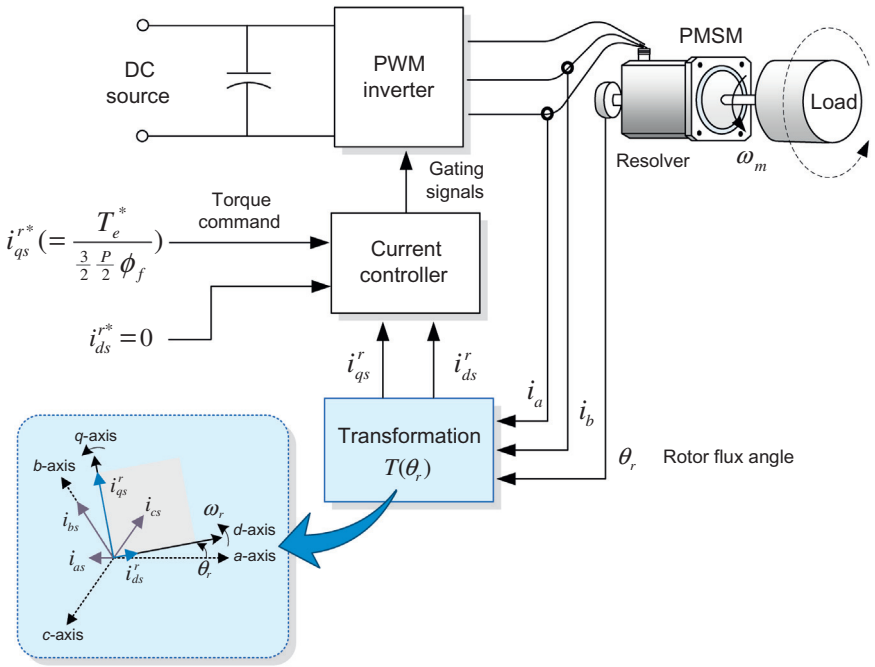



**FIGURE 5.25**

Block diagram of a vector control system for a PMSM.

In this system the $d$-axis current command $i_{ds}^{r*} = 0$, while the $q$-axis current command is given by using Eq. (5.70) from the required torque command $T_e^*$ as

$$i_{ds}^{r*} = 0 \tag{5.69}$$

$$i_{qs}^{r*} = \frac{T_e^*}{\frac{P}{2}\frac{3}{2}\phi_f} \tag{5.70}$$

If the stator currents of the SPMSM can be regulated rapidly to follow these current commands by using a current regulator, then the instantaneous torque control can be achieved. As a current regulator, a synchronous reference frame current regulator is usually adopted due to its excellent current control performance, which will be discussed in Chapter 6, in more detail. For the synchronous current regulators, we need to transform the three-phase stator currents, $i_{as}$, $i_{bs}$, $i_{cs}$, of the SPMSM into the synchronous $dq$ stator currents $i_{ds}^r$ and $i_{qs}^r$ by using the rotor flux angle $\theta_r$.

### 5.5.2 VECTOR CONTROL OF AN INTERIOR PERMANENT MAGNET SYNCHRONOUS MOTOR

Next, we will examine the vector control strategy for an IPMSM, where $L_{ds} \neq L_{qs}$. In the vector control of an IPMSM the $d-q$ axes currents required for the MTPA are different from those of an SPMSM. This is because, in contrast to that of SPMSMs, the torque of IPMSMs consists of two terms as

$$T_e = \frac{P}{2}\frac{3}{2}\left[\phi_f i_{qs}^r + (L_{ds} - L_{qs}) i_{ds}^r i_{qs}^r\right] \tag{5.71}$$

In addition to the first term of Eq. (5.71) that represents the *magnetic torque* of an SPMSM, an IPMSM has a *reluctance torque*, the second term, which is produced by the difference between the inductance values of the two axes. To produce the reluctance torque, both the $d$- and the $q$-axes components of the stator current are required. In most commonly used parallel topology IPMSMs as described in Chapter 4, the $q$-axis inductance $L_{qs}$ is typically larger than the $d$-axis inductance $L_{ds}$. Thus, the $d$-axis current must have a negative polarity for the reluctance torque to be added to the magnet torque, i.e., $i_{ds}^r < 0$. Similar to an induction motor, the stator current of an IPMSM needs to be divided into $d$-and $q$-axes components as shown in Fig. 5.26.

In this case, we need to know how the stator current is divided into the $d$-and $q$-axes stator currents properly to produce the MTPA. These optimal currents can be obtained as follows.

As seen in Eq. (5.71), there are many different combinations of $d$- and $q$-axes currents that produces the same torque. Fig. 5.27 shows the curve consisting of

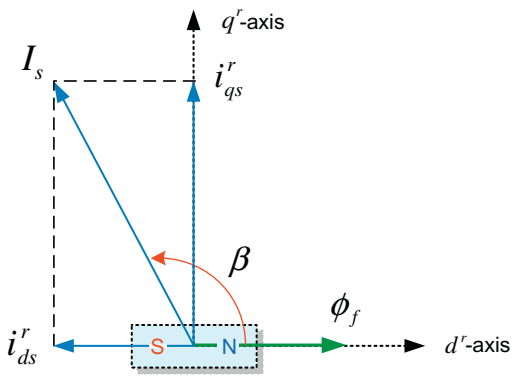



**FIGURE 5.26**

*d–q* currents in the vector control of an IPMSM.

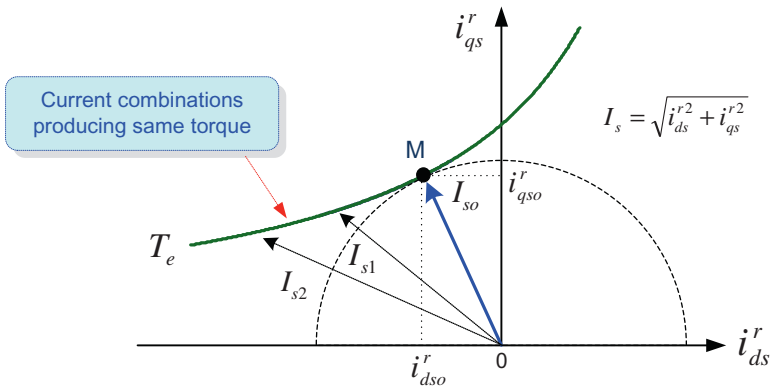



**FIGURE 5.27**

Curve consisting of current combinations producing the same torque.

these currents. Among these combinations, there is an optimal one that gives the smallest stator current. This optimal combination is the point M, $I_{sc}(i^r_{dso}, i^r_{qso})$, at which the circle with a radius of $I_{so}$ is tangent to the curve. If an IPMSM operates with the *d*-and *q*-axes currents at this optimal point, then it can produce the MTPA. Such operation method with the optimal combination of *d*-and *q*-axes currents that leads to the smallest stator current for producing the given torque command is called the *MTPA control*. The optimal combination of the *d*-and *q*-axes currents varies with the required torque.

Now we will find out the optimal combination of $d$-and $q$-axes currents for a given torque command [8]. First, the torque expression and $d$-and $q$-axes currents are normalized as

$$T_{en} = \frac{T_e}{T_b}, \quad i_{dn} = \frac{i_{ds}^r}{i_b}, \quad i_{qn} = \frac{i_{qs}^r}{i_b} \tag{5.72}$$

where $i_b (= \phi_f/(L_{ds} - L_{qs}))$ and $T_b (= \frac{P}{2}\frac{3}{2}\phi_f i_b)$.

The normalized torque can be rewritten as

$$\begin{aligned} T_{en} = \frac{T_e}{T_b} &= \frac{\left[ i_{qs}^r + (L_{ds} - L_{qs}) \dfrac{i_{ds}^r i_{qs}^r}{\phi_f} \right]}{i_b} \\ &= \frac{i_{qs}^r}{i_b} - \frac{i_{qs}^r i_{ds}^r}{i_b^2} = i_{qn}(1 - i_{dn}) \end{aligned} \tag{5.73}$$

The process of obtaining the optimal stator current for the MTPA control is as follows. First, find the smallest $d$-axis current $i_{dno}$ for producing the torque command $T_{en}$. Using Eq. (5.73), the stator current can be expressed as a function of $i_{dno}$ as

$$I_{sno}^2 = i_{dno}^2 + i_{qno}^2 = i_{dno}^2 + \left( \frac{T_{en}}{1 - i_{dno}} \right) \tag{5.74}$$

Differentiating Eq. (5.74) with respect to $i_{dno}$ and making the result equal to zero gives

$$i_{dno}^4 - 3i_{dno}^3 + 3i_{dno}^2 + i_{dno} - T_{en}^2 = 0 \tag{5.75}$$

The optimal $d$-axis current $i_{dno}$ can be obtained by solving Eq. (5.75) for the given torque command.

Likewise, we can find the smallest $q$-axis current $i_{qno}$ for producing the torque command $T_{en}$. After expressing the stator current of Eq. (5.74) as a function of $i_{qno}$, differentiating this with respect to $i_{qno}$ gives

$$i_{qno}^4 + T_{en} i_{qno} - T_{en}^2 = 0 \tag{5.76}$$

The optimal $q$-axis current $i_{qno}$ can be obtained by solving Eq. (5.76) for the given torque command.

Fig. 5.28 shows the optimal current commands for the MTPA operation by solving Eqs. (5.75) and (5.76) for the torque commands. A look-up table for the optimal current commands is commonly used instead of online calculations.

In a speed controller the command to produce the output torque is often given as a stator current. For this stator current command $I_s^*$, we can obtain the

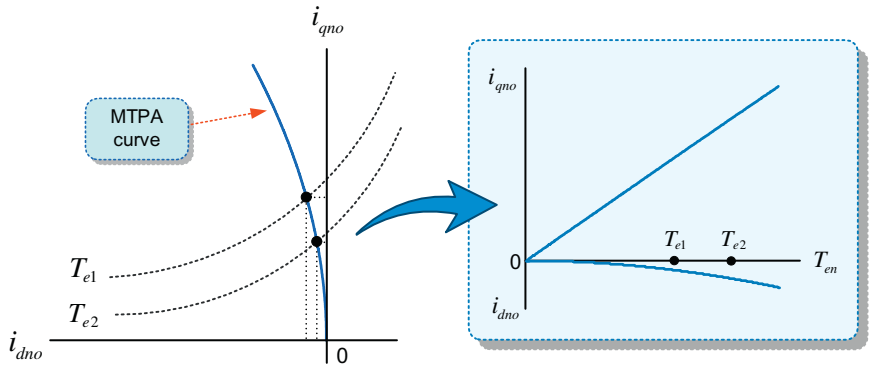



**FIGURE 5.28**

*d*–*q* axes current commands for MTPA operation.

$d-q$ axes stator current commands for the MTPA operation as follows [9]. The torque expression of Eq. (5.71) can be rewritten as a function of the stator current $I_s^*$ as

$$T_e = \frac{P}{2}\frac{3}{2}\left[\phi_f I_s^* \sin\beta + \frac{(L_{ds}-L_{qs})}{2} I_s^{*2} \sin 2\beta\right] \tag{5.77}$$

where $\beta$ denotes the angle between the $d$-axis and the stator current vector $I_s^*$ as shown in Fig. 5.26.

The $\beta_{max}$ for producing the maximum torque can be obtained by solving $dT_e/d\beta = 0$ as

$$\begin{aligned} &\frac{\partial T_e}{\partial \beta} = \frac{P}{2}\frac{3}{2}\left[\phi_f I_s^* \cos\beta + (L_{ds}-L_{qs}) I_s^{*2} \cos 2\beta\right] = 0 \\ &\rightarrow \beta_{\max} = \cos^{-1}\left(\frac{-\phi_f + \sqrt{\phi_f^2 + 8(L_{ds}-L_{qs})^2 I_s^{*2}}}{4(L_{ds}-L_{qs}) I_s^*}\right) \end{aligned} \tag{5.78}$$

From $\beta_{max}$, the optimal $d$- and $q$-axes current commands are given as

$$\begin{aligned} i_{dso}^r &= I_s^* \cos\beta_{\max} \\ &= \frac{-\phi_f + \sqrt{\phi_f^2 + 8(L_{ds}-L_{qs})^2 I_s^{*2}}}{4(L_{ds}-L_{qs})} \end{aligned} \tag{5.79}$$

$$i_{qso}^r = I_s^* \sin\beta_{\max} \tag{5.80}$$

To obtain the optimal currents for the MTPA operation by using the methods just mentioned, the exact knowledge of stator inductances and magnetic

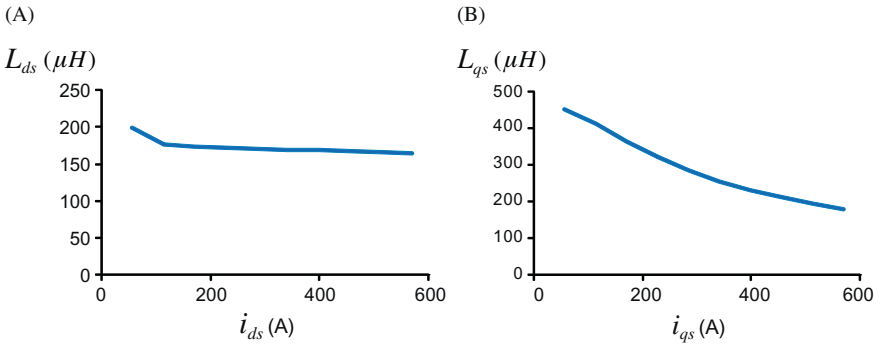



**FIGURE 5.29**

Variation of inductances with currents. (A) *d*-axis inductance and (B) *q*-axis inductance.

flux is necessary. The magnetic flux varies considerably with the operating temperature. In addition, each inductance value of $d-q$ axes depends on the magnitude of the current of each axis. As an example, the variation of $d-q$ axes inductances of an 80-kW IPMSM according to each current is shown in Fig. 5.29. Because of the presence of a permanent magnet, the *d*-axis magnetic circuit is in the saturated condition even without the current. Thus the *d*-axis inductance does not change much with the *d*-axis current as shown in Fig. 5.29A. On the other hand, the *q*-axis magnetic circuit consists of an iron core which is easily saturated with its current, and thus the *q*-axis inductance may be changed significantly with the *q*-axis current as shown in Fig. 5.29B.

Furthermore, it is also known that each inductance of $d-q$ axes may change with the current of the other axis due to cross-saturation effect between the $d-q$ axes [10,11]. Therefore the exact knowledge of the inductances and magnetic flux at various operating conditions is very important for a successful fulfillment of the MTPA control.

The diagram of the vector control system for an IPMSM is shown in Fig. 5.30. For the output torque command, the $d-q$ axes stator current commands for the MTPA operation are given from the calculations or a look-up table as stated earlier. If the stator currents of the IPMSM can be regulated rapidly to follow these current commands by using a synchronous reference frame current regulator, then the instantaneous torque control of the IPMSM can be achieved. When using this synchronous current regulator, we need to transform the three-phase stator currents, $i_{as}$, $i_{bs}$, $i_{cs}$, of the IPMSM into synchronous $dq$ currents $i^r_{ds}$ and $i^r_{qs}$ by using the rotor flux angle $\theta_r$.

Fig. 5.31 shows the experimental results for the vector control on an 800-W, 8-pole IPMSM when the speed command is changed from 200 to 2000 r/min.

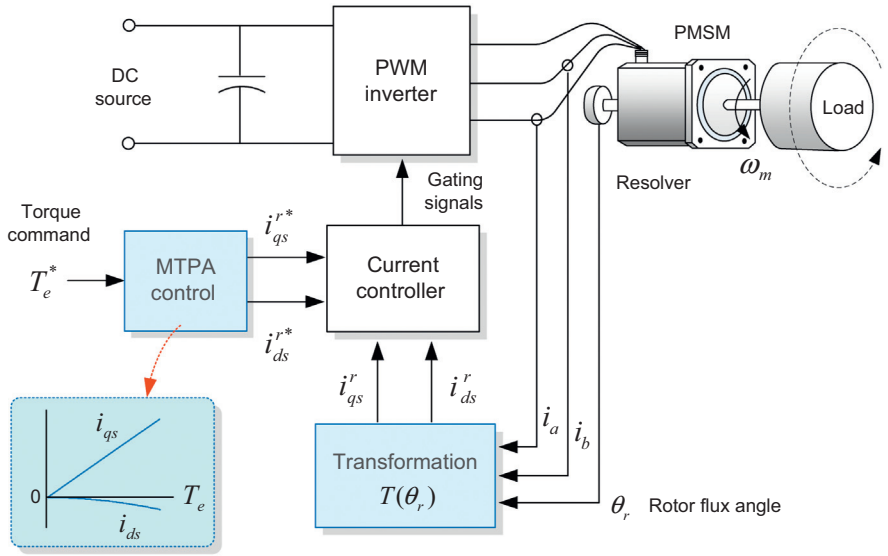



**FIGURE 5.30**

Block diagram of the vector control system for a PMSM.

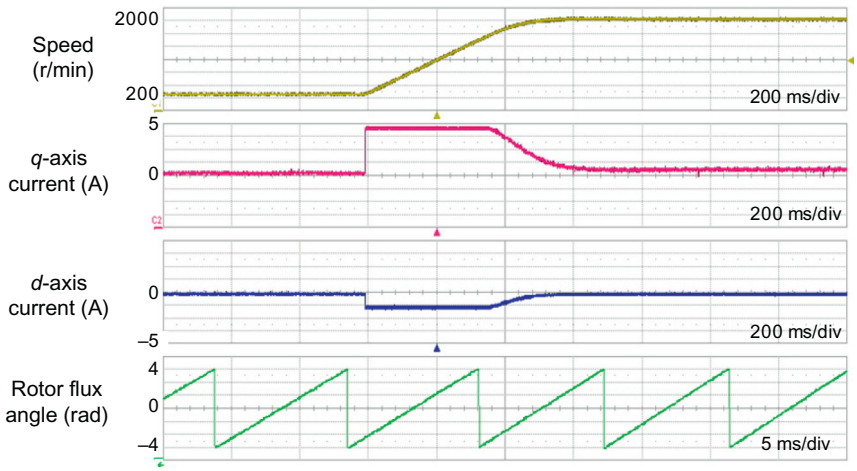
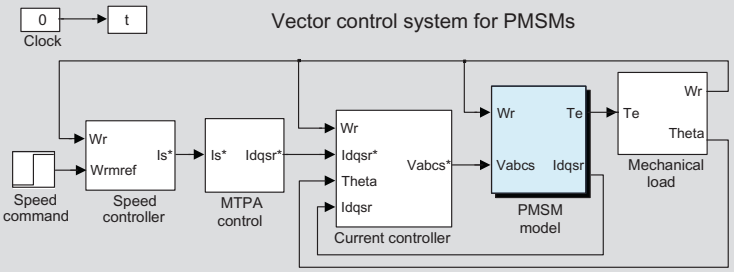



**FIGURE 5.31**

Experimental results for the vector control on an 800-W IPMSM.

## MATLAB SIMULINK SIMULATION: VECTOR CONTROL OF A PERMANENT MAGNET SYNCHRONOUS MOTOR

- Overall simulation block (not including an inverter)




- PMSM model block
  $d-q$ axes model in the rotor reference frame (see Chapter 4)

$$v_{ds}^r = R_s i_{ds}^r + \frac{d\lambda_{ds}^r}{dt} - \omega_r \lambda_{qs}^r$$

$$v_{qs}^r = R_s i_{qs}^r + \frac{d\lambda_{qs}^r}{dt} + \omega_r \lambda_{ds}^r$$

$$\lambda_{ds}^r = L_{ds} i_{ds}^r + \phi_f$$

$$\lambda_{qs}^r = L_{qs} i_{ds}^r$$

$$T_e = \frac{P}{2}\frac{3}{2}\left[\phi_f i_{qs}^r + (L_{ds} - L_{qs}) i_{ds}^r i_{qs}^r\right]$$

- MTPA control block

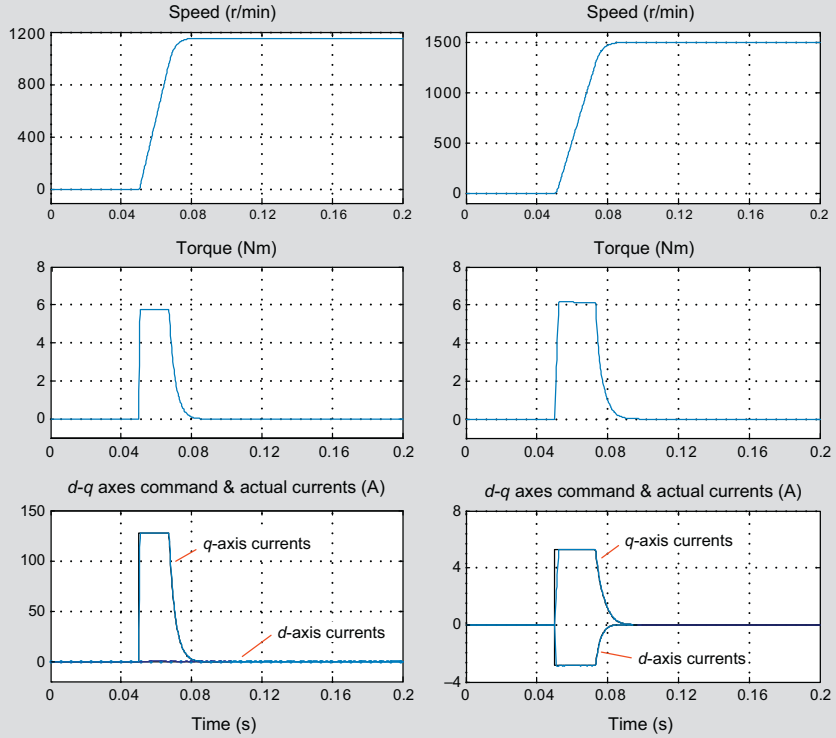
$$d\text{-axis current command:} \quad I_{ds}^r = \frac{-\phi_f + \sqrt{\phi_f^2 + 8(L_{ds} - L_{qs})^2 I_s^2}}{4(L_{ds} - L_{qs})}$$

$$q\text{-axis current command:} \quad I_{qs}^r = \sqrt{I_s^2 - I_{ds}^{r2}}$$

- Other blocks
  - Mechanical load model: refer to Chapter 1.
  - Speed controller model: refer to Chapter 2.
  - Current controller model: Chapter 6.
- Simulation conditions
  A SPMSM and an IPMSM will be simulated for acceleration characteristics when speed commands are 1200 r/min (SPMSM) and 1500 r/min (IPMSM), respectively.
- Simulation results

(*Continued*)

**MATLAB SIMULINK SIMULATION: VECTOR CONTROL OF A PERMANENT MAGNET SYNCHRONOUS MOTOR (CONTINUED)**




## REFERENCES

[1] M. Ruff, H. Grotstollen, Off-line identification of the electrical parameters of an industrial servo drive system, in: Conf. Rec. IEEE IAS Annu. Meeting, 1996, pp. 213–220.

[2] T.M. Rowan, R.J. Kerkman, D. Leggate, A simple on-line adaptation for indirect field orientation of an induction machine, in: Conf. Rec. IEEE IAS Annu. Meeting, 1989, pp. 579–587.

[3] J.K. Seok, S.I. Moon, S.K. Sul, Induction machine parameter identification using PWM inverter at standstill, IEEE Trans. Energy Convers. 12 (2) (Jun. 1997) 127–132.

[4] K.B. Nordin, D.W. Novotny, D.S. Zinger, The influence of motor parameters deviations in feedforward field orientation drive systems, IEEE Trans. Ind. Appl. IA-21 (4) (Jul./ Aug. 1985) 1009–1015.
[5] D. Fodor, D. Diana, G. Griva, F. Profumo, IFO control performance considering parameters detuning and rotor speed error, in: Conf. Rec. IEEE IAS Annu. Meeting, 1994, pp. 719–725.
[6] P.L. Jansen, R.D. Lorenz, A physically insightful approach to the design and accuracy assessment of flux observers for field oriented induction machine drives, IEEE Trans. Ind. Appl. 30 (1) (Jan./Feb. 1994) 101–110.
[7] H. Kuboda, M. Matsuse, T. Nakano, DSP-based speed adaptive flux observer of induction motor, IEEE Trans. Ind. Appl. 29 (2) (Mar./Apr. 1993) 344–348.
[8] T.M. Jahns, G.B. Kliman, T.W. Neumann, Interior permanent-magnet synchronous motors for adjustable-speed drives, IEEE Trans. Ind. Applicat. IA-22 (4) (Jul./Aug. 1986) 738–747.
[9] S. Morimoto, T. Hirasa, Servo drive system and control characteristics of salient pole permanent magnet synchronous motor, IEEE Trans. Ind. Appl. 29 (2) (Mar./Apr. 1993) 338–343.
[10] T. Gopalarathnam, R. McCann, Saturation and armature reaction effects in surface-mount PMAC Motors, in: Proc. IEEE international Conf. IEMDC 2001, 2001, pp. 618–621.
[11] B. Stumberger, et al., Evaluation of saturation and cross-magnetization effects in interior permanent-magnet synchronous motor, IEEE Trans. Ind. Appl. 39 (5) (Sept./ Oct. 2003) 1264–1271.

CHAPTER

# Current regulators of alternating current motors

# 6

A current regulator plays a role in making a motor current achieve its desired value, and is an essential part of the vector control system for alternating current (AC) motors. For an accurate instantaneous torque control by using the vector control, the actual motor currents must follow the current commands required to produce the flux and torque regardless of hindrances such as back-electromotive force (back-EMF), leakage inductance, and resistance of windings. Thus for the implementation of the vector control system, it is very important to design the current regulator well. In this chapter we will examine the current regulation techniques for the vector control system of AC motors.

The system configuration for the current control of a three-phase load is shown in Fig. 6.1. The current regulator plays a role in generating gating signals for the switching devices of a pulse width modulation (PWM) inverter, which can produce the output voltage to make the required current flow into the three-phase load.

In other words, the main function of the current regulator is to transform the current error into gating signals for the switching devices in the time domain.

For the case of using a voltage source type PWM inverter, there have been four different types of current regulators researched as:

- Predictive current regulator
- Hysteresis current regulator
- Ramp comparison current regulator or sine-triangle comparison regulator
- $d-q$ axes current regulator

A current regulator consists of an error compensation part and a voltage modulation part as shown in Fig. 6.2. The error compensation part produces a command voltage to reduce the error between the actual and command currents, whereas the voltage modulation part generates gating signals for switching devices to accurately produce the command voltage given by the error compensation part.

In the conventional regulators, such as a predictive current regulator, hysteresis current regulator, and ramp comparison current regulator, the error compensation part and the voltage modulation part are formed as one. In contrast, in a $d-q$ axes current regulator, these two parts are constructed separately. In this regulator a proportional integral (PI) controller is commonly used for the error compensation. Various PWM techniques are used for the voltage modulation, which will be described in Chapter 7.

**Electric Motor Control. DOI:** http://dx.doi.org/10.1016/B978-0-12-812138-2.00006-4
© 2017 Elsevier Inc. All rights reserved.



Hesai Exhibit 1030, page 250

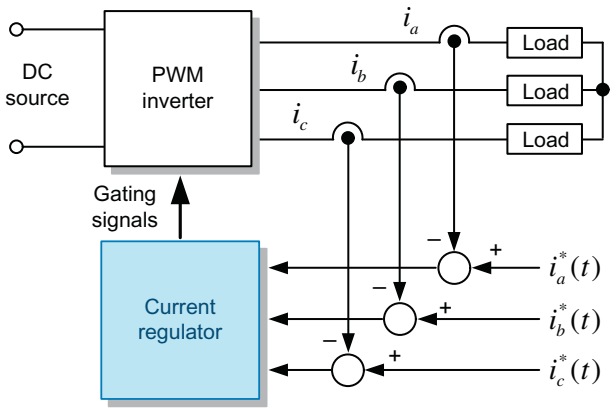



**FIGURE 6.1**

Current control of a three-phase load.

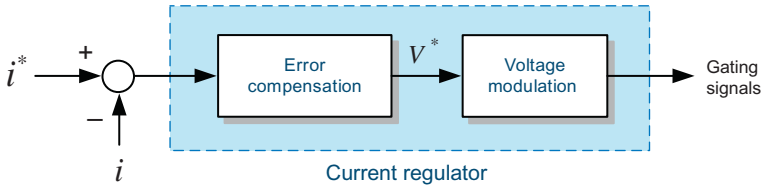



**FIGURE 6.2**

Configuration of a current regulator.

Now we will explore these current regulators. First, we discuss briefly the predictive current regulator, which is based on a mathematical model of the load. In the predictive current regulator the current error is calculated at every current control period, and the required voltage is determined to minimize the error using the load mathematical model. Afterward, the on/off states of the switching devices are directly chosen to produce the required voltage. The actual load current in the predictive current regulator may lag behind the command current by more than one sampling time. Furthermore, its performance will be greatly affected by the variation of parameters used in the load mathematical model. Next, we will examine the rest of the current regulators in more detail.

## 6.1 HYSTERESIS REGULATOR

As a type of bang−bang control, a hysteresis regulator is the simplest current controller, directly controlling the on/off states of switches according to the current error. The operation principle of a hysteresis controller is as follows [1].

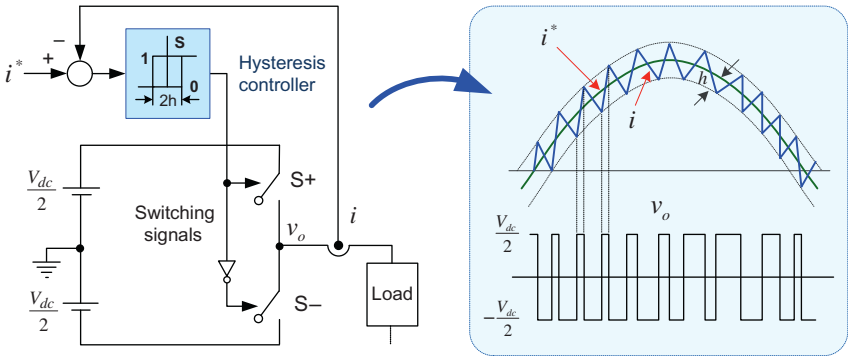



**FIGURE 6.3**

Operation principle of a hysteresis regulator.

In the hysteresis regulator, as shown in Fig. 6.3, if the error between the actual current and the command current is more than the preset value $h$ (called *hysteresis band*), then the state of the switch is changed to reduce the error. In other words, the state of the switches is changed whether the actual current is greater or less than the command current by the hysteresis band $h$ as:

- $i^* - i \leq -h$: lower switch S$-$ is turned on to decrease the load current by producing a negative voltage $(-\frac{1}{2}V_{dc})$
- $i^* - i \geq h$: upper switch S$+$ is turned on to increase the load current by producing a positive voltage $(\frac{1}{2}V_{dc})$

Fig. 6.4 describes the operating range of an actual current vector **i** in the complex plane for the hysteresis control. For example, if the actual current of the phase $a$ increases more than its command, then the actual current vector **i** moves to the positive (+) of the phase $a$ axis. If the current error of the phase $a$ is equal to the hysteresis band $-h$, then the current vector **i** reaches the $-$A line. At this moment, the lower switch (S$-$) of the phase $a$ will be turned on and the output voltage will become $-V_{dc}/2$. This will cause the current to decrease. On the contrary, if the current error of the phase $a$ becomes $h$, then the current vector **i** reaches the $+$A line. Thus the upper switch (S$+$) will be turned on and the output voltage will become $V_{dc}/2$. This will cause the current to increase.

Likewise, for the phases $b$ and $c$, the switching actions can be done independently with their own hysteresis band. Since the error of each phase current is limited within $h$ by the hysteresis action, the operating area of the current vector **i** can be considered to be inside the hexagon consisting of the six switching lines of the three-phase axes. However, in practice, the current errors can vary up to double the hysteresis band, $2h$, for a Y(wye)-connected three-phase load with a floating neutral point. In that load, the sum of the three-phase currents is zero (i.e., $i_{as} + i_{bs} + i_{cs} = 0$), and thus all three-phase currents cannot be controlled independently. This results in the current errors of 2h.

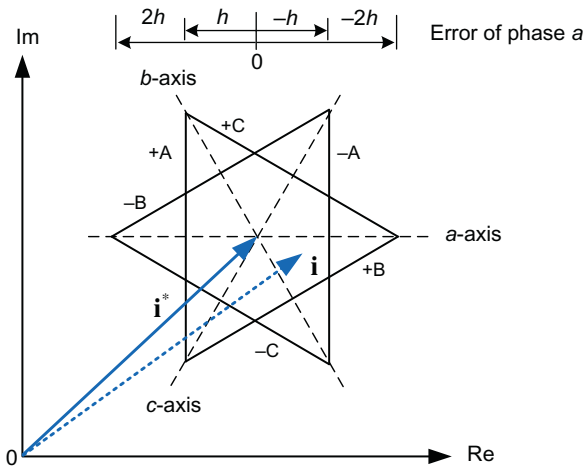



**FIGURE 6.4**

Operating range of current vector for hysteresis control [1].

Hysteresis current regulators have been widely used for small systems because of their simple implementation and an excellent dynamic performance. However, hysteresis controllers are inherently an analog controller. In addition, the switching frequency is not constant since the turn-on/off instants of switches can change with the back-EMF and load condition. This makes the thermal design of a switching power converter and the filter design of switching noise elimination difficult because the losses and the harmonics generated by the switching actions are a function of the switching frequency. For these reasons, its usage nowadays is limited. In addition, the switching frequency may increase sharply (called *limit cycle*) at low operating frequencies, where only the effective voltage vectors are more likely to be selected due to a small back-EMF. This problem may be improved by adding an offset to the hysteresis band.

## 6.2 RAMP COMPARISON CURRENT REGULATOR [1]

In a ramp comparison current regulator as shown in Fig. 6.5, the switching states are determined by comparing the current error with the triangular carrier wave based on the following principle:

- Current error $i_{err} >$ carrier wave: upper switch S + is turned on to produce a positive voltage ($\frac{1}{2}V_{dc}$).
- Current error $i_{err} <$ carrier wave: lower switch S − is turned on to produce a negative voltage ($-\frac{1}{2}V_{dc}$).

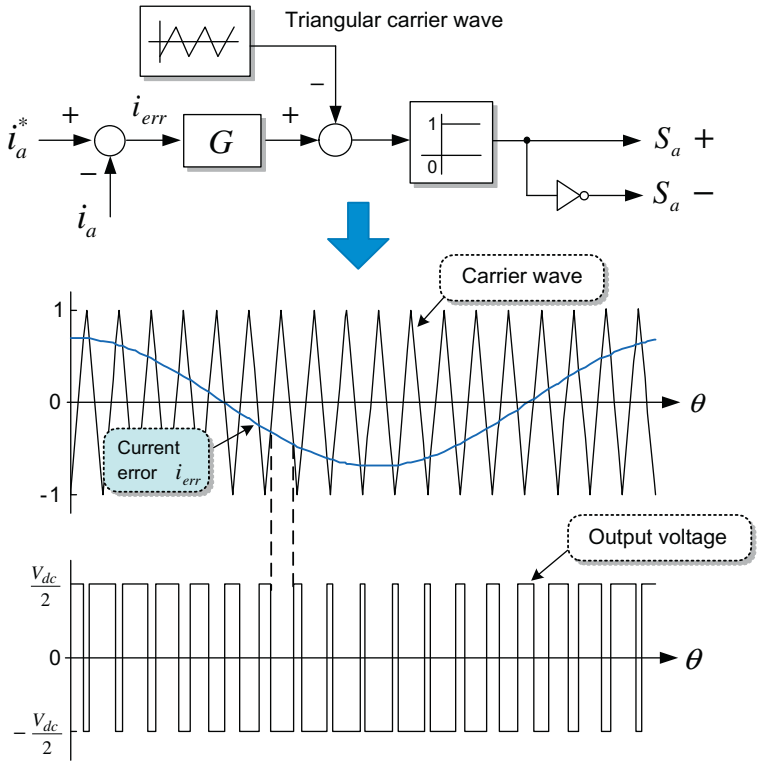



**FIGURE 6.5**

Operation principle of the ramp comparison current regulator.

For a proper operation of this regulator, the current error should be less than the triangle carrier wave. In this regulator it can be seen that the switching states are changed only at the intersection of the current error and the triangular carrier wave. Thus the switching frequency is equal to the triangle wave frequency and becomes constant. This is a big advantage of this regulator over the hysteresis regulators. However, one major drawback of this regulator is that it has steady-state magnitude and phase errors in the resultant current.

The performance of this regulator is shown in Fig. 6.6. We can see that the actual current has steady-state errors in amplitude and phase with regard to the reference current. These errors increase with the back-EMF, and thus it is hard to obtain a good current regulation performance at high speed operation. A compensator $G$ such as a $P$ (proportional) or PI controller is often used to reduce these errors as shown in Fig. 6.5. Although larger gains can reduce the errors, there is a limit to increasing the gains due to the increase in noise sensitivity. Moreover, a PI controller is unsatisfactory for alternating current (AC) regulation because it can eliminate the control error completely for only direct current (DC) regulation.

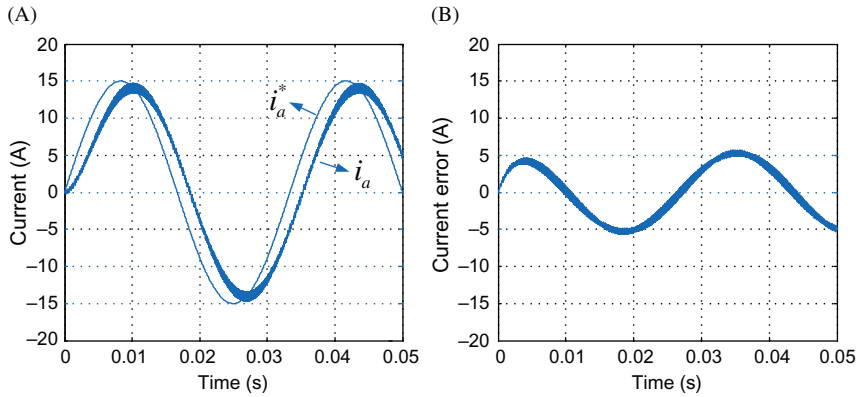



**FIGURE 6.6**

Performance of the ramp comparison current control. (A) Reference current and actual current and (B) current error.

## 6.3 *d-q* AXES CURRENT REGULATORS

Since a three-phase AC motor has three stator currents, we may consider at first that three current controllers are needed to regulate their currents individually. However, since their windings are commonly connected in wye with a floating neutral point, the sum of their currents is equal to zero and thus only two of the currents are controllable independently. In addition, the vector control uses the two currents of *d*- and *q*-axes, which the three-phase currents are transformed into. Therefore it is natural to use only two independent current controllers for the control of the three-phase currents of an AC motor.

Now we will introduce the regulator to control the two currents of *d*- and *q*-axes.

### 6.3.1 STATIONARY REFERENCE FRAME *d-q* CURRENT REGULATOR [2,3]

To begin with, consider the current control for a typical three-phase load as shown in Fig. 6.7. A three-phase load can be generalized as a circuit of $R-L$ and back-EMF and can be expressed as

$$\begin{aligned} v_{as} &= Ri_{as} + L\frac{di_{as}}{dt} + e_{as} \\ v_{bs} &= Ri_{bs} + L\frac{di_{bs}}{dt} + e_{bs} \\ v_{cs} &= Ri_{cs} + L\frac{di_{cs}}{dt} + e_{cs} \end{aligned} \tag{6.1}$$

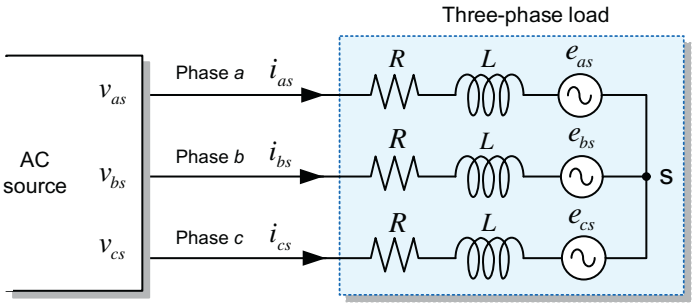



**FIGURE 6.7**

Three-phase load.

where $v_{as}$, $v_{bs}$, $v_{cs}$, $i_{as}$, $i_{bs}$, $i_{cs}$, and $e_{as}$, $e_{bs}$, $e_{cs}$ are three-phase voltages, currents, and back-EMFs, respectively, and $R$ and $L$ are the resistance and inductance of the load, respectively.

Applying the axis transformation described in Chapter 4 we can transform the three-phase voltage equations of Eq. (6.1) into $d-q$ forms in the stationary reference frame as

$$v_{ds}^{s} = Ri_{ds}^{s} + L\frac{di_{ds}^{s}}{dt} + e_{ds}^{s} \tag{6.2}$$

$$v_{qs}^{s} = Ri_{qs}^{s} + L\frac{di_{qs}^{s}}{dt} + e_{qs}^{s} \tag{6.3}$$

The current regulator for the $d$- and $q$-axes currents in the stationary reference frame based on Eqs. (6.2) and (6.3) is shown in Fig. 6.8.

In this stationary reference frame $d-q$ axes current regulator, the three-phase load currents $i_{as}$, $i_{bs}$, $i_{cs}$ should be transformed into the stationary frame $d-q$ currents to be used as feedback currents. The PI control is normally used to regulate these currents to the desired values. The PI regulators produce $d-q$ axes reference voltages $v_{ds}^{s*}$, $v_{qs}^{s*}$ to eliminate the current errors, and these voltages are transformed into three-phase reference voltages $v_{as}^{*}$, $v_{bs}^{*}$, $v_{cs}^{*}$. A voltage source PWM inverter, which will be discussed in detail in Chapter 7.

Let us evaluate the characteristic of the stationary reference frame $d-q$ current regulator. Fig. 6.9 shows the block diagram of this regulator.

The transfer function of this system is given as

$$I_{dqs}(s) = \frac{K_p s + K_i}{Ls^2 + (R + K_p)s + K_i} I_{dqs}^{*}(s) - \frac{s}{Ls^2 + (R + K_p)s + K_i} E_{dqs}(s) \tag{6.4}$$

From Eq. (6.4), it can be seen that if the current reference $I_{dqs}^{*}(s)$ is an AC quantity (i.e., $s \neq 0$), the actual current $I_{dqs}(s)$ never follows its reference $I_{dqs}^{*}(s)$ unless the current regulator has infinite gains. Thus when AC currents are regulated by the stationary regulator, the amplitude and phase errors will exist in the steady state.

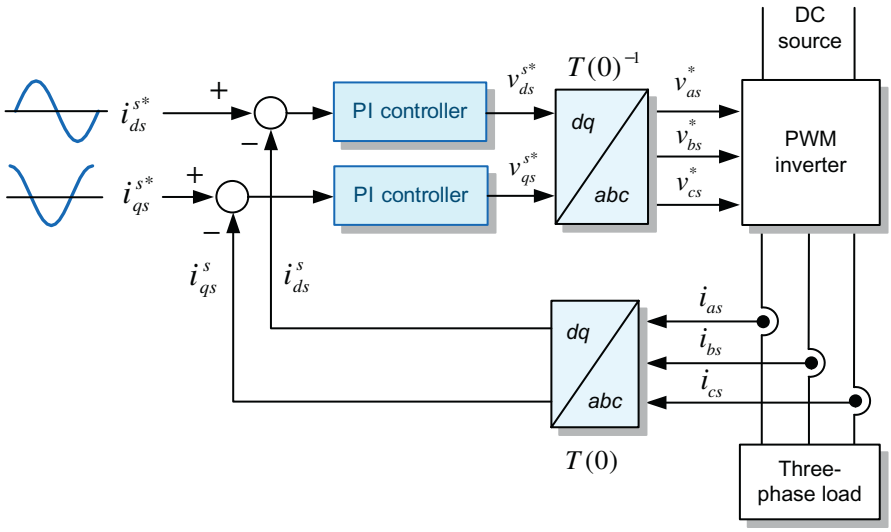



**FIGURE 6.8**

Stationary reference frame $d-q$ axes current regulator.

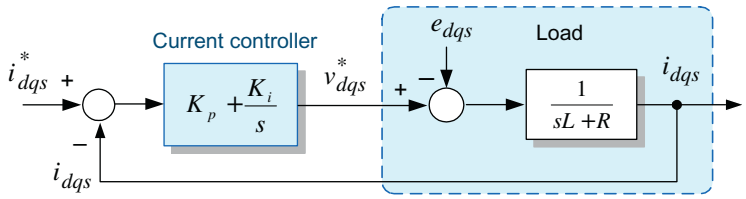



**FIGURE 6.9**

Block diagram for one axis of a stationary frame current regulator.

On the other hand, if the current reference $I^*_{dqs}(s)$ is a DC quantity (i.e., $s = 0$), Eq. (6.4) becomes

$$\frac{I_{dqs}(s)}{I^*_{dqs}(s)}|_{s=0} = 1 \tag{6.5}$$

This indicates that the actual current $I_{dqs}(s)$ can follow its reference value $I^*_{dqs}(s)$ accurately, i.e., the steady-state error is zero. This fact implies that instead of controlling the load current as an AC quantity directly, it is desirable to control the load current transformed as a DC quantity. For this purpose, the current control needs to be performed in the synchronous reference frame, where the currents of the AC load can be given as DC quantities. This regulator is called the *synchronous reference frame d−q current regulator*, which is widely used for the current control of AC systems.

### 6.3.2 SYNCHRONOUS REFERENCE FRAME *d-q* CURRENT REGULATOR [2]

Transforming the stationary frame voltage equations of Eqs. (6.2) and (6.3) into the synchronous reference frame, which is rotating at the electrical angular frequency $\omega_e$ corresponding to the operating frequency of the three-phase currents, gives

$$v_{ds}^e = Ri_{ds}^e + L\frac{di_{ds}^e}{dt} - \omega_e Li_{qs}^e + e_{ds}^e \tag{6.6}$$

$$v_{qs}^e = Ri_{qs}^e + L\frac{di_{qs}^e}{dt} + \omega_e Li_{ds}^e + e_{qs}^e \tag{6.7}$$

Unlike the stationary reference frame, in these equations, all the electrical variables such as currents, voltages, and back-EMFs are all DC quantities in the steady state. It should be noted that, in addition to the back-EMFs $e_{ds}^e$ and $e_{qs}^e$, there are $-\omega_e Li_{qs}^e$ and $\omega_e Li_{ds}^e$ (called *speed voltages*) in the synchronous reference frame expressions of Eqs. (6.6) and (6.7). These speed voltages are cross-coupled between *d*- and *q*-axes. Thus a change in the *d*-axis current may affect the control of the *q*-axis current and vice versa. These are the major disturbances on this synchronous current regulator. Thus the feedforward compensation of the speed voltages as well as the back-EMF voltages should be employed to achieve a good current control performance. This will be discussed in detail in a later section.

The block diagram for a current regulator operating on the synchronous reference frame is shown in Fig. 6.10.

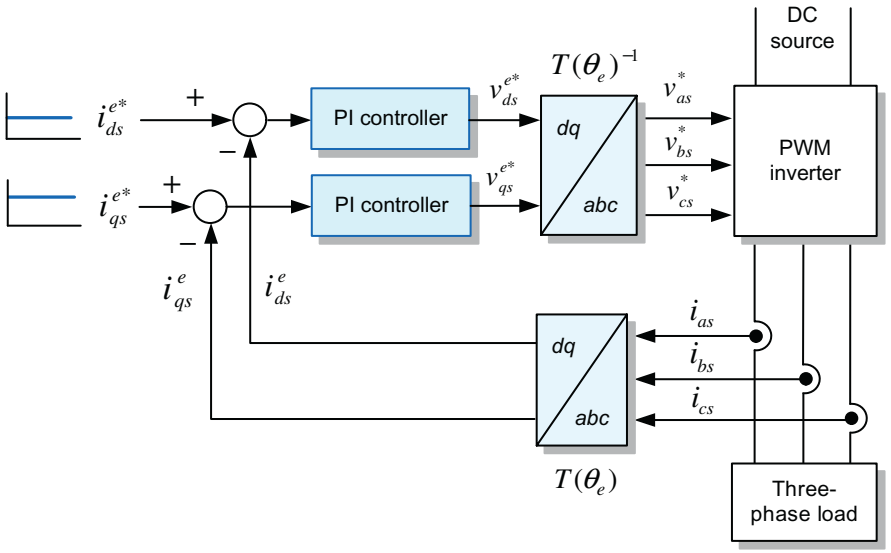



**FIGURE 6.10**

Block diagram of a synchronous frame current regulator.

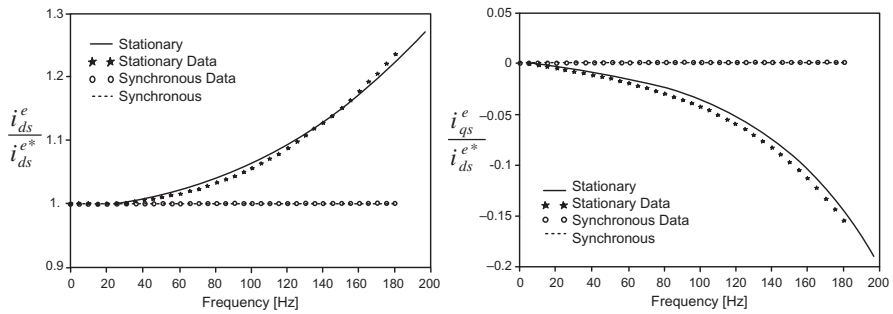



**FIGURE 6.11**

Comparison between the stationary and the synchronous frame regulators [2].

The structure of this regulator seems to be similar to that of a stationary frame current regulator in Fig. 6.8, but the controlled currents are DC quantities and a different transformation is used in this system. Since the synchronous reference frame uses DC quantities, the currents can be regulated well by using a PI controller.

Fig. 6.11 depicts the performance comparison between the stationary frame and the synchronous frame current regulators in the steady state for $R-L$ load [2]. From the left figure showing the performance of the $d$-axis current control, it can be seen that the steady-state error for the stationary frame current regulator increases with the operating frequency of the reference current. On the other hand, the synchronous frame current regulator has no steady-state error, regardless of the operating frequency. In addition, we can see that there is a cross-coupling between the axes for the stationary frame current regulator in the right figure. The control error for the $q$-axis current increases as the operating frequency of the $d$-axis reference current increases for the stationary frame current regulator.

### 6.3.3 GAIN SELECTION OF THE SYNCHRONOUS REFERENCE FRAME PI CURRENT REGULATOR

In Chapter 2, we described how to select the PI gains of a current controller for DC motors. Since a synchronous reference frame current regulator also controls DC quantities, we can directly use such method to select the PI gains of a synchronous reference frame current regulator. By referring to the gain selection of the current controller for a DC motor in Section 2.6, we can determine the proportional gain and the integral gain of a synchronous reference frame current regulator for the three-phase AC load as:

$$\text{Proportional gain:} \quad K_p = L \cdot \omega_c \tag{6.8}$$

$$\text{Integral gain:} \quad K_i = R \cdot \omega_c \tag{6.9}$$

where $R$ and $L$ denote the resistance and inductance of the load, respectively, and $\omega_c$ denotes the control bandwidth of the current regulator. Here, the proportional gain is determined by the required control bandwidth $\omega_c$ of the current regulator, and the integral gain is determined by the relationship of $K_p/K_i = L/R$ *(pole-zero cancellation)*.

On the basis of the current control for the three-phase AC load as mentioned earlier, it can readily be seen that it is better to use a synchronous frame current regulator for the current control of AC motors. For this case, the PI gains can be obtained directly from Eqs. (6.8) and (6.9). However, since the resistance and inductance values differ from system to system, we need to find the equivalent $R$ and $L$ values corresponding to the chosen AC motor. The values of these equivalent parameters for induction motors and synchronous motors can be obtained as follows.

#### 6.3.3.1 Proportional–integral gains for induction motors

From Eqs. (4.86) and (4.87), the $d-q$ voltage equations of an induction motor in the synchronous reference frame are given as

$$v_{ds}^e = Ri_{ds}^e + p\lambda_{ds}^e - \omega_e\lambda_{qs}^e \tag{6.10}$$

$$v_{qs}^e = Ri_{qs}^e + p\lambda_{qs}^e + \omega_e\lambda_{ds}^e \tag{6.11}$$

The stator flux linkages in these equations can be expressed as the rotor flux linkages and the stator currents as

$$\begin{aligned}\lambda_{ds}^e &= L_s i_{ds}^e + L_m i_{dr}^e \\ &= L_s i_{ds}^e + L_m\left(\frac{\lambda_{dr}^e - L_m i_{ds}^e}{L_r}\right) = \sigma L_s i_{ds}^e + \frac{L_m}{L_r}\lambda_{dr}^e\end{aligned} \tag{6.12}$$

$$\begin{aligned}\lambda_{qs}^e &= L_s i_{qs}^e + L_m i_{qr}^e \\ &= L_s i_{qs}^e + L_m\left(\frac{\lambda_{qr}^e - L_m i_{qs}^e}{L_r}\right) = \sigma L_s i_{qs}^e + \frac{L_m}{L_r}\lambda_{qr}^e\end{aligned} \tag{6.13}$$

where $\sigma = 1 - L_m^2/L_sL_r$ and the rotor currents can be obtained from the rotor flux linkages as

$$i_{dr}^e = \frac{\lambda_{dr}^e - L_m i_{ds}^e}{L_r} \leftarrow \lambda_{dr}^e = L_r i_{dr}^e + L_m i_{ds}^e \tag{6.14}$$

$$i_{qr}^e = \frac{\lambda_{qr}^e - L_m i_{qs}^e}{L_r} \leftarrow \lambda_{qr}^e = L_r i_{qr}^e + L_m i_{qs}^e \tag{6.15}$$

Substituting Eqs. (6.12) and (6.13) into Eqs. (6.10) and (6.11) gives

$$\begin{aligned} v_{ds}^e &= R_s i_{ds}^e + p\lambda_{ds}^e - \omega_e \lambda_{qs}^e \\ &= R_s i_{ds}^e + p\left(\sigma L_s i_{ds}^e + \frac{L_m}{L_r}\lambda_{dr}^e\right) - \omega_e\left(\sigma L_s i_{qs}^e + \frac{L_m}{L_r}\lambda_{qr}^e\right) \\ &= \left(R_s + R_r\frac{L_m^2}{L_r^2}\right) i_{ds}^e + \sigma L_s \frac{di_{ds}^e}{dt} - \omega_e \sigma L_s i_{qs}^e - R_r \frac{L_m}{L_r^2}\lambda_{dr}^e - \omega_r \frac{L_m}{L_r}\lambda_{qr}^e \end{aligned} \tag{6.16}$$

$$\begin{aligned} v_{qs}^e &= R_s i_{qs}^e + p\lambda_{qs}^e + \omega_e \lambda_{ds}^e \\ &= R_s i_{qs}^e + p\left(\sigma L_s i_{qs}^e + \frac{L_m}{L_r}\lambda_{qr}^e\right) + \omega_e\left(\sigma L_s i_{ds}^e + \frac{L_m}{L_r}\lambda_{dr}^e\right) \\ &= \left(R_s + R_r\frac{L_m^2}{L_r^2}\right) i_{qs}^e + \sigma L_s \frac{di_{qs}^e}{dt} + \omega_e \sigma L_s i_{ds}^e - R_r \frac{L_m}{L_r^2}\lambda_{qr}^e + \omega_r \frac{L_m}{L_r}\lambda_{dr}^e \end{aligned} \tag{6.17}$$

In the vector control, since $\lambda_{qr}^e = 0$, the above equations will be reduced as

$$v_{ds}^e = \left(R_s + R_r\frac{L_m^2}{L_r^2}\right) i_{ds}^e + \sigma L_s \frac{di_{ds}^e}{dt} - \omega_e \sigma L_s i_{qs}^e - R_r \frac{L_m}{L_r^2}\lambda_{dr}^e \tag{6.18}$$

$$v_{qs}^e = \left(R_s + R_r\frac{L_m^2}{L_r^2}\right) i_{qs}^e + \sigma L_s \frac{di_{qs}^e}{dt} + \omega_e \sigma L_s i_{ds}^e + \omega_r \frac{L_m}{L_r}\lambda_{dr}^e \tag{6.19}$$

From these, the equivalent $R$ and $L$ values of induction motors are given as

$$R = R_s + R_r\left(\frac{L_m}{L_r}\right)^2 \tag{6.20}$$

$$L = \sigma L_s \tag{6.21}$$

Thus the PI gains of a synchronous reference frame current regulator for induction motors are given as

$$\text{Proportional gain:} \quad K_p = \sigma L_s \cdot \omega_c \tag{6.22}$$

$$\text{Integral gain:} \quad K_i = \left[R_s + R_r\left(\frac{L_m}{L_r}\right)^2\right] \cdot \omega_c \tag{6.23}$$

#### 6.3.3.2 Proportional–integral gains for permanent magnet synchronous motors

From Eqs. (4.106), (4.107), (4.113), and (4.114), the $d-q$ voltage equations of a permanent magnet synchronous motor (PMSM) in the synchronous reference frame rotating at the angular frequency $\omega_r$ of the rotor are given as

$$v_{ds}^r = R_s i_{ds}^r + L_{ds}\frac{di_{ds}^r}{dt} - \omega_r L_{qs} i_{qs}^r \tag{6.24}$$

$$v_{qs}^r = R_s i_{qs}^r + L_{qs}\frac{di_{qs}^r}{dt} + \omega_r (L_{ds} i_{ds}^r + \phi_f) \tag{6.25}$$

From these, it can be seen that the equivalent $R$ value of a PMSM for the synchronous frame current regulator is the stator resistance $R_s$, and the equivalent $L$ value is the stator inductance. For a surface-mounted PMSM, the $d$- and $q$-axes inductances have the same value. However, since they are different for an interior PMSM, the equivalent $L$ value according to the axis is different as the following.

$$R = R_s \tag{6.26}$$

$$L = L_{ds} \quad (d\text{-axis}), \quad L = L_{qs} \quad (q\text{-axis}) \tag{6.27}$$

Thus the PI gains of the synchronous frame current regulator for a PMSM are given as

$$\text{Proportional gain:} \quad K_{pd} = L_{ds} \cdot \omega_c, \quad K_{pq} = L_{qs} \cdot \omega_c \tag{6.28}$$

$$\text{Integral gain:} \quad K_i = R_s \cdot \omega_c \tag{6.29}$$

## 6.4 FEEDFORWARD CONTROL

As described in the Section 6.3.2, a synchronous frame PI current regulator has been widely used for the current control for AC systems because it can achieve zero steady-state error and provide a good transient performance in spite of its simple structure. We saw in Section 6.3.2 that the voltage expressions of an AC system in the synchronous reference frame have cross-coupling components, $-\omega_e L i_{qs}^e$ and $\omega_e L i_{ds}^e$, between the axes in addition to back-EMF as

$$v_{ds}^e = R i_{ds}^e + L\frac{di_{ds}^e}{dt} - \omega L i_{qs}^e + e_{ds}^e \tag{6.30}$$

$$v_{qs}^e = R i_{qs}^e + L\frac{di_{qs}^e}{dt} + \omega L i_{ds}^e + e_{qs}^e \tag{6.31}$$

These are described as a block diagram in Fig. 6.12.

These voltage components can have a negative influence on the feedback current control although a synchronous frame current regulator is used. In particular, at high operating frequencies where they become large, these components can incur an oscillatory current response. If the bandwidth of the current controller is large enough, then their influence can be reduced. However, as explained in Section 2.6.1.1, the value of the gains is limited by the switching frequency and the current sampling frequency. Moreover, large gains make the system more sensitive to noise. To eliminate the effect of these disturbance components and improve the performance of the current control, the *feedforward control*

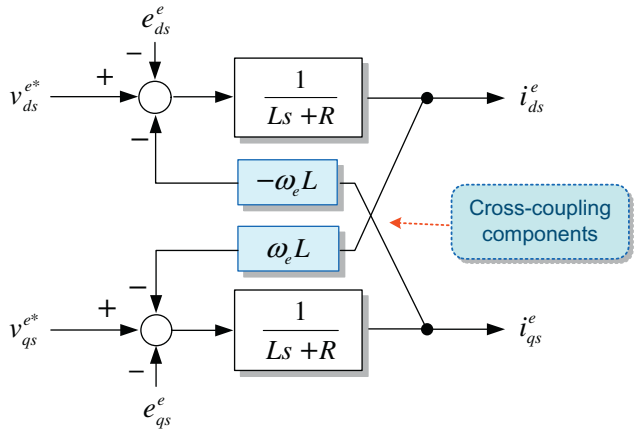



**FIGURE 6.12**

Voltage expressions in the synchronous frame.

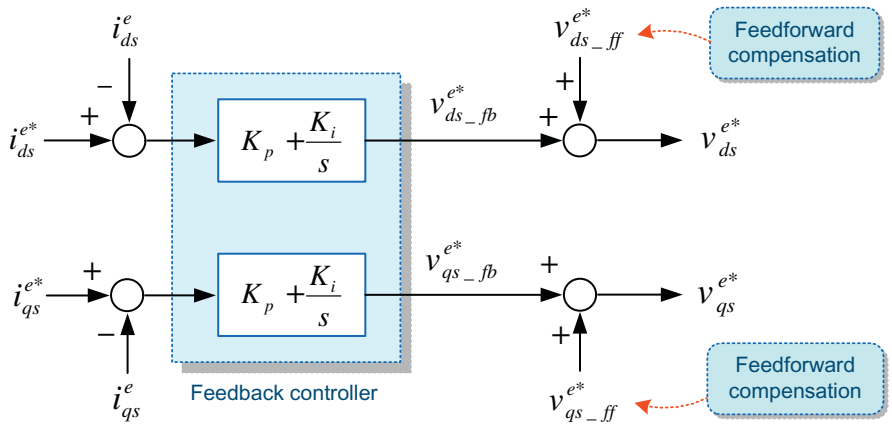



**FIGURE 6.13**

Current regulator with the feedforward control.

(also called the *decoupling control*), described in Section 2.5, is usually used along with the feedback control [4].

Fig. 6.13 shows a synchronous frame current regulator with the feedforward control for decoupling the cross-coupling.

When using the feedforward control, the output voltage of the synchronous frame current regulator consists of two components as follows:

$$v^{e*}_{ds} = v^{e*}_{ds\_fb} + v^{e*}_{ds\_ff} \tag{6.32}$$

$$v^{e*}_{qs} = v^{e*}_{qs\_fb} + v^{e*}_{qs\_ff} \tag{6.33}$$

where $v_{ds\_fb}^{e*}$, $v_{qs\_fb}^{e*}$ are the feedback voltage components produced by the PI current controller and $v_{ds\_ff}^{e*}$, $v_{qs\_ff}^{e*}$ are the feedforward voltage components. From Eqs. (6.30) and (6.31), the $d-q$ axes feedforward components for a three-phase $R-L$ load are given as

$$v_{ds\_ff}^{e*} = -\omega_e L i_{qs}^e + e_{ds}^e \tag{6.34}$$

$$v_{qs\_ff}^{e*} = \omega_e L i_{ds}^e + e_{qs}^e \tag{6.35}$$

In the current control of AC motors, the feedforward components vary depending on the motor. The feedforward components for an induction motor and a PMSM can be obtained as follows.

### 6.4.1 FEEDFORWARD CONTROL FOR INDUCTION MOTORS

To identify the feedforward voltage components for an induction motor, Eqs. (6.18) and (6.19) are rewritten as

$$v_{ds}^e = \left(R_s + R_r \frac{L_m^2}{L_r^2}\right) i_{ds}^e + \sigma L_s \frac{di_{ds}^e}{dt} \underline{- \omega_e \sigma L_s i_{qs}^e - R_r \frac{L_m}{L_r^2} \lambda_{dr}^e} \tag{6.36}$$

$$v_{qs}^e = \left(R_s + R_r \frac{L_m^2}{L_r^2}\right) i_{qs}^e + \sigma L_s \frac{di_{qs}^e}{dt} \underline{+ \omega_e \sigma L_s i_{ds}^e + \omega_r \frac{L_m}{L_r} \lambda_{dr}^e} \tag{6.37}$$

Here, the third and the fourth underlined terms on the right-hand side express the feedforward voltage components. Thus

$$v_{ds\_ff}^e = -\omega_e \sigma L_s i_{qs}^e - R_r \frac{L_m}{L_r^2} \lambda_{dr}^e \tag{6.38}$$

$$v_{qs\_ff}^e = \omega_e \sigma L_s i_{ds}^e + \omega_r \frac{L_m}{L_r} \lambda_{dr}^e \tag{6.39}$$

### 6.4.2 FEEDFORWARD CONTROL FOR PERMANENT MAGNET SYNCHRONOUS MOTORS

To identify the feedforward voltage components for an PMSM, Eqs. (6.24) and (6.25) are rewritten as

$$v_{ds}^r = R_s i_{ds}^r + L_{ds} \frac{di_{ds}^r}{dt} \underline{- \omega_r L_{ds} i_{qs}^r} \tag{6.40}$$

$$v_{qs}^r = R_s i_{qs}^r + L_{qs} \frac{di_{qs}^r}{dt} \underline{+ \omega_r L_{ds} i_{ds}^r + \omega_r \phi_f} \tag{6.41}$$

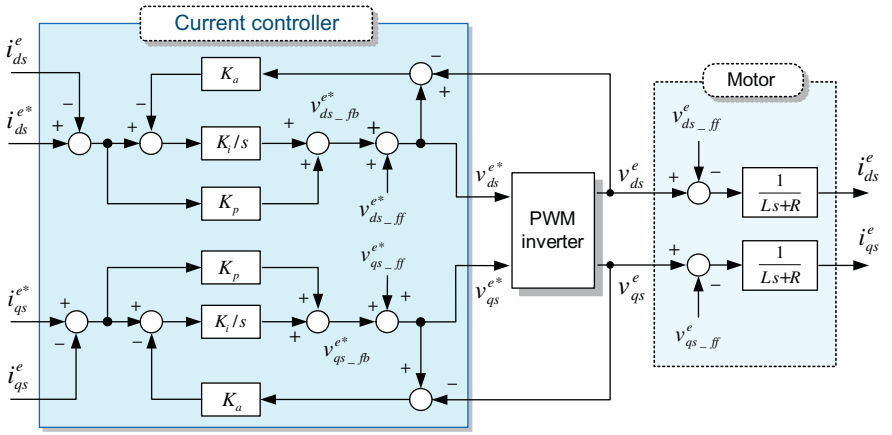



**FIGURE 6.14**

Synchronous frame PI current regulator with the feedforward control. *PI*, proportional–integral.

Here, the third and the fourth underlined term on the right-hand side express the feedforward voltage components. Thus

$$v^{r*}_{ds\_ff} = -\omega_r L_{qs} i^r_{qs} \tag{6.42}$$

$$v^{r*}_{qs\_ff} = \omega_r L_{ds} i^r_{ds} + \omega_r \phi_f \tag{6.43}$$

By using such feedforward control, the motor can be simplified to an $R-L$ passive circuit, so an improved current control performance can be achieved. An accurate feedforward compensation requires an accurate knowledge of inductances, flux linkage, and speed. Even when there are errors in these quantities, the feedforward control can largely reduce the effect of the disturbances by back-EMFs and cross-coupling components on the current control when compared with the feedback control alone.

In the feedforward control, it is desirable to estimate the feedforward voltage components by using the measured currents. Such feedforward control that uses measured currents for estimation is called *state feedback decoupling control*.

Fig. 6.14 shows a synchronous frame PI current regulator with the feedforward control, which has become the industry standard for the high-performance current control of AC motors. A PI current regulator needs to include an anti-windup controller to prevent integrator saturation, which was described in detail in Section 2.6.2.

## 6.5 COMPLEX VECTOR CURRENT REGULATOR

An ideal synchronous reference frame current regulator has a time response independent of the operating frequency. However, in reality, its transient performance degrades as the operating frequency approaches the bandwidth of the current regulator.

In the design of a PI current controller, as described in Chapter 2, the zero of the PI controller is made equal to the pole of the plant for pole-zero cancellation, i.e., $K_p/K_i = L/R$. At low operating frequencies, the controller zero can cancel the plant pole relatively completely. This allows a faster response of the system corresponding to the given control bandwidth. However, as the operating frequency increases, the plant pole and the controller zero move apart, resulting in a degradation of the system performance. The decoupling control as mentioned in Section 6.4 can make the performance of the current regulator to be independent of the operating frequency, i.e., the plant pole to be independent of the operating frequency.

A synchronous frame current regulator with the state feedback decoupling control is shown in Fig. 6.15. An accurate decoupling control requires the correct knowledge of system parameters (here, the inductance value). If the system parameters are incorrect, then the estimated value of the feedforward compensation becomes inaccurate, so the controller cannot cancel the plant pole completely. To solve this problem, a complex vector synchronous frame current regulator was proposed [5–7]. In this strategy, by using a complex vector notation, the two-input/two-output system of the synchronous frame $d-q$ current regulator is simplified to an equivalent single-input/single-output complex vector system. Because a complex vector notation is used for the analysis and design of current regulators for multiphase AC loads, this current regulator is called the *complex vector synchronous frame current regulator*.

In contrast to a current regulator with the state feedback decoupling control, a complex vector synchronous frame current regulator has decoupling control inside the PI controller without using any system parameter as shown in Fig. 6.16.

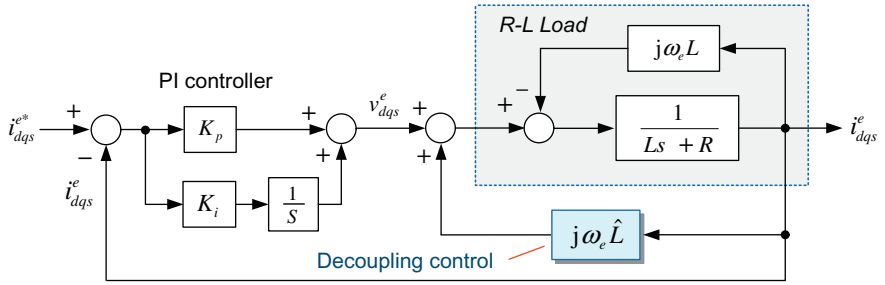



**FIGURE 6.15**

Synchronous current regulator with the state feedback decoupling control.

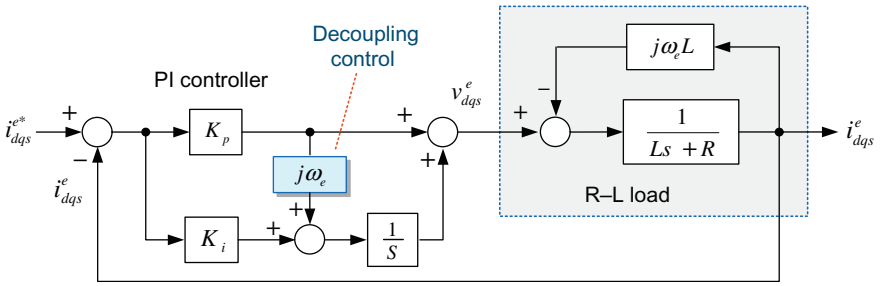



**FIGURE 6.16**

Complex vector synchronous frame current regulator.

Thus its performance is less sensitive to errors in system parameters, i.e., inductances, and is independent of the operating frequency. However, its response may be slightly oscillatory. If the system parameters used for decoupling control are identical to the actual system parameters, then the performances of these two current regulators are identical.

## REFERENCES

[1] D.M. Brod, D.W. Novotny, Current control of VSI-PWM inverters, IEEE Trans. Ind. Appl. IA-21 (4) (1985) 562–570.

[2] T.M. Rowan, R.J. Kerkman, A new synchronous current regulator and an analysis of current-regulated PWM inverter, IEEE Trans. Ind. Appl. IA-22 (4) (1986) 678–690.

[3] M.P. Kazmierkowski, L. Malesani, Current control techniques for three-phase voltage-source PWM converters: a survey, IEEE Trans. Ind. Electron. 45 (5) (1998) 691–703.

[4] F. Briz, M.W. Degner, R.D. Lorenz, Performance of feedforward current regulators for field-oriented induction machine controllers, IEEE Trans. Ind. Appl. IA-23 (4) (1987) 597–602.

[5] F. Briz, M.W. Degner, R.D. Lorenz, Analysis and design of current regulators using complex vectors, in: Conference Record of the IEEE-IAS Annual Meeting, 1997, pp. 1504–1511.

[6] F. Briz, M.W. Degner, R.D. Lorenz, Dynamic analysis of current regulators for AC motors using complex vectors, IEEE Trans. Ind. Appl. 35 (6) (1999) 1424–1432.

[7] H. Kim, R.D. Lorenz, Analysis and design of current regulators using complex vectors, in: Conference Record of the IEEE-IAS Annual Meeting, 2004, pp. 856–863.

CHAPTER

# Pulse width modulation inverters

7

In Chapter 6, it was described that the current regulators produce voltage commands for regulating the $d-q$ axes currents required in the vector control of an alternating current (AC) motor. These voltage commands are normally implemented by a pulse width modulation (PWM) inverter. As described in Chapter 3, the variable speed drives of induction motors by the *V/f* control require a PWM inverter. Inverters use the voltage modulation techniques (PWM techniques) for generating the actual voltages applied to the motor in accordance with the given voltage commands. Thus the voltage modulation technique of an inverter is a crucial factor in the AC motor drives.

In this chapter we will explore the configurations of an inverter and its voltage modulation techniques in detail.

## 7.1 INVERTERS

An inverter is a power electronics equipment that converts direct current (DC) power to AC power. Since an inverter can control the voltage and frequency of AC power at any value, it is essential for AC motor drives that require variable voltage and variable frequency.

Inverters can be classified into two groups according to the type of DC input source: *voltage source inverter* (VSI) and *current source inverter* (CSI). The configurations, output voltage, and current waveforms of these two inverters are shown in Fig. 7.1.

VSIs are powered by a DC voltage source. At the DC-link side of a VSI, there is usually a shunt capacitor with large capacitance to smooth out the DC input voltage. Since a VSI uses a voltage source, if the output terminals of a VSI are short-circuited, then it can be highly risky since a large current can flow. A typical output of VSI is an AC voltage of a square waveform, as shown in Fig. 7.1A. The magnitude and waveform of its output AC current depend on the connected load.

In contrast, CSIs are powered by a DC current source. Since in most cases DC current source is not available, it is normally obtained by using a large series inductor in the DC-link side powered by a DC voltage source. For CSIs, it can be dangerous when the circuit is opened because a high voltage can be produced by

Electric Motor Control. DOI: http://dx.doi.org/10.1016/B978-0-12-812138-2.00007-6
© 2017 Elsevier Inc. All rights reserved.


Hesai Exhibit 1030, page 268

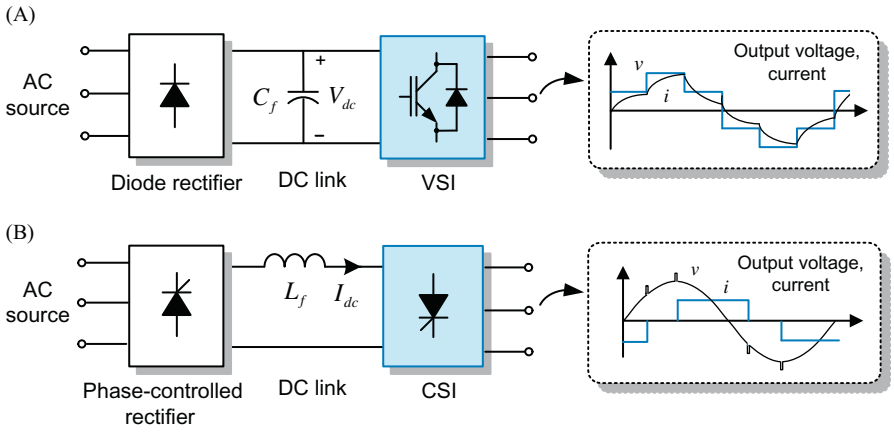



**FIGURE 7.1**

Two types of inverters. (A) VSI and (B) CSI.

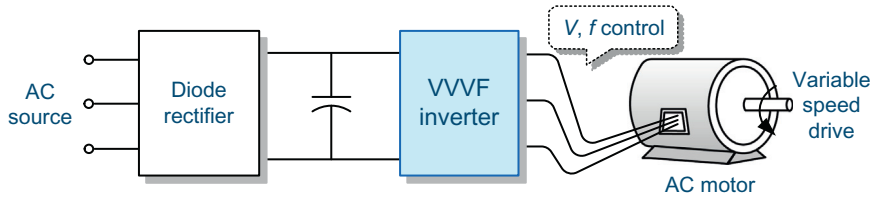



**FIGURE 7.2**

Inverter for AC motor drives.

$Ldi/dt$. A typical output of CSIs is an AC current source of a square waveform, as shown in Fig. 7.1B. The magnitude and waveform of the output voltage depend on the connected load.

During the early years of the inverter usage, CSIs were adopted in many applications. However, nowadays, VSIs have become the industry standard rather than CSIs that need a large inductor.

The inverters are used in two major applications: *AC motor drive applications* and *AC power supply applications.* In the inverter for AC motor drive applications as shown in Fig. 7.2, both the amplitude and frequency of the AC output voltages can often be varied for the variable speed drives. Thus this type of inverter is often called the *Variable Voltage Variable Frequency (VVVF)* inverter.

On the other hand, the inverter for AC power supply applications is used as a replacement of the AC voltage source supplied by the utility mains. In such an inverter both the amplitude and the frequency of the AC output voltages are fixed in accordance with the standards regarding the distribution of electricity, and thus

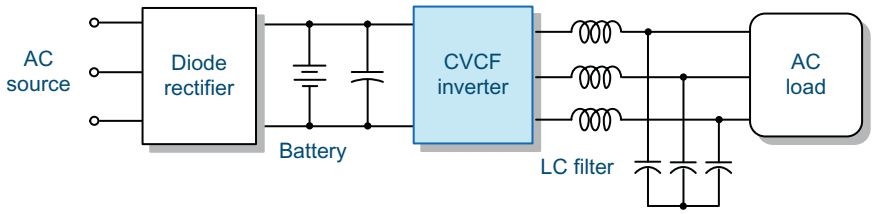



**FIGURE 7.3**

Example of an inverter for AC power supply.

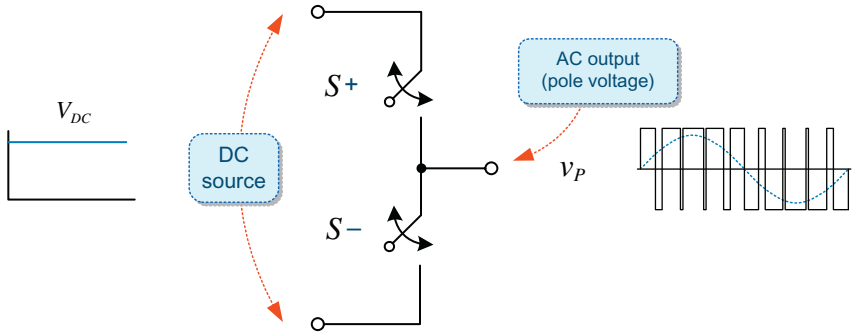



**FIGURE 7.4**

Basic circuit of an inverter.

this type of inverter is called the *constant voltage constant frequency (CVCF)* inverter. Typical examples of such an inverter are an *uninterruptible power supply* (UPS) that provides AC power to the load when the utility mains are not available, and a *power conditioning system* that supplies AC power from renewable energy sources like fuel cells, solar panels, or wind turbines as shown in Fig. 7.3.

Now we will describe the VSI in detail. VSIs can be classified according to whether or not the amplitude of the output voltage can be controlled. One type of VSI is the *square wave inverter*, whose frequency is controlled while the amplitude of the output voltage remains constant. Another is the *PWM inverter* in which both the amplitude and the frequency of the output voltage are controlled.

First, we will begin by looking at the basic circuit configuration of a VSI.

### 7.1.1 BASIC CIRCUIT CONFIGURATION OF A VOLTAGE SOURCE INVERTER

The basic circuit that forms a VSI is shown in Fig. 7.4. This basic circuit is called a *pole, arm*, or a *leg*. The basic circuit consists of a pair of switches that operate in a complementary manner to perform a rapid switching function to convert the DC power to AC power.

A DC input power source is applied to both ends of the basic circuit, and an AC output voltage is produced between the two switches. This AC output voltage, $v_P$, is called a *pole voltage*.

As switching devices used in the basic circuit, semiconductor power devices such as gate turn-off (GTO) thyristor, integrated gate commutated thyristor (IGCT), insulated gate bipolar transistor (IGBT), or metal oxide semiconductor field effect transistor (MOSFET) as shown in Fig. 7.5 are available on the market today. These devices are mainly selected according to the required power capacity and switching frequency. The GTO thyristor and IGCT have a high-power handling capability, but their switching frequency is very low, being below 1 kHz. The IGBT is now most widely used for medium- to high-power applications. Some of the IGBTs have switching frequencies up to 100 kHz, but most are normally below 20 kHz. The MOSFET, which can support a high switching frequency beyond 100 kHz, is the most suitable device for small-power applications. Besides these active switching devices, for driving inductive loads, it should be noted that an antiparallel diode should be connected across each switch to provide an alternate path for the load current when the switch is turned off as shown in Fig. 7.5.

Most inverter topologies have a configuration composed of basic circuits connected in parallel. However, inverters for high-power applications often employ another basic circuit with four switches connected in series as shown in Fig. 7.6.

In an inverter topology composed of the basic circuit as shown in Fig. 7.4, the waveform of the output voltage has a two-level, i.e., 0 and $+V_{dc}$, so it is called a *two-level inverter*. On the other hand, in an inverter topology composed of the basic circuit as shown in Fig. 7.6, the waveform of the output voltage has a three-level, i.e., 0, $-V_{dc}$, and $+V_{dc}$, so it is often referred to as a *three-level inverter*. A *neutral-point clamped (NPC) inverter* is a typical example of the three-level inverter [1]. An inverter circuit can even be expanded to four- or five-level topology configurations. These inverters are called a *multilevel inverter*. In this chapter, only the typical two-level inverter will be discussed.

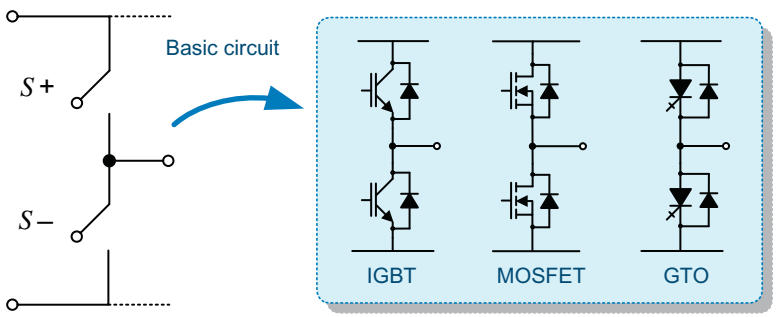



**FIGURE 7.5**

Switching devices for an inverter.

#### 7.1.1.1 The output voltage of the basic circuit

The output voltage of the basic circuit, i.e., pole voltage, $v_P$, is determined by the switching states of two devices, $S+$ and $S-$, but is independent of the load. The pole voltage of an inverter normally is not equal to the load voltage.

There are four different situations of the basic circuit according to the on-/off-state of the two switches. When the two switches are both turned on, the DC power source is short-circuited (called *shoot-through condition*) as shown in Fig. 7.7, and this causes a current large enough to destroy the switching devices to flow. This situation should be inhibited at all times.

Hence, the two devices switch alternately, i.e., while one is on, the other one is off. Even in this case, there is still a possibility of a shoot-through when the switching devices are changing their on/off states because the turn-off time of a device is always longer than its turn-on time. Thus, to prevent a shoot-through during the switching transients, a gating signal of the turning-on device is applied after a certain delay. This is to ensure that the turning-on device is turned on after

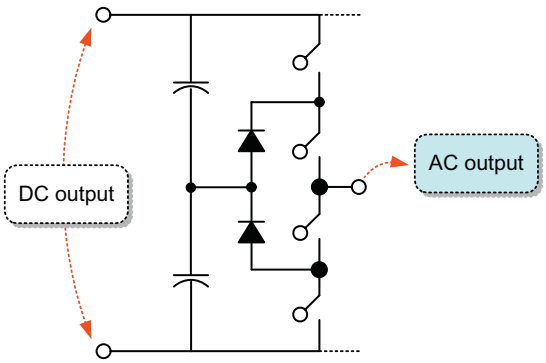



**FIGURE 7.6**

Basic circuit used in a three-level inverter.

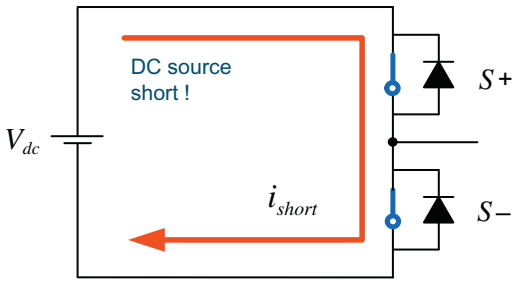



**FIGURE 7.7**

Shoot-through condition.

the turning-off device is completely turned off. This delay time is called *dead time*. The required value of the dead time differs depending on the type and the power rating of the device used. The dead time will be explained in more detail in Section 7.6.

Except in the case when both switches are turned on, there are three possible situations of the basic circuit. When the upper switch $S+$ is turned on and the lower switch $S-$ is turned off as shown in Fig. 7.8A, the pole voltage becomes a positive voltage as

$$v_P = \frac{V_{dc}}{2} \tag{7.1}$$

On the other hand, when $S+$ is turned off and $S-$ is turned on as shown in Fig. 7.8B, the pole voltage becomes a negative voltage as

$$v_P = -\frac{V_{dc}}{2} \tag{7.2}$$

Lastly, even if $S+$ and $S-$ are both turned off, the pole voltage can be produced if a current is flowing through the load. In this case, the pole voltage depends on the direction of the current as shown in Fig. 7.9. For example, if the

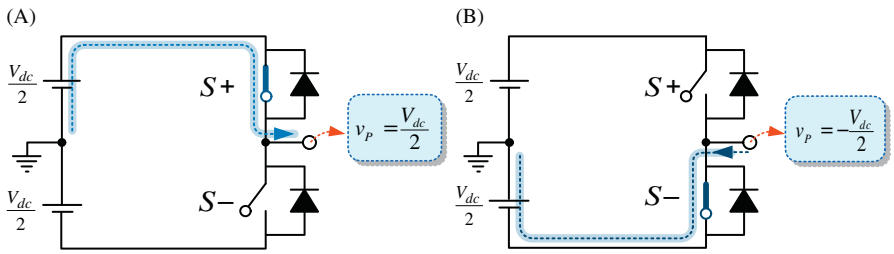



**FIGURE 7.8**

Circuit configurations according to the switching states. (A) $S+$ On, $S-$ Off and (B) $S+$ Off, $S-$ On.

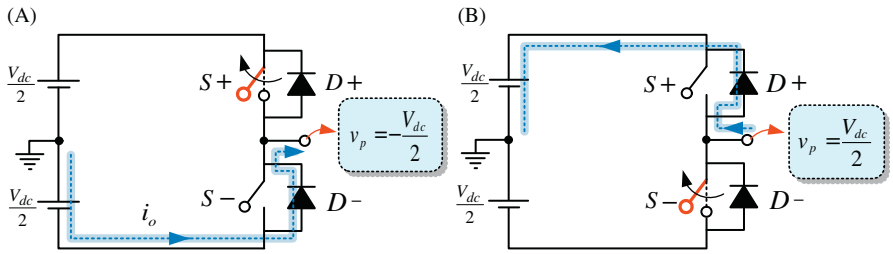



**FIGURE 7.9**

Circuit configurations when both switches are turned off. (A) $i_o > 0$ and (B) $i_o < 0$.

switch $S+$ is turned off when a positive current ($i_o > 0$) is flowing as shown in Fig. 7.8A, then the current flows through the lower diode so the pole voltage $v_P$ becomes $-V_{dc}/2$ as shown in Fig. 7.9A.

On the other hand, if the switch $S-$ is turned off when a negative current ($i_o < 0$) is flowing in Fig. 7.8B, then the current flows through the upper diode so it becomes $V_{dc}/2$ as shown in Fig. 7.9B.

From the switching situations stated above, the pole voltage of the basic circuit of an inverter can be expressed using a switching function $S$ describing the states of switch as

$$v_P = V_{dc}\left(S - \frac{1}{2}\right) \tag{7.3}$$

Here, the switching function $S$ is defined as "1" when the upper switch $S+$ is turned on and as "0" when it is turned off.

An inverter has two operation modes depending on which device the current flows through: *powering mode* and *regeneration mode*. If the current flows through the switching device, then the inverter operates in the powering mode in which the AC power is supplied into the load from the DC power source. In contrast, if the current flows through the diode, then it operates in the regeneration mode in which the AC power is returned into the DC source from the load.

## 7.1.2 SINGLE-PHASE HALF-BRIDGE INVERTERS

The simplest inverter that generates single-phase AC voltage from a DC source is a *single-phase half-bridge inverter*. This inverter consists of one basic circuit as shown in Fig. 7.10.

We can simply produce a single-phase AC voltage from this inverter by turning the two switches on and off alternately every half a period $T/2$. An inverter that uses this modulation is called a *square wave inverter*. In this case the inverter produces the maximum output voltage. In this half-bridge inverter the pole voltage $v_P$ is equal to the voltage $v_o$ applied to the load.

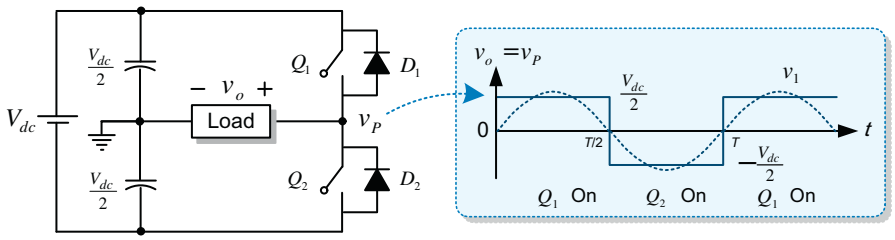



**FIGURE 7.10**

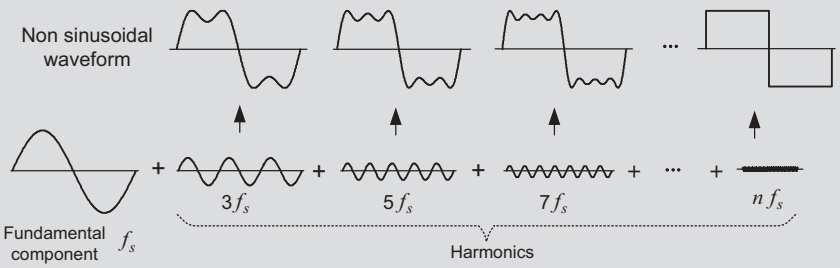
Single-phase half-bridge inverter and its output voltage.

The pole voltage is not a pure sinusoidal but a square wave, which contains many harmonics. To evaluate the fundamental and harmonic components included in the pole voltage, the Fourier series expansion of the pole voltage is written as

$$v_P = \frac{2V_{dc}}{\pi} \sum_{n=1,3,5\ldots}^{\infty} \frac{\sin n\omega t}{n} \tag{7.4}$$

## FOURIER SERIES

Any periodic waveform of any shape can be represented as the sum of a sine wave (so-called *fundamental component*) that has the same frequency as the original waveform and other sine waves (so-called *harmonics*) that have frequencies of integral multiples of the fundamental frequency. To find out these frequency components, we can decompose the periodic waveform into the sum of a set of sines and cosines by using a *Fourier series*. We can see the change of the shape in the waveform by combining other frequency components from the following figure.




- Fourier series representation for a periodic waveform is given as

$$f(t) = a_0 + \sum_{n=1}^{\infty}(a_n \cos n\omega t + b_n \sin n\omega t)$$

$$= a_0 + \sum_{n=1}^{\infty} c_n \sin(n\omega t + \phi_n) \quad \left(c_n = \sqrt{a_n^2 + b_n^2},\ \phi_n = \tan^{-1}\frac{a_n}{b_n}\right)$$

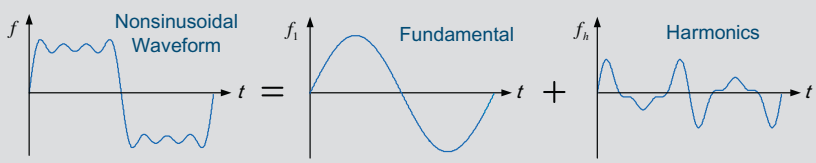
Here, the Fourier coefficients are computed as follows:

$$a_0 = \frac{1}{T}\int_0^T f(t)dt,\ a_n = \frac{2}{T}\int_0^T f(t)\cos n\omega t d,\ b_n = \frac{2}{T}\int_0^T f(t)\sin n\omega t dt$$

- Periodic waveform is expressed as:

$$f(t) = a_0 + c_1\sin(\omega t + \phi_1) + \sum_{n=2}^{\infty} c_n \sin(n\omega t + \phi_n)$$

$$= \underset{\text{DC component}}{f_{DC}} + \underset{\text{fundamental concept}}{f_1(t)} + \underset{\text{harmonic components}}{f_h(t)}$$



These frequency components are depicted in Fig. 7.11. Out of all the frequency components, only the fundamental component voltage can supply effective power to the load. For the square wave output of a half-bridge inverter, the fundamental rms voltage is given from Eq. (7.4) as

$$V_{P1\_rms} = \frac{1}{\sqrt{2}}\frac{2V_{dc}}{\pi} = 0.45\ V_{dc} \tag{7.5}$$

Thus this inverter can provide the load with AC rms voltage corresponding to 45% of the DC input voltage $V_{dc}$. Unlike the fundamental component, the harmonics will be converted into unnecessary losses such as heat or noise. Thus it is desirable for harmonics included in the output voltage to be fewer. Besides, because the harmonics cause waveform distortions, if the output AC voltage includes fewer harmonics, their shape approaches a pure sinusoidal wave.

From Eq. (7.4), we can see that the pole voltage contains only odd order harmonics, whose amplitudes are inversely proportional to the order of the harmonics. Thus low-order harmonics such as the third, fifth, and seventh components can cause a problem. This is because they have large amplitude, so they are a major source of waveform distortions. Furthermore, a large-sized, low-pass filter is required to filter them.

To measure the amount of distortion of voltage or current waveforms, we commonly use the *total harmonic distortion* (THD) defined as

$$\text{Total harmonic distortion (THD)} = \sqrt{\frac{\sum_{h>1}^{\infty} f_{h,rms}^2}{f_{1,rms}^2}} \times 100\% \tag{7.6}$$

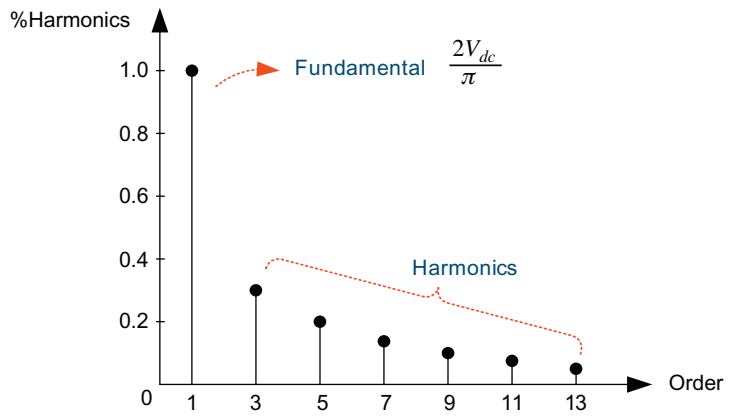



**FIGURE 7.11**

Harmonics in pole voltage $v_P$.

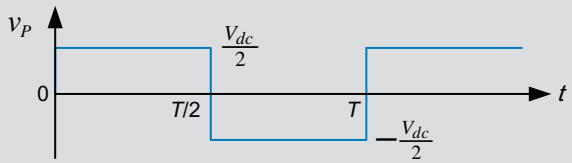
Here, $f_{1\_rms}$ and $f_{h\_rms}$ denote the rms values of the fundamental and harmonic components, respectively. A higher THD value indicates a more distorted waveform, i.e., the waveform deviates from the pure sinusoidal wave.

**EXAMPLE 1**

Calculate the THD of the output AC voltage of the single-phase half-bridge inverter.

**Solution**

To calculate the THD of the output voltage of the single-phase half-bridge inverter, we need to evaluate the harmonic components included in its output voltage as shown below.




Its output voltage, i.e., pole voltage, has odd quarter-wave symmetry, and thus we need to calculate only the Fourier coefficient $b_n(n = \text{odd})$ as

$$v_P(t) = a_0 + \sum_{n=1}^{\infty}(a_n \cos n\omega t + b_n \sin n\omega t)$$

$$a_0 = 0,\ a_n = 0,\ b_{n-even} = 0$$

$$b_{n-odd} = \frac{2}{T}\int_0^T f(t)\sin n\omega t dt = \frac{4}{\pi}\int_0^{\pi/2}\frac{V_{dc}}{4}\sin n\omega t dt = \frac{2V_{dc}}{n\pi}$$

Thus Fourier series representation for the output voltage is given as

$$\therefore\ v_P(t) = \frac{2V_{dc}}{\pi}\left[\sin \omega t + \frac{1}{3}\sin 3\omega t + \frac{1}{5}\sin 5\ \omega t + \frac{1}{7}\sin 7\omega t + \cdots\right]$$

- Fundamental component:

$$v_{P1}(t) = \frac{2V_{dc}}{\pi}\sin \omega t$$

- Harmonic components:

$$v_h(t) = \sum_{n=3,5,7\cdots}^{\infty}\frac{2V_{dc}}{n\pi}\sin n\omega t$$

The THD of the output AC voltage can be calculated as

$$\text{THDv} = \sqrt{\frac{\sum_{h>1}^{\infty} V_{h,rms}^2}{V_{1,rms}^2}} \times 100\% = \sqrt{\frac{V_3^2 + V_5^2 + V_7^2 + \cdots}{V_1^2}} \times 100\%$$

$$= \sqrt{\left(\frac{1}{3}\right)^2 + \left(\frac{1}{5}\right)^2 + \left(\frac{1}{7}\right)^2 + \cdots} = 46.2\%$$

### 7.1.3 SINGLE-PHASE FULL-BRIDGE INVERTERS

As can be seen in the Section 7.1.2, a half-bridge inverter has a poor DC voltage utilization of 0.45 $V_{dc}$. Therefore a commonly used inverter topology for producing a single-phase AC voltage is the *full-bridge inverter* as shown in Fig. 7.12. This inverter consisting of two basic circuits can produce an output voltage twice as much as that of the half-bridge inverter using the same DC voltage.

In the single-phase full-bridge inverter, the load voltage $v_o$ is the difference between two pole voltages, $v_H$ and $v_L$, as

$$v_o = v_H - v_L \tag{7.6}$$

Here, each pole switches independently. The available load voltages of the full-bridge inverter according to the state of four switches $Q_1 \sim Q_4$ are shown in Table 7.1.

To produce the effective load voltage in this inverter, the phase difference between two pole voltages needs to be 180 electrical degrees as shown in Fig. 7.13. In this case, the voltage of the full-bridge inverter is double the pole voltage.

For inductive loads, the operation of the inverter is shown in Fig. 7.14. The inverter operates alternately in the powering mode and regeneration mode.

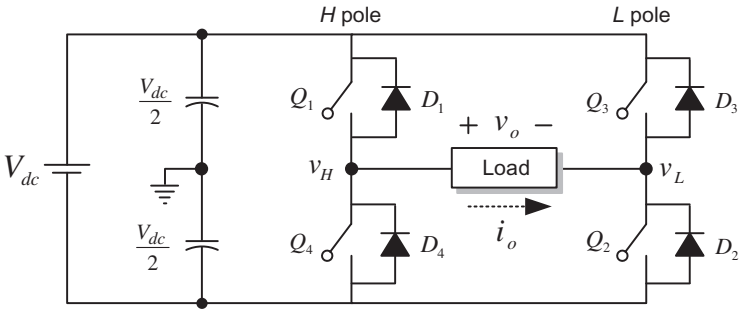



**FIGURE 7.12**

Single-phase full-bridge inverter.

**Table 7.1** Pole Voltage and Load Voltage According to the State of Four Switches

| Switch State | Pole Voltage | | Load Voltage |
|---|---|---|---|
| | $v_H$ | $v_L$ | $v_o = v_H - v_L$ |
| $Q_1$, $Q_2$ On | $\frac{V_{dc}}{2}$ | $-\frac{V_{dc}}{2}$ | $V_{dc}$ |
| $Q_4$, $Q_3$ On | $-\frac{V_{dc}}{2}$ | $\frac{V_{dc}}{2}$ | $-V_{dc}$ |
| $Q_1$, $Q_3$ On | $\frac{V_{dc}}{2}$ | $\frac{V_{dc}}{2}$ | 0 |
| $Q_4$, $Q_2$ On | $-\frac{V_{dc}}{2}$ | $-\frac{V_{dc}}{2}$ | 0 |

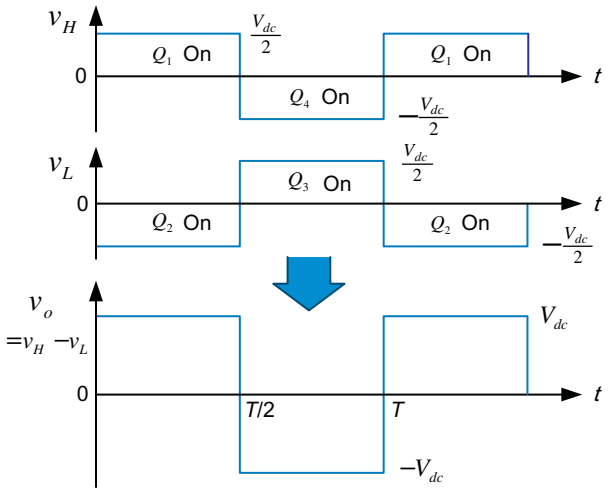



**FIGURE 7.13**

Load voltage of single-phase full-bridge inverter.

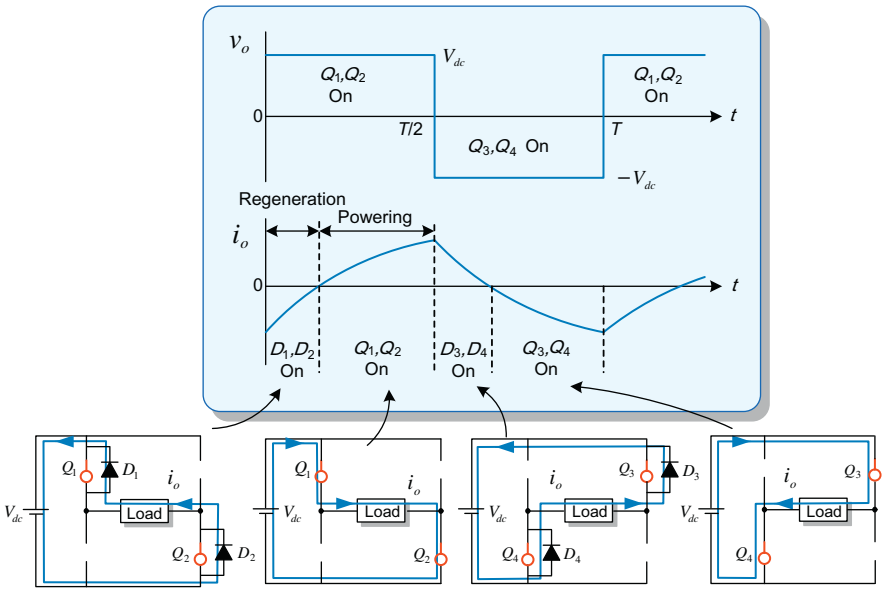



**FIGURE 7.14**

Operation of single-phase full-bridge inverter for inductive load.

The load voltage in a full-bridge inverter is a square waveform like the pole voltage, so it contains a lot of harmonics. Its harmonic orders are the same as those of the pole voltage. Using Fourier series expansion, the load voltage can be presented as

$$v_o = \frac{4V_{dc}}{\pi} \sum_{n=1,3,5\cdots}^{\infty} \frac{\sin n\omega t}{n} \quad (n = 1, 3, 5, \ldots) \tag{7.7}$$

This inverter can provide the load with AC rms voltage corresponding to 90% of the DC input voltage $V_{dc}$ as

$$V_{o1\_rms} = \frac{1}{\sqrt{2}} \frac{4V_{dc}}{\pi} = 0.9V_{dc} \tag{7.8}$$

This voltage is double the voltage of the half-bridge inverter under an equal DC voltage.

We can express the output voltage $v_o$ of this inverter using the switching function $S$. Assume that the switching functions for $H$ and $L$ poles are $S_H$ and $S_L$, respectively. As described previously, the switching function $S$ is defined as "1" when the upper switch is turned on and as "0" when it is turned off. As in Eq. (7.3), the pole voltages $v_H$ and $v_L$ can be expressed using switching functions as

$$v_H = V_{dc}\left(S_H - \frac{1}{2}\right) \tag{7.9}$$

$$v_L = V_{dc}\left(S_L - \frac{1}{2}\right) \tag{7.10}$$

From these pole voltage expressions, the output voltage $v_o$ is given as

$$v_o = v_H - v_L = V_{dc}(S_H - S_L) \tag{7.11}$$

The output voltage can be easily obtained by using this expression from the states of four switches.

### 7.1.4 THREE-PHASE SQUARE WAVE INVERTERS (SIX-STEP INVERTER)

The circuit configuration of a three-phase inverter as shown in Fig. 7.15 consists of three poles. Each pole is switched independently of each other, and the two switches in each pole are alternately switched.

In a three-phase inverter, each pole is in charge of the production of one-phase voltage. To do so, the switches of each pole will be turned on and off alternately every half period (180° conduction interval) in the same way as the single-phase inverters.

However, to achieve three-phase voltages, each pole voltage should be displaced from each other by 120 electrical degrees. In such switching, three of

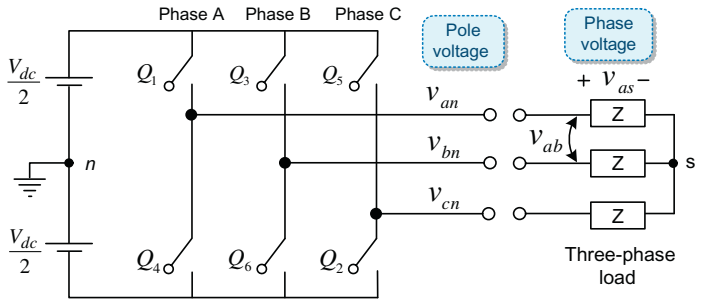



**FIGURE 7.15**

Configuration of the three-phase inverter circuit.

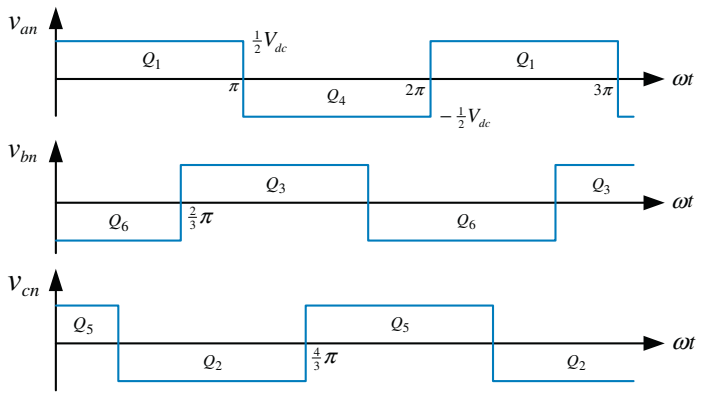



**FIGURE 7.16**

Pole voltages of the three-phase inverter.

six switches are always turned on, and their switching sequence goes on in the order of switch numbers shown in Fig. 7.16 such as . . .123, 234, 345, 456, 561, 612 and back to 123. In this case, there are six different sections in one fundamental period of the output voltage. The inverter operated by this switching scheme is called *square wave inverter*, in which the amplitude of output voltages remains constant while only their frequency can be controlled.

Line-to-line voltage is the difference between two pole voltages (e.g., $v_{ab} = v_{an} - v_{bn}$) as shown in Fig. 7.17. It is a quasi-square wave and has 120° conduction interval.

Next we will look at the phase voltages applied to the load when a three-phase inverter drives a load. We need to know the phase voltages to solve the voltage equations of AC motors as described in Chapter 4.

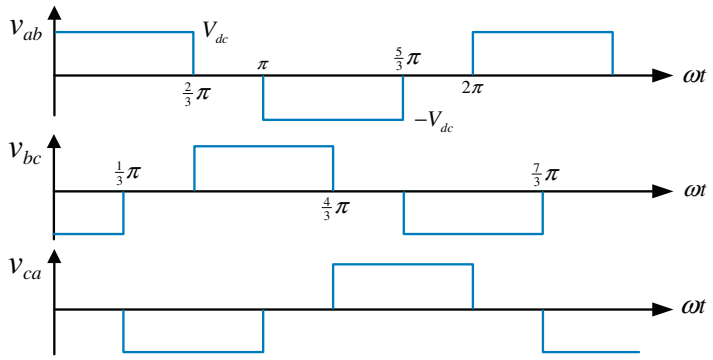



**FIGURE 7.17**

Line-to-line voltages.

Assume a balanced Y-connected load as shown in Fig. 7.15. In this case the line to neutral voltage, or the phase voltage, is the load voltage. From line-to-line voltages, the phase voltages for the three-phase loads can be obtained as

$$v_{as} = \frac{1}{3}(v_{ab} - v_{ca}) \tag{7.12}$$

$$v_{bs} = \frac{1}{3}(v_{bc} - v_{ab}) \tag{7.13}$$

$$v_{cs} = \frac{1}{3}(v_{ca} - v_{bc}) \tag{7.14}$$

We can see that the pole voltage of the inverter depends on the states of switches in only its own pole, but the phase voltage depends on the states of switches of other poles as well as the corresponding pole. Thus the phase voltage is determined by the states of all switches of an inverter.

The phase voltage can be also obtained directly from the states of all the six switches of an inverter as follows. First, consider the first section in Fig. 7.16, where three switches of $Q5$, $Q6$, and $Q1$, are turned on. In this section, the system can be described as the circuit shown in Fig. 7.18A. In this case, we can readily see that the phase voltages are given as

$$v_{as} = \frac{1}{3}V_{dc}, \quad v_{bs} = -\frac{2}{3}V_{dc}, \quad v_{cs} = \frac{1}{3}V_{dc} \tag{7.15}$$

Next, consider the second section, where $Q6$, $Q1$, and $Q2$ are turned on. In this section, the inverter circuit can be described as shown in Fig. 7.18B, and thus the phase voltages can be obtained as

$$v_{as} = \frac{2}{3}V_{dc}, \quad v_{bs} = -\frac{1}{3}V_{dc}, \quad v_{cs} = \frac{1}{3}V_{dc} \tag{7.16}$$

In the same way we can obtain the phase voltages for all the sections as shown in Fig. 7.19. Since there are six steps in one cycle of the phase voltage waveform,

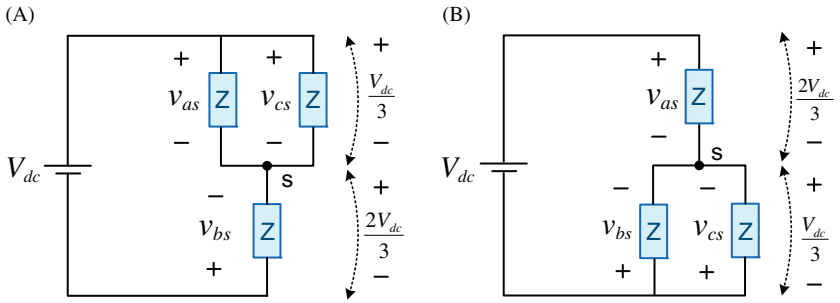



**FIGURE 7.18**

Phase voltages for the two different sections. (A) *Q*6, *Q*5, *Q*1 On and (B) *Q*6, *Q*1, *Q*2 On.

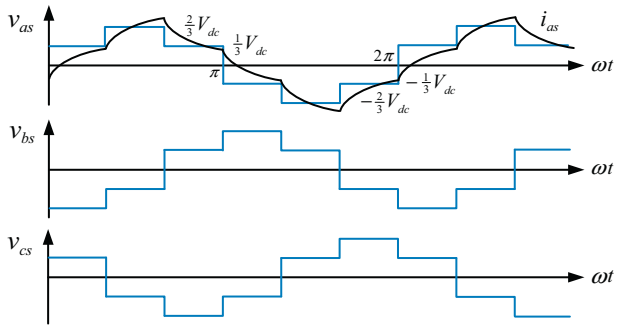



**FIGURE 7.19**

Phase voltages and currents.

this type of inverter is often referred to as the *six-step inverter*. When these square waveform voltages are applied to inductive loads such as motors, the load currents are not a square waveform, because the harmonics of the voltage is filtered by the inductive component of the load.

Table 7.2 summarizes the pole voltage and the phase voltage (load voltage) in a three-phase inverter according to the states of the switches. Here, the switching state is defined as "1" when the upper switch is in on-state and as "0" when it is in off-state. For the six switches of a three-phase inverter, there are only eight possible switch combinations, i.e., eight different switching states.

As mentioned earlier, the output voltages of a three-phase inverter have the shape of a square wave not a pure sinusoidal wave, so they include many harmonics. Now we will evaluate the fundamental and harmonic components included in the output voltages.

**Table 7.2** Pole Voltages and Phase Voltages According to the States of Switches

| Switch States | | | Pole Voltages | | | Phase Voltages | | |
|---|---|---|---|---|---|---|---|---|
| $S_a$ | $S_b$ | $S_c$ | $v_{an}$ | $v_{bn}$ | $v_{cn}$ | $v_{as}$ | $v_{bs}$ | $v_{cs}$ |
| 0 | 0 | 0 | $-\frac{1}{2}V_{dc}$ | $-\frac{1}{2}V_{dc}$ | $-\frac{1}{2}V_{dc}$ | 0 | 0 | 0 |
| 0 | 0 | 1 | $-\frac{1}{2}V_{dc}$ | $-\frac{1}{2}V_{dc}$ | $\frac{1}{2}V_{dc}$ | $-\frac{1}{3}V_{dc}$ | $-\frac{1}{3}V_{dc}$ | $\frac{2}{3}V_{dc}$ |
| 0 | 1 | 0 | $-\frac{1}{2}V_{dc}$ | $\frac{1}{2}V_{dc}$ | $-\frac{1}{2}V_{dc}$ | $-\frac{1}{3}V_{dc}$ | $\frac{2}{3}V_{dc}$ | $-\frac{1}{3}V_{dc}$ |
| 0 | 1 | 1 | $-\frac{1}{2}V_{dc}$ | $\frac{1}{2}V_{dc}$ | $\frac{1}{2}V_{dc}$ | $-\frac{2}{3}V_{dc}$ | $\frac{1}{3}V_{dc}$ | $\frac{1}{3}V_{dc}$ |
| 1 | 0 | 0 | $\frac{1}{2}V_{dc}$ | $-\frac{1}{2}V_{dc}$ | $-\frac{1}{2}V_{dc}$ | $\frac{2}{3}V_{dc}$ | $-\frac{1}{3}V_{dc}$ | $-\frac{1}{3}V_{dc}$ |
| 1 | 0 | 1 | $\frac{1}{2}V_{dc}$ | $-\frac{1}{2}V_{dc}$ | $\frac{1}{2}V_{dc}$ | $\frac{1}{3}V_{dc}$ | $-\frac{2}{3}V_{dc}$ | $\frac{1}{3}V_{dc}$ |
| 1 | 1 | 0 | $\frac{1}{2}V_{dc}$ | $\frac{1}{2}V_{dc}$ | $-\frac{1}{2}V_{dc}$ | $\frac{1}{3}V_{dc}$ | $\frac{1}{3}V_{dc}$ | $-\frac{2}{3}V_{dc}$ |
| 1 | 1 | 1 | $\frac{1}{2}V_{dc}$ | $\frac{1}{2}V_{dc}$ | $\frac{1}{2}V_{dc}$ | 0 | 0 | 0 |

The pole voltage is always a square wave regardless of the number of the phase. Hence, Fourier series for three-phase pole voltages is the same as Eq. (7.4), but there is a phase difference as

$$v_{an} = \frac{2V_{dc}}{\pi} \sum_{n=1,3,5,\ldots}^{\infty} \frac{\sin n\omega t}{n} \tag{7.17}$$

$$v_{bn} = \frac{2V_{dc}}{\pi} \sum_{n=1,3,5,\ldots}^{\infty} \frac{\sin[n(\omega t - 120^\circ)]}{n} \tag{7.18}$$

$$v_{cn} = \frac{2V_{dc}}{\pi} \sum_{n=1,3,5,\ldots}^{\infty} \frac{\sin[n(\omega t + 120^\circ)]}{n} \tag{7.19}$$

Fourier series expansion for the line-to-line voltage, $v_{ab}$, is expressed as

$$\begin{aligned} v_{ab} &= v_{an} - v_{bn} \\ &= \frac{4V_{dc}}{n\pi} \sum_{n=1,3,5,\ldots}^{\infty} \cos\frac{n\pi}{6} \sin n\left(\omega t + \frac{\pi}{6}\right) \\ &= \frac{2\sqrt{3}V_{dc}}{\pi}\left[\sin\left(\omega t + \frac{\pi}{6}\right) - \frac{1}{5}\sin 5\left(\omega t + \frac{\pi}{6}\right) - \frac{1}{7}\sin 7\left(\omega t + \frac{\pi}{6}\right)\right. \\ &\quad \left. + \frac{1}{11}\sin 11\left(\omega t + \frac{\pi}{6}\right) + \frac{1}{13}\sin 13\left(\omega t + \frac{\pi}{6}\right) + \cdots\right. \end{aligned} \tag{7.20}$$

Because the line-to-line voltage is given as the difference between two pole voltages, it does not have any harmonics that are multiples of three, which exist in the pole voltages. Since the pole voltages have a phase difference of 120° with each other, the harmonics of multiples of three included in these will have a phase difference that are multiples of 360° with each other and thus they are actually in phase with each other. Therefore the harmonics of multiples of three are absent in the line-to-line voltages. Accordingly, the line-to-line voltage contains harmonics of order $6n \pm 1$ ($n$ = integer).

The phase voltages also have harmonics of order $6n \pm 1$ like line-to-line voltages. From Eq. (7.20), Fourier series expansion for phase *as* voltage can be written as

$$v_{as} = \frac{2V_{dc}}{\pi}\left[\sin \omega t - \frac{1}{5}\sin 5\omega t - \frac{1}{7}\sin 7\omega t + \frac{1}{11}\sin 11\omega t + \cdots\right] \tag{7.21}$$

Phase *bs* and *cs* voltages have harmonics identical to phase *as* voltage, but their phases are different. Fig. 7.20 shows the frequency spectrum of the line-to-line voltages and the phase voltages. Among harmonics, low-order ones such as the fifth and seventh harmonic are the major cause of waveform distortions.

In a three-phase inverter with a balanced Y-connected three-phase load, the neutral voltage $v_{sn}$ of the load is not zero but fluctuates at a frequency which is three times the output frequency as shown in Fig. 7.21. This is because the inverter output voltages are not pure sinusoidal.

Using Fourier series, the neutral voltage can be presented as

$$v_{sn} = \frac{4}{\pi}\frac{V_{dc}}{6}\sum_{n=1,3,5,\ldots}^{\infty}\frac{1}{n}\sin 3n\omega t \tag{7.22}$$

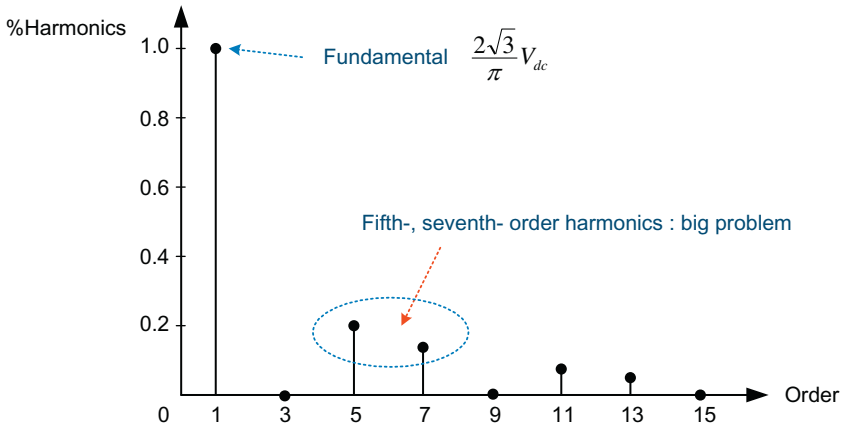



**FIGURE 7.20**

Frequency spectrum of line-to-line voltage and phase voltage.

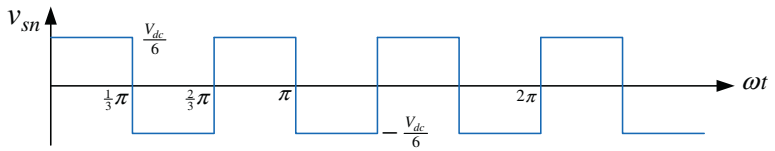



**FIGURE 7.21**

Neutral voltage in a Y-connected three-phase load.

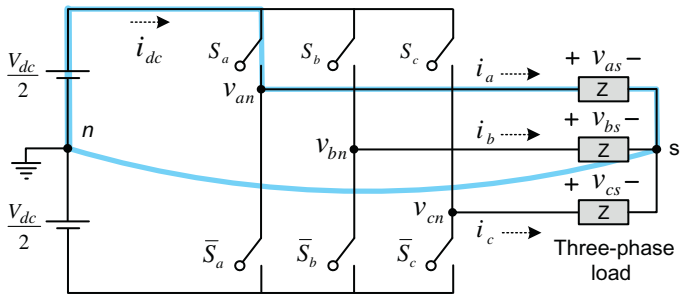



**FIGURE 7.22**

Three-phase inverter.

**EXAMPLE 2**

Calculate the maximum output voltage available by a three-phase inverter.

**Solution**

From Eq. (7.20), the maximum fundamental component of the line-to-line voltage, which a three-phase inverter can apply to the load, is

$$V_{ll-1rms} = \sqrt{3}\frac{2V_{dc}}{\pi}\frac{1}{\sqrt{2}} = \frac{\sqrt{6}}{\pi}V_{dc} \cong 0.78\ V_{dc}$$

To support a 220-$V_{rms}$ load, a three-phase inverter requires at least 282 V DC voltage.

### 7.1.5 MODELING OF A THREE-PHASE INVERTER USING SWITCHING FUNCTIONS

As mentioned earlier, the phase voltages of a three-phase inverter depends on the states of all six switches. These phase voltages can be expressed by using the switching function describing the states of switches in a pole. This switching function expression for the phase voltages are useful for analysis and simulation of a three-phase inverter.

Let us find the expressions of the phase voltages by the switching function. As shown in Fig. 7.22, assume a balanced Y-connected load with a floating neutral point $S$.

Let $S_a$, $S_b$ and $S_c$ be the switching functions for $a$, $b$, and $c$ poles, respectively. Again, the switching function is defined as "1" when the upper switch is turned on and as "0" when it is turned off.

When Kirchhoff's voltage law is applied to the closed-loop in the circuit shown in Fig. 7.22, the voltage equation is written as

$$v_{an} = v_{as} + v_{sn} \tag{7.23}$$

For two other phase circuits, we can obtain the voltage equations as

$$v_{bn} = v_{bs} + v_{sn} \tag{7.24}$$

$$v_{cn} = v_{cs} + v_{sn} \tag{7.25}$$

Using the corresponding switch function, each pole voltage is given as

$$v_{an} = V_{dc}\left(S_a - \frac{1}{2}\right) \tag{7.26}$$

$$v_{bn} = V_{dc}\left(S_b - \frac{1}{2}\right) \tag{7.27}$$

$$v_{cn} = V_{dc}\left(S_c - \frac{1}{2}\right) \tag{7.28}$$

The sum of these three equations is

$$v_{an} + v_{bn} + v_{cn} = v_{as} + v_{bs} + v_{cs} + 3v_{sn} \tag{7.29}$$

Here, the sum of three-phase voltages is zero for a balanced Y-connected load with a floating neutral point, i.e.,

$$v_{as} + v_{bs} + v_{cs} = Z(i_{as} + i_{bs} + i_{cs}) = 0 \tag{7.30}$$

Hence the neutral voltage $v_{sn}$ is given as the average of three pole voltages, i.e.,

$$v_{sn} = \frac{1}{3}(v_{an} + v_{bn} + v_{cn}) = \frac{V_{dc}}{3}\left(S_a + S_b + S_c - \frac{3}{2}\right) \tag{7.31}$$

By substituting this neutral voltage into Eqs. (7.23)–(7.25), we can obtain the phase voltages. For example, by substituting Eq. (7.31) into Eq. (7.23), the voltage of phase $as$ is given as

$$\begin{aligned} v_{as} = v_{an} - v_{sn} \quad &= V_{dc}\left(S_a - \frac{1}{2}\right) - \frac{V_{dc}}{3}\left(S_a + S_b + S_c - \frac{3}{2}\right) \\ &= \frac{V_{dc}}{3}(2S_a - S_b - S_c) \end{aligned} \tag{7.32}$$

Likewise, the expressions of phase $bs$ and $cs$ voltages can be obtained.

The expressions of phase voltages in a three-phase inverter using switching functions are as follows:

$$v_{as} = \frac{V_{dc}}{3}(2S_a - S_b - S_c) \tag{7.33}$$

$$v_{bs} = \frac{V_{dc}}{3}(2S_b - S_c - S_a) \tag{7.34}$$

$$v_{cs} = \frac{V_{dc}}{3}(2S_c - S_a - S_b) \tag{7.35}$$

These expressions are also obtained directly by combining Eqs. (7.12)–(7.14) with Eqs. (7.26)–(7.28). Fig. 7.23 shows the voltage of phase *as* obtained by using Eq. (7.33) and the switching functions.

The input DC current in a three-phase inverter can also be expressed by using switching functions. The input DC current $i_{dc}$ can be expressed as one-phase current for each section as follows:

$$\begin{aligned} i_{dc} = &-i_b\left(0 \le \omega t \le \frac{\pi}{3}\right) \\ &i_a\left(\frac{\pi}{3} \le \omega t \le \frac{2\pi}{3}\right) \\ &-i_c\left(\frac{2\pi}{3} \le \omega t \le \pi\right) \\ &i_b\left(\pi \le \omega t \le \frac{4\pi}{3}\right) \\ &-i_a\left(\frac{4\pi}{3} \le \omega t \le \frac{5\pi}{3}\right) \\ &i_c\left(\frac{5\pi}{3} \le \omega t \le \frac{2\pi}{3}\right) \end{aligned} \tag{7.36}$$

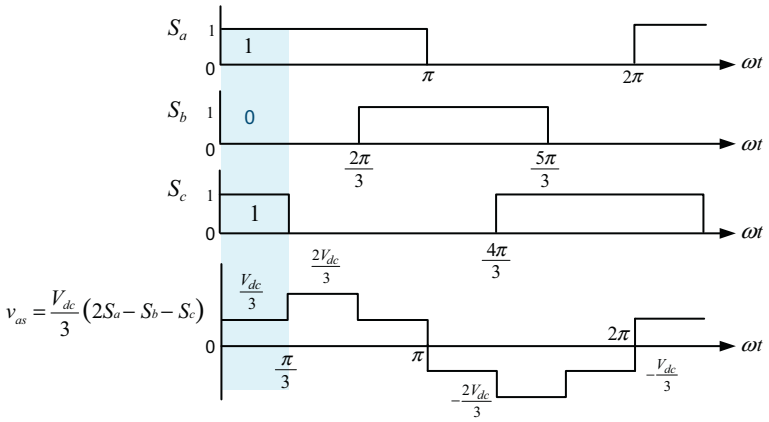



**FIGURE 7.23**

Phase *as* voltage obtained by using switching functions.

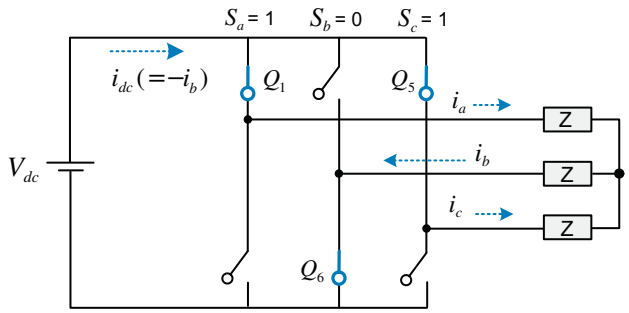



**FIGURE 7.24**

Input DC current and phase currents.

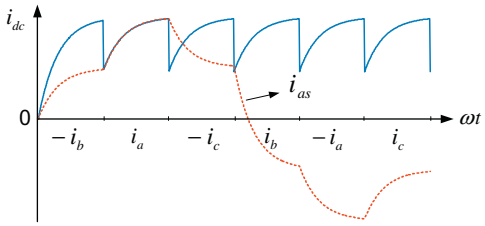



**FIGURE 7.25**

Input DC current of a three-phase inverter.

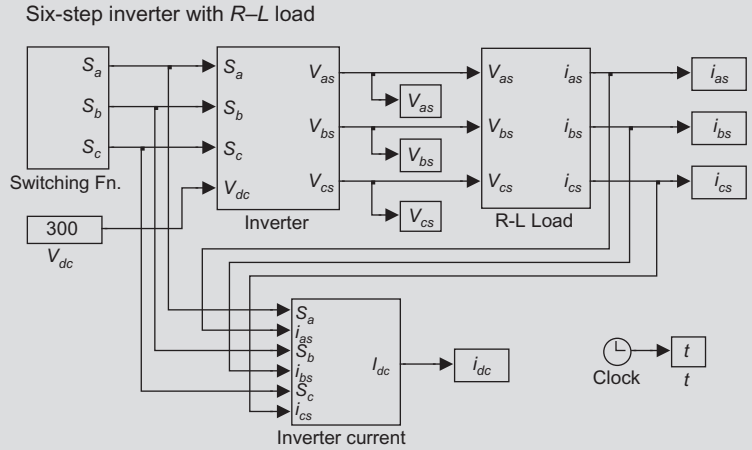
As one example, Fig. 7.24 shows that the input current $i_{dc}$ is $-i_b(=i_a+i_c)$ in the first section where $Q5$, $Q6$, and $Q1$ are turned on. From Eq. (7.36), the input current of a three-phase inverter can be expressed as switching functions as

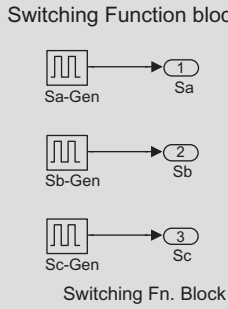
$$i_{dc} = S_a i_a + S_b i_b + S_c i_c \tag{7.37}$$

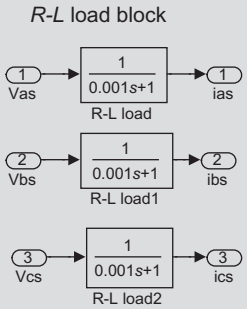
The input current for the six-step operation is shown in Fig. 7.25. We can see that it has a ripple component six times the output frequency. We need to consider this component in the filter design for reducing the DC voltage ripple.

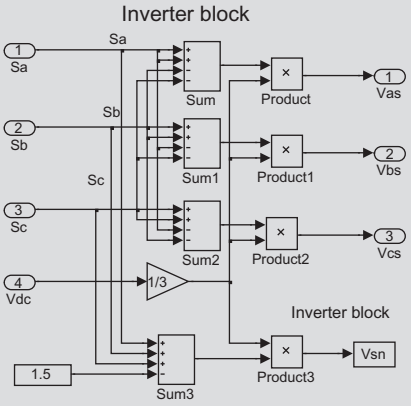
## MATLAB/SIMULINK SIMULATION: SIX-STEP INVERTER

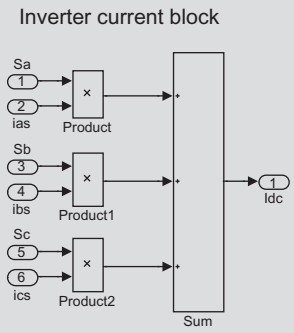
- Simulation conditions: $V_{dc} = 300$ V, $R$–$L$ load, output frequency 60 Hz
- Overall simulation block diagram



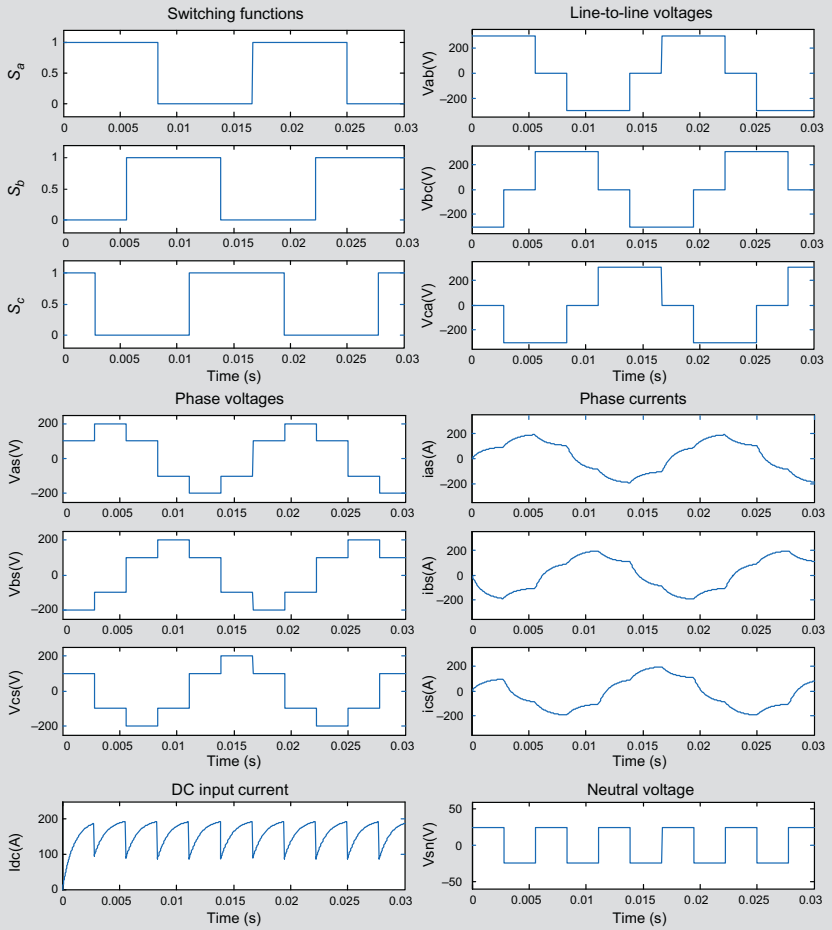




(*Continued*)

## MATLAB/SIMULINK SIMULATION: SIX-STEP INVERTER (CONTINUED)

- Simulation results




## 7.2 PULSE WIDTH MODULATION INVERTERS

In the Section 7.1, we illustrated a square wave inverter where only the frequency of the output voltage could be controlled, not its amplitude. We can use this square wave operation for producing the maximum output voltage of an inverter, i.e., for the maximum DC voltage utilization of an inverter. To control the

amplitude and the frequency of the output voltage of a VSI, the PWM technique is commonly used as shown in Fig. 7.26.

For such PWM inverters, the following control is possible:

- Linear control of the fundamental output voltage
- Control of frequency of the fundamental output voltage
- Control of harmonics included in the output voltage

The ultimate goal of the PWM is to generate gating pulses of the switches for the inverter to produce an output voltage with the desired fundamental amplitude and frequency. In this modulation process, the switching patterns to eliminate unnecessary harmonics and/or to minimize switching losses can be also developed. To improve these control performances, a variety of PWM techniques have been proposed ever since the sinusoidal pulse width modulation (SPWM) was first introduced in 1964 [2].

There are several performance criteria to evaluate the PWM techniques. First, the range of linearly controllable fundamental output voltage under a given DC voltage is assessed. It is obvious that a larger linear range means better DC voltage utilization. Next, harmonics included in the output voltage is assessed. If the output voltage contains fewer harmonics, it approaches a pure sinusoidal AC. Thus this item is important in assessing the quality of the inverter output voltage. Commonly a higher switching frequency leads to fewer harmonics, and thus this item should be evaluated under the same switching frequency. For the inverter utilized in AC motor drives, since the developed torque of the motor depends on its current, the harmonics included in the current instead of the output voltage is often evaluated. Finally the losses of the switching devices and the losses of the motor generated by adopting PWM are assessed.

Over the past 40 years, many PWM techniques, different in concept and performance, have been developed to improve these criteria. These techniques can be classified into three groups as follows:

- Programmed/optimal PWM
- Carrier-based PWM
- Space vector PWM

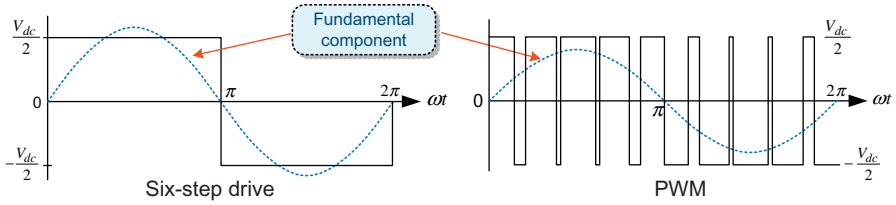



**FIGURE 7.26**

Output voltage control of an inverter.

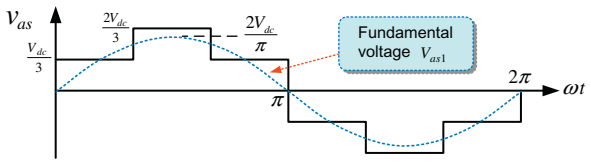



**FIGURE 7.27**

Fundamental phase voltage of a six-step inverter.

Among these, the carrier-based PWM techniques have been the most widely used method ever since the early development of PWM technology. However, the space vector pulse width modulation (SVPWM) is known to be the most superior in terms of the voltage linearity range and harmonic content.

Before describing these PWM techniques, it is helpful to define the *modulation index* (*MI*) term, which indicates the voltage utilization level as

$$\text{Modulation index:} \quad MI = \frac{V_{1peak}}{\left(\frac{V_{dc}}{2}\right)} \tag{7.38}$$

The modulation index denotes the ratio of the fundamental component magnitude, $V_{1peak}$, of the inverter phase voltage to the half of DC-link voltage, $V_{dc}/2$. For example, the *MI* in the six-step inverter shown in Fig. 7.27 becomes

$$MI = \frac{V_{1\ peak}}{\left(\frac{V_{dc}}{2}\right)} = \frac{\left(\frac{2V_{dc}}{\pi}\right)}{\left(\frac{V_{dc}}{2}\right)} = \frac{4}{\pi} = 1.273 \tag{7.39}$$

This modulation index value is the maximum *MI* attainable from a three-phase inverter.

Now we will look at a detailed description of the typical PWM techniques of the three groups.

### 7.2.1 PROGRAMMED PWM TECHNIQUE [3]

In this technique, the PWM switching patterns for generating an output voltage with the desired amplitude of the fundamental component are precalculated off-line and then stored in memory for online access. Inverters are operated by using the PWM switching patterns read in accordance with the operating condition from the memory. Thus, this technique is called programmed PWM.

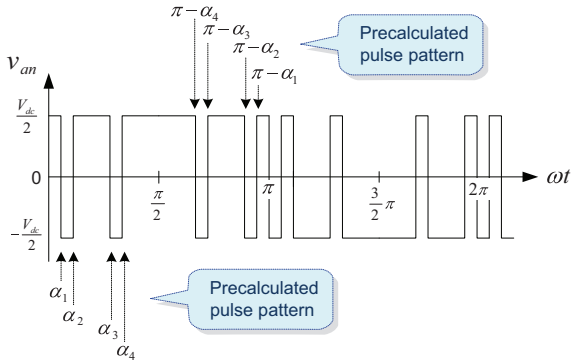



**FIGURE 7.28**

Programmed PWM technique.

This PWM technique not only controls the fundamental component of the inverter output voltage but also optimizes the desired performance criteria such as eliminating unnecessary low-order harmonics, reducing total harmonics, reducing harmonic torque, or minimizing the switching frequency. Thus this technique is also called *optimal PWM*.

Fourier series are used to obtain the switching instants in this PWM technique. For example, consider eliminating unnecessary low-order harmonics, while producing the desired fundamental component. Suppose that the number of switching angles $\alpha_k$ in 1/4 period for the quarter-wave symmetry square wave is $k$ (e.g., $k = 4$ in Fig. 7.28). In this case, $k$ equations, which can control $k$ frequency components of output voltage, can be obtained from Fourier series representation of the waveform with $k$ switching angles. By solving these $k$ equations, the switching angles $\alpha_k$ can be obtained for producing the desired fundamental voltage while eliminating $k - 1$ harmonics.

Besides eliminating unnecessary harmonics, the switching patterns can be obtained to optimize specific performance criteria such as harmonic losses or harmonic torque. This technique has advantages of better DC voltage utilization and optimization of switching frequency. However, a considerable computational effort is required to solve transcendental equations when obtaining switching patterns. Moreover, these precalculated steady-state switching patterns are difficult to produce the desired output voltage correctly in the transient state or DC-link voltage variation. Thus this technique cannot be used for systems requiring a fast dynamic.

### 7.2.2 SINUSOIDAL PWM TECHNIQUE [2]

Sinusoidal PWM is a typical PWM technique. In this PWM technique, the sinusoidal AC voltage reference $v_{ref}$ is compared with the high-frequency triangular carrier wave $v_c$ in real time to determine switching states for each pole in the

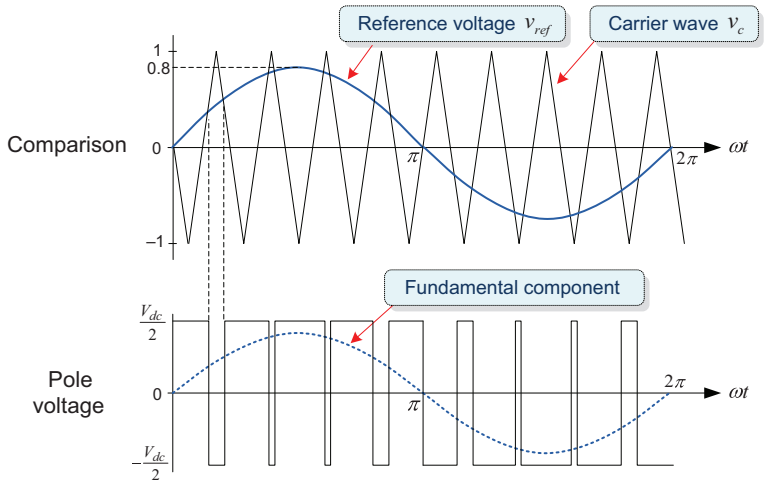



**FIGURE 7.29**

Sinusoidal PWM technique.

inverter. After comparing, the switching states for each pole can be determined based on the following rule:

- Voltage reference $v_{ref} >$ Triangular carrier $v_c$: upper switch is turned on (pole voltage $= V_{dc}/2$)
- Voltage reference $v_{ref} <$ Triangular carrier $v_c$: lower switch is turned on (pole voltage $= -V_{dc}/2$)

Here, the peak-to-peak value of the triangular carrier wave is given as the DC-link voltage $V_{dc}$. In this PWM technique, the necessary condition for linear modulation is that the amplitude of the voltage reference $v_{ref}$ must remain below the peak of the triangular carrier $v_c$, i.e., $v_{ref} \leq V_{dc}/2$. Since this PWM technique utilizes a high-frequency carrier wave for voltage modulation, this kind of PWM technique is called a carrier-based PWM technique. Especially, this carrier-based technique is called SPWM since the reference is given as the shape of a sine wave. This is also called the triangle-comparison PWM technique since this uses the carrier of a triangular wave. Fig. 7.29 depicts the sinusoidal PWM technique for one phase.

### MODULATING WAVE AND CARRIER WAVE

In the carrier-based PWM techniques, the desired voltage reference waveform is referred to as *modulating wave*. In addition, a wave which is modulated with the modulating wave is referred to as *carrier wave* or *carrier*. The carrier wave usually has a much higher frequency than the modulating wave. The triangular waveform is the most commonly used carrier in the PWM technique for modulating AC voltage. On the other hand, different forms of modulating wave can be used according to the PWM technique. Typical SPWM technique uses the sinusoidal modulating waveform.

**Difference Between Pole Voltage and Phase Voltage References**
An inverter output determined by comparing a voltage reference with the triangular carrier wave is the pole voltage. Thus the voltage reference that is compared with the triangular carrier wave is considered as the pole voltage reference. Typical SPWM technique uses a phase voltage reference as the pole voltage reference. On the other hand, different pole voltage reference can be used according to the PWM techniques.

In this PWM based on comparison with the triangular wave, if the ratio of carrier frequency to fundamental frequency is large enough (greater than 21), then the fundamental component of the output voltage varies linearly with the reference voltage $v_{ref}$ for a constant DC-link voltage as

$$v_{o1} = v_{ref} \sin \omega t \tag{7.40}$$

In addition, the fundamental frequency of the output voltage is identical to that of the reference voltage.

The output voltage of Eq. (7.40) can be rewritten in terms of the modulation index $MI$ as

$$v_{01} = \frac{V_{dc}}{2} MI \sin \omega t \tag{7.41}$$

Here, since $v_{ref} \leq V_{dc}/2$, so $0 \leq MI \leq 1$.

The range of $0 \leq MI \leq 1$ is called the *linear modulation range* because, in this range, the inverter can generate an output voltage linearly proportional to the reference voltage as shown in Fig. 7.30. In this case, the PWM inverter is considered to be simply a voltage amplifier with a unit gain.

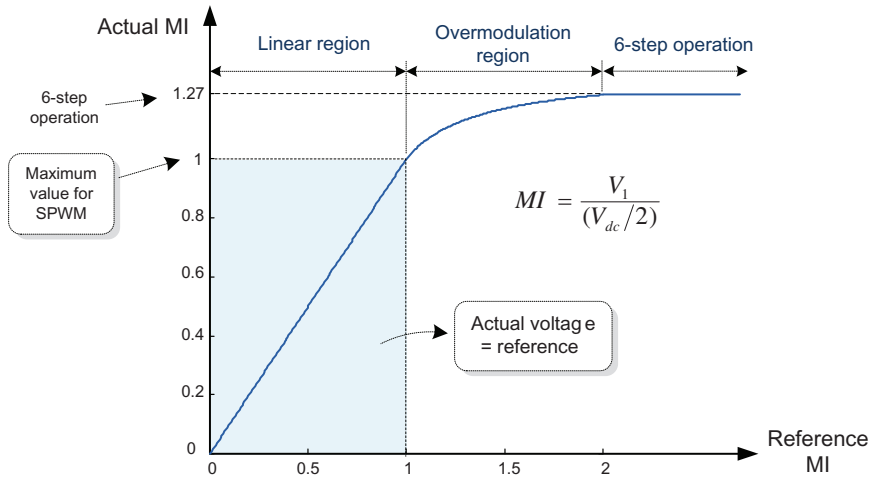



**FIGURE 7.30**
Voltage modulation range for SPWM.

However, when the reference exceeds the peak of the triangular carrier (i.e., $MI > 1$), the inverter cannot produce an output voltage linearly proportional to the voltage reference. The range of $MI > 1$ is called *overmodulation region*, where the linearity of the modulation is lost. We will discuss the overmodulation techniques in Section 7.5.

The maximum linear output voltage, $V_{dc}/2$, attainable by the SPWM technique corresponds to 78.5% of the maximum output voltage, $2V_{dc}/\pi$, by the six-step inverter. Therefore, when using the PWM technique, the attainable maximum limit of the linear modulation range is inevitably less than the maximum output voltage of an inverter.

Fig. 7.31 shows the SPWM technique for a three-phase inverter.

In the SPWM technique, the switching frequency of an inverter is equal to that of a carrier wave. From Figs. 7.29 and 7.31, we can see that the switch is turned on/off once every period of the triangular carrier wave. Thus the SPWM technique has an advantage of having a constant switching frequency. A constant switching frequency makes it possible to calculate the losses of switching devices, so the thermal design for them becomes easier. In addition, since the harmonic characteristics will be well-defined, the design of a low-pass filter to eliminate the harmonics will become easier.

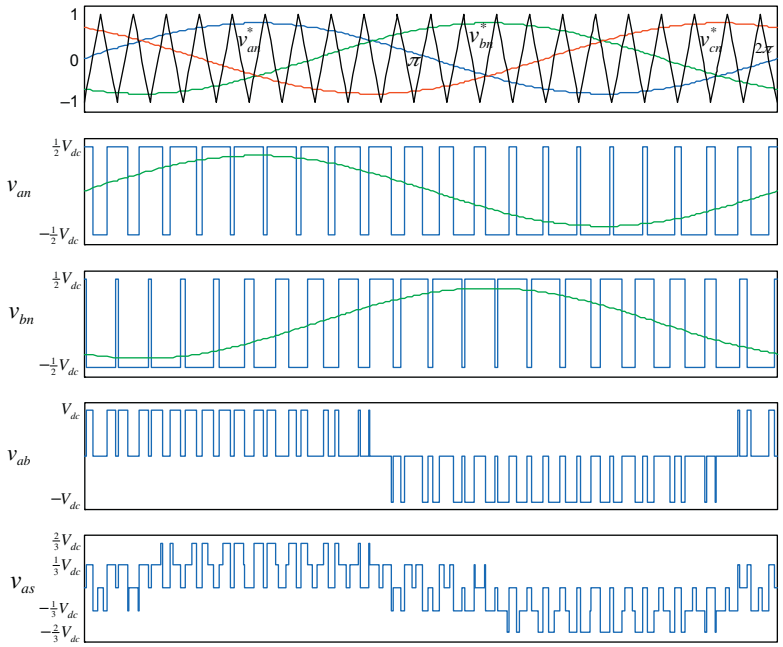



**FIGURE 7.31**

SPWM technique for a three-phase inverter.

Now we will evaluate which harmonics are contained in the output voltage generated by the SPWM technique. First, we will investigate the harmonic components of the pole voltage $v_P$ as shown in Fig. 7.29. It is widely known that the pole voltage contains harmonics at the carrier frequency $f_c$ and frequencies of its integer multiples ($M$), and the sidebands ($N$) of all these frequencies [4]. Thus these harmonics, which are known as switching frequency harmonics, can be expressed as

$$\begin{aligned} v_{o-h} &= V_h \sin[2\pi(Mf_c \pm Nf_o)t + \phi_h] \\ &= V_h \sin[2\pi f_o(Mm_f \pm N)t + \phi_h] \end{aligned} \tag{7.42}$$

Here, $f_o$ is the fundamental frequency of the output voltage and $m_f$ is the *frequency modulation index*, which denotes the ratio of the carrier frequency to the fundamental frequency, i.e., $m_f = f_c/f_o$. $M$ and $N$ are integers, and $M + N$ is odd. $\phi_h$ denotes the phase of harmonic component. From Eq. (7.42), the orders of harmonics are given as

$$\begin{aligned} &m_f,\ m_f \pm 2,\ m_f \pm 4,\ m_f \pm 6, \ldots \\ &2m_f \pm 1,\ 2m_f \pm 3,\ 2m_f \pm 5,\ 2m_f \pm 7, \ldots \\ &3m_f,\ 3m_f \pm 2,\ 3m_f \pm 4,\ 3m_f \pm 6, \ldots \\ &4m_f \pm 1,\ 4m_f \pm 3,\ 4m_f \pm 5,\ 4m_f \pm 7, \ldots \end{aligned} \tag{7.43}$$

Among the harmonics, the component of order $m_f$ has the largest magnitude. This means that the harmonic with the frequency equal to the switching frequency $f_c$ is the largest one.

As an example, Fig. 7.32 shows the frequency spectrum for the pole voltage of $f_o = 50$ Hz and $m_f = 21$. In this case, the harmonic of 1050 Hz($= 21 \times 50$ Hz), i.e., the switching frequency is the largest component.

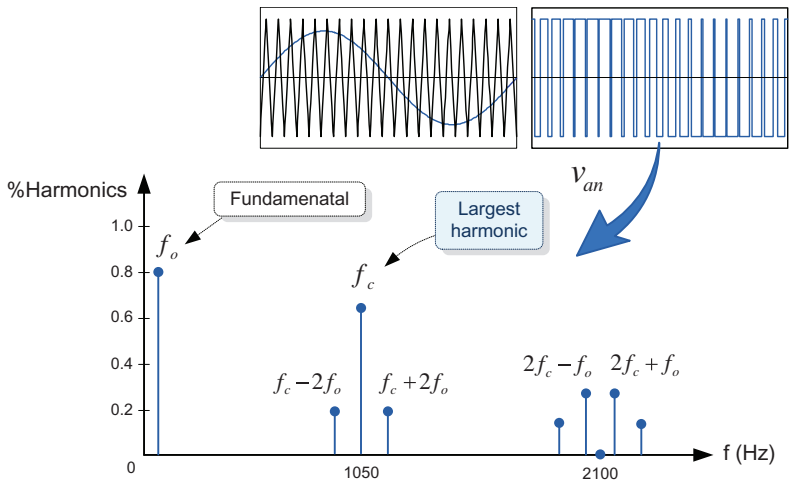



**FIGURE 7.32**

Frequency spectrum of the pole voltage for the SPWM.

The higher the switching frequency is, the higher the order of the major harmonic is. Thus, when a higher switching frequency is used, the quality of the voltage waveform can be improved and filtering can be made easier. However, this leads to greater switching losses. Therefore it is important to consider the overall performance of the system when selecting the switching frequency.

Next we will examine the harmonic components for the line-to-line and phase voltages. Since the line-to-line voltage is the difference between the two pole voltages, they do not have any harmonic at multiples of three, which exist in the pole voltages. As mentioned earlier, this is because the harmonics at multiples of three included in the pole voltages will have no phase difference with each other. Hence, if we select the value of $m_f$ as multiples of three, then the total harmonics will be reduced in the line-to-line voltage due to the elimination of the harmonics at multiples of three. For this reason, the value of $m_f$ is usually selected as multiples of three. Furthermore, among these values, only the odd values can eliminate the even harmonics for the symmetry of three-phase PWM patterns. In that case, the harmonic of order $2m_f \pm 1$ becomes the largest component for the range of $MI < 0.9$, while $m_f \pm 2$ around $MI = 1$. For example, Fig. 7.33 depicts the harmonic spectrum for the line-to-line voltage in the case of $m_f = 21$ and $MI = 0.8$. In this case, unlike that of the pole voltage, the largest harmonic component becomes the order of $2m_f \pm 1$. The phase voltages have harmonic components identical to those of the line-to-line voltages, but their magnitudes are different.

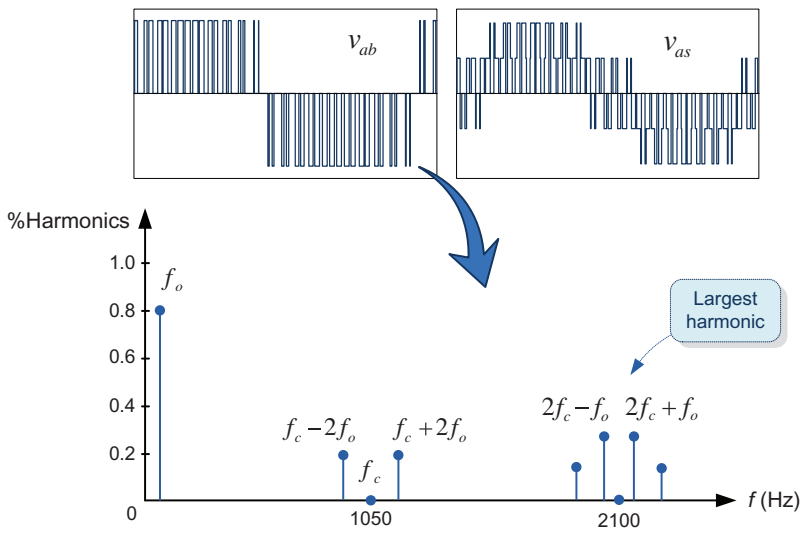



**FIGURE 7.33**

Frequency spectrum of the line-to-line voltage for the SPWM ($MI = 0.8$, $m_f = 21$).

The SPWM technique has been widely popular due to the simplicity of its principle and analog implementation. In the analogue implementation of the SPWM (referred to as *naturally sampled PWM*), an analog integrator is used to generate a triangular carrier wave, and an analog comparator is used to determine the intersection instants of the triangular carrier wave and modulating signal.

In contrast, its software-based implementation using a digital technique or microprocessor is not easy because this requires solving the transcendental equation, which defines points of intersection used to determine the switching instants. Instead, as shown in Fig. 7.34, the so-called *regular-sampled PWM* is used in which the sinusoidal reference is held at a constant sampled value for the carrier interval, and the sampled value is compared with the carrier wave to determine the switching instants [5]. In the regular-sampled PWM, there are two types of sampling, *symmetric* and *asymmetric*. In the symmetrical sampling of Fig. 7.34A, the sinusoidal reference is sampled once at the peak of the triangular carrier wave, whereas in the asymmetrical sampling of Fig. 7.34B, it is sampled twice at both the positive and negative peaks of the triangular carrier wave. Nowadays, its digital implementation can be easily done by using microcontrollers supporting the dedicated module for the PWM signal generation.

Since the SPWM technique can perform voltage modulation every sampling interval with a fixed switching frequency, it exhibits a better dynamic performance than the programmed PWM. However, this technique has a limited voltage linearity range (only 78.5% of six-step operation) and a poor waveform quality in the high modulation range. To overcome these problems, many improved PWM techniques have been developed. Improvements to extend the voltage linearity range have been mainly done through the modification of the modulating signal, resulting in nonsinusoidal modulating signals. As a typical example of the improvement, the *third harmonic injection PWM* makes it possible to increase the fundamental component of the output voltages by 15.5% more than the conventional SPWM technique. Now we will discuss the third harmonic injection PWM.

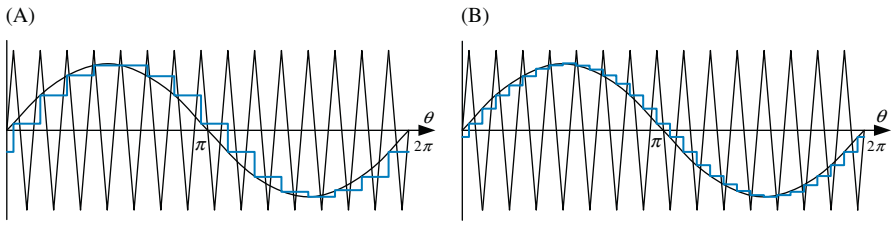



**FIGURE 7.34**

Regular-sampled PWM technique (A) Symmetrically sampling and (B) asymmetrically sampling.

### 7.2.3 THIRD HARMONIC INJECTION PWM TECHNIQUE [6]

The SPWM technique operates properly when the sinusoidal voltage reference $v^*$ remains below the peak of the triangular carrier. This limits the range of linear modulation in the SPWM technique. When the peak of the voltage reference $v^*$ exceeds the peak of the triangular carrier (i.e., $MI > 1$) as shown in Fig. 7.35, a pulse dropping, which indicates no intersection between the voltage reference and the triangular carrier, happens. As a result, the linear relationship between the voltage reference and the output voltage cannot be maintained.

Recall that the only effective voltage to a load is the fundamental component contained in the output voltage. Thus, if we select the voltage reference of whose fundamental component exceeds the peak of the triangular carrier but its own peak does not, then it can be expected that the linear modulation range can be extended. By adding a third harmonic to the voltage reference waveform, this improvement can be attainable. This is because when a third harmonic is added to the voltage reference waveform, the peak of the resultant waveform becomes less than that of the original waveform as shown in Fig. 7.36. The technique that adopts this principle is the *third harmonic injection pulse width modulation* (THIPWM). By using the THIPWM, the fundamental of the output voltage can be increased by 15.5% more than the conventional SPWM technique.

This deliberate third harmonic voltage is not present on the line-to-line and phase voltages for a three-phase load with a floating neutral point such as AC

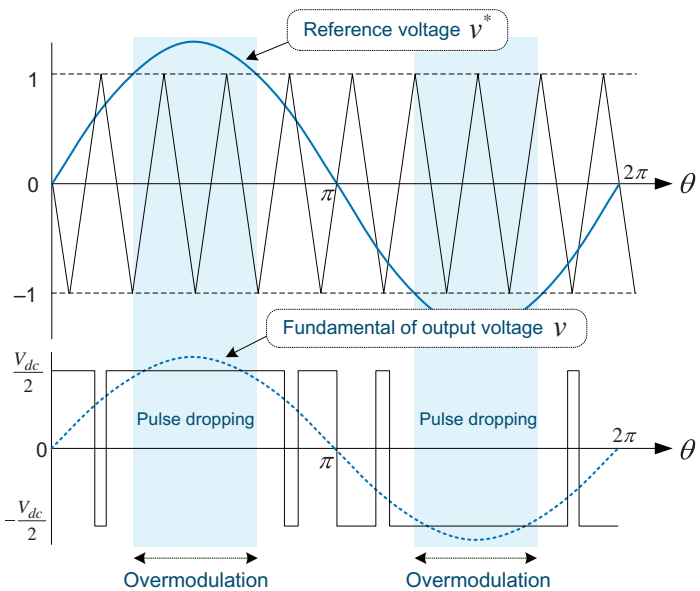



**FIGURE 7.35**

Overmodulation in the SPWM technique.

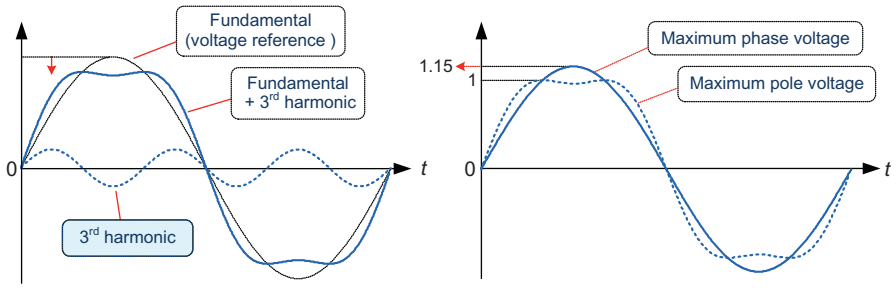



**FIGURE 7.36**

Principle of THIPWM.

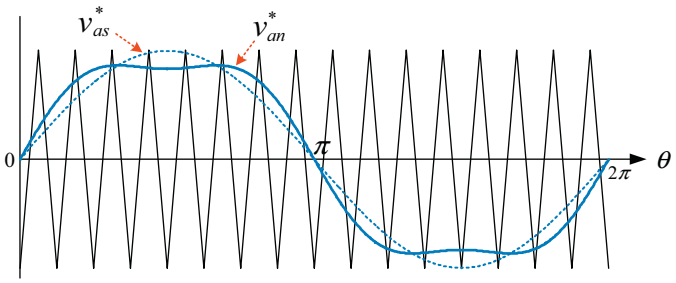



**FIGURE 7.37**

Third harmonic injection pulse width modulation.

motors. Thus the injected third harmonic voltage does not cause any distortion on the line-to-line and phase voltages.

Let us find the third harmonic voltage that gives an optimal performance in the THIPWM. Assume that the voltage reference of phase *as* is $v_{as}^* = V_1 \sin\omega t$ as shown in Fig. 7.37.

By adding the third harmonic to this voltage reference, the resultant voltage reference becomes

$$v_{an}^* = V_1 \sin \omega t + V_3 \sin 3\omega t \tag{7.44}$$

For Eq. (7.44), the optimum value of $V_3$ that maximizes the fundamental of the phase voltage is $V_1/6$ [6]. The addition of a third harmonic with an amplitude of 1/6 of the voltage reference can reduce the peak value of the voltage reference by a factor of 0.866 without changing the amplitude of the fundamental component. Accordingly, the fundamental component of the phase voltage can be increased by 15.5% (=1/0.866). This value corresponds to 90.7% of the output voltage for a six-step inverter.

Instead of the factor of 1/6, it is known that a third harmonic with an amplitude of 1/4 of the voltage reference can lead to a minimum harmonic distortion on the output voltage. However, this amplitude incurs a slight decrease in the maximum linear modulation value to $MI = 1.12$. The THIPWM technique has a disadvantage of implementation complexity of the third harmonic and steady-

state current harmonic characteristics inferior to the SVPWM method. In addition to the third harmonic, there is another THIPWM technique that uses a higher order triple harmonic such as the ninth harmonic.

### 7.2.4 SPACE VECTOR PWM TECHNIQUE [7]

In the PWM techniques mentioned previously, the three-phase voltage references are modulated individually. Unlike these, there is a PWM technique that uses a different approach based on the concept of a space vector, called SVPWM. In the SVPWM technique, the three-phase voltage references are represented as a space vector $\boldsymbol{v}_{abc}$ in the complex plane, and this voltage reference vector is modulated by output voltage vectors available from an inverter. The SVPWM technique is now widely used in many three-phase inverter applications because it produces fundamental output voltage 15.5% more than the one produced by the SPWM technique and gives less harmonic distortion of the load current, lower torque ripple in AC motors, and lower switching losses.

The concept of the space vector required in this PWM technique was discussed in Section 4.3. For this PWM technique, since the three-phase voltage references are given as a voltage space vector, the possible output voltages of an inverter also need to be expressed as a space vector. In the Section 7.1.4, we saw that there are eight possible switching states in a three-phase inverter. The output voltage vectors, $V_o - V_7$, corresponding to the eight possible switching states, are shown in Table 7.3. Refer to Example 3, which shows how to obtain these vectors. Fig. 7.38 depicts these output voltage vectors of a three-phase inverter in the complex plane.

**Table 7.3** Output Voltage Vectors Corresponding to Switching States

| Switch States | | | Phase Voltages | | | Space Voltage Vector |
|---|---|---|---|---|---|---|
| $S_a$ | $S_b$ | $S_c$ | $v_{as}$ | $v_{bs}$ | $v_{cs}$ | $V_n(n = 1-7)$ |
| 0 | 0 | 0 | 0 | 0 | 0 | $V_0 = 0\angle 0^\circ$ |
| 1 | 0 | 0 | $\frac{2}{3}V_{dc}$ | $-\frac{1}{3}V_{dc}$ | $-\frac{1}{3}V_{dc}$ | $V_1 = \frac{2}{3}V_{dc}\angle 0^\circ$ |
| 1 | 1 | 0 | $\frac{1}{3}V_{dc}$ | $\frac{1}{3}V_{dc}$ | $-\frac{2}{3}V_{dc}$ | $V_2 = \frac{2}{3}V_{dc}\angle 60^\circ$ |
| 0 | 1 | 0 | $-\frac{1}{3}V_{dc}$ | $\frac{2}{3}V_{dc}$ | $-\frac{1}{3}V_{dc}$ | $V_3 = \frac{2}{3}V_{dc}\angle 120^\circ$ |
| 0 | 1 | 1 | $-\frac{2}{3}V_{dc}$ | $\frac{1}{3}V_{dc}$ | $\frac{1}{3}V_{dc}$ | $V_4 = \frac{2}{3}V_{dc}\angle 180^\circ$ |
| 0 | 0 | 1 | $-\frac{1}{3}V_{dc}$ | $-\frac{1}{3}V_{dc}$ | $\frac{2}{3}V_{dc}$ | $V_5 = \frac{2}{3}V_{dc}\angle 240^\circ$ |
| 1 | 0 | 1 | $\frac{1}{3}V_{dc}$ | $-\frac{2}{3}V_{dc}$ | $\frac{1}{3}V_{dc}$ | $V_6 = \frac{2}{3}V_{dc}\angle 300^\circ$ |
| 1 | 1 | 1 | 0 | 0 | 0 | $V_7 = 0\angle 0^\circ$ |

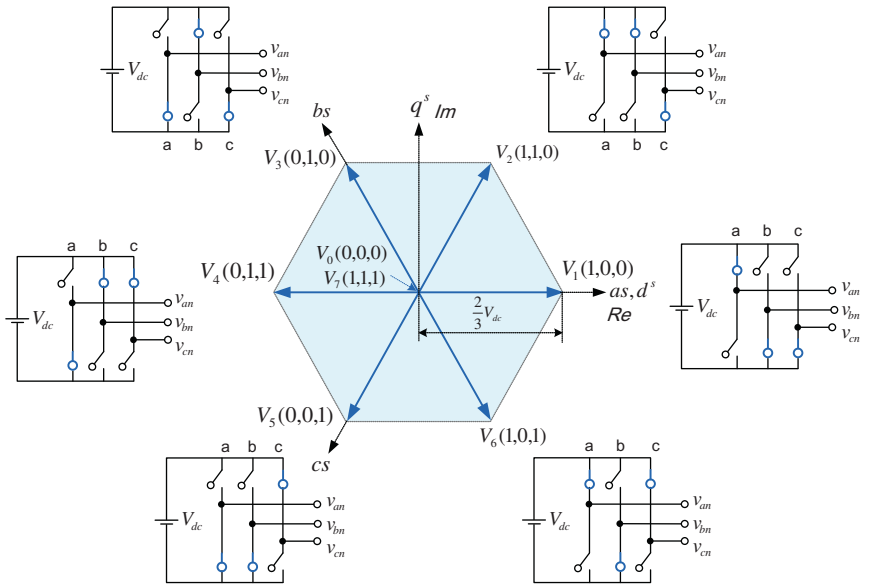



**FIGURE 7.38**

Output voltage vectors in the complex plane (or $d$–$q$ axes stationary frame).

Six of these vectors, $V_1 - V_6$, which are called *active voltage vecto*r, offer an effective voltage to the load. The magnitude of all active vectors is equal to $2V_{dc}/3$. However, they are 60° out of phase with each other. By contrast, the two vectors, $V_0$ and $V_7$, are called *zero voltage vector*, which cannot yield an effective voltage to the load.

**EXAMPLE 3**

Express the output phase voltage of a three-phase inverter as a space vector.

**Solution**

As an example, we will find the voltage vector $V_2$ for the switching state of $S_a = 1$, $S_b = 1$, $S_c = 0$.

- Voltage space vector definition:

$$V = \frac{2}{3}(v_{as} + av_{bs} + a^2 v_{cs}) = v_{as} + \mathrm{j}\frac{1}{\sqrt{3}}(v_{bs} - v_{cs})$$

(Here, $a = e^{\mathrm{j}2\pi/3} = -\frac{1}{2} + \mathrm{j}\frac{\sqrt{3}}{2}$, $a^2 = e^{\mathrm{j}4\pi/3} = -\frac{1}{2} - \mathrm{j}\frac{\sqrt{3}}{2}$)

- Phase voltages: $v_{as} = \frac{1}{3}V_{dc}$, $v_{bs} = \frac{1}{3}V_{dc}$, $v_{cs} = -\frac{2}{3}V_{dc}$
  - Voltage vector $V_2 = \left(\frac{1}{3} + \mathrm{j}\frac{1}{\sqrt{3}}\right)V_{dc} = \frac{2}{3}V_{dc} \angle 60^\circ$

We can obtain voltage vectors for the remaining switching states in a similar manner as shown in Table 7.3.

### 7.2.4.1 Principle of space vector pulse width modulation technique

As the three-phase voltage references vary with time, the voltage reference vector $V^*$ rotates in the counterclockwise direction in the complex plane as illustrated in Fig. 7.39. This vector completes one revolution per electrical period of the reference voltage.

In the SVPWM technique, a voltage reference is given as a space vector of $V^*$ and this voltage reference vector $V^*$ is generated by using the output voltage vectors of a three-phase inverter. By using the two active voltage vectors adjacent to $V^*$ and the zero vectors among the available eight voltage vectors, the SVPWM technique produces a voltage that has the same fundamental volt-second average as the given voltage reference vector $V^*$ over a modulation period $T_s$.

Now we will describe how to generate a voltage reference vector. The voltage reference vector $V^*$ is assumed to be inside a hexagon, which is formed by six output voltage vectors of a three-phase inverter. Only when this condition is satisfied, the voltage reference vector can be modulated properly.

For example, consider a voltage reference vector $V^*$ given in sector ① of the six segments in the hexagon shown in Fig. 7.39. In this case, the inverter cannot generate the required voltage reference vector directly because there is no inverter output vector that has the magnitude and the phase equal to those of the voltage reference vector. Thus as an alternative, of the six active vectors, the two voltage vectors adjacent to the voltage reference vector and the zero vectors are used to generate a voltage that has the same fundamental volt-second average as the given voltage reference vector $V^*$. This modulation repeats each modulation period $T_s$ depending on the switching frequency.

Let us now examine this modulation process in more detail. The voltage reference vector $V^*$ is assumed to remain constant over the modulation period $T_s$. The process to synthesize the voltage vectors for generating the reference vector $V^*$ consists of three steps as shown in Fig. 7.40.

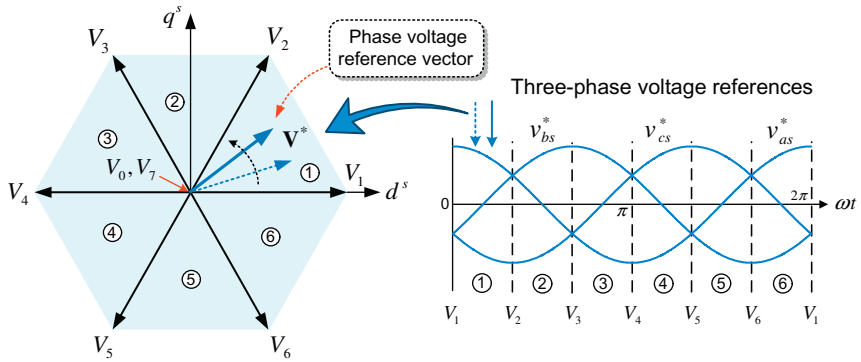



**FIGURE 7.39**

Rotation of voltage vector.

In the first step, one of the two adjacent active voltage vectors, $V_1$, is applied first during time $T_1$. As a result, an output voltage with the magnitude of $V_1 \cdot (T_1/T_s)$ in the direction of the vector $V_1$ is generated. Next, another vector $V_2$ is applied during time $T_2$ to meet the magnitude and the phase of the voltage reference vector $V^*$. Through these two steps, it is possible to generate the same output voltage as the voltage reference vector over the modulation period $T_s$. Lastly, if $T_1 + T_2 < T_s$, then one of the zero vectors, $V_0$ or $V_7$, is applied during the remaining time $T_0 (= T_s - T_1 - T_2)$.

The duration time ($T_1$, $T_2$, and $T_0$) of each voltage vector for generating a given reference vector $V^*$ can be calculated as follows. The above modulation process can be expressed mathematically as

$$\int_0^{T_s} V^* dt = \int_0^{T_s} V_n dt + \int_{T_1}^{T_1+T_2} V_{n+1} dt + \int_{T_1+T_2}^{T_s} V_{0,7} dt \tag{7.45}$$

Assuming a constant DC-link voltage during $T_s$, Eq. (7.45) can be rewritten as

$$V^* \cdot T_s = V_n \cdot T_1 + V_{n+1} \cdot T_2 \tag{7.46}$$

As an example, if the voltage reference vector $V^*$ is given in the first sector ① ($0 \le \theta \le 60^\circ$), Eq. (7.46) can be decomposed into two components as

$$\begin{cases} T_s \cdot |V^*| \cos\theta = T_1 \cdot \left(\frac{2}{3} V_{dc}\right) + T_2 \cdot \left(\frac{2}{3} V_{dc}\right) \cos 60^\circ \\ T_s \cdot |V^*| \sin\theta = T_2 \cdot \left(\frac{2}{3} V_{dc}\right) \sin 60^\circ \end{cases} \tag{7.47}$$

Solving Eq. (7.47) yields the duration times as

$$T_1 = T_s \cdot a \cdot \frac{\sin(60^\circ - \theta)}{\sin 60^\circ} \tag{7.48}$$

$$T_2 = T_s \cdot a \cdot \frac{\sin\theta}{\sin 60^\circ} \tag{7.49}$$

$$T_0 = T_s - (T_1 + T_2) \tag{7.50}$$

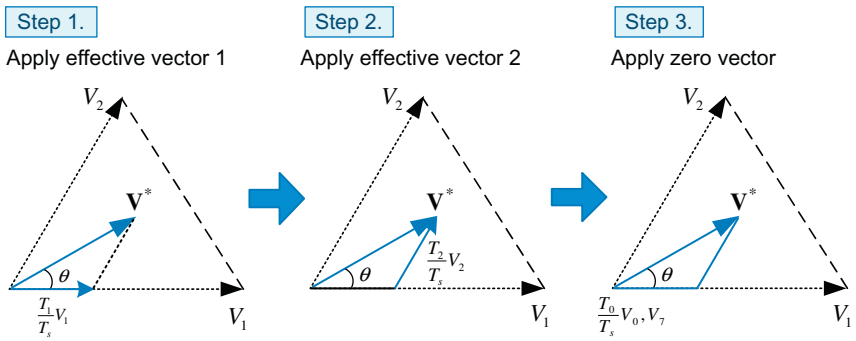



**FIGURE 7.40**

Modulation process for voltage generation.

Here, $a = |V^*|/\frac{2}{3}V_{dc}$. The duration times for the voltage reference vector in the other sectors ②–⑥ can be calculated in a similar manner.

Let us examine the achievable range of the output voltage by using the SVPWM technique. In the SVPWM technique, the sum of the duration times for the two active voltage vectors should not exceed the modulation period, i.e., $T_1 + T_2 \leq T_s$. Using Eqs. (7.48) and (7.49), the magnitude of the voltage reference to meet this requirement can be obtained as

$$T_1 + T_2 \leq T_s \;\rightarrow\; \mathrm{V}^* \leq \frac{V_{dc}}{\sqrt{3}} \frac{1}{\sin(60^\circ + \theta)} \tag{7.51}$$

This equation indicates that the possible range of the voltage reference vector $V^*$ is inside the hexagon formed by joining the extremities of the six active vectors as shown in Fig. 7.41. However, for a voltage reference vector over one electrical period, the range of the voltage reference vector should be inside the inscribed circle of the hexagon to obtain the equal magnitude. Therefore the radius of the inscribed circle, $V_{dc}/\sqrt{3}$, is the maximum fundamental phase voltage in the SVPWM technique. This value is about 15.5% larger than that of the SPWM technique and is equal to that of the THIPWM technique. The value corresponds to 90.7% of the output voltage in the six-step operation.

### 7.2.4.2 Symmetrical space vector pulse width modulation technique

In the Section 7.2.4.1, we described how to obtain the duration times of the active and the zero voltage vectors to produce a given voltage reference vector. For given selected vectors and their duration times, there are many ways to place them within the modulation interval $T_s$.

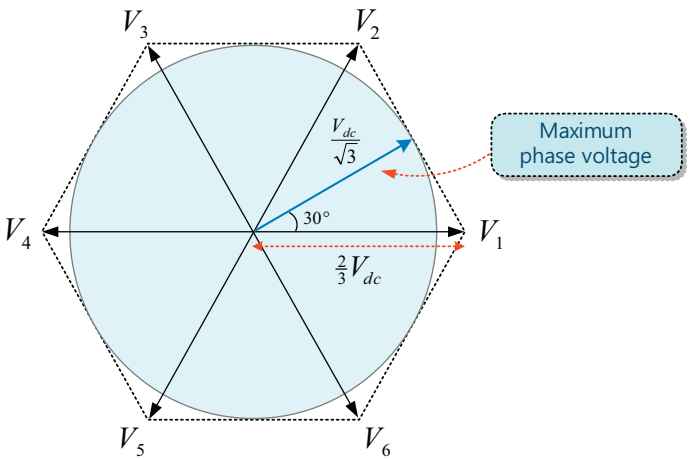



**FIGURE 7.41**

Possible range of the voltage reference vector in the SVPWM.

The placement of these vectors does not affect the average value of the output voltage over the interval $T_s$, but it significantly influences the linear modulation range and harmonic characteristics of the output voltage. In particular, the placement of the effective voltage vectors is important. Fig. 7.42 compares how the magnitude and frequency of the current ripple of the load can vary with the placement of the effective voltage vectors. Fig. 7.42A shows a case where the effective voltage vector is placed in the middle of the modulation interval. Compared with Fig. 7.42B, this placement results in a smaller current ripple and a higher ripple frequency. Thus the placement of Fig. 7.42A can give a better harmonic performance than that of Fig. 7.42B.

It was known that placing the effective voltage vectors at the center of the modulation interval shows superior harmonic characteristics as shown in Fig. 7.42A [8,9]. The SVPWM technique of this placement scheme is called *symmetrical SVPWM* technique. Moreover, this centering can increase the pulse width further to modulate the effective voltage, resulting in an improved voltage modulation range. The placement of the zero voltage vectors determines the position of the effective voltage vectors within the modulation interval $T_s$. Thus, in the *symmetrical SVPWM* technique, the two zero vectors, $V_0$ and $V_7$, during an equal time of $T_0/2$ are distributed at the beginning and the end of the modulation interval $T_s$ as shown in Fig. 7.43. Furthermore, in this case, to obtain the minimum switching frequency, it is necessary to arrange the switching sequence in the order of $V_0(000) \rightarrow V_1(100) \rightarrow V_2(110) \rightarrow V_7(111)$.

For this purpose, the two zero vectors of $V_0$ and $V_7$ are used alternately in the interval $T_s$. In such a switching sequence, the transition from one vector to another vector can be performed by switching only one switch. In the next interval, the switching sequence is reversed, i.e., $V_7 \rightarrow V_2 \rightarrow V_1 \rightarrow V_0$ as shown in Fig. 7.44 [9]. This interval also requires only one switching for the transition.

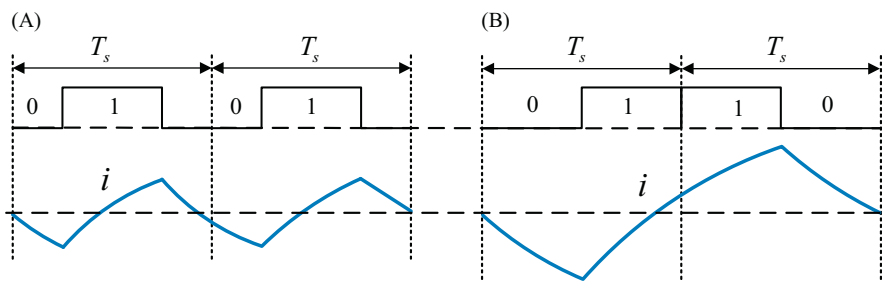



**FIGURE 7.42**

Current characteristics according to the placement of active voltage pulses. (A) Best case and (B) worst case.

*D.G. Holmes, The significance of zero space vector placement for carrier-based PWM schemes, IEEE Trans. Ind. Appl., 32 (5) (1996) 1122–1129.*

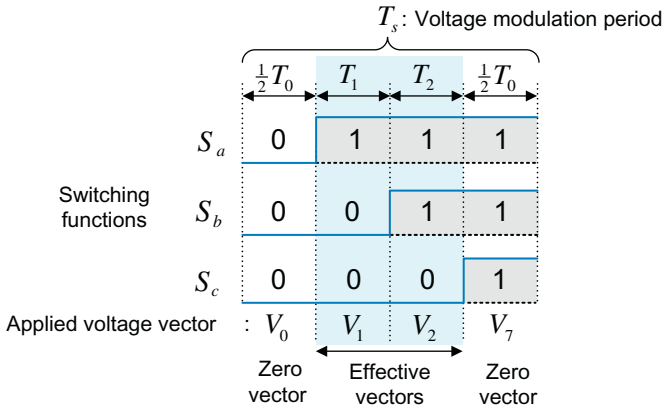



**FIGURE 7.43**

Switching sequence.

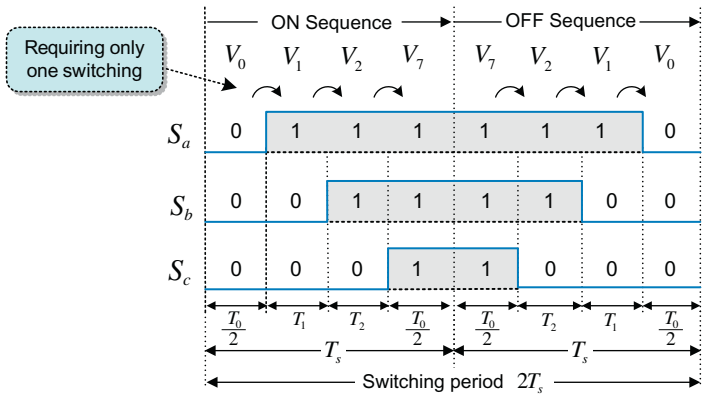



**FIGURE 7.44**

Alternate switching sequence.

Such alternating switching sequences at every modulation interval allow the switching frequency to be reduced.

Fig. 7.45 shows the switching sequences in all six sectors for the symmetrical *SVPWM* technique.

For this alternate switching sequence, the two modulation intervals $2T_s$ become one switching period. For example, the modulation interval $T_s$ of 100 μs indicates a switching frequency of 5 kHz. Commonly, the modulation interval $T_s$ refers to the current control period. This is because a new voltage reference is given at every current control period.

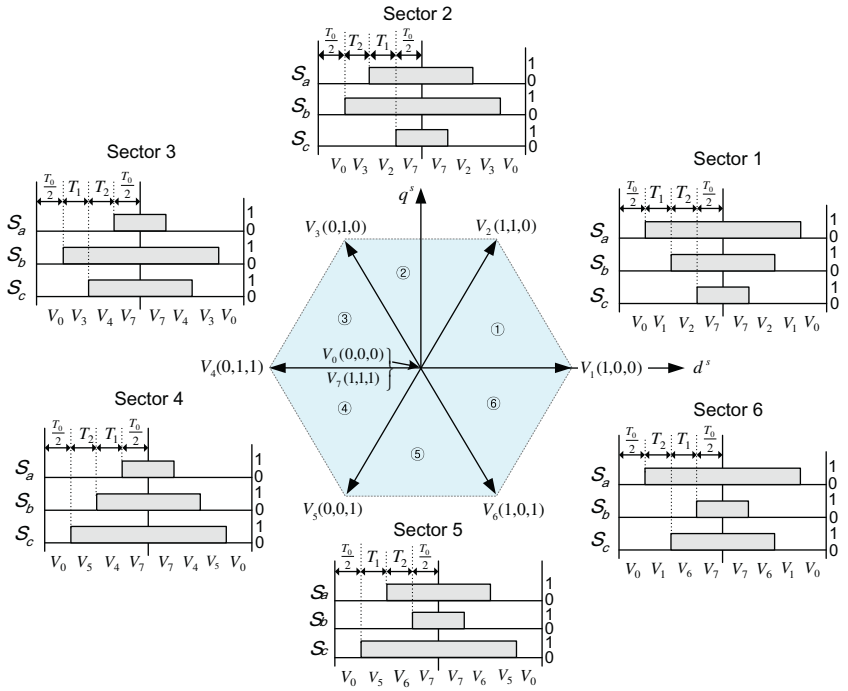



**FIGURE 7.45**

Switching sequences in six sectors.

## EXAMPLE 4

Describe the pole voltage for the symmetrical SVPWM technique.

**Solution**

From the vector duration times calculated for each sector as shown in Fig. 7.45, we can obtain the pole *an* voltage for the SVPWM technique. The pole *an* voltage for a given command vector $V^*$ in the first sector ① ($0^\circ \le \theta \le 60^\circ$) from Eqs. (7.48) and (7.49) is

$$v_{an1} = \frac{T_1 + T_2}{T_s} \cdot \frac{V_{dc}}{2} = \frac{\sqrt{3}}{2} |V^*| \cos\left(\frac{\pi}{6} - \theta\right)$$

In a similar manner, the pole voltages for the remaining sectors can be obtained as:

Sector ② ($60^\circ \le \theta \le 120^\circ$):

$$v_{an2} = \frac{T_1 - T_2}{T_s} \cdot \frac{V_{dc}}{2} = \frac{3}{2} |V^*| \cos\left(\frac{\pi}{6} - \theta\right)$$

Sector ③ ($120^\circ \le \theta \le 180^\circ$):

$$v_{an3} = \frac{-T_1 - T_2}{T_s} \cdot \frac{V_{dc}}{2} = -\frac{3}{2} |V^*| \cos\left(\frac{\pi}{6} - \theta\right)$$

Sector ④ ($180° \le \theta \le 240°$):

$$v_{an4} = \frac{-T_1 - T_2}{T_s} \cdot \frac{V_{dc}}{2} = -\frac{3}{2}|V^*|\cos\left(\frac{\pi}{6} - \theta\right)$$

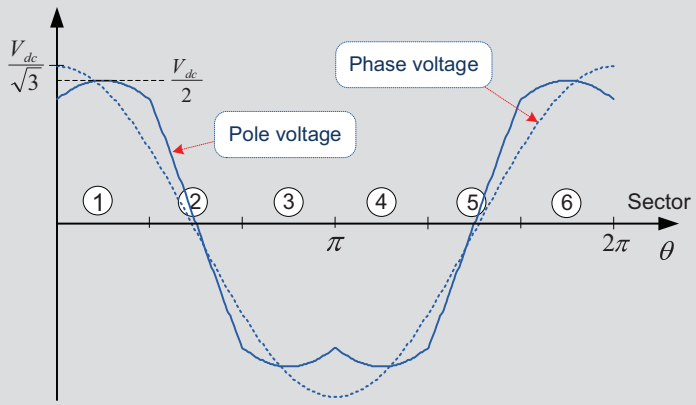
Sector ⑤ ($240° \le \theta \le 300°$):

$$v_{an5} = \frac{-T_1 + T_2}{T_s} \cdot \frac{V_{dc}}{2} = \frac{3}{2}|V^*|\cos\left(\frac{\pi}{6} - \theta\right)$$

Sector ⑥ ($300° \le \theta \le 360°$):

$$v_{an6} = \frac{T_1 + T_2}{T_s} \cdot \frac{V_{dc}}{2} = \frac{\sqrt{3}}{2}|V^*|\cos\left(\frac{\pi}{6} - \theta\right)$$

The following figure shows the pole *an* voltage obtained in all sectors for $MI = 1$ (i.e., $|V^*| = V_{dc}/\sqrt{3}$).




As can be seen in Example 4, it is interesting to note that the pole voltage is not a pure sinusoidal wave but a waveform that contains a third harmonic component similar to the modulation waveform of the THIPWM technique. In the THIPWM technique, we can see that the addition of a third harmonic to the voltage reference can increase the fundamental of the phase voltage. Since the SVPWM technique also exploits the third harmonic component, it can also be considered to extend the linear modulation range more than the SPWM technique.

Fig. 7.46 compares the output torque and the harmonic distortion of the load current for the SPWM and the SVPWM techniques [7]. It can be readily seen that the SVPWM technique allows a value of *MI* up to 1.15 and can produce a harmonic distortion lower than that of the SPWM technique in the high modulation range.

Contrary to the symmetrical SVPWM technique, the effective voltages in the SPWM technique are not placed at the center, resulting in harmonic characteristics inferior to those of the symmetrical SVPWM technique.

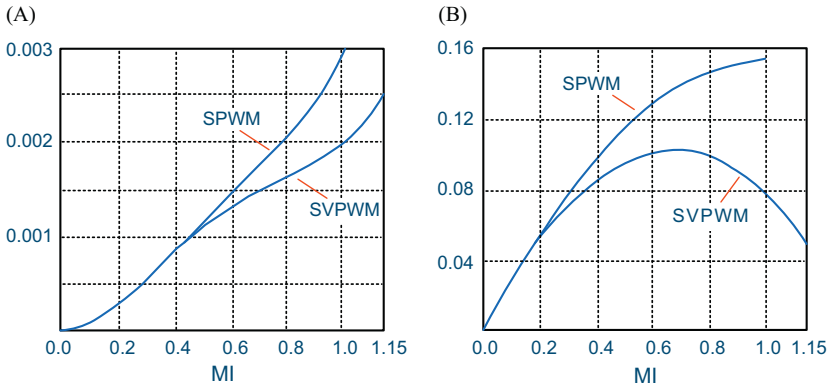



**FIGURE 7.46**

Comparison between the SPWM and the SVPWM techniques. (A) Square of rms harmonic current and (B) torque harmonic.

*H.W. Van Der Broeck, et al., Analysis and realization of a pulse width modulator based on voltage space vectors, IEEE Trans. Ind. Appl., 24 (1) (1988) 142–150.*

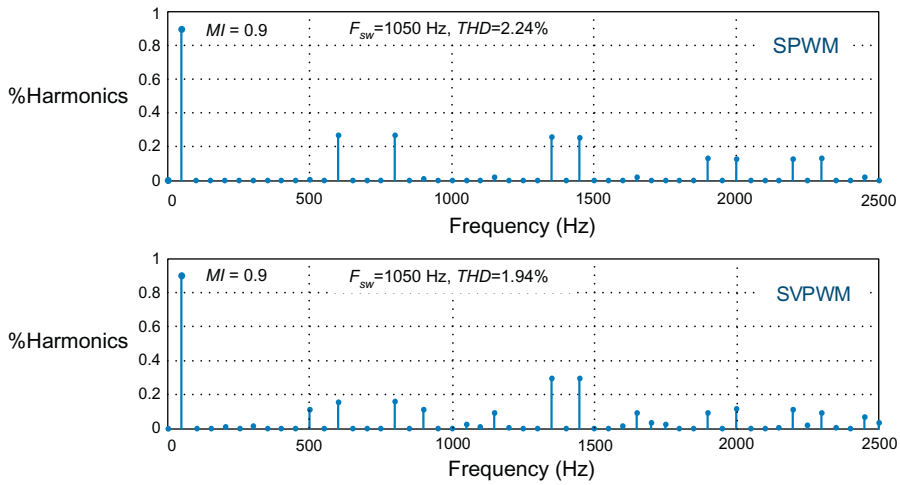



**FIGURE 7.47**

Frequency spectrum of the phase voltages for the SPWM and SVPWM.

The harmonic orders contained in the SVPWM technique are similar to those of the SPWM technique expressed in Eq. (7.42). However, from Fig. 7.47, it can be seen that the relative magnitude of the switching frequency harmonics for the SVPWM technique is smaller than that of the SPWM technique, and the SVPWM

technique spreads its switching harmonic energy effectively into the sidebands. Consequently, the THD of the SVPWM technique is less than that of the SPWM technique, even though the harmonic of the double switching frequencies for the SVPWM technique increases.

The disadvantage of the SVPWM technique is that it requires trigonometric calculations and a greater computational effort to calculate the switching times of active voltage vectors. However, nowadays, this method can be simply implemented by the carrier-based PWM technique using an offset voltage. This technique will be discussed in more detail in Section 7.4.

The SVPWM technique described above uses the symmetrical modulation method in which the two zero vectors are distributed during an equal duration time. In this case, all switches in three poles operate at every modulation period. Thus this is called *three-phase modulation* or *continuous modulation*. By contrast, we can select different duration times for two zero vectors. Depending on the selection, we can obtain various modulation methods, which differ in modulation performances such as harmonic characteristics, voltage linearity, and switching losses. Thus the placement of the zero vectors is a degree of freedom for modulation in the SVPWM technique. A typical example of having unequally distributed zero vectors is a modulation technique in which switches in only two of the three poles operate to reduce the switching frequency. This is called *two-phase modulation* or *discontinuous modulation* in which the switches of one leg are kept inactive in the modulation interval as shown in Fig. 7.48. In this discontinuous modulation technique, only one zero vector, either $T_0$ or $T_7$, is used. Accordingly, this causes a loss of symmetry in the placement of effective voltage vectors. However, due to switching in only two of the three poles, the overall switching frequency can be reduced by 1/3 compared to the three-phase modulation. In the higher modulation range, the discontinuous modulation produces a lower harmonic distortion because of its higher net switching frequency. However, in the low modulation range, due to a loss of symmetry, the discontinuous modulation has a harmonic distortion higher than the continuous modulation.

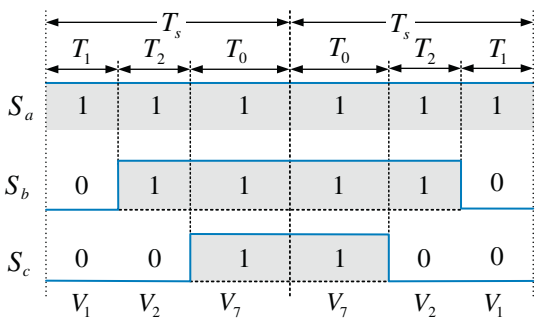



**FIGURE 7.48**

Switching sequence in two-phase modulation.

## 7.3 DISCONTINUOUS PWM TECHNIQUES [10]

The PWM techniques described previously use a continuous modulation in which the switching actions occur in all the three poles of an inverter. By contrast, in a discontinuous modulation (or two-phase modulation) that reduce the switching frequency, the switching actions occur in only two of the three poles. Though the aim of the discontinuous modulation is to reduce the switching frequency, some characteristics such as switching losses, harmonics, and voltage linearity vary according to the location of the interval of the switches being kept inactive (i.e., unmodulated section). Thus there could be various discontinuous PWM (DPWM) techniques according to the location of the unmodulated section. Here, six popular discontinuous PWM techniques will be described.

For the symmetry in a three-phase system, the scope where the modulation ceases can be a total of 120° section at most per fundamental cycle as shown in Fig. 7.49. This indicates that, by using the unmodulated section fully, the effective switching frequency can be reduced to 66.7% of the frequency of the continuous PWM (CPWM) methods. Though the unmodulated section can be placed at any position, it is normally placed around the peak of the phase current to reduce the switching losses effectively. This is because the switching losses are proportional to the magnitude of the current. Thus it is necessary to place unmodulated sections differently according to the power factor of a load.

### 7.3.1 60° DISCONTINUOUS PWM TECHNIQUE

This 60° discontinuous pulse width modulation (DPWM) technique ceases to switch each switching device for two 60° sections around both the positive and the negative

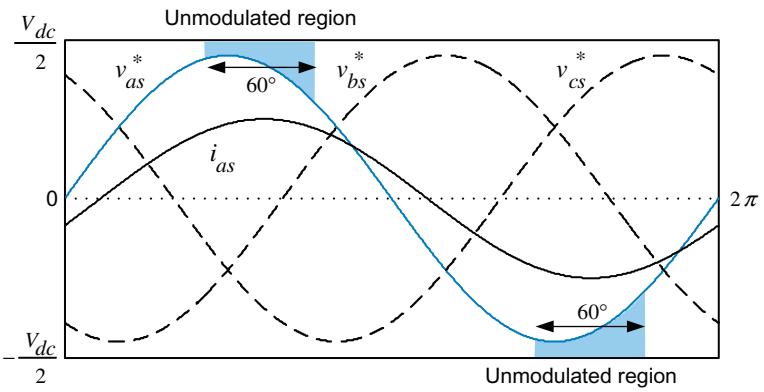



**FIGURE 7.49**

Unmodulated sections.

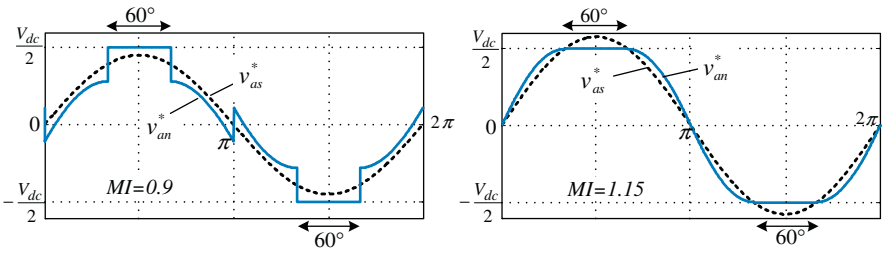



**FIGURE 7.50**

60° discontinuous PWM technique: pole voltage and phase voltage.

peaks of each phase voltage waveform. This DPWM technique shows the minimum switching loss characteristic for near unity power factor loads such as utility interface, UPS applications, and permanent magnet synchronous motors.

Fig. 7.50 shows the waveforms of the pole and phase voltages for $MI = 0.9$ and 1.15, respectively, by using the 60° DPWM technique. In the 60° DPWM technique, the pole voltage reference $v^*_{an}$ is clamped to the positive DC rail $(V_{dc}/2)$ for the 60° section around the positive peak of the phase voltage waveform $v^*_{as}$. So, the upper switch is kept on the "on" state for that section as shown in Fig. 7.50. In addition, the pole voltage reference is clamped to the negative DC rail $(-V_{dc}/2)$ for the 60° section around the negative peak of the phase voltage waveform. So, the lower switch is kept on the "on" state for that section. Otherwise, the magnitude of the pole voltage reference $v^*_{an}$ is adjusted to produce the desired fundamental voltage.

We will discuss how to obtain the pole voltage reference for the DPWM technique in the next section.

### 7.3.2 60° (±30°) DISCONTINUOUS PWM TECHNIQUE

To achieve the minimum switching losses for lagging power factor loads such as induction motor drives, it is desirable that the modulation cease for the 60° section shifted by +30° phase with respect to the peaks of the phase voltage as shown in Fig. 7.51A. On the other hand, the minimum switching losses for leading power factor loads such as induction generators will need the 60° unmodulated section shifted by -30° with respect to the peaks of the phase voltage waveform as shown in Fig. 7.51B.

### 7.3.3 ±120° DISCONTINUOUS PWM TECHNIQUE

For simplicity, there is a 120° DPWM technique in which the modulation ceases for a total of 120° section. The unmodulated section can be either the largest or the lowest 120° section of the phase voltage waveform as shown in Fig. 7.52.

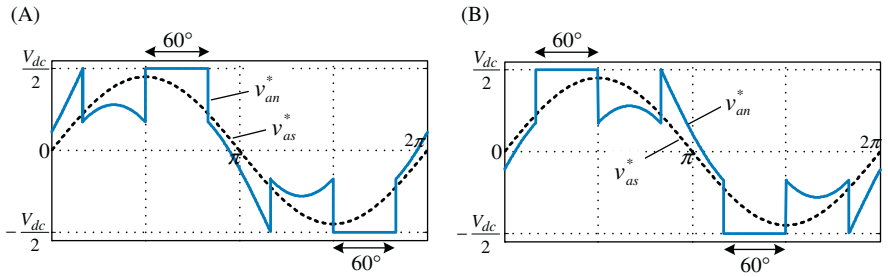



**FIGURE 7.51**

60° ( ± 30°) DPWM technique: pole and phase voltages ($MI = 0.9$) (A) 60° (+30°) DPWM and (B) 60° (−30°) DPWM.

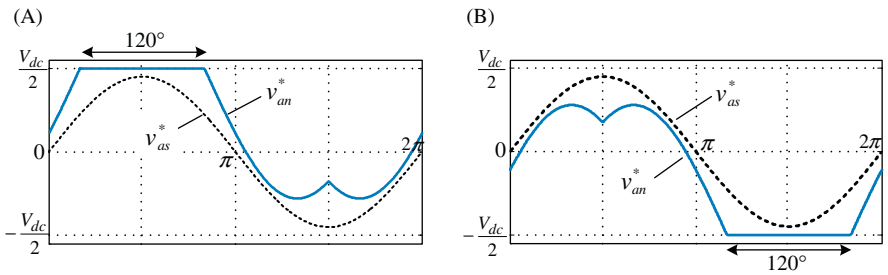



**FIGURE 7.52**

120° DPWM technique: pole and phase voltages ($MI = 0.9$). (A) +120° DPWM and (B) −120° DPWM.

However, these techniques have nonuniform thermal stress on the switching devices.

### 7.3.4 30° DISCONTINUOUS PWM TECHNIQUE

This 30° DPWM technique has less harmonic distortion than other DPWM techniques. As shown in Fig. 7.53, the 30° DPWM technique has four unmodulated sections, each equal to 30° section.

It should be noted that, as shown in Fig. 7.50–7.53, the pole voltage references in the DPWM techniques become a nonsinusoidal waveform whose shape depends on the position of the unmodulated section.

The DPWM techniques can lead to a reduction in the switching losses and an improved waveform quality in the high modulation range. However, a poor low modulation range performance and its implementation complexity have limited the application of these DPWM techniques. In addition, they exhibit a nonlinear

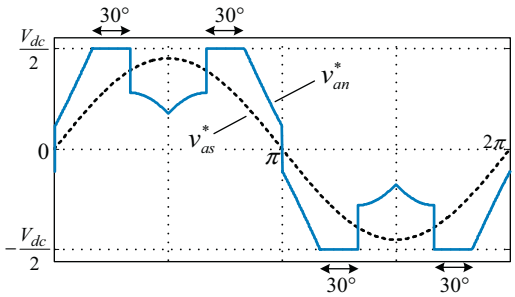



**FIGURE 7.53**

30° DPWM technique: pole and phase voltages ($MI = 0.9$).

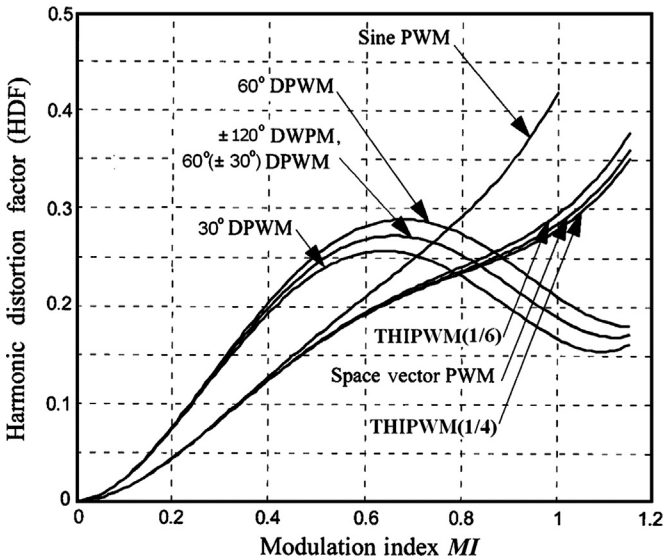



**FIGURE 7.54**

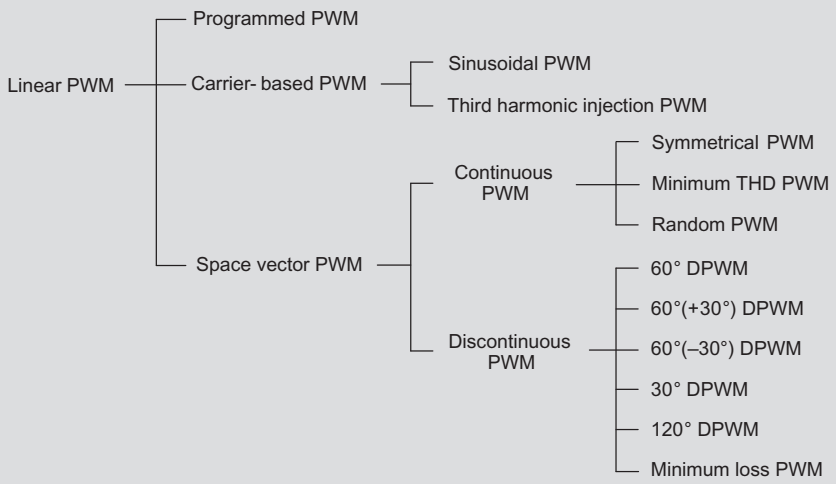
HDF comparison with different voltage modulation techniques.

*A.M. Hava, R.J. Kerkman, T.A. Lipo, A high-performance generalized discontinuous PWM algorithm, IEEE Trans. Ind. Appl., 34 (5) (1998) 1059–1071.*

relation between the reference and output voltage in very low modulation range. Fig. 7.54 shows harmonic distortion factor (HDF) curves of all the discussed PWM techniques under an equal inverter average switching frequency (thus the HDF of the DPWM methods is multiplied by $(2/3)^2$) [10]. We can see from the

HDF curves that the CPWM methods have a better HDF in the low modulation range, while the DPWM techniques are superior in the high modulation range of $MI > 0.8$.

**LINEAR PULSE WIDTH MODULATION TECHNIQUES**




The DPWM techniques explained above can be equivalently implemented by changing the duration time of zero vectors, $V_0$ and $V_7$, in the SVPWM technique. This implies that modifying the pole voltage in the triangle-comparison PWM (or carrier-based PWM) technique is considered to be equivalent to changing the duration time of zero vectors in the SVPWM technique. Like this, we can see that there is a correlation between the SVPWM and the triangle-comparison PWM techniques.

Fig. 7.55 shows the six discontinuous PWM techniques and their distribution of zero vectors [11,12]. Here, $\mu$ denotes the distribution factor (or apportioning factor), which indicates the distribution of zero vectors inside the modulation interval as

$$\mu = \frac{t_{0\_v7}}{t_{0\_v0} + t_{0\_v7}} \tag{7.46}$$

where $t_{0\_v0}$ and $t_{0\_v7}$ are the duration times of zero vectors, $V_0$ and $V_7$, respectively. The distribution factor has a range of $0 \le \mu \le 1$. The range of $0 < \mu < 1$ results in a continuous modulation, while $\mu = 0$ or 1 results in a discontinuous modulation. The best choice is $\mu = 0.5$ (i.e., $t_{0\_v0} = t_{0\_v7} = T_0/2$), which results in the conventional symmetrical SVPWM technique. The use of $\mu = 1$ (i.e., $t_{0\_v0} = 0$ and $t_{0\_v7} = T_0$) in which only the zero vector of $V_7$ is employed, results in $+120^\circ$ DPWM technique. On the other hand, the use of $\mu = 0$ (i.e.,

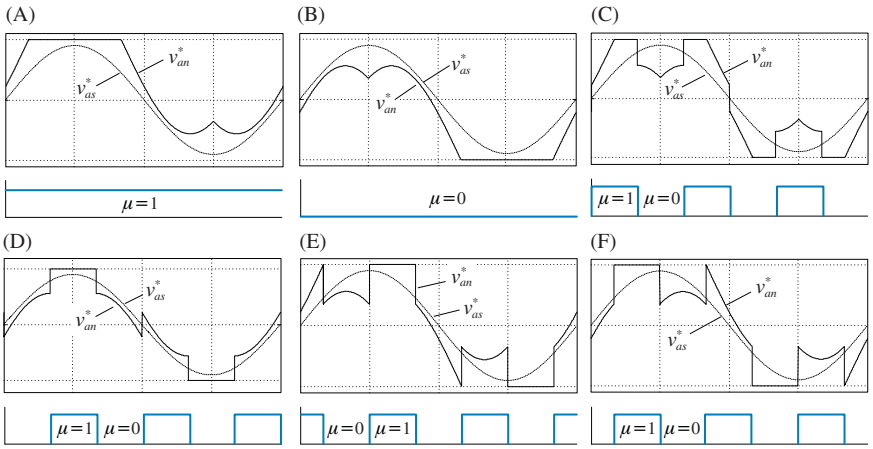



**FIGURE 7.55**

Several DPWM techniques and their distribution of zero vectors. (A) +120° DPWM, (B) −120° DPWM, (C) 30° DPWM, (D) 60° DPWM, (E) 60°(+30°) DPWM, (F) +60°(−30°) DPWM.

*E. Silva, E. Santos Jr., C. Jacobina, Pulsewidth modulation strategies nonsinusoidal carrier-based PWM and space vector modulation techniques, IEEE Trans. Ind. Electron. Mag. (2011) 37–45.*

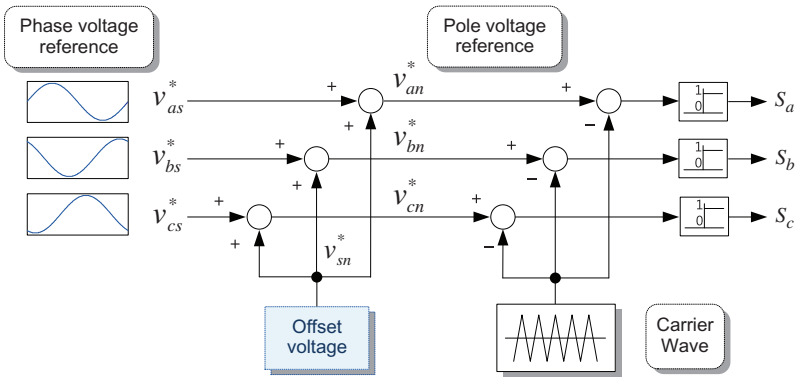



**FIGURE 7.56**

PWM technique employing the zero-sequence injection principle.

$t_{0\_v0} = T_0$ and $t_{0\_v7} = 0$) in which only the zero vector of $V_0$ is employed, results in −120° DPWM technique. The alternating use of $\mu = 0$ or 1 for each 60° section can realize other four DPWM techniques as shown in Fig. 7.55C–F. In all the PWM techniques discussed above, it is interesting to note that all the phase

voltage references are a pure sinusoidal waveform. However, they are different in the pole voltage references, i.e., the modulating signals, resulting in a different modulation performance.

## 7.4 PWM TECHNIQUE BASED ON OFFSET VOLTAGE [13,14]

In the Section 7.3.4, we saw that there is a correlation between the SVPWM and the triangle-comparison PWM techniques. In this section, we will discuss a new PWM technique as shown in Fig. 7.56, which allows the SVPWM technique to be implemented easily based on the triangle-comparison PWM technique.

In addition to the SVPWM technique, this generalized PWM technique can actually allow almost all the PWM techniques to be implemented based on the triangle-comparison PWM technique. This technique can reproduce the existing PWM techniques by modifying the pole voltage with the *offset voltage* (or the *zero-sequence voltage*).

Prior to explaining this technique, it should be noted that the output voltage of an inverter is the pole voltage. Thus, in the triangle-comparison PWM techniques, the modulating wave, which is compared with the triangular carrier wave, is the pole voltage reference. The SPWM technique use the phase voltage reference as the modulating wave as shown in Fig. 7.57. Thus, in the SPWM technique, the pole voltage reference is equal to the phase voltage reference.

On the other hand, in the THIPWM technique, the voltage reference, which is produced by adding a third harmonic to the phase voltage reference, is compared with the triangular carrier wave as shown in Fig. 7.37. Thus the pole voltage reference is not equal to the phase voltage reference. In addition, we can see from Section 7.3 that the DPWM techniques use pole voltage references that are different from the phase voltage reference.

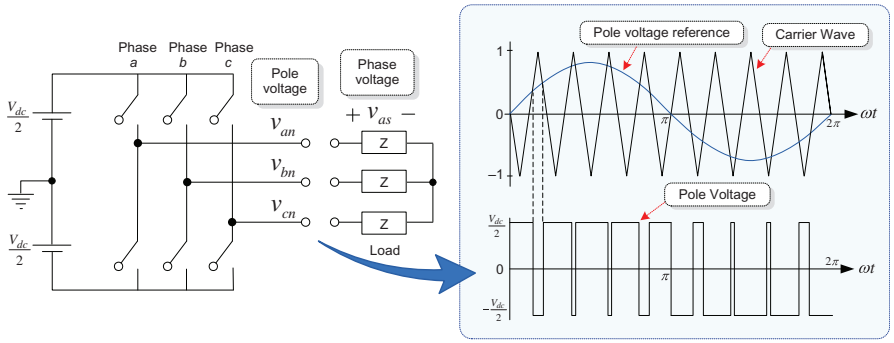



**FIGURE 7.57**

SPWM technique.

Based on this knowledge, we can generalize that the pole voltage reference in the PWM techniques can be given by adding an offset voltage $v_{sn}$ to the phase voltage reference as

$$\begin{aligned} v_{an}^{*} &= v_{as}^{*} + v_{sn} \\ v_{bn}^{*} &= v_{bs}^{*} + v_{sn} \\ v_{cn}^{*} &= v_{cs}^{*} + v_{sn} \end{aligned} \tag{7.52}$$

This is based on the fact that the added offset voltage disappears in the line-to-line voltages and the phase voltages for the three-phase inverter. Since the line-to-line voltage is given as the difference between two pole voltages, this offset voltage is canceled in both the line-to-line voltages and the phase voltages as

$$v_{ab}^{*} = v_{an}^{*} - v_{bn}^{*} \tag{7.53}$$

$$v_{as}^{*} = \frac{1}{3}\left(v_{ab}^{*} - v_{ca}^{*}\right) \tag{7.54}$$

Therefore, although the phase voltage reference in an inverter is always given as a pure sinusoidal waveform, the pole voltage reference can be modified by the applied offset voltage. According to the applied offset voltage, the modulation performance such as voltage linearity, harmonics, and switching losses can be changed.

The choice of this offset voltage $v_{sn}$ is completely arbitrary. However, there is a limitation on the value of the offset voltage. For the linear modulation, since the reference voltage should not exceed the peak of the triangular carrier wave, the value of the offset voltage should be chosen so that the resultant pole voltage references $v_{an}^{*}, v_{bn}^{*}, v_{cn}^{*}$ satisfy the following condition.

$$-\frac{V_{dc}}{2} \le v_{an}^{*}, v_{bn}^{*}, v_{cn}^{*} \le \frac{V_{dc}}{2} \tag{7.55}$$

By adding the arbitrary offset voltage within the allowed range, various pole voltage references can be obtained. Therefore the offset voltage is considered to be the degree of freedom in choosing various modulation techniques.

In the SPWM technique shown in Fig. 7.58A, the output voltage is determined by comparing the phase voltage reference with the triangular carrier wave.

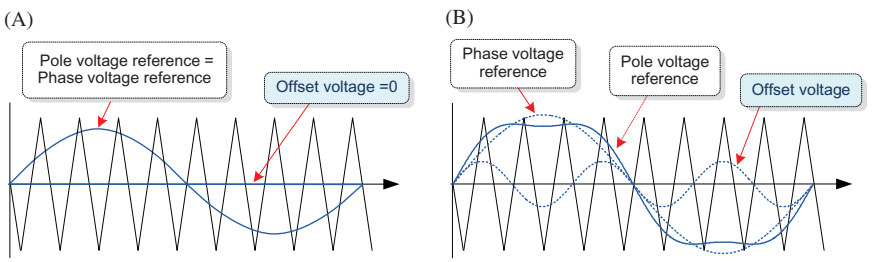



**FIGURE 7.58**

Offset voltage for (A) SPWM and (B) THIPWM techniques.

Thus the phase voltage reference is equal to the pole voltage reference (e.g., $v_{an}^{*} = v_{as}^{*}$). In this case, the offset voltage $v_{sn} = 0$.

On the other hand, in the THIPWM technique shown in Fig. 7.58B, since the pole voltage reference generated by adding a third harmonic to the phase voltage reference is compared with the triangular carrier wave, the offset voltage $v_{sn}$ is the third harmonic voltage.

Now we will discuss how the symmetrical SVPWM technique can be equivalently implemented as the triangle-comparison PWM technique employing the offset voltage.

### 7.4.1 SPACE VECTOR PWM TECHNIQUE IMPLEMENTATION BASED ON OFFSET VOLTAGE

In the symmetrical SVPWM technique, the effective voltage vectors are always placed at the center of the modulation interval $T_s$. In the triangle-comparison PWM technique, if the absolute values of the maximum $V_{max}$ and the minimum $V_{min}$ in the three-phase voltage references are equal to each other, then the resultant effective voltage generated from the comparison with a triangular carrier wave is also placed at the center of the modulation interval as shown in Fig. 7.59.

If this requirement is met by adding the offset voltage, then the original SVPWM can be equivalently implemented as the triangle-comparison PWM

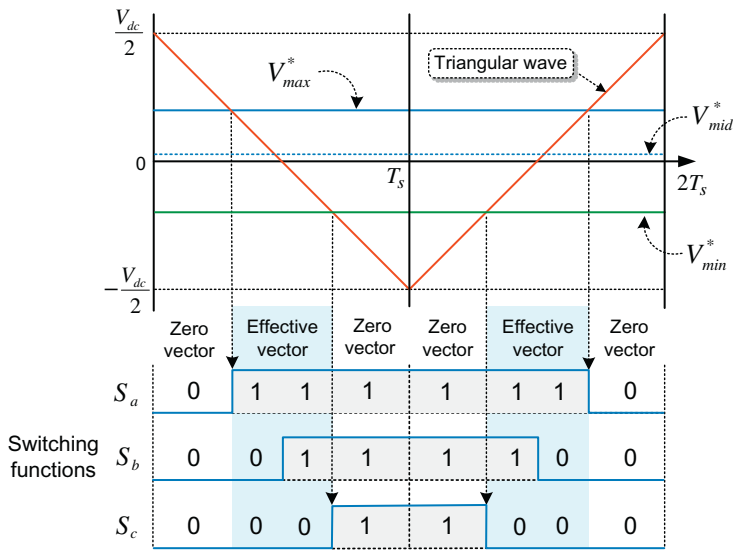



**FIGURE 7.59**

Symmetrical SVPWM technique.

technique. For this purpose, we establish the offset voltage to obtain the same absolute values of the maximum and the minimum voltage references as

$$V_{max} + v_{sn} = -(V_{min} + v_{sn}) \;\rightarrow\; v_{sn} = -\frac{V_{max} + V_{max}}{2} \tag{7.56}$$

Using the pole voltage references obtained by adding the offset voltage of Eq. (7.56) to the phase voltage references, an equivalent SVPWM technique can be readily implemented without a complicated calculation as shown in Fig. 7.60.

Fig. 7.61 shows the pole voltage reference, the phase voltage reference, and the offset voltage in this equivalent SVPWM technique for $MI = 0.9$. It can be seen that the SVPWM technique employs the pole voltage obtained by adding the offset voltage, which is a third harmonic in the shape of a triangular wave. This modified pole voltage is equal to the pole voltage as shown in Example 4.

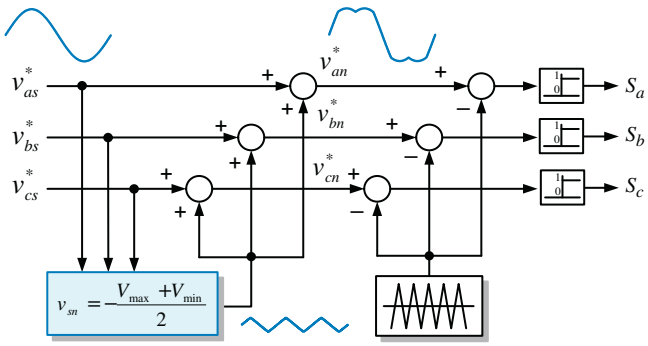



**FIGURE 7.60**

Equivalent SVPWM technique by using the offset voltage.

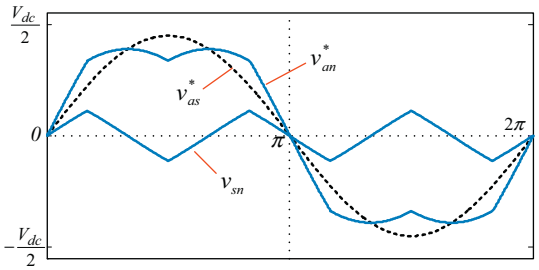



**FIGURE 7.61**

Voltages for equivalent SVPWM by using the offset voltage ($MI = 0.9$).

Next gives a description on the THIPWM technique implementation by using the triangle-comparison PWM technique. As noted in the earlier section, the THIPWM technique uses the pole voltage obtained by adding a third harmonic with the amplitude of 1/6 of the phase voltage reference to the phase voltage reference. Thus this third harmonic is considered to be an offset voltage. From the three-phase voltage references, we can find that the offset voltage is given as [12]

$$v_{sn} = -\frac{v_{as}^{*} v_{bs}^{*} v_{cs}^{*}}{v_{as}^{*2} + v_{bs}^{*2} + v_{cs}^{*2}} \tag{7.57}$$

Fig. 7.62 shows the pole voltage reference, the phase voltage reference, and the offset voltage for this case.

Likewise, other DPWM techniques can be also implemented by choosing an appropriate offset voltage as shown in Fig. 7.63. As one example, the offset voltage for the $+120^{\circ}$ DPWM technique is given as [13]

$$v_{sn} = \frac{V_{ref}}{2} - V_{max} \tag{7.58}$$

In this manner, various PWM techniques can be effectively implemented based on the modified pole voltage reference by using an offset voltage. This modification results in the change of the distribution time of zero vectors. As shown in Fig. 7.64, when the three pole voltage references are changed by the offset voltage, the position of the effective voltages is changed without any change in its duration time. Thus the SVPWM and the triangle-comparison PWM techniques have different approaches for the modulation, but there is a close correlation between the two techniques.

The pole voltage references used in each PWM technique ultimately defines the switching instants by their comparison with the triangular carrier wave. However, without such comparison, the switching instant of the gating pulse for each switch can be easily calculated as follows. For example, the

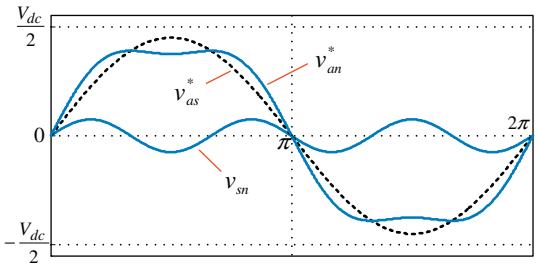



**FIGURE 7.62**

THIPWM technique implementation by using the offset voltage ($MI = 0.9$).

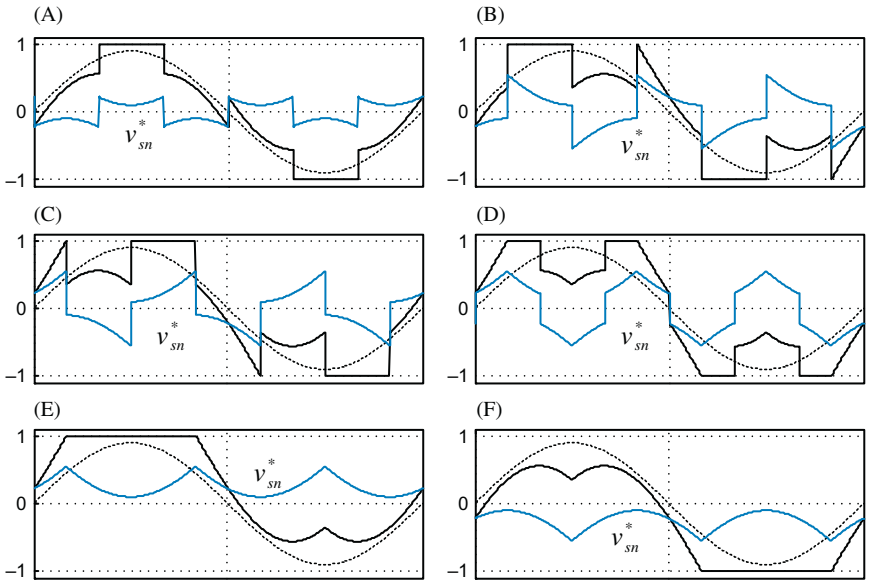



**FIGURE 7.63**

Implementation of different DPWM techniques by using the offset voltage. (A) +60° DPWM, (B) 60° (−30°) DPWM, (C) 60°(+30°) DPWM, (D) 30° DPWM, (E) +120° DPWM, (F) −120° DPWM.

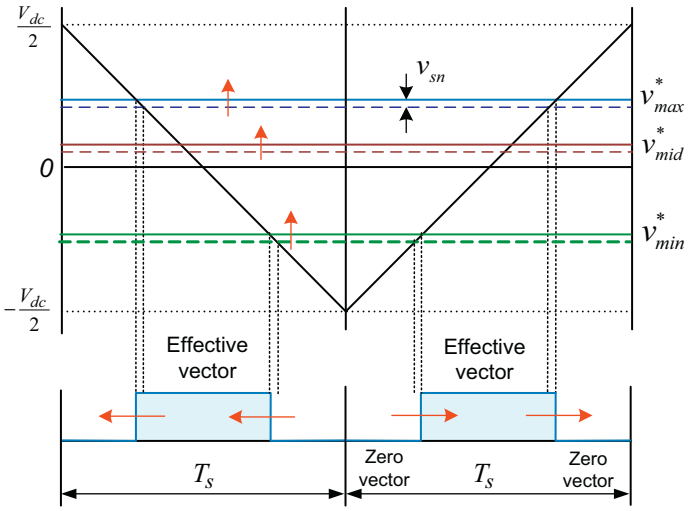



**FIGURE 7.64**

Position change of the effective voltage according to the offset voltage.

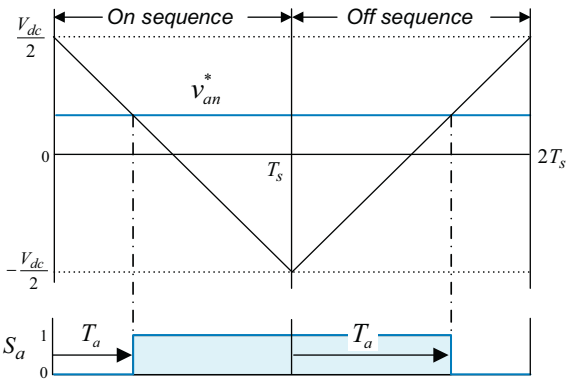



**FIGURE 7.65**

Switching instant of the gating pulse for each switch.

switching instant of the gating pulse for the upper switch of phase *as* in Fig. 7.65 can be calculated as:

- Off gating sequence:

$$\frac{T_a}{T_s} = \frac{\frac{V_{dc}}{2} + v_{an}^*}{V_{dc}} = \frac{1}{2} + \frac{v_{an}^*}{V_{dc}} \rightarrow T_a = \frac{T_s}{2} + \frac{v_{an}^*}{V_{dc}} T_s \tag{7.59}$$

- On gating sequence:

$$T_a = \frac{T_s}{2} - \frac{v_{an}^*}{V_{dc}} T_s \tag{7.60}$$

## 7.5 OVERMODULATION

A PWM inverter can correctly generate the required voltage reference by adopting any PWM technique previously explained. However, the linear modulation range for its output voltage is limited and varies with PWM techniques. In the SPWM technique, when the amplitude of the voltage reference wave becomes larger than the peak of the triangular carrier wave, or in the SVPWM technique when the voltage reference vector lies outside the hexagon boundaries as shown in Fig. 7.66, the PWM inverter cannot correctly produce the desired voltage reference. These conditions are called *overmodulation.*

The beginning of the overmodulation region depends on the type of PWM technique used as shown in Fig. 7.67. For the SPWM technique, the overmodulation starts at 78.5% ($V_{dc}/2$) in reference to the output voltage of six-step operation ($2V_{dc}/\pi$). On the other hand, for the conventional SVPWM, the overmodulation starts at 90.7% ($V_{dc}/\sqrt{3}$).

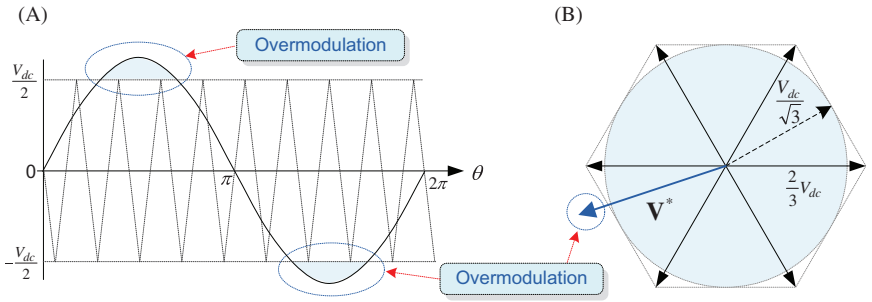



**FIGURE 7.66**

Overmodulation. (A) SPWM and (B) SVPWM.

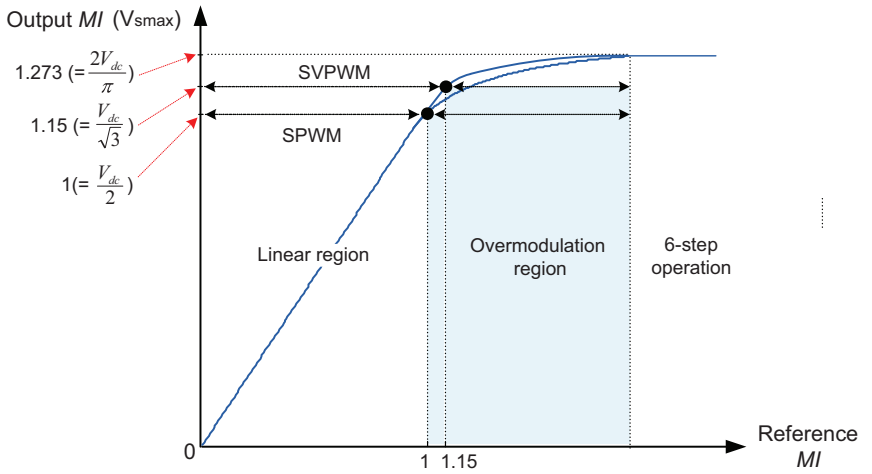



**FIGURE 7.67**

Overmodulation region.

In the overmodulation region, the voltage linearity is lost because the output voltage fundamental component becomes less than its command value. Furthermore, the output voltage contains a lot of harmonics. As a result, the performance of the current regulator will be degraded, and the vector control may not be performed correctly. When a voltage reference exceeds the linear modulation range of an inverter output voltage, an appropriate overmodulation method is necessary to modify the voltage reference within the linear modulation range or to produce the output voltage equal to its reference on average.

The overmodulation method can be classified into two groups: *dynamic overmodulation method* for the transient operation and *steady-state overmodulation method* for the steady-state operation.

- *Dynamic overmodulation methods* [15,16]
  The dynamic overmodulation methods handle the excessive voltage during transients such as the change of speed command or load torque. This is necessary for improving the dynamic response of a closed-loop current regulator in the high-performance AC motor drives such as vector control.
- *Steady-state overmodulation methods* [17,18]
  The steady-state overmodulation methods handle the overmodulation range voltage required in the steady-state operation. This method is important for the AC motor drives that require full inverter voltage utilization such as traction drives. In this case, the overmodulation methods should support a smooth transition from linear PWM operation to six-step mode operation.

Several overmodulation methods for the two popular SPWM and SVPWM techniques have been developed. However, we will describe overmodulation methods for only the SVPWM technique.

## 7.5.1 DYNAMIC OVERMODULATION METHODS

In the SVPWM technique, if the voltage reference vector lies outside the hexagon, an inverter cannot produce that vector, and thus a new voltage reference vector on the hexagon boundary must be selected instead. There are three choices for modification of a voltage reference vector as follows.

### 7.5.1.1 *Minimum-phase-error pulse width modulation method*

This method modifies the voltage reference vector $\boldsymbol{V}^*$ so that its magnitude is limited to the hexagon boundary while the phase is maintained as shown in Fig. 7.68.

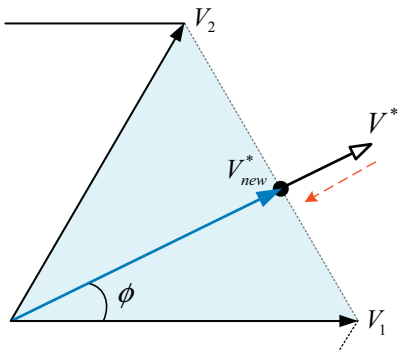



**FIGURE 7.68**

Minimum-phase-error PWM method.

This method is widely used due to its simplicity in implementation. However, since the new reference vector, $\boldsymbol{V}^*_{\text{new}}$, is selected irrespective of the magnitude of the original reference vector as shown in Fig. 7.68, this method has sluggish transient dynamics. In addition, it is impossible to carry out six-step operation with this method, and thus full DC input voltage utilization of an inverter cannot be achieved. For implementation of this method, the switching times of active vectors for generating a voltage reference vector can be simply modified as

$$T'_1 = \frac{T_s}{T_1 + T_2} T_1 \tag{7.61}$$

$$T'_2 = \frac{T_s}{T_1 + T_2} T_2 \tag{7.62}$$

### 7.5.1.2 Minimum-magnitude-error pulse width modulation method

This method focuses on maintaining the magnitude of the voltage reference vector $\boldsymbol{V}^*$ rather than its phase. To minimize the magnitude error between the modified and the original voltage reference vector, the modified voltage vector, $\boldsymbol{V}^*_{\text{new}}$, which is perpendicular to the hexagon boundary, is selected as shown in Fig. 7.69.

For implementation of this method, the switching times of active vectors for generating a voltage reference vector can be modified as

$$T'_1 = T_1 - \frac{T_1 + T_2 - T_s}{2} \tag{7.63}$$

$$T'_2 = T_2 - \frac{T_1 + T_2 - T_s}{2} \tag{7.64}$$

This overmodulation strategy has a better dynamic performance than the minimum-phase-error pulse width modulation method (MPEPWM) and also enables a smooth transition to six-step operation.

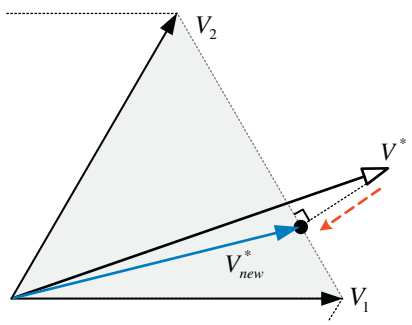



**FIGURE 7.69**

Minimum-magnitude-error pulse width modulation method.

#### 7.5.1.3 Overmodulation method considering the direction of current [16]

This is an overmodulation strategy that is focused on the transient performance of the current controller in the high-performance AC motor drives. The voltage reference vector $\boldsymbol{V}^*$ for regulating motor currents consists of the PI output voltage vector $\boldsymbol{V}_{PI}^*$ and the back-EMF vector as was described in Chapter 6. The direction of the PI output voltage vector $\boldsymbol{V}_{PI}^*$ determines the transient response of the current. Thus this method selects a modified vector $\boldsymbol{V}_{\text{new}}^*$ that can maintain the direction of the PI output voltage vector as shown in Fig. 7.70. Even though this overmodulation strategy shows a better dynamic performance, its implementation is complex and needs information on back-EMF.

### 7.5.2 STEADY-STATE OVERMODULATION METHODS

Here, we will introduce two techniques to handle the overmodulation range voltage required in the steady-state operation.

First, we begin with the steady-state overmodulation method by using the compensated modulation technique [17]. An inverter can be considered as a voltage amplifier with unit gain, which can produce a fundamental component of the output voltage equal to its reference value. However, as the modulation index increases in the overmodulation region, the voltage gain reduces sharply in a nonlinear manner. In other words, the output voltage becomes less than its reference value. The reduction of the voltage gain $G$ of the inverter depends on the modulation technique as shown in Fig. 7.71. Here, since the modulation index $MI$ in the overmodulation region becomes greater than 1, we redefine the modulation index $M = v_{ref}/(2V_{dc}/\pi)$ as the ratio of the fundamental output voltage to the fundamental voltage of six-step operation. Thus, the output voltage of six-step operation, $2V_{dc}/\pi$, corresponds to $M = 1$.

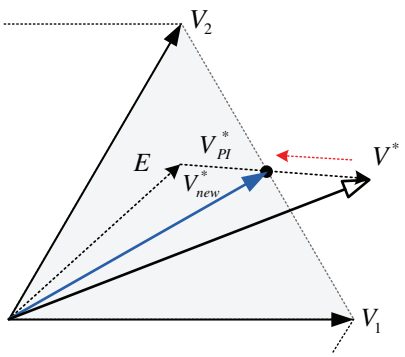



**FIGURE 7.70**

Method considering the direction of current.

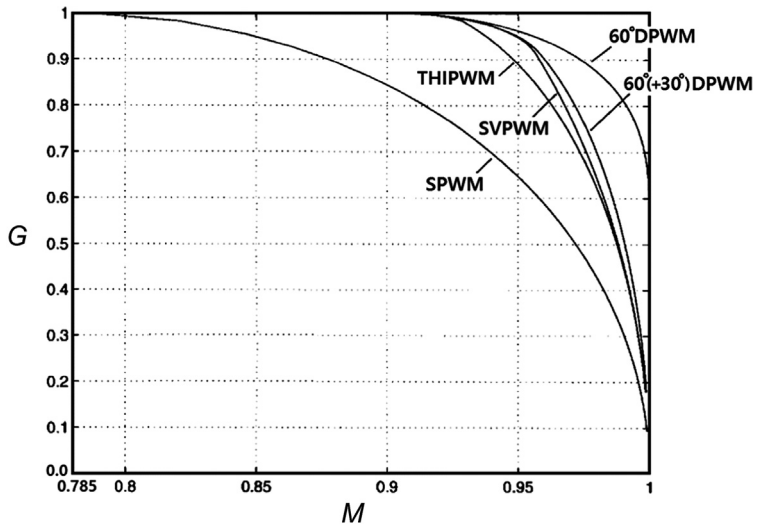



**FIGURE 7.71**

Voltage gain $G$ for various PWM techniques [17].

*A.M. Hava, R.J. Kerkman, T.A. Lipo, Carrier-based PWM-VSI overmodulation strategies: analysis, comparison, and design, IEEE Trans. Power Electron., 13 (4) (1998) 674–689.*

For the SPWM method, the overmodulation begins at $M = 0.785$, and its nonlinear voltage gain $G$ in the overmodulation region can be expressed in terms of the modulation index as

$$G = \frac{2}{\pi}\left[\sin^{-1}\left(\frac{1}{M}\right) + \frac{1}{M}\sqrt{1 - \frac{1}{M^2}}\right] \tag{7.65}$$

The compensated modulation technique compensates for the reduced gain in the overmodulation region. In this method, after calculating the voltage gain for each PWM technique, the voltage reference is multiplied by its inverse function so that the nonlinearity is canceled as shown in Fig. 7.72. However, the drawback of this method is that the online computation of the gain function and its inverse are very difficult.

Next we will discuss another steady-state overmodulation method, which modifies the voltage reference vector in the SVPWM technique. In the SVPWM technique, when the voltage reference vector $\boldsymbol{V}^*$ lies outside the hexagon boundaries, a PWM inverter cannot correctly produce the required voltage. Thus this method modifies the magnitude and/or the phase of the voltage reference vector to produce an output voltage equal to its reference on average per fundamental cycle [18]. As shown in Fig. 7.73, the phase and the magnitude of the voltage

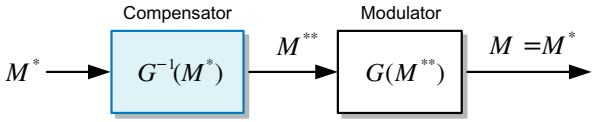



**FIGURE 7.72**

Steady-state overmodulation by using compensated modulation technique.

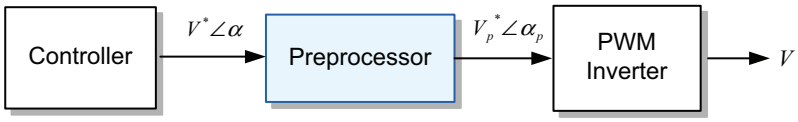



**FIGURE 7.73**

Steady-state overmodulaion method for the SVPWM technique.

reference vector is changed by a preprocessor. The modified reference vector is then fed to the modulator.

In this method, the overmodulation region is subdivided into two different modes: *mode* I ($0.907 \leq M \leq 0.952$) and *mode* II ($0.952 < M \leq 1.0$).

### 7.5.2.1 Overmodulation mode I ($0.907 \leq M \leq 0.9523$)

In this range, the preprocessor modifies the magnitude of the voltage reference vector $\boldsymbol{V}^*$ while its phase is transmitted without any change. Although the SVPWM technique utilizes a linear modulation range limited up to $V_{dc}/\sqrt{3}$, it can modulate more voltage according to the position of the voltage vector. For example, a voltage of $2V_{dc}/3$ can be achieved at the vertex of the hexagon. Exploiting this fact, the reduced fundamental component around the center portion of the hexagon sides can be compensated by producing more fundamental around the vertices as shown in Fig. 7.74.

Accordingly, it is possible to produce an output voltage equal to its reference on average per fundamental cycle. In Fig. 7.74, the *dashed circle* represents the trajectory of the the required reference vector $\boldsymbol{V}^*$ and the *solid line* represents the trajectory of the new reference vector $\boldsymbol{V}^*_{new}$ modified by the preprocessor. The limit of the overmodulation mode I is reached when the modified trajectory fully coincides with the hexagon. The maximum modulation index of this mode is $M = 0.9523$. This value can be calculated from the radius of a circle with an area equal to that of the hexagon as

$$V_{max} = \sqrt{\frac{2}{\pi\sqrt{3}}} V_{dc} = 0.606\ V_{dc} \tag{7.66}$$

Fig. 7.75 depicts the actual phase voltage reference according to the modulation index $M$ in the overmodulation mode I. As the modulation index $M$ increases,

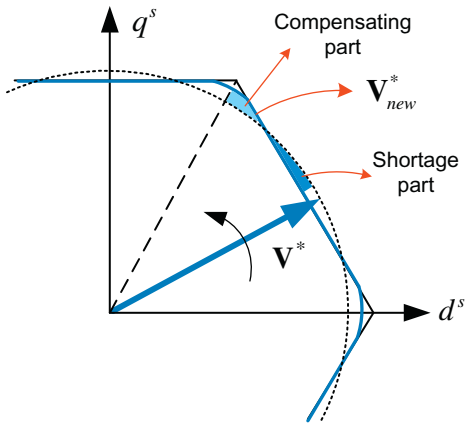



**FIGURE 7.74**

Overmodulation mode I.

*J. Holtz, W. Lotzkat, A. Khambadkone, On continuous control of PWM inverter in the overmodulation range including the six-step mode, in Conf. Rec. IEEE IECON, 1992, pp. 307–312.*

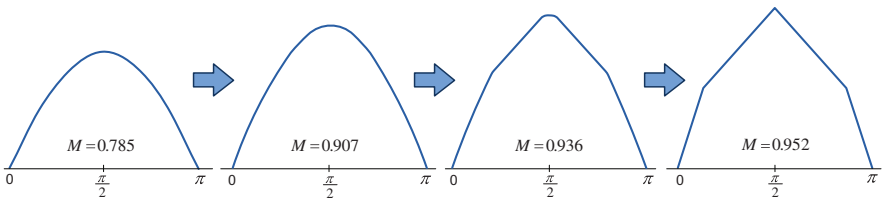



**FIGURE 7.75**

Phase voltage reference in the overmodulation mode I.

the actual phase voltage reference is turned into a nonsinusoidal waveform. This implies that the harmonics are increased along with the fundamental content of the voltage reference.

### 7.5.2.2 Overmodulation mode II ($0.9523 < M \leq 1$)

In this range from $M > 0.9523$ to six-step operation mode, the preprocessor changes both the magnitude and the phase of the voltage reference vector $\boldsymbol{V}^*$. In the six-step operation producing the maximum output voltage, the six output vectors placed at the vertices of the hexagon are held sequentially within each discrete 60° interval. Based on this fact, in this mode, an output voltage equal to its reference on average can be achieved by adjusting the duration time for which the six vectors are held. Fig. 7.76 illustrates this more in detail. Although the voltage reference vector $\boldsymbol{V}^*$ moves along a circle with the fundamental angular frequency, the modified reference vector $\boldsymbol{V}^*_P$ remains fixed at the vertex for a

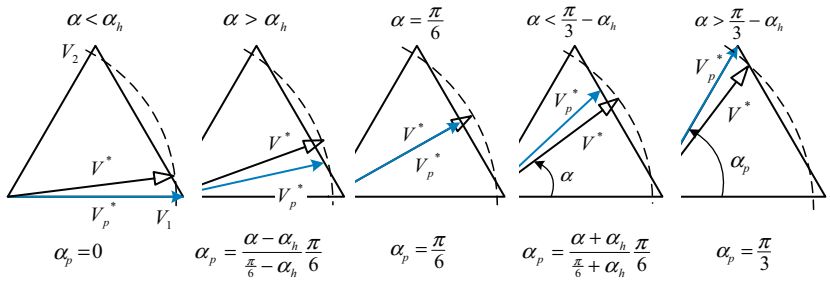



**FIGURE 7.76**

Overmodulation mode II.

*J. Holtz, W. Lotzkat, A. Khambadkone, On continuous control of PWM inverter in the overmodulation range including the six-step mode, in Conf. Rec. IEEE IECON, 1992, pp. 307–312.*

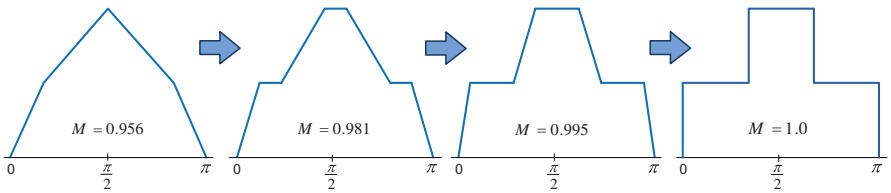



**FIGURE 7.77**

Actual phase voltage reference in the overmodulation mode II.

particular interval (is called a hold angle $\alpha_h$) and moves along the side of the hexagon for the rest of the fundamental period. Here, $\alpha$ and $\alpha_P$ are the angles of the voltage reference vector and the modified reference vector, respectively.

The hold angle $\alpha_h$ controls the fundamental voltage and is given as a nonlinear function of the modulation index $M$ [18]. Fig. 7.77 depicts the actual phase voltage reference according to the modulation index $M$ in the overmodulation mode II. As the modulation index $M$ increases, the actual phase voltage reference turns into a typical square waveform of the six-step operation. In this method, the waveform of the phase voltage is adjusted according to the modulation index $M$, as can be seen in Figs. 7.75 and 7.77, while Ref. [19] proposed a overmodulation method by adjusting the waveform of the pole voltage directly according to $M$.

## 7.6 DEAD TIME [20–23]

When both switches in an inverter leg are turned on simultaneously, the DC source is short-circuited, resulting in a current dangerous enough to destroy switches. Hence, this switching state should be inhibited at all times. Therefore, the pair of switches in a leg always changes their switching states in a

complementary manner. Nevertheless, there is a possibility of an unexpected short-circuit of the leg. The main reason is that, due to the storage time in the turn-off process, the turn-off time of a switching device is always longer than the turn-on time. For example, Fig. 7.78 clearly shows a difference between the turn-on and the turn-off times from device characteristics for an IGBT [24].

Therefore, when the gating signals for changing the switching states are given at the same time, a momentary short-circuit is likely to happen. This is because one of the devices is being driven "on" while the other one may be still conducting. To prevent such undesirable short-circuit of the DC-link, the incoming switch is turned on after a sufficient time has passed to allow the turn-off of the outgoing switch as shown in Fig. 7.79.

Such small time delay, which is inserted prior to the gate signal of the turning-on device, is called *dead time* or *blanking time*. The dead time depends on the type and the size of a semiconductor device. A value of $1-3\ \mu s$ is typical for a medium-power IGBT.

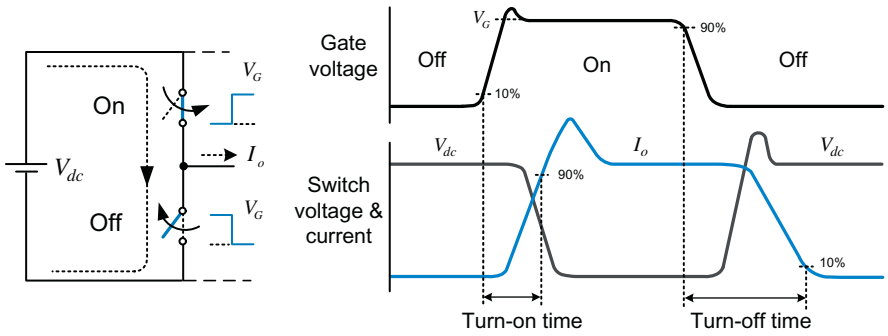



**FIGURE 7.78**

Switching characteristics of an IGBT.

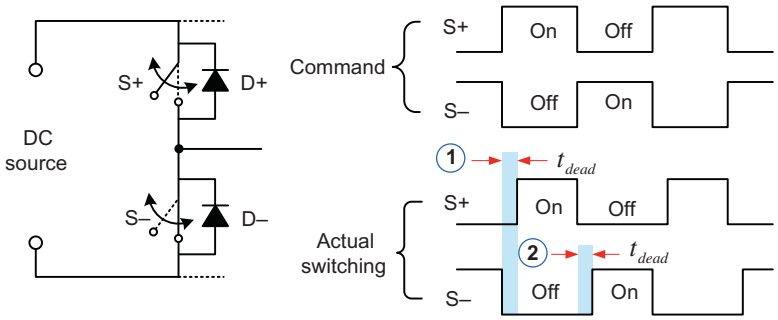



**FIGURE 7.79**

Dead time injection.

### 7.6.1 DEAD TIME EFFECT

During the dead time, there is a problem of which the output voltage of the inverter may be different from the voltage command. Thus we need to examine the effects of the dead time on the output voltage. During the dead time, since the load current does not conduct through a switching device but through a diode, the output voltage of the inverter is different according to the direction of the current. For example, examine the output voltage for section ① of the dead time as shown in Fig. 7.79. In this section, the lower switch $S-$ changes from on-state to off-state, and the upper switch $S+$ changes from off-state to on-state. In addition, the turn-on signal of $S+$ is delayed by the dead time. During the dead time, if the load current is negative, then the current will flow through the upper diode $D+$. This results in an output voltage of $V_{dc}/2$ equal to the desired voltage command. On the other hand, if the load current is positive as shown in Fig. 7.80, then it flows through the lower diode $D-$. In this case, the output voltage

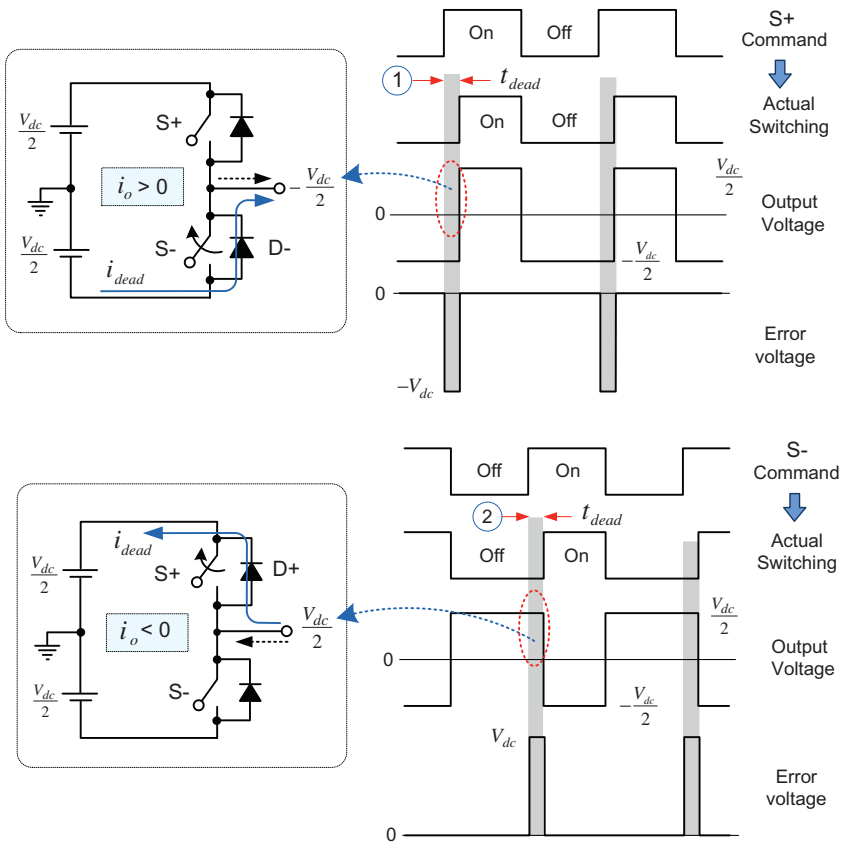



**FIGURE 7.80**

Voltage error due to the dead time.

becomes $-V_{dc}/2$, and thus there is an error value of $-V_{dc}$ when compared with the voltage command. On the other hand, in Section 7.2, the lower switch $S$- changes from off-state to on-state in order to produce the output voltage of $-V_{dc}/2$ and the turn-on signal of $S$- is delayed by the dead time. In this case, if the load current is negative as shown in Figure 7.80, then the current will flow through the upper diode $D+$ during the dead time. The output voltage becomes $V_{dc}/2$, and thus, there is an error value of $V_{dc}$ when compared to the voltage command.

Fig. 7.81 shows the voltage errors due to the dead time over one cycle of the voltage reference. The magnitude of each error is $V_{dc}$ and its width is the dead time $t_{dead}$, and its polarity depends on the direction of the current. Although each error is small, the accumulation of these errors over a half cycle is often sufficient to distort the output voltage. The average magnitude of the voltage error $V_{err}$ is expressed as [20]

$$V_{err} = t_{dead} V_{dc} f_{sw} \tag{7.67}$$

where $f_{sw}$ is the switching frequency.

This voltage deviation causes fundamental voltage drop and voltage waveform distortion. The distorted voltage induces the low-order harmonics of fifth and seventh in motor currents, causing current waveform distortion. This also results in torque pulsations as well as additional losses. Moreover, due to the dead-time effect, the estimated flux angle for the vector control of an induction motor includes the sixth-order harmonic. Fig. 7.82 shows that the phase currents and the estimated flux angle are distorted due to the dead-time effect. In particular, the dead-time effect becomes more significant at low speeds. Since the motor voltage

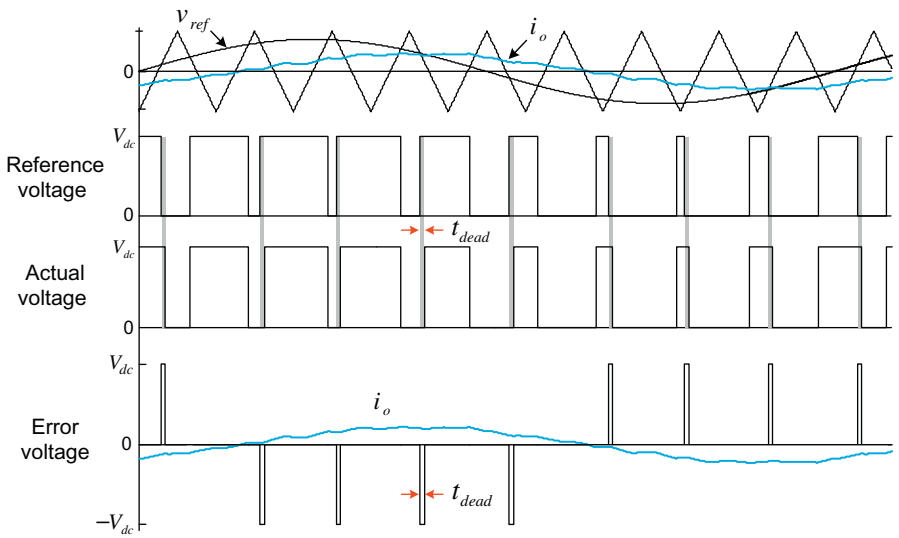



**FIGURE 7.81**

Actual output voltage and voltage error due to dead time.

in the low-speed region is low, it is susceptible to the distortion voltage. In the open-loop AC motor drives, the instability problem may occur at a light load or no load (implying low current) [21]. Thus it is necessary to compensate the voltage deviation due to the dead time.

In addition to the dead time, the nonlinearity caused by the turn-on/off delay and the voltage drop across power switches and diodes as shown in Fig. 7.83 can distort

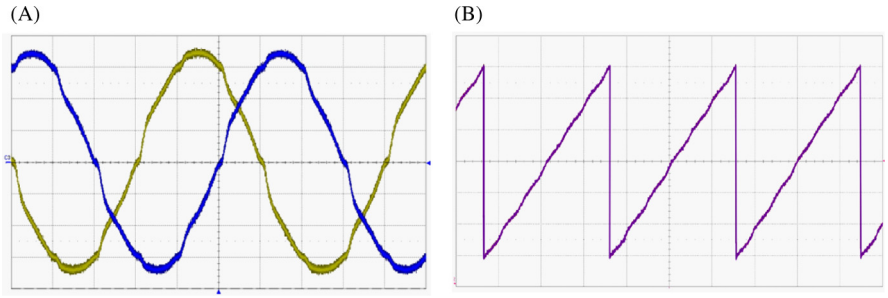



**FIGURE 7.82**

Dead-time effects. (A) Phase currents and (B) flux angle.

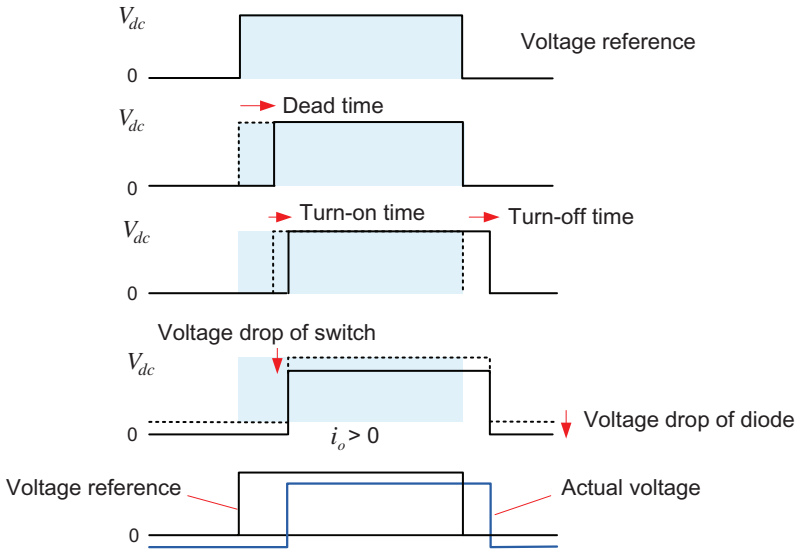



**FIGURE 7.83**

Nonlinearity of an inverter.

*N. Urasaki, T. Senjyu, T. Funabashi, A novel method utilizing trapezoidal voltage to compensate for inverter nonlinearity adaptive dead-time compensation strategy for permanent magnet synchronous motor drive, IEEE Trans. Energy Conv., 22 (2) (2007), 271–280.*

the output voltage of an inverter [22]. Thus it is necessary to compensate the voltage distortion due to the nonlinearity of an inverter in addition to the dead-time effect.

There are two types of dead-time compensation techniques. One is *feedforward compensation technique* that adds the error voltage to the voltage reference and the other is the *pulse-based compensation technique* that corrects the pulse errors due to the dead-time effect on a pulse-by-pulse basis. The feedforward compensation technique has a better performance than the pulse-based compensation technique. However, the pulse-based compensation technique can be easily implemented. Now we will discuss the pulse-based dead time compensation technique in detail.

## 7.6.2 DEAD TIME COMPENSATION [23]

In the pulse-based dead time compensation technique, the voltage distortion is corrected by adjusting the switching instants. Since the voltage error due to the dead time is different depending on the direction of the current, the voltage error needs to be compensated according to the sign of the operating current as follows. Now we will examine the dead time compensation for a switching sequence with a dead time added to the turning-on pulse.

### 7.6.2.1 *Positive current:* $i_o > 0$

If $i_o > 0$ during the dead time $t_{dead}$, then the current conducts through the lower diode, and thus the output voltage always becomes $-V_{dc}/2$. Hence, as shown in Fig. 7.84, when $S+$ is turning on and $S-$ is turning off, the actual voltage

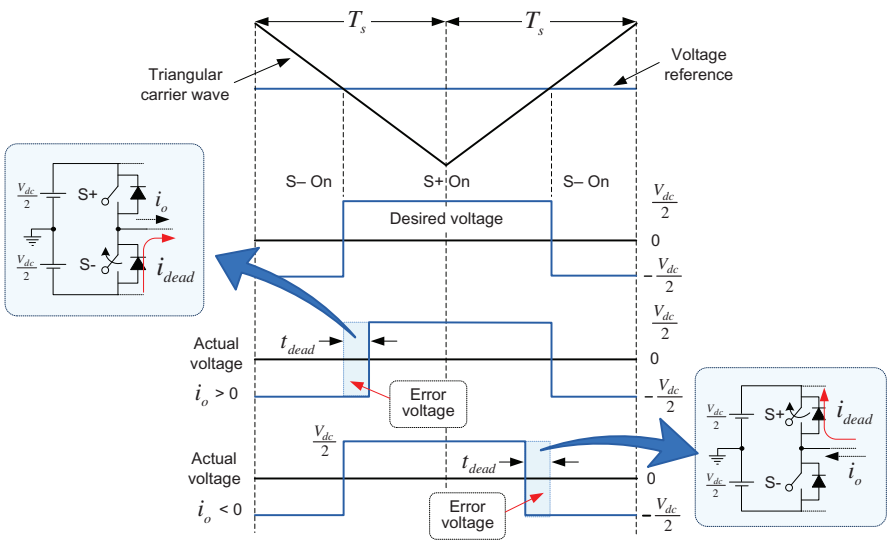



**FIGURE 7.84**

Dead-time effect.

of $-V_{dc}/2$ is less than the voltage reference of $V_{dc}/2$ during the dead time. The resultant error is $-V_{dc}$. On the other hand, if $S-$ is turning on and $S+$ is turning off, then the actual voltage during the dead time is equal to the voltage reference.

The left side of Fig. 7.85 shows the compensation for the voltage error by the dead time when $S+$ is turning on and $S-$ is turning off. In this case, the pulse transition time is advanced by the dead time $t_{dead}$ to obtain the actual voltage identical to the voltage reference.

### 7.6.2.2 Negative current: $i_o < 0$

If $i_o < 0$ during the dead time $t_{dead}$, then the current conducts through the upper diode, and thus the output voltage always becomes $V_{dc}/2$. Hence, when $S+$ is turning on and $S-$ is turning off, the actual voltage during the dead time becomes equal to the voltage reference of $V_{dc}/2$. On the other hand, when $S-$ is turning on and $S+$ is turning off, the actual voltage of $V_{dc}/2$ during the dead time becomes greater than the voltage reference of $-V_{dc}/2$. The resultant error is $V_{dc}$. The right side of Fig. 7.85 shows the compensation for the voltage error by the dead time when $S-$ is turning on and $S+$ is turning off. In this case the

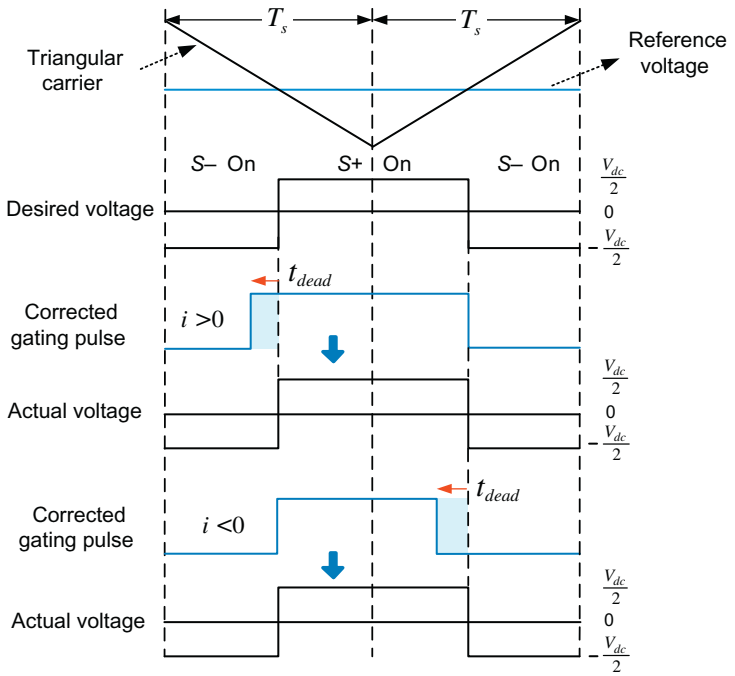



**FIGURE 7.85**

Dead-time compensation.

pulse transition time is advanced by the dead time $t_{dead}$ to obtain the actual voltage identical to the voltage reference.

As explained above, the dead-time compensation technique is based on information of the polarity of the phase current. Hence, an accurate measurement of the polarity of the current is needed to correctly compensate for the dead time. In particular, it is important to detect the current exactly around the zero crossings, where the detection of the current polarity is susceptible to noise and switching ripple.

## 7.7 CURRENT MEASUREMENT [25,26]

The current regulator is essential for accomplishing the torque control of AC motors. The torque control performance greatly depends on the performance of the current regulator. As described in Chapter 6, since the current regulation is performed using a feedback current, an accurate current measurement is the most important. In addition, the attainable current control bandwidth depends on the current sampling method. The motor current driven by a PWM inverter contains not only the fundamental component but also ripple components due to the switching action. We need to detect only the fundamental component, which produces effective torque and flux.

For measuring the fundamental component, the instantaneous sampling method has gained a wide acceptance [25]. This method demonstrates that it is possible to detect the fundamental component of current by sampling the current at the midpoints of zero vectors in the pulse patterns of the SVPWM technique. The typical waveforms of the voltage and phase current in the symmetrical SVPWM technique are shown in Fig. 7.86. It can be seen that the instantaneous value sampled at the midpoints of zero vectors in the PWM pulse patterns is equal to the fundamental current component. As we discussed in Section 7.4, the midpoints of the zero vectors in the SVPWM technique correspond to the peaks of the triangular carrier wave. Thus an instantaneous current sampling synchronized with the triangular carrier wave is normally used. The current can be sampled at the two peaks of the triangular carrier wave, i.e., top and bottom points (i.e., twice per switching period) or only at one peak (once per switching period). The attainable bandwidth of the current control depends directly on the number of sampling [26]. When sampling the currents twice per switching period, which is called the *double sampling*, the maximum attainable bandwidth of the synchronous reference frame current regulator is about 1/10 of the switching frequency.

Even though the current is sampled at the midpoints of the zero vectors, it may deviate from the fundamental component due to a delay in the feedback loop. When the current is being measured from a sensor, the signal of the sensor is first filtered to eliminate the noise on the signal and then converted into a digital value. Due to the phase delay caused by the low-pass filter, the sampled current through the filter may be different from the actual current at the desired

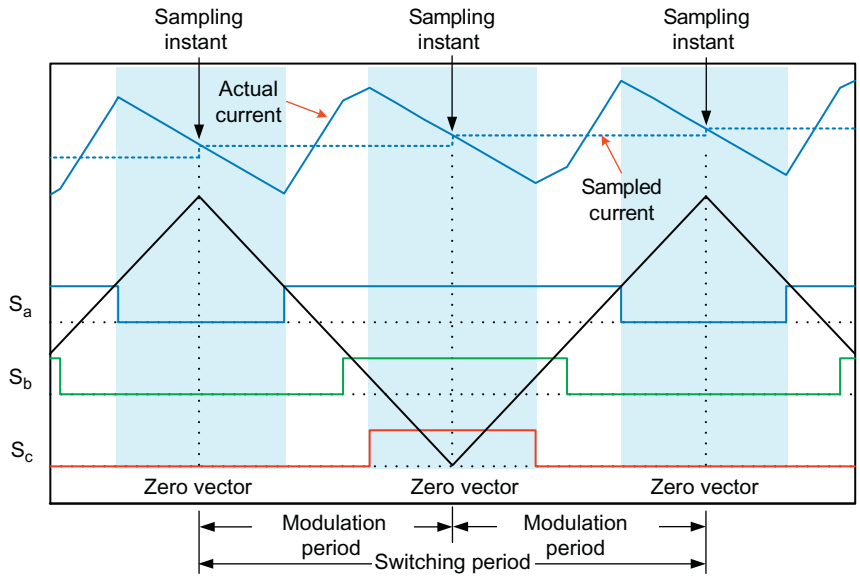



**FIGURE 7.86**

Typical waveforms of voltage and phase current in the symmetrical SVPWM.

instant. Moreover, a ripple component rather than the fundamental component of the current may be sampled. In Ref. [25], the delayed sampling method was used to reduce the current sampling error caused by the filter delay.

## REFERENCES

[1] A. Nabae, I. Takahashi, H. Akagi, A new neutral-point-clamped PWM inverter, IEEE Trans. Ind. Appl. IA-17 (5) (Sep./Oct., 1981) 518–523.

[2] A. Schnung, H. Stemmler, Static frequency changers with 'subharmonic' control in conjunction with reversible variable-speed A.C. drives, Brown Boveri Rev. (Aug./Sep., 1964) 555–577.

[3] H.S. Patel, R.G. Hoft, Generalized techniques of harmonic elimination and voltage control in thyristor inverters: part I-harmonic elimination, IEEE Trans. Ind. Appl. IA-9 (3) (May/Jun., 1973) 310–317.

[4] V.G. Agelidis, P.D. Ziogas, G. Joos, 'Dead-Band' PWM switching patterns, IEEE Trans. Power Electron. 11 (4) (July, 1996) 522–531.

[5] S.R. Bowes, R.R. Clements, Computer-aided design of PWM inverter systems, IEE Proc. 129, Pt. B (1) (Jan. 1982) 1–17.

[6] J.A. Houldsworth, D.A. Grant, The use of harmonic distortion to increase the output voltage of a three-phase PWM inverter, IEEE Trans. Ind. Appl. IA-20 (5) (Sep./Oct. 1984) 1224–1228.

[7] H.W. Van Der Broeck, et al., Analysis and realization of a pulse width modulator based on voltage space vectors, IEEE Trans. Ind. Appl. 24 (1) (Jan./Feb. 1988) 142–150.
[8] D.G. Holmes, The significance of zero space vector placement for carrier-based PWM schemes, IEEE Trans. Ind. Appl. 32 (5) (Sep./Oct. 1996) 1122–1129.
[9] J. Sun, H. Grotstollen, Optimized space vector modulation and regular-sampled PWM: a reexamination, in: Conf. Rec. IEEE IAS Annu. Meeting, 1996, pp. 956–963.
[10] A.M. Hava, R.J. Kerkman, T.A. Lipo, A high-performance generalized discontinuous PWM algorithm, IEEE Trans. Ind. Appl. 34 (5) (Sep./Oct. 1998) 1059–1071.
[11] E. Silva, E. Santos Jr., C. Jacobina, Pulsewidth modulation strategies nonsinusoidal carrier-based pwm and space vector modulation techniques, IEEE Trans. Ind. Electron. Mag. (2011) 37–45.
[12] V. Blasko, A hybrid PWM strategy combining modified space vector and triangle comparison methods," in: Proc. IEEE Power Electronics Specialists Conference (PESC'96), 1996, pp. 1872–1878.
[13] D.W. Chung, J.S. Kim, S.K. Sul, Unified voltage modulation technique for real-time three-phase power conversion, IEEE Trans. Ind. Appl. 34 (2) (Mar./Apr. 1998) 374–380.
[14] A.M. Hava, R.J. Kerkman, T.A. Lipo, Simple analytical and graphical methods for carrier-based PWM-VSI drives, IEEE Trans. Power Electron. 14 (1) (Jan. 1999) 49–61.
[15] A.M. Hava, S.K. Sul, R.J. Kerkman, T.A. Lipo, Dynamic overmodulation characteristics of triangle intersection PWM methods, IEEE Trans. Ind. Appl. 35 (4) (Jul./Aug. 1999) 896–907.
[16] J.K. Seok, J.S. Kim, S.K. Sul, Overmodulation strategy for high-performance torque control, IEEE Trans. Power Electron. 13 (4) (Jul. 1998) 786–792.
[17] A.M. Hava, R.J. Kerkman, T.A. Lipo, Carrier-based PWM-VSI overmodulation strategies: analysis, comparison, and design, IEEE Trans. Power Electron. 13 (4) (Jul. 1998) 674–689.
[18] J. Holtz, W. Lotzkat, A. Khambadkone, On continuous control of PWM inverter in the overmodulation range including the six-step mode, in: Conf. Rec. IEEE IECON, 1992, pp. 307–312.
[19] D.-W. Han, S.-H. Kim, An overmodulation strategy for SVPWM Inverter using pole voltage, Trans. Korean Inst. Power Electron. 7 (2) (Apr. 2002) 149–157.
[20] Y. Murai, T. Watanabe, H. Iwasaki, Waveform distortion and correction circuit for PWM inverters with switching lag-times, IEEE Trans. Ind. Appl. IA-23 (5) (Sep./Oct. 1987) 881–886.
[21] S.-G. Jeong, M.-H. Park, The analysis and compensation of dead- time effects in PWM inverters, IEEE Trans. Ind. Electron. 38 (2) (Apr. 1991) 108–114.
[22] Y.S. Park, S.K. Sul, A novel method utilizing trapezoidal voltage to compensate for inverter nonlinearity, IEEE Trans. Power Electron. 27 (12) (Dec. 2012) 4837–4846.
[23] D. Leggate, J. Kerkman, Pulse-based dead-time compensator for pwm voltage inverters, IEEE Trans. Ind. Electron. 44 (2) (Apr. 1997) 191–197.
[24] IGBT Basics 1, Application Note 9016, Fairchild Semiconductor, 2001.
[25] S.H. Song, J.W. Choi, S.K. Sul, Current measurements in digitally controlled AC drives, IEEE Ind. Appl. Mag. (Jul./Aug. 2000) 51–62.
[26] V. Blasko, V. Kaura, W. Niewiadomski, Sampling of discontinuous voltage and current signals in electrical drives: a system approach, IEEE Trans. Ind. Appl. 35 (5) (Sep./Oct. 1987) 1123–1130.

CHAPTER

# High-speed operation of alternating current motors

8

In variable speed drive applications such as alternating current (AC) servo and traction drive systems, a high-speed operation capability as well as a fast torque response of motors are needed. For example, for spindle drives in machine tools, a high-speed operation of more than several 10,000 r/min is required for enhancing cutting efficiency and accuracy. Traction drives such as electric cars, electric trains, electric forklifts, and dehydration of washing machines also require a high-speed operation of several times the rated speed. In addition, motors for driving compressors or motors for driving a torpedo and a missile need to be operated at a high-speed region of several 10,000 r/min. In this chapter, we will discuss the high-speed operation of AC motors. We introduce the field-weakening methods, which achieve the maximum torque capability of motors as well as a high-speed operation.

In the variable speed drives, the voltage applied to the motor should be increased with the operating speed. This is to maintain the current needed for the torque production of the motor. Since the back-EMF increases with the operating speed, the motor voltage should also be increased to control the current properly. As the speed increases, the motor reaches a speed (commonly called *base speed*) at which the applied motor voltage is equal to its rated value. From this speed, since the motor voltage is fixed at the rated voltage, we need to limit the back-EMF to a suitable level despite the increase in the speed.

For this purpose, a field-weakening control to reduce the field flux of the motor is necessary. As can be seen from Chapter 2 and Chapter 3, the back-EMF of direct current (DC) motors and AC motors is directly proportional to the operating speed $\omega_m$ (or frequency $f$) and the field flux as

$$E_{DC} \propto \phi \cdot \omega_m \quad \text{or} \quad E_{AC} \propto \phi \cdot f \tag{8.1}$$

If the field flux of a motor decreases with the increased speed, then the back-EMF is limited to a suitable level. Thus the voltage margin to control the current correctly can be maintained.

As an example, consider a high-speed operation in the DC motor drives. First, we will assume that the field flux $\phi$ is constant and the torque production to drive

Electric Motor Control. DOI: http://dx.doi.org/10.1016/B978-0-12-812138-2.00008-8
© 2017 Elsevier Inc. All rights reserved.


Hesai Exhibit 1030, page 344

a load requires an armature current $I_a$. From the voltage equation of Eq. (2.1), the armature current in the steady-state is given as

$$I_a = \frac{V_a - E_a}{R_a} = \frac{V_a - k_e \phi \omega_m}{R_a} \tag{8.2}$$

Since the back-EMF increases as the operating speed increases, the armature voltage $V_a$ applied to the motor should be increased with the increase in the speed to achieve the required current $I_a$. However, there is a limitation to the voltage applied to the motor because the motor voltage should not be greater than the rated voltage. Therefore the motor voltage required to regulate the command current may be insufficient in the high-speed region. As shown in Fig. 8.1, when the back-EMF is close to the full voltage of the motor as the speed increases, the current (thus output torque) of the motor is decreased rapidly. As a result, the speed no longer increases.

However, as shown in Fig. 8.2, if we limit the back-EMF to a constant value over the high-speed region by using the field-weakening control, which reduces the field flux in proportion to the inverse of the speed, then the voltage margin that regulates the current can be maintained and the output torque can be developed adequately. As a result, the speed of the motor can increase more than the rated speed.

For DC motors, the back-EMF can easily be maintained at a constant by reducing the field flux in proportion to the inverse of the speed so that the high-speed operation can function properly. However, the high-speed operation of AC motors cannot be achieved by such a simple method, and the high-speed

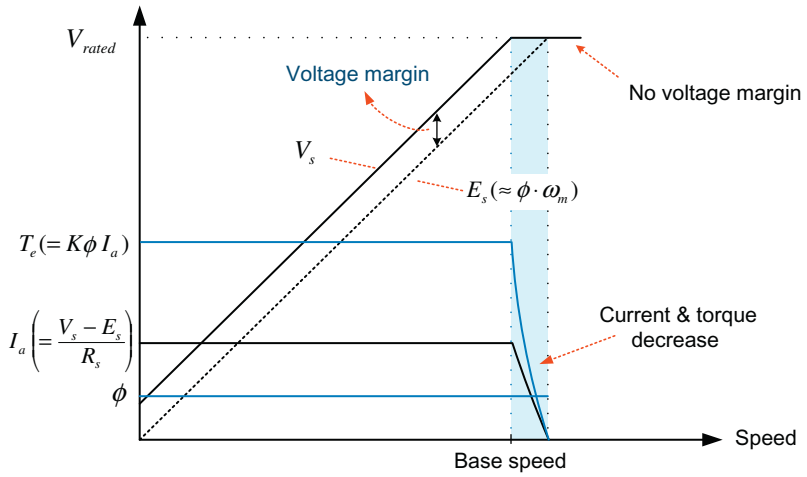



**FIGURE 8.1**

Motor characteristics according to speed (without field-weakening control).

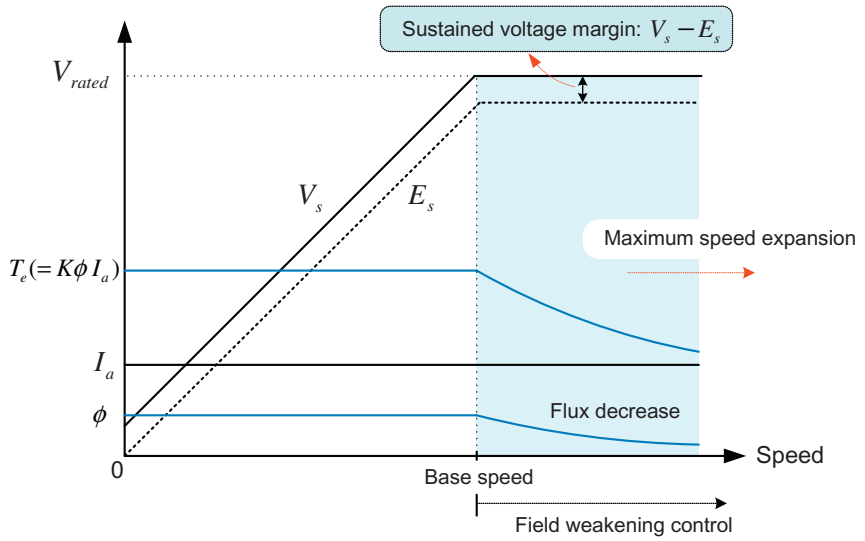



**FIGURE 8.2**

Motor characteristics according to speed (with field-weakening control).

operation method is different depending on the type of AC motor. Now we will discuss the field-weakening method for the high-speed operation of vector-controlled AC motors. We will start with an induction motor.

## 8.1 FIELD-WEAKENING CONTROL FOR INDUCTION MOTORS [1,2]

Induction motors are beneficial for high-speed operations due to their mechanical robustness. In addition, the output torque characteristic of induction motors in the constant power region matches well with a load (i.e., load torque inversely proportional to speed) requiring high-speed operation. Moreover, since the field flux of the vector-controlled induction motor can be easily weakened by reducing the *d*-axis current as the rotor speed increases, high-speed operations can be done easily. However, even though the same voltage and current are used, the developed torque capability of the motor at high speeds can vary according to the applied field-weakening strategy.

The field-weakening control method for induction motors can be classified into two methods: the *feedforward method* [1], which derives the flux command required for high-speed operation from the steady-state voltage equations of an induction motor, and the *feedback method* [2], which obtains the flux command from the voltage feedback. Now we will discuss the feedforward field-weakening control method in the vector control based on the rotor flux of induction motors.

### 8.1.1 CLASSIC FIELD-WEAKENING CONTROL METHOD

The method that was previously used for the field-weakening operation of induction motors was to simply vary the flux-producing current, i.e., $d$-axis stator current $i_{ds}^{e}$ in proportion to the inverse of the rotor speed $\omega_r$ in the same way for DC motors as

$$i_{ds}^{e^*} = \frac{\omega_{r\text{-}base}}{\omega_r} \cdot I_{d\text{-}rated} \tag{8.3}$$

where $I_{d\text{-}rated}$ is the rated $d$-axis current and $\omega_{r\text{-}base}$ is the base speed.

From this $d$-axis current command, the rotor flux command according to the speed in the field-weakening region is given as

$$\lambda_{dr}^{e^*} = L_m i_{ds}^{e^*} = L_m \left( \frac{\omega_{r\text{-}base}}{\omega_r} \right) \cdot I_{d\text{-}rated} \tag{8.4}$$

However, the flux command $\lambda_{dr}^{e^*}$ given by Eq. (8.4) cannot properly retain the voltage margin required for current control in the high-speed region. This is because the command flux level is too high to reduce the back-EMF appropriately. As a result, it is impossible to regulate the current commands required to perform the vector control properly, and thus the output torque capability of the induction motor is degraded. Moreover, the drive system may even fail to operate.

In Ref. [1], the authors introduced the optimal field-weakening method, which achieve the maximum torque capability of the induction motor and the high-speed operation. Now we will discuss this feedforward field-weakening method in more detail.

Since the developed torque of a motor depends on the available voltage and current, we need to begin with investigating the range of voltage and current available for an induction motor. The voltage applied to the motor is never greater than the rated value. On the other hand, the current often has a short-time rating, being two to three times greater than the rated current for a high-acceleration/high-deceleration torque production. Therefore we need to consider the available motor voltage and current for deriving the effective field-weakening method.

### 8.1.2 VOLTAGE- AND CURRENT-LIMIT CONDITIONS

In this section, we will examine the boundary of the current available for the torque production of an induction motor. This boundary can be obtained from the available voltage and current as follows.

#### *8.1.2.1 Voltage-limit condition*

For an inverter-driven motor, the motor voltage is supplied by an inverter. The maximum output voltage $V_{s\ max}$ of an inverter is determined by the available DC input voltage $V_{dc}$. Even under the same DC voltage, the maximum output voltage depends on the pulse width modulation (PWM) technique used. For example, as

stated in Chapter 7, the space vector pulse width modulation (SVPWM) technique can produce a maximum voltage of $V_{dc}/\sqrt{3}$, while the sinusoidal pulse width modulation (SPWM) technique can produce that of $V_{dc}/2$.

For the maximum voltage $V_{s\,max}$ of a motor, the $d-q$ axes stator voltages should always satisfy the following relation.

$$v_{ds}^2 + v_{qs}^2 \le V_{s\,max}^2 \tag{8.5}$$

This is called *voltage-limit condition*. Here, the selection of the value of the maximum phase voltage $V_{s\,max}$ has a strong influence on the field-weakening operation performance. Considering the voltage drops of the switching devices, dead-time effects, and control stability, it is desirable to set this value at 90−95% of the maximum attainable voltage by a PWM technique in an inverter. If the value of $V_{s\,max}$ is inappropriately selected, then it can cause degradation or even a failure of high-speed operations.

The synchronous $d-q$ axes voltage equations of a vector-controlled induction motor based on the rotor flux are rewritten from Eqs. (6.16) and (6.17) as

$$v_{ds}^e = R_s i_{ds}^e + p\left(\sigma L_s i_{ds}^e + \frac{L_m}{L_r}\lambda_{dr}^e\right) - \omega_e \sigma L_s i_{qs}^e \tag{8.6}$$

$$v_{qs}^e = R_s i_{qs}^e + p\sigma L_s i_{qs}^e + \omega_e\left(\sigma L_s i_{ds}^e + \frac{L_m}{L_r}\lambda_{dr}^e\right) \tag{8.7}$$

When considering high-speed operations, the voltage drops on the stator resistance is negligible compared to the back-EMFs, so the above equations can be simplified in the steady-state as

$$v_{ds}^e \approx -\omega_e \sigma L_s i_{qs}^e \tag{8.8}$$

$$v_{qs}^e \approx \omega_e\left(\sigma L_s i_{ds}^e + \frac{L_m}{L_r}\lambda_{dr}^e\right) \approx \omega_e L_s i_{ds}^e \tag{8.9}$$

By substituting these equations into Eq. (8.5), the voltage-limit condition can be expressed in terms of $d-q$ axes stator currents as

$$\left(\omega_e \sigma L_s i_{qs}^e\right)^2 + \left(\omega_e L_s i_{ds}^e\right)^2 \le V_{s\,max}^2 \tag{8.10}$$

This expression illustrates the boundary of the controllable $d-q$ axes currents by using the maximum available voltage $V_{s\,max}$. This voltage-limit boundary is expressed as an ellipse equation, which is a function of operating frequency $\omega_e$ as shown in Fig. 8.3. The inside of the ellipse indicates the controllable current region. Any $d-q$ current command inside the ellipse is controllable by using the given voltage $V_{s\,max}$. Thus the current commands should remain inside the voltage-limit ellipse given at each operating frequency. The radius of the ellipse becomes smaller as the operating frequency increases. This means that, under a given voltage, the boundary of controllable currents becomes smaller. This is because the back-EMF increases as the operating frequency increases. Unlike DC

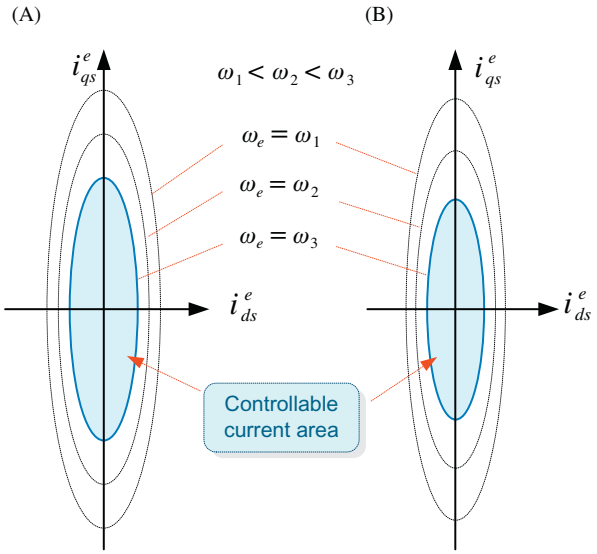



**FIGURE 8.3**

Voltage-limit condition. (A) Small leakage factor and (B) large leakage factor.

motors, the back-EMF of induction motors increases with the operating frequency rather than the rotor speed.

Fig. 8.3A and B shows several ellipses for different operating frequencies. We can see from Eq. (8.10) that the leakage inductance (or leakage factor $\sigma$) has a significant influence on the shape of the ellipse at a specific operation frequency. The area of the ellipse is smaller for an induction motor with a large leakage factor as in Fig. 8.2B than for one with a small leakage factor as in Fig. 8.2A at the same operating frequency. This implies that for an induction motor with a large leakage factor, more voltage is necessary for regulating an equal value of current commands. As stated in Chapter 3, an induction motor with a large leakage factor has a narrow range of the constant power region. This is because the leakage factor has an influence on the maximum values of the slip. Fig. 8.3 explains this phenomenon. Hence, the leakage factor is an important factor in the design of an induction motor.

Next, we will discuss the current-limit condition for a motor.

### 8.1.2.2 Current-limit condition

The motor current is usually limited by the rated current. A 150−300% rated current, however, is often allowed for a short period of time to produce a high-acceleration/high-deceleration torque, given that it does not exceed the motor thermal rating. The current rating of an inverter should be selected so that it can provide the maximum motor current.

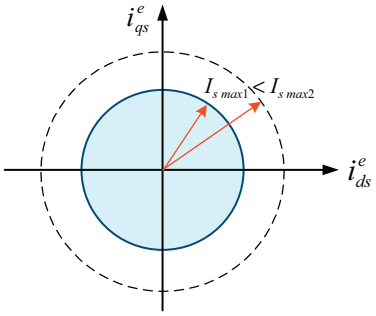



**FIGURE 8.4**

Current-limit condition.

Under the maximum available stator current $I_{s\,max}$, the $d-q$ axes stator currents of an induction motor are restricted to the following condition.

$$i_{ds}^2 + i_{qs}^2 \leq I_{s\,max}^2 \tag{8.11}$$

This is referred to as *current-limit condition*. This current-limit boundary can be expressed as a circle in the $d-q$ axes current plane as shown in Fig. 8.4, whose radius is the maximum stator current $I_{s\,max}$. To satisfy this current-limit condition, the $d-q$ axes stator current commands should always be inside this circle. Unlike the voltage-limit condition, the boundary of the current-limit condition remains constant regardless of the operating frequency.

When we drive an induction motor, the two conditions of the voltage- and current-limit should be always satisfied. Considering both the voltage- and the current-limit conditions, the region of the controllable currents is the common area between the current-limit circle and the voltage-limit ellipse for a given operating frequency, which is the *dark area* shown in Fig. 8.5.

Thus the $d-q$ axes stator current commands in the induction motor drive must be inside this area for a given operating frequency.

Now we will find out the optimal flux under the voltage- and the current-limit conditions for the field-weakening control, which can obtain the maximum output torque capability of an induction motor over the whole high-speed region.

### 8.1.3 FIELD-WEAKENING CONTROL FOR PRODUCING THE MAXIMUM TORQUE

In a vector-controlled induction motor, the output torque can be expressed as a function of $d-q$ axes stator currents as

$$T_e = \frac{3}{2}\frac{P}{2}\frac{L_m^2}{L_r} i_{ds}^e i_{qs}^e = k i_{ds}^e i_{qs}^e \quad \left(k = \frac{3}{2}\frac{P}{2}\frac{L_m^2}{L_r}\right) \tag{8.12}$$

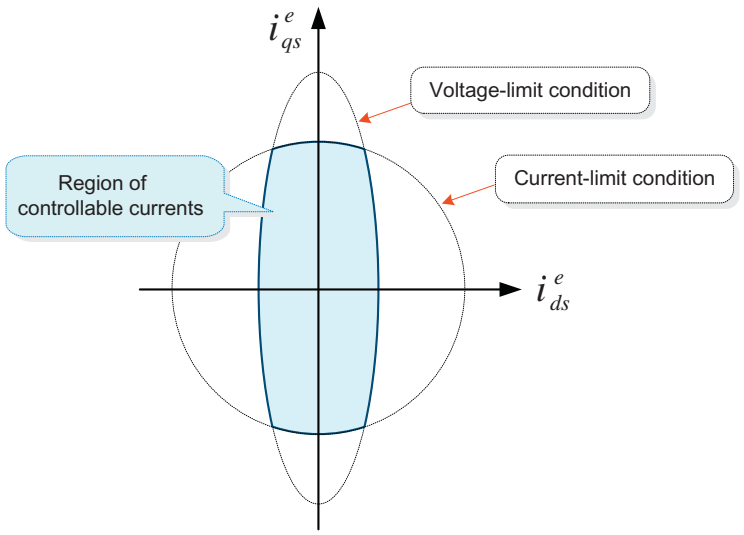



**FIGURE 8.5**

Region of controllable currents for voltage- and current-limit conditions.

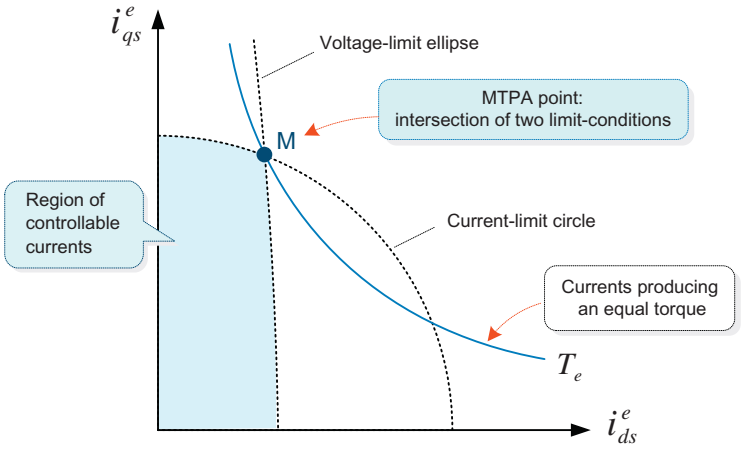



**FIGURE 8.6**

Voltage- and current-limit conditions and MTPA point.

The value of the output torque varies according to the chosen combinations of $d-q$ axes stator currents, $i_{ds}^{e}$ and $i_{qs}^{e}$. Fig. 8.6 illustrates numerous combinations of the stator currents to produce an equal output torque, along with the voltage- and the current-limit conditions. Here, we will consider only Quadrant 1, which indicates the motoring operation mode for the forward driving.

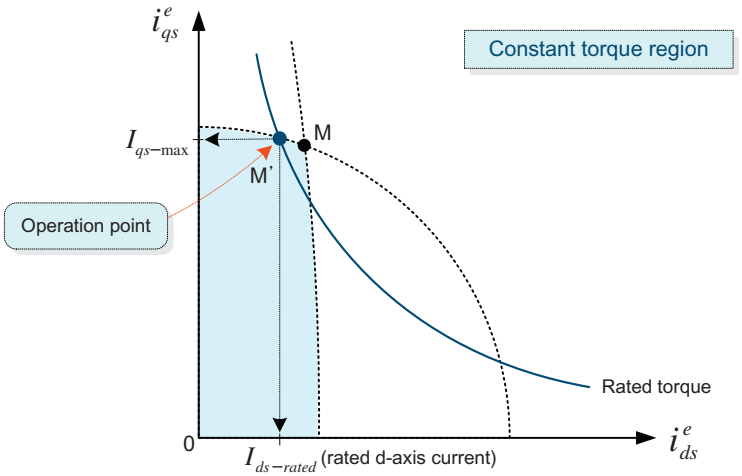



**FIGURE 8.7**

Optimal operating point in the constant torque region.

In the available region under both the voltage- and current-limit conditions, the optimal current combination maximizing the output torque becomes the value at the intersection (M point) of the circle and the ellipse at a given operating frequency. This operating point indicates the minimum stator current for producing the required torque. Thus this is the *maximum torque per ampere* (MTPA) operating point. This optimal operating point varies according to the operating speed, and it can be obtained as follows.

#### 8.1.3.1 Constant torque region ($\omega_e \leq \omega_{base}$)

In the low- and mid-speed range, the *d*-axis stator current at the optimal operating point M is usually greater than rated *d*-axis current $I_{ds\text{-}rated}$ for producing the rated rotor flux linkage $\lambda^e_{dr\text{-}rated}$ as shown in Fig. 8.7. Even if the *d*-axis current is increased above the rated value, the flux level does not increase accordingly because of the saturation of the iron core. For this reason, in this speed range, the *d*-axis stator current command (thus, rotor flux command) is maintained at the rated value as

$$i^{e*}_{ds} = I_{ds\text{-}rated} \tag{8.13}$$

$$\lambda^{e*}_{dr} = \lambda^e_{dr\text{-}rated} = L_m i^{e*}_{ds} = L_m I_{ds\text{-}rated} \tag{8.14}$$

In this case, the available output torque depends only on the available *q*-axis stator current. The available *q*-axis stator current is limited by the *d*-axis current command as

$$i^{e*}_{qs\text{-}max} = \sqrt{I^2_{s\ max} - i^{e*2}_{ds}} = \sqrt{I^2_{s\ max} - I^2_{ds\text{-}rated}} \tag{8.15}$$

Thus, in this speed range, the operating point is given as M′ point as shown in Fig. 8.7. This condition is still held at operating speeds below the rated speed (more accurately, the base speed).

Next, we will examine the optimal flux for producing the maximum torque in the high-speed range. The high-speed region, which is called *field-weakening region*, has two subregions as follows.

### 8.1.3.2 Constant power region ($\omega_{base} \leq \omega_e < \omega_{BT}$): Field-weakening region I

In the constant torque region as stated earlier, when the operating frequency is increased, the boundary of the voltage-limit ellipse will be reduced. This indicates that, due to a limited $V_{s\,max}$, the controllable current region is reduced as the back-EMF increases with the operating frequency.

Even though the voltage-limit ellipse is reduced by the increase in operating frequency, the rated *d*-axis current can still be used, provided that the controllable current region includes the rated *d*-axis current. As the operating frequency is further increased, the *d*-axis stator current at the intersection of the circle and ellipse will coincide with the rated *d*-axis current as shown in Fig. 8.8. The operating frequency at this moment is the onset frequency at which the constant power region begins. The speed at this onset frequency is called the *base speed* $\omega_{base}$. For the operation above the base speed, the *d*-axis stator current should be lowered below the rated *d*-axis current. In other words, the field-weakening operation should start reducing the flux level.

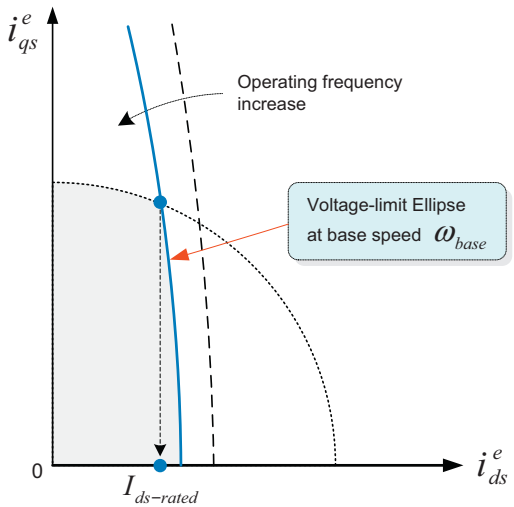



**FIGURE 8.8**

Onset of field-weakening operation.

From Eqs. (8.10) and (8.11), the base speed is given as

$$\omega_{base} = \frac{\sqrt{V_{s\,max}^2[(L_sI_d)^2+(\sigma L_sI_q)^2]^2+[R_sI_dI_q(L_s-\sigma L_s)]^2}-R_sI_dI_q(L_s-\sigma L_s)}{(L_sI_d)^2+(\sigma L_sI_q)^2} \tag{8.16}$$

here, $I_d = I_{ds\text{-}rated}$ and $I_q = \sqrt{I_{s\,max}^2 - I_d^2}$ are the $d-q$ axes stator currents used in the constant torque region, respectively.

The base speed depends heavily on the motor parameters, and thus, varies with motors. Even for the same motor, the base speed varies according to the flux level used in the constant torque region and the available stator voltage and current. A higher flux level, low $V_{s\,max}$, or high $I_{s\,max}$ results in a lower base speed, and thus in such cases, the field-weakening operation should start at a lower speed.

From the base speed and the slip frequency, the base rotor speed is obtained by

$$\omega_{r\text{-}base} = \omega_e - \omega_{sl} \tag{8.17}$$

This base rotor speed may be different from the rated rotor speed according to operating conditions.

In this field-weakening region, the optimal current combination (i.e., optimal current vector) producing the maximum output torque is always given as the value at the intersection (M point) of the circle and ellipse. The optimal current vector moves along the current-limit boundary as shown in Fig. 8.9 because the voltage-limit ellipse dwindles as the operating frequency increases. This means that the $d$-axis stator current, and thus the rotor flux linkage $\lambda_{dr}^e$ should be reduced as the operating frequency increases.

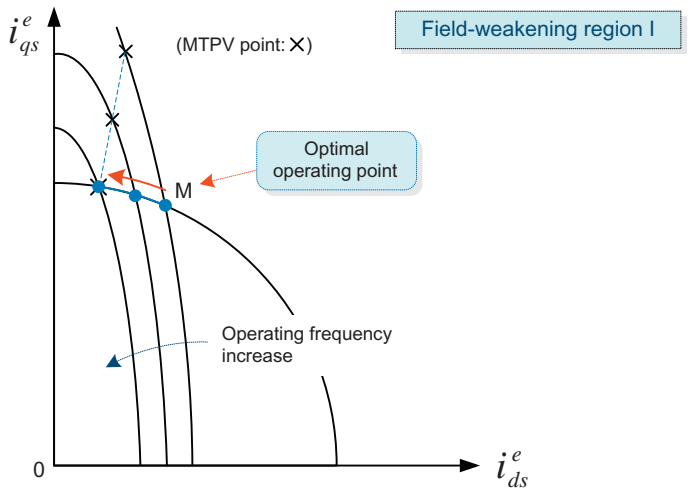



**FIGURE 8.9**

Optimal current trajectory in the field-weakening region I.

The $d$-axis stator current at this optimal point can be derived from the voltage- and current- limit conditions as

$$i_{ds}^{e} = \sqrt{\frac{\left(\frac{V_{s\,max}}{\omega_e}\right)^2 - (\sigma L_s I_{s\,max})^2}{L_s^2(1-\sigma)}} \tag{8.18}$$

In this case, the available maximum $q$-axis stator current can be increased by the decreasing amount of the $d$-axis current to use the allowable stator current $I_{s\,max}$ fully as

$$i_{qs\text{-}max}^{e} = \sqrt{I_{s\,max}^2 - i_{ds}^{e*2}} \tag{8.19}$$

From the optimal $d$-axis stator current, the optimal rotor flux command is given as

$$\lambda_{dr}^{e*} = L_m i_{ds}^{e*} = L_m \sqrt{\frac{\left(\frac{V_{s\,max}}{\omega_e}\right)^2 - (\sigma L_s I_{s\,max})^2}{L_s^2(1-\sigma)}} \tag{8.20}$$

It is important to note that the magnetizing inductance $L_m$ varies due to the flux reduction in this region. Thus the optimal flux should be obtained by considering this inductance variation. Also, as stated in Chapter 5, since the relation between the $d$-axis stator currents $i_{ds}^{e}$ and the rotor flux linkage $\lambda_{dr}^{e}$ is a first-order lag, a flux controller should be used to control the flux accurately for an effective field-weakening operation.

In this region the stator voltage and current are maintained at a constant as $V_{s\,max}$ and $I_{s\,max}$, respectively. Thus this region is referred to as *constant power (constant VA) region*. In this region, as we can see from the slip equation of Eq. (5.32), the slip frequency increases as the operating frequency increases because the $d$-axis stator current decreases and the $q$-axis stator current increases. As the operating frequency is further increased, the slip frequency reaches its maximum value, and then the field-weakening region II begins.

#### 8.1.3.3 Breakdown torque region ($\omega_e > \omega_{BT}$): Field-weakening region II

As the operating frequency is further increased in the field-weakening region I, the voltage-limit ellipse will be reduced further, and a large portion will be included in the current-limit circle as shown in Fig. 8.10. This implies that the voltage-limit condition is included in the current-limit condition.

Furthermore, if the optimal current for producing the maximum torque subject to only the voltage-limit condition (point X on the voltage-limit ellipse) is included inside the current-limit circle, we can consider only the voltage-limit condition for obtaining the optimal flux. This situation corresponds to *field-weakening region II*. This optimal point subject to only the voltage-limit condition is called the *maximum torque per voltage* (MTPV) operating point.

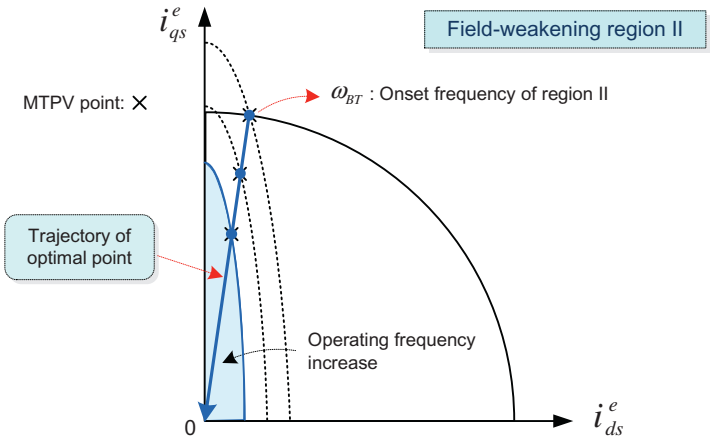



**FIGURE 8.10**

Maximum torque operation point for the field-weakening region II.

The onset speed of the field-weakening region II is the frequency $\omega_{BT}$, at which the optimal current vector for the MTPV operation is just on the circumference of the current-limit circle, and can be given as

$$\omega_{BT} = \sqrt{\frac{1+\sigma^2}{2(\sigma L_s)^2}} \times \left(\frac{V_{s\,max}}{I_{s\,max}}\right) \tag{8.21}$$

This onset frequency $\omega_{BT}$ depends on the leakage inductance as well as the maximum values of the voltage and current. Induction motors with a large leakage factor will begin the operation of the field-weakening region II at a lower speed. Thus they have a narrow range of the constant power region.

In this field-weakening region II, the optimal stator currents for producing the maximum torque are given as

$$i^e_{ds} = \frac{V_{s\,max}}{\sqrt{2}\omega_e L_s} \tag{8.22}$$

$$i^e_{qs} = \frac{V_{s\,max}}{\sqrt{2}\omega_e \sigma L_s} \tag{8.23}$$

From the optimal $d$-axis stator current, the optimal rotor flux command is given as

$$\lambda^{e^*}_{dr} = L_m i^{e^*}_{ds} = \frac{V_{s\,max} L_m}{\sqrt{2}\omega_e L_s} \tag{8.24}$$

In this region, the optimal stator vector moves into the origin as the frequency increases as shown in Fig. 8.10. Thus, unlike the field-weakening region I, $i^{e^*}_{qs}$ is

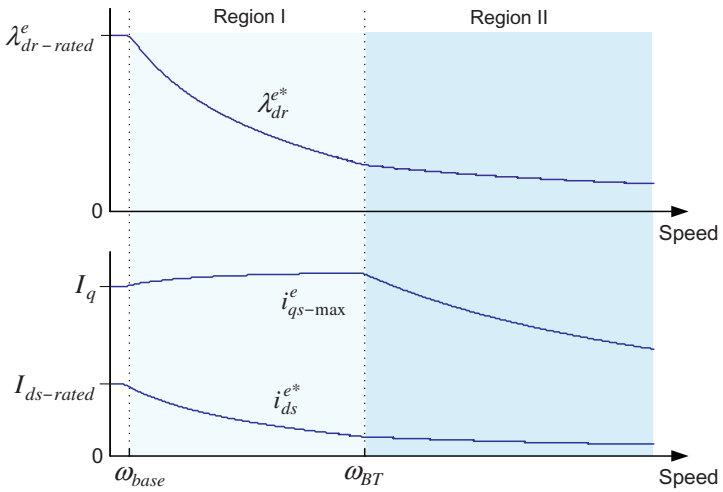



**FIGURE 8.11**

Optimal currents and flux in the field-weakening regions I and II.

also decreased along with the reduction of $i^{e*}_{ds}$. As a result, the total stator current will be reduced, and the output power will also be reduced. Fig. 8.11 shows the optimal $d-q$ currents and the rotor flux command according to the speed in the field-weakening regions I and II.

From the optimal $d-q$ axes currents of Eqs. (8.22) and (8.23), we can readily see that the slip frequency remains constant over this region as its maximum value, which is given as

$$\omega_{sl\text{-}max} = \frac{1}{T_r}\frac{i^e_{qs}}{i^e_{ds}} = \frac{1}{T_r\sigma} \tag{8.25}$$

The maximum torque developed by an induction motor in this region is quickly reduced by $1/\omega_e^2$ as

$$T_{e\text{-}max} = \frac{3}{2}\frac{P}{2}\frac{1}{2\sigma L_s^2}\left(\frac{V_{s\ max}}{\omega_e}\right)^2 \tag{8.26}$$

Fig. 8.12 compares the high-speed performance of the optimal field-weakening operation with that of the "$1/\omega_r$" method.

Since the level of the rotor flux command given at each operating frequency is inappropriate in the "$1/\omega_r$" method, the drive system does not exploit the output torque capability of the motor fully. Moreover, it will be hard to regulate the $q$-axis stator current command as the speed increases, so the vector control cannot be carried out in the high-speed region. As a result, the drive system will lose its controllability.

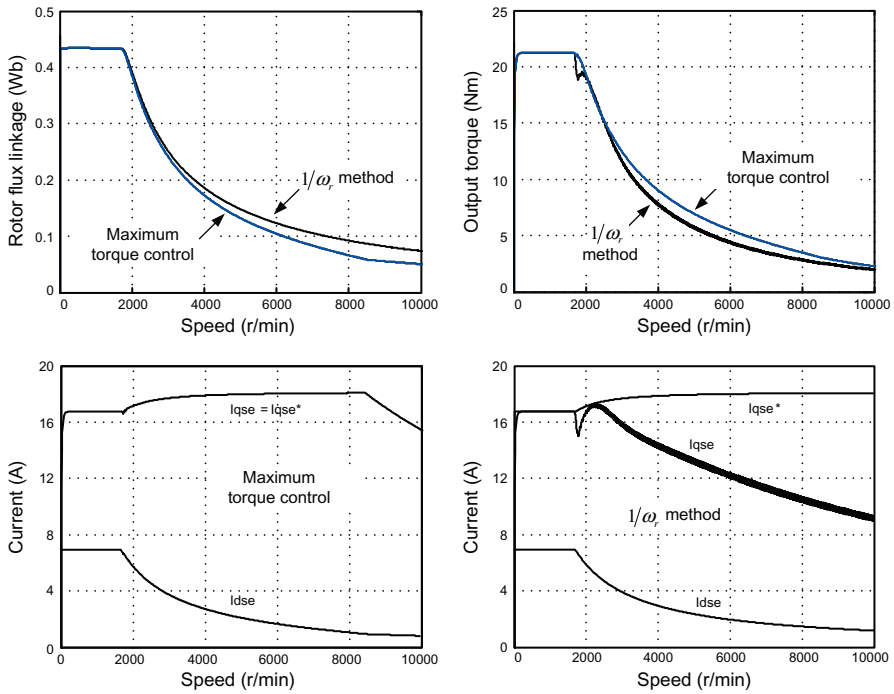



**FIGURE 8.12**

Comparison of the performance of the field-weakening methods (5-hp, 4-pole).

Fig. 8.13 shows a vector-controlled induction motor drive system with the field-weakening control for high-speed operations. The optimal flux reference can be given from Eq. (8.20) or (8.24) according to the operating speed.

Fig. 8.14 shows the experimental results on a 6-pole, 2.2-kW induction motor for the vector control system as shown in Fig. 8.13 [1]. The induction motor was accelerated up to 3000 r/min in the field-weakening region II by using the optimal strategy just described. The *d*-axis stator current is regulated to reduce the rotor flux according to the operating speed. Here, since the flux linkage is estimated by the voltage model, we can see that the estimated flux is inaccurate below the mid-speed range. While the *q*-axis current is increased in the field-weakening region I, it is decreased in the field-weakening region II.

To successfully carry out the optimal field-weakening operation, the optimal rotor flux reference at each operating frequency needs to be calculated correctly. In this feedforward field-weakening control method, the accuracy of the calculated optimal flux reference depends on the motor parameters such as the magnetizing inductance and leakage inductance. The magnetizing inductance will especially vary significantly due to the variation of the rotor flux level in the field-weakening operation. Therefore the variation of the magnetizing

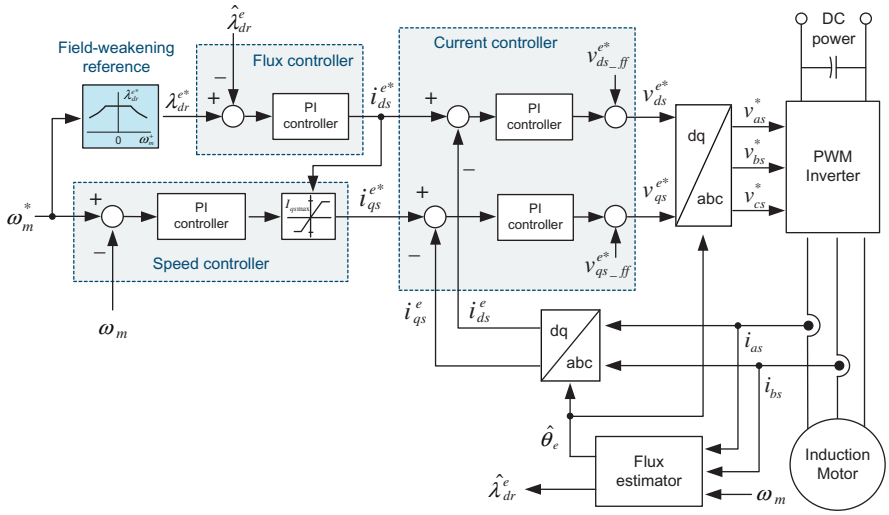



**FIGURE 8.13**

Vector control system of an induction motor with the field-weakening control.

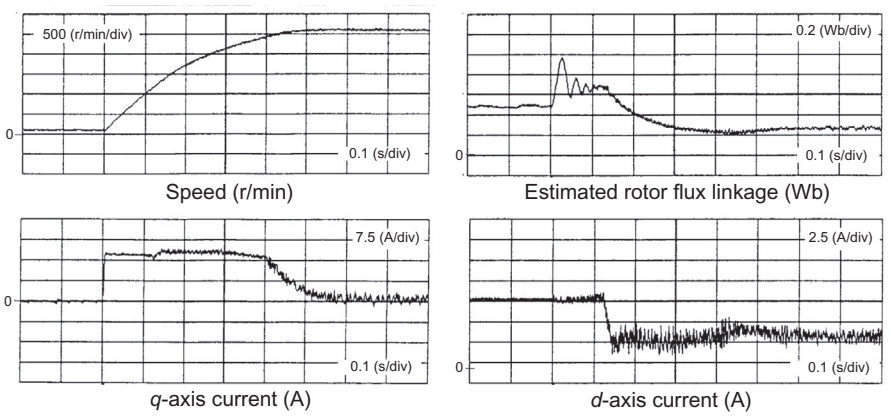



**FIGURE 8.14**

Optimal field-weakening operation (6-pole, 2.2-kW IM).

inductance should be considered. On the other hand, the leakage inductance is not dependent on the variation of the rotor flux level but on the magnitude of the stator current.

Unlike the feedforward field-weakening method sensitive to motor parameters, Kim and Sul [2] proposed another field-weakening control strategy that uses the feedback of the motor voltage without any motor parameter as shown

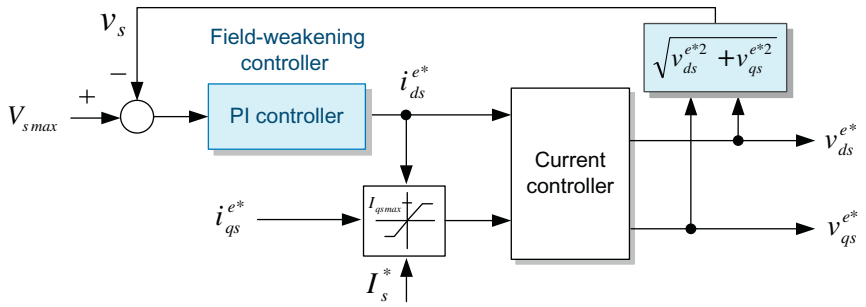



**FIGURE 8.15**

Field-weakening control strategy using the voltage feedback.

in Fig. 8.15. The feedback field-weakening control strategy is insensitive to motor parameters but cannot give dynamic response as fast as the feedforward strategy can.

The concept of the optimal field-weakening control methods of induction motors can be also used for high-speed operation of permanent magnet synchronous motors (PMSMs) as follows.

## 8.2 FLUX-WEAKENING CONTROL FOR PERMANENT MAGNET SYNCHRONOUS MOTORS [3–6]

As stated in Section 4.6, surface-mounted permanent magnet synchronous motors (SPMSMs) with magnets mounted on the surface of the rotor are unsuitable for high-speed operations with a higher centrifugal force. Furthermore, a reduction in stator inductance due to the magnets on the surface of the rotor hinders the flux-weakening operation, which reduces the magnet flux. On the contrary, interior permanent magnet synchronous motor (IPMSMs) are favorable for the high-speed operation since their magnets are inserted inside the rotor core and have a large inductance. For these reasons, IPMSMs are widely used for applications requiring a high-speed operation. Now we will discuss the flux-weakening control for the high-speed operation of PMSMs in more detail.

For motors such as an induction motor, separately excited DC motor, and synchronous motor with a field winding on the rotor, the field flux can be reduced directly by controlling the field current for high-speed operation. This technique is referred to as *field-weakening control*. By contrast, for PMSMs such as IPMSM or SPMSM, the field flux cannot be controlled directly because it is generated by a permanent magnet. As can be seen from Eq. (4.113), the stator flux linkage of PMSMs is given by

$$\lambda_{ds}^r = L_{ds} i_{ds}^r + \phi_f \tag{8.27}$$

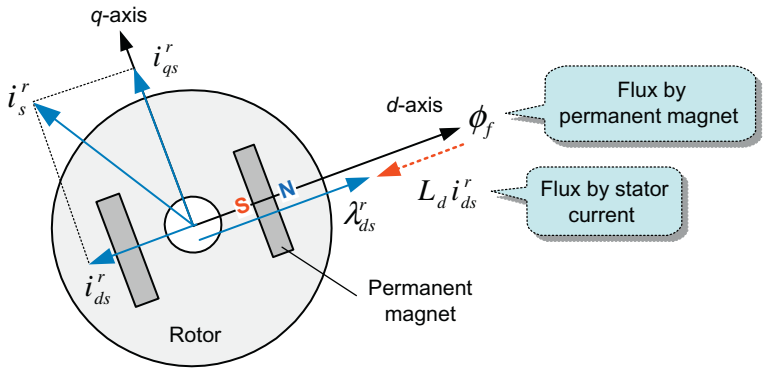



**FIGURE 8.16**

Concept of flux weakening.

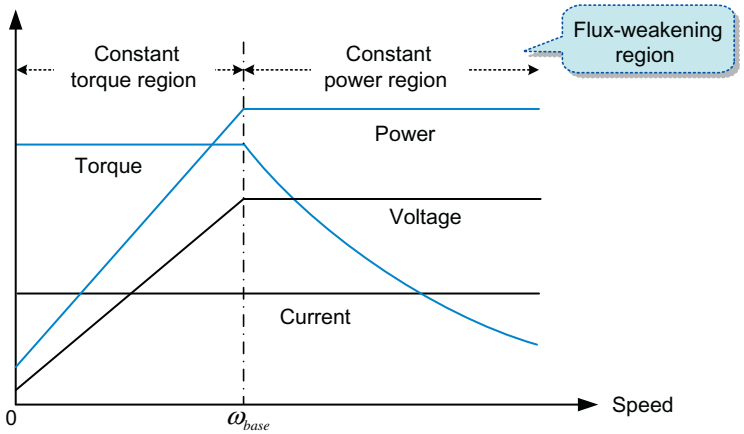



**FIGURE 8.17**

Operation region of PMSMs.

For PMSMs, if we produce the flux in the direction opposite of the magnet flux by using the negative *d*-axis stator current as shown in Fig. 8.16, we can reduce the effective stator flux linkage. This technique is referred to as *flux-weakening control*. From Eq. (8.27), we can see that a large *d*-axis inductance is desirable for an effective flux-weakening control.

The operation region of PMSMs can be normally divided into the following two speed regions.

- *Constant torque region*: Speed range below base speed
- *Constant power region*: Speed range above base speed (flux-weakening region)

Fig. 8.17 shows the characteristics in two speed regions.

The speed regions of PMSMs are basically similar to those of separately excited DC motors. However, PMSMs may have an additional flux-weakening region similar to the breakdown torque region of induction motors depending on their magnetic system design. This is determined by the magnitude relation between the magnet flux $\phi_f$ and the maximum $d$-axis stator flux linkage (i.e., $L_{ds}I_{s\ max}$). More practically, Fig. 8.18 shows the output power characteristics of the PMSMs according to the design. In the case of $\phi_f = L_{ds}I_{s\ max}$, PMSMs have a characteristic nearly similar to the ideal characteristic as shown in Fig. 8.17. The characteristics according to the magnetic system design will be explained in more detail in the Section 8.2.1.

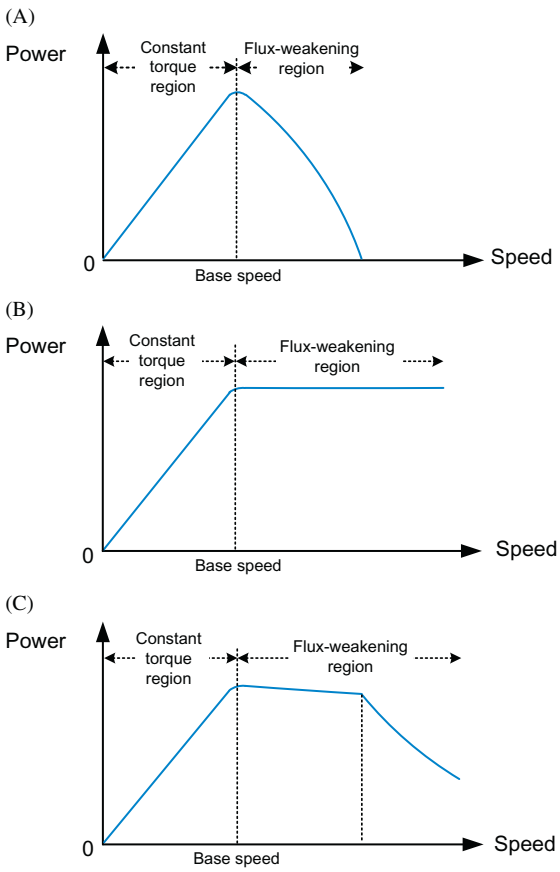



**FIGURE 8.18**

Output power according to speed regions of PMSM. (A) $\phi_f > L_{ds}I_{s\ max}$, (B) $\phi_f = L_{ds}I_{s\ max}$, and (C) $\phi_f < L_{ds}I_{s\ max}$.

The flux-weakening control techniques for the high-speed operation of PMSMs can be divided into three methods: *feedforward method*, which obtains the current commands required for the high-speed operation from steady-state voltage equations, *feedback method*, which obtains the current commands from the voltage feedback, and a *combined method* of these two techniques [3–5]. Here, we will explore the feedforward flux-weakening control method for IPMSMs and SPMSMs, separately.

## 8.2.1 HIGH-SPEED OPERATION OF AN INTERIOR PERMANENT MAGNET SYNCHRONOUS MOTOR

Before examining the high-speed operation of an IPMSM, we will first review the operation of an IPMSM in the constant torque region.

### 8.2.1.1 Constant torque region ($\omega_e \leq \omega_{base}$)

For the operation of an IPMSM in the constant torque region, which indicates an operating range below the base speed, the MTPA control is used as shown in Fig. 8.19.

In Section 5.5, we discussed how to obtain the optimal currents for MTPA operation. In the MTPA operation, the output torque of an IPMSM is mainly limited by only the maximum available stator current $I_{s\ max}$. However, for the high-speed range, where the back-EMF voltage becomes large, the voltage margin is insufficient to control the current commands for the MTPA operation. Thus the output torque of an IPMSM is limited by the available voltage rather than the available current.

Now we will examine the speed attainable under the maximum available stator voltage $V_{s\ max}$. In the vicinity of rated speed with a large back-EMF, since the

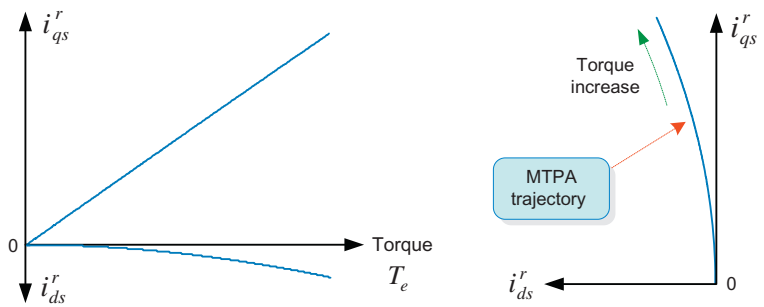



**FIGURE 8.19**

*d–q* axes current commands for MTPA operation.

voltage drops on the stator resistance is negligible, the $d-q$ axes stator voltages of an IPMSM in the steady-state are given from Eqs. (6.24) and (6.25) as

$$v_{ds}^{r} = -\omega_r L_{qs} i_{qs}^{r} \tag{8.28}$$

$$v_{qs}^{r} = \omega_r (L_{ds} i_{ds}^{r} + \phi_f) \tag{8.29}$$

These stator voltages should satisfy the following relation, which is the *voltage-limit condition* stated in Section 8.1.

$$v_{ds}^{r2} + v_{qs}^{r2} \le V_{s\,max}^{2} \tag{8.30}$$

From Eqs. (8.28)−(8.30), the maximum speed $\omega_{r\text{-}base}$ of the constant torque operation region can be obtained as

$$\omega_{r\text{-}base} = \frac{V_{s\,max}}{\sqrt{(L_{ds} I_{ds}^{r} + \phi_f)^2 + (L_{qs} I_{qs}^{r})^2}} \tag{8.31}$$

where $I_{ds}^{r}$ and $I_{qs}^{r}$ are the $d-q$ axes currents used for MTPA operation, respectively.

The speed $\omega_{r\text{-}base}$ is the base speed at which the flux-weakening control should start for the constant power operation. The base speed varies with the required current (or torque) and the available voltage.

Next, we will discuss the flux-weakening control method in the constant power region.

#### 8.2.1.2 Constant power region ($\omega_e > \omega_{base}$)

Similar to induction motors, the IPMSM operation is also confined to the voltage- and the current-limit conditions, which was explained in Section 8.1.2. Thus we need to find out the optimal flux-weakening control method that ensures a maximum torque production in the high-speed region under the voltage- and the current-limit conditions.

To begin with, we will express the voltage- and the current-limit boundaries for an IPMSM in the $d-q$ axes current plane. Similar to an induction motor, under the maximum available stator current $I_{s\,max}$, the $d-q$ axes stator currents of an IPMSM are restricted to the following condition.

$$i_{ds}^{r2} + i_{qs}^{r2} \le I_{s\,max}^{2} \tag{8.32}$$

The current-limit boundary in the $d-q$ axes currents plane is shown in Fig. 8.20. This current-limit boundary is expressed as a circle, whose radius is $I_{s\,max}$. On the other hand, the voltage-limit boundary can be expressed from Eqs. (8.28)−(8.30) as

$$(\omega_r L_{qs} i_{qs}^{r})^2 + (\omega_r L_{ds} i_{ds}^{r} + \omega_r \phi_f)^2 \le V_{s\,max}^{2} \tag{8.33}$$

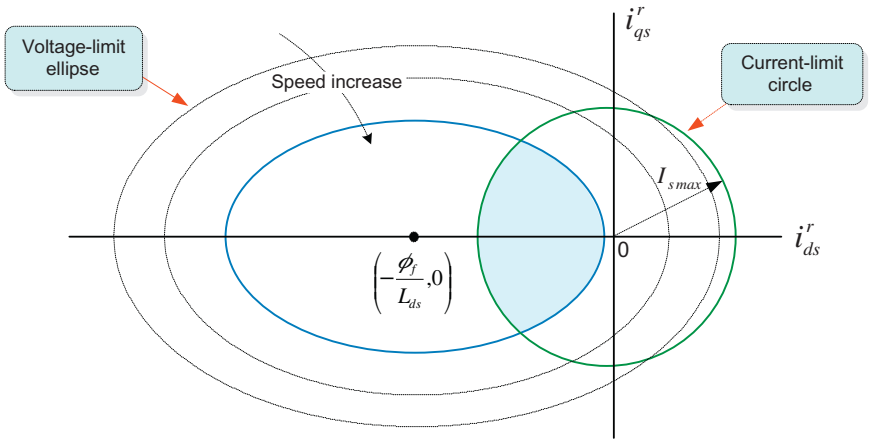



**FIGURE 8.20**

Voltage- and current-limit boundaries.

This voltage-limit boundary as shown in Fig. 8.20 is an ellipse equation, whose center is given as

$$(i^r_{ds0}, i^r_{qs0}) = \left(-\frac{\phi_f}{L_{ds}}, 0\right) \tag{8.34}$$

This expression illustrates the boundary of controllable $d-q$ axes currents by using the given maximum stator voltage $V_{s\,max}$. The inner region of the ellipse reduces as the operating speed $\omega_r$ increases. This indicates that the boundary of controllable currents becomes smaller as the operating speed increases. This is because the back-EMF increases as the operating speed increases.

The IPMSM drives should always satisfy both the voltage- and the current-limit conditions. Considering these two limit conditions, the region of controllable currents is the common area between the current-limit circle and the voltage-limit ellipse for a given operating speed, which is the *dark area* shown in Fig. 8.20. Thus the $d-q$ axes stator current commands must be inside this area for a given operating speed.

Now let us investigate the optimal operating point for producing the maximum output torque under these voltage- and current-limit conditions. For an IPMSM, as can be seen in Fig. 8.18, the maximum operating speed and the output power characteristic vary according to the magnitude relationship between the magnet flux $\phi_f$ and the maximum $d$-axis stator flux linkage (i.e., $L_{ds}I_{s\,max}$). This relationship can also be expressed by whether or not the center of the voltage-limit ellipse is inside the current-limit circle. According to this relationship, a different flux-weakening control strategy is required [6].

The maximum attainable operating speed of an IPMSM can be given by letting $i^r_{ds} = -I_{s\,max}$, $i^r_{qs} = 0$ in Eq. (8.31) as

$$\omega_{r\text{-}max} = \frac{V_{s\,max}}{\phi_f - L_{ds}I_{s\,max}} \tag{8.35}$$

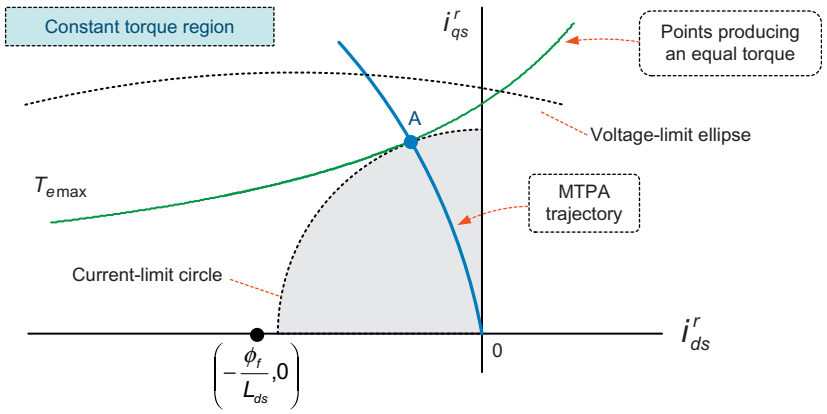



**FIGURE 8.21**

Current-limit circle and MTPA trajectory.

In the case of $\phi_f > L_{ds}I_{s\ max}$ it can be seen from Eq. (8.34) that there is a limitation on the operating speed at which the magnetic flux can be reduced by using the stator current, i.e., this type of motor has a *finite maximum speed*. On the other hand, in the case of $\phi_f < L_{ds}I_{s\ max}$, the maximum operating speed is theoretically infinite because the magnetic flux can be reduced fully by using the stator current, i.e., this type of motor has an *infinite maximum speed*. In this case, the operating speed is limited only by the mechanical strength. For these two cases, we need to use different flux-weakening control methods. First, let us take a look at the flux-weakening operation in the case of $\phi_f > L_{ds}I_{s\ max}$.

Fig. 8.21 illustrates numerous combinations of the current commands to produce an equal output torque, along with the voltage- and current-limit boundaries in the $d-q$ axes current plane.

In the low- and mid-speed range, the voltage-limit ellipse is large enough to encompass the current-limit circle. Thus we do not have to be concerned about the voltage-limit constraint, and the output torque depends only on the available current. In this case the optimal operating point is on the MTPA trajectory according to the given torque command. The maximum torque $T_{e\text{-}max}$ is produced at the intersection A of the current-limit circle and the MTPA trajectory. As the rotor speed increases, the boundary of the voltage-limit ellipse will be reduced. The boundary of the voltage-limit ellipse will encounter the MTPA operation point A at a specific speed as shown in Fig. 8.22. This specific speed is the base speed $\omega_{r\text{-}base}$ at which the flux-weakening control begins. When the operating speed is further increased above the base speed $\omega_{r\text{-}base}$, the voltage-limit ellipse shrinks more, so the operation point A will be outside the ellipse. As shown in Fig. 8.22, at speed $\omega_B (> \omega_{r\text{-}base})$, it can be readily seen that the currents at point A can be no longer regulated because it deviates from the region of controllable currents, i.e., the voltage is insufficient to regulate those currents.

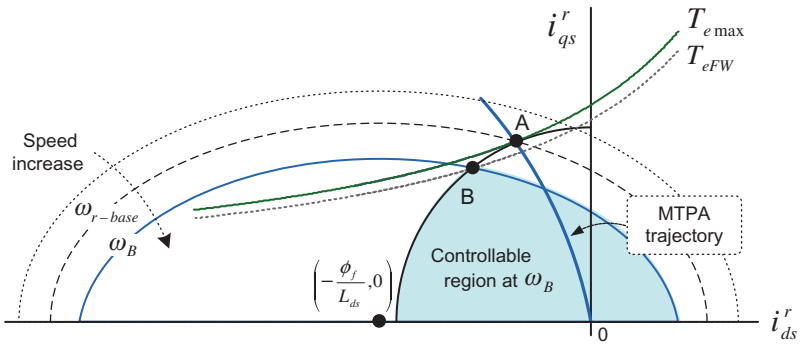



**FIGURE 8.22**

Onset of flux-weakening operation.

Thus the current command should be moved to the controllable operating point. Considering both the voltage-limit and the current-limit conditions, the optimal point for producing the maximum output torque is the intersection (point B) of the circle and the ellipse. The developed torque $T_{eFW}$ at this point is less than the maximum torque $T_{e\text{-}max}$ in the constant torque region.

In such operation, the $d$-axis current increases in the negative direction. This is the flux-weakening control that reduces the effective stator flux linkage. The optimal $d-q$ axes currents for the stator current command $I_s$ given as a torque command are expressed as

$$i^r_{ds} = \frac{L_{ds}\phi_f - \sqrt{(L_{ds}\phi_f)^2 + (L^2_{qs} - L^2_{ds})\left(\phi_f^2 + (L_{qs}I_s)^2 - \left(\frac{V_{s\,max}}{\omega_r}\right)^2\right)}}{(L^2_{qs} - L^2_{ds})} \tag{8.36}$$

$$i^r_{qs} = \sqrt{I^2_{s\,max} - i^{r*2}_{ds}} \tag{8.37}$$

The trajectory of the optimal point moves along the current-limit boundary in a counterclockwise direction as the operating speed increases as shown in Fig. 8.23. Accordingly, the $d$-axis stator current increases in the negative direction while the $q$-axis stator current decreases.

This operation continues until $i^*_{ds} = I_{s\,max}$ and $i^{r*}_{qs} = 0$, at which the operating speed reaches its maximum. Thus we can identify that this type of motor has a *finite maximum speed*. In such a flux-weakening operation, the stator voltage and current of an IPMSM remain constant, resulting in constant power operation. Fig. 8.24 shows the optimal currents in the flux-weakening operation of an IPMSM.

Next, let us take a look at the flux-weakening operation in the case of $\phi_f < L_{ds}I_{s\,max}$. In this case the center of the voltage-limit ellipse is inside the current-limit circle as shown in Fig. 8.25, and the trajectory of the optimal current is somewhat different from the case of $\phi_f > L_{ds}I_{s\,max}$. In the beginning of the flux-weakening operation, the trajectory of the optimal point moves along the

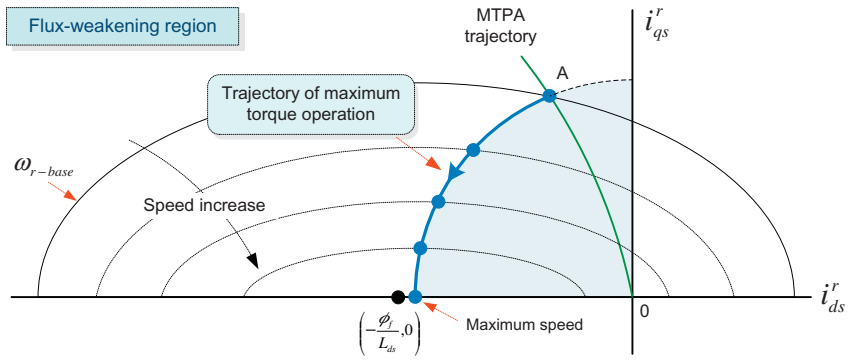



**FIGURE 8.23**

Optimal current vector in the flux-weakening operation ($\phi_f \geq L_{ds} I_{s\ max}$).

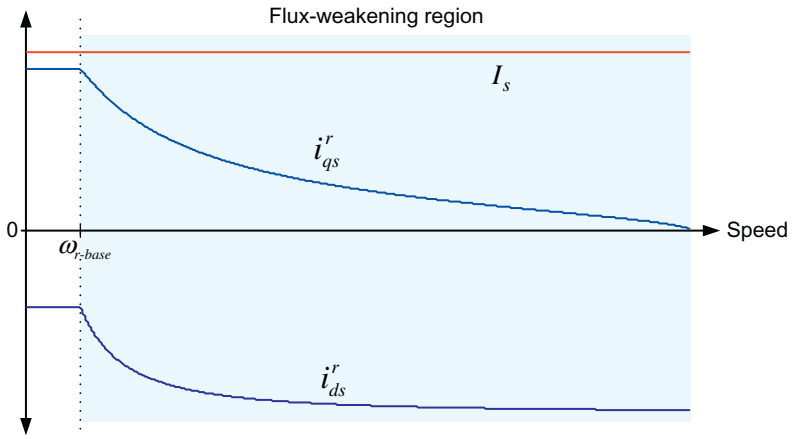



**FIGURE 8.24**

Optimal currents in the flux-weakening operation ($\phi_f > L_{ds} I_{s\ max}$).

current-limit boundary as the speed increases as in the case of $\phi_f > L_{ds} I_{s\ max}$. However, above a certain speed, the voltage-limit ellipse is gradually included in the current-limit circle. This means that the voltage-limit condition is included in the current-limit condition. If the optimal currents for the maximum torque subject to only the voltage-limit condition are included inside the current-limit circle (e.g., point C), then only the voltage-limit is the constraint that should be considered for obtaining the optimal currents. In this case the optimal point should move into the center of the ellipse as the speed increases instead of moving along the current-limit circle as shown in Fig. 8.25. Thus the optimal point is not point D, but point C. This flux-weakening operation is called as the MTPV (the maximum torque per voltage) operation. This operation region corresponds to the field-weakening region II of an induction motor.

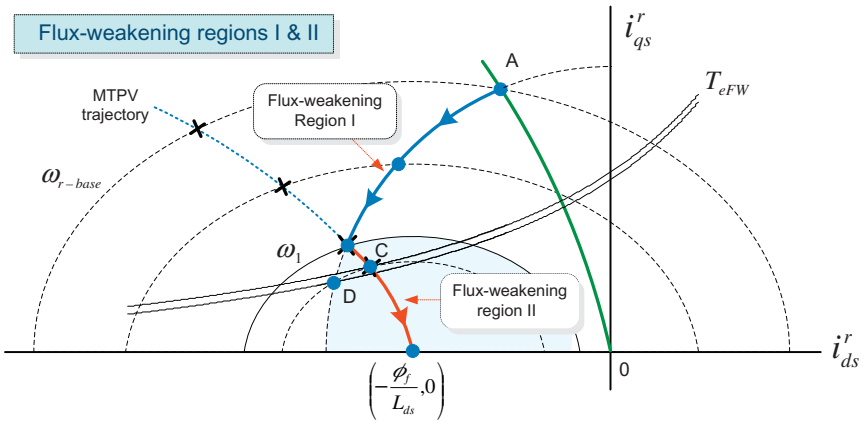



**FIGURE 8.25**

Optimal current trajectory in the flux-weakening region ($\phi_f < L_{ds} I_{s\ max}$)

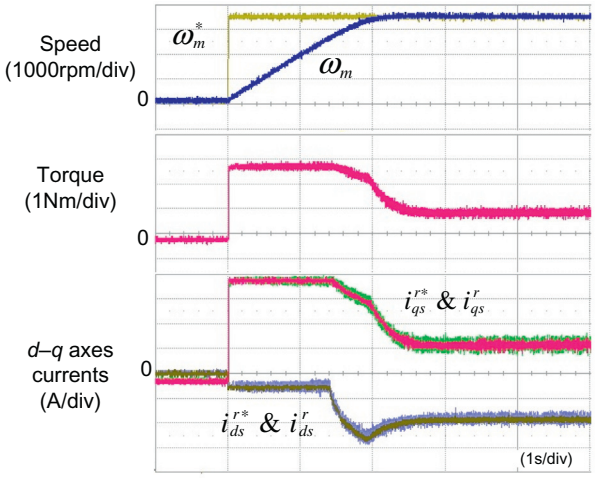



**FIGURE 8.26**

Flux-weakening operation of an 800-W IPMSM.

Fig. 8.26 shows the experimental results on the flux-weakening control for a 800-W, 8-pole IPMSM when the speed command is given as 3500 r/min. For this IPMSM, $\phi_f > L_{ds} I_{s\ max}$ and the base speed is 2500 r/min.

### 8.2.2 HIGH-SPEED OPERATION OF A SURFACE-MOUNTED PERMANENT MAGNET SYNCHRONOUS MOTOR

Unlike IPMSMs, the typical operating range of SPMSMs is the constant torque region. However, the high-speed operation of SPMSMs is often required in

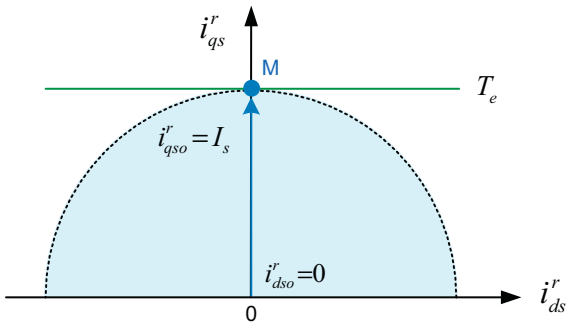



**FIGURE 8.27**

Optimal currents under the current-limit condition for an SPMSM.

several applications such as washing machines. The flux-weakening operation of SPMSMs is almost similar to that of IPMSMs. Now we will study the flux-weakening operation of SPMSMs. Similar to other motors, we will find out the optimal flux-weakening control method that ensures the maximum torque operation under the voltage- and the current-limit conditions.

The current-limit condition of an SPMSM is given as

$$i^{r2}_{ds} + i^{r2}_{qs} \le I^2_{s\ max} \tag{8.38}$$

The current-limit boundary in the $d-q$ axes currents plane can be expressed as a circle whose radius is the maximum stator current $I_{s\ max}$ as shown in Fig. 8.27.

As stated in Section 5.5.1, for the MTPA operation of SPMSMs in the constant torque region, all the available current should be assigned to the $q$-axis stator current $i^r_{qs}$ while making the $d$-axis stator current $i^r_{ds}$ zero. Thus the optimal currents for the MTPA operation of the SPMSM under a given available stator current $I_{s\ max}$ become

$$i^{r*}_{dso} = 0 \tag{8.39}$$

$$i^{r*}_{qso} = I_{s\ max} \tag{8.40}$$

Fig. 8.27 depicts point M of the optimal currents under the current-limit condition. Similar to other motors, the possibility of the operation at this optimal point M depends on the following voltage-limit condition.

$$v^{r2}_{ds} + v^{r2}_{qs} \le V^2_{s\ max} \tag{8.41}$$

For an SPMSM, neglecting the voltage drop of the stator resistance, from Eqs. (6.24) and (6.25), the steady-state $d-q$ axes voltage equations are expressed as

$$v^r_{ds} = -\omega_r L_s i^r_{qs} \tag{8.42}$$

$$v^r_{qs} = \omega_r (L_s i^r_{ds} + \phi_f) \tag{8.43}$$

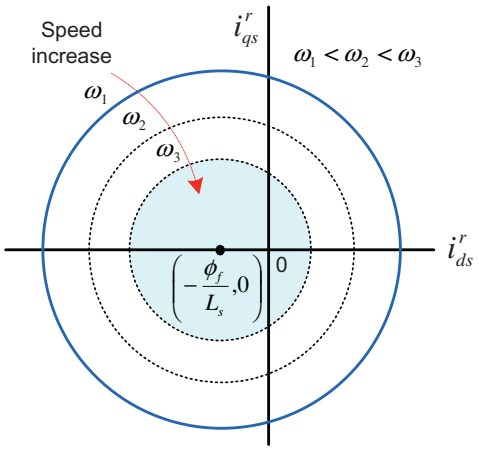



**FIGURE 8.28**

Voltage-limit condition for an SPMSM.

Thus the voltage-limit condition of Eq. (8.41) can be expressed from Eqs. (8.42) and (8.43) as

$$(\omega_r L_s i_{qs}^r)^2 + (\omega_r L_s i_{ds}^r + \omega_r \phi_f)^2 \leq V_{s\,max}^2 \tag{8.44}$$

Unlike an IPMSM, the voltage-limit condition is expressed as a circle with the center $(-\phi_f/L_s, 0)$ in the $d$–$q$ axes currents plane as shown in Fig. 8.28. Under a given maximum stator voltage $V_{s\,max}$, the boundary of this circle becomes smaller as the operating speed increases.

The voltage- and current-limit conditions for a certain speed below the base speed are shown in Fig. 8.29. In this case, the optimal currents for producing the maximum torque (i.e., point M) are inside the voltage-limit circle, so they are controllable.

#### 8.2.2.1 Constant power region ($\omega_e > \omega_{base}$)

The voltage-limit circle dwindles with the increase in the speed. When point M begins to move out of the voltage-limit circle, the operating point should be changed. This indicates that the flux-weakening operation starts and the speed becomes the base speed.

In that case, the optimal point for producing the maximum output torque is the value at the intersection of two circles. From Eqs. (8.38) and (8.44), the optimal currents at this point are given as

$$i_{ds}^{r*} = \frac{\left(\frac{V_{s\,max}}{\omega_r}\right)^2 - \phi_f^2 - (L_s I_{s\,max})^2}{2L_s\phi_f} \tag{8.46}$$

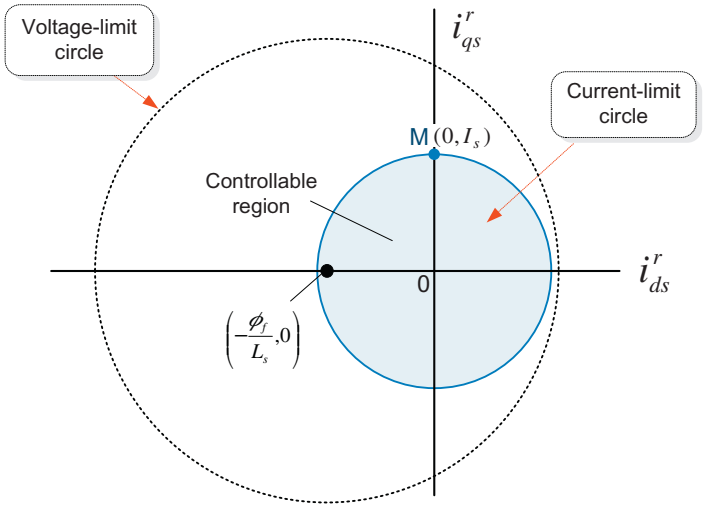



**FIGURE 8.29**

Voltage- and current-limit conditions for an SPMSM.

$$i_{qs}^{r*} = \sqrt{I_{s\,max}^2 - i_{ds}^{r*2}} \tag{8.47}$$

The trajectory of the optimal point moves along the current-limit boundary in a counterclockwise direction as the operating speed increases as shown in Fig. 8.30. Accordingly, the *d*-axis stator current increases in the negative direction while the *q*-axis stator current decreases.

Similar to an IPMSM, the maximum operating speed and the output power characteristic of an SPMSM vary according to the magnitude relationship between the magnet flux $\phi_f$ and the maximum *d*-axis stator flux linkage (i.e., $L_s I_{s\,max}$). In the case of $\phi_f > L_s I_{s\,max}$, the center of the voltage-limit circle is outside the current-limit circle, and there exists a limit on the operating speed (*finite maximum speed motor*). On the other hand, in the case of $\phi_f < L_s I_{s\,max}$, there is no limit on the maximum operating speed theoretically (*infinite maximum speed motor*) and also, there exists a speed range, which corresponds to the field-weakening region II of an induction motor. The optimal *d*-axis current of Eq. (8.46) corresponds to an SPMSM with $\phi_f > L_s I_{s\,max}$. This optimal *d*-axis current can be applied up to the maximum speed. The maximum operating speed is obtained when the *d*-axis current is equal to the stator maximum current, i.e., $i_{ds}^{r*} = I_{s\,max}$. However, in this case, the *q*-axis current becomes zero, so the maximum attainable speed will actually be less than that speed.

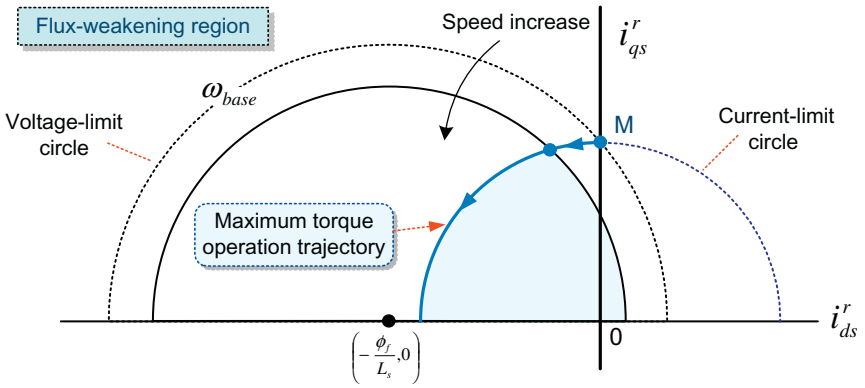



**FIGURE 8.30**

Trajectory of the optimal current vector (in case of $\phi_f > L_s I_{s\ max}$).

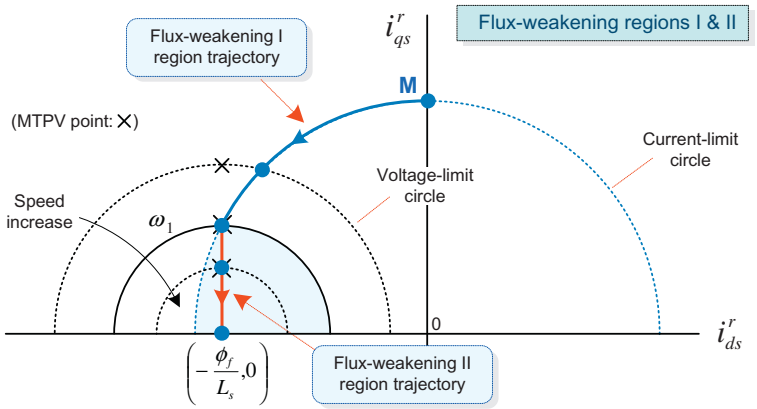



**FIGURE 8.31**

Trajectory of the optimal current vector (in case of $\phi_f < L_s I_{s\ max}$).

Next, we will discuss the case of $\phi_f < L_s I_{s\ max}$. In this case, the trajectory of the optimal current is identical to that in the case of $\phi_f > L_s I_{s\ max}$ in the beginning of the flux-weakening operation. However, if the optimal current for producing the maximum torque subject to only the voltage-limit constraint (the MTPV operation point X) is included inside the current-limit circle as shown in Fig. 8.31, then the MTPV operation needs to be carried out. In this operation, the $d$-axis stator current remains constant, while the $q$-axis stator current reduces as the speed increases.

## REFERENCES

[1] S.-H. Kim, S.K. Sul, Maximum torque control of an induction machine in the field weakening region, IEEE Trans. Ind. Appl. 31 (4) (Jul./Aug. 1995) 787–794.

[2] S.-H. Kim, S.K. Sul, Voltage control strategy for maximum torque operation of an induction machine in the field-weakening region, IEEE Trans. Ind. Electron. 44 (4) (Aug. 1997) 512–518.

[3] J.M. Kim, S.K. Sul, Speed control of interior permanent magnet synchronous motor drive for the flux weakening operation, IEEE Trans. Ind. Appl. 33 (1) (Jan./Feb. 1997) 787–794.

[4] S.R. Macminn, T.M. Jahns, Control techniques for improved high-speed performance of interior PM synchronous motor drives, IEEE Trans. Ind. Appl. 27 (5) (Sep./Oct. 1991) 997–1004.

[5] T.S. Kwon, G.Y. Choi, M.S. Kwak, S.K. Sul, Novel flux-weakening control of an IPMSM for quasi-six-step operation, IEEE Trans. Ind. Appl. 27 (5) (Nov./Dec. 2008) 1722–1731.

[6] W.L. Soong, T.J.E. Miller, Field-weakening performance of brushless synchronous AC motor drives, IEE Proc. Elec. Power Appl. 141 (6) (Nov., 1994) 331–340.

CHAPTER

# 9 Speed estimation and sensorless control of alternating current motors

For the position/speed control of a motor, it is necessary for its speed/position information to be used as a feedback signal for the speed/position control loop. As it can be seen in Chapter 5, for the vector control of alternating current (AC) motors, the information on the rotor position is also necessary. To measure the position/speed of the motor, an analog or a digital position sensor is used. Resolver, synchro, and tacho-generator are well known as analog position sensors. A rotary encoder is the most widely used as the digital position sensor.

In this chapter, we will introduce position sensors used in the motor drive systems and examine the speed estimation method from the position sensor signal. Finally, we will introduce the sensorless control methods of AC motors, which do not use position sensors.

## 9.1 POSITION SENSORS

Besides the position/speed control of a motor, for the vector control of AC motors, a position sensor is needed. In the vector control, a different type of position sensor is used according to the motor used. As discussed in Chapter 5, the absolute position of the rotor (i.e., permanent magnet) is required for the vector control of permanent magnet synchronous motors (PMSMs). Among analog position sensors, a resolver, which can provide information on the absolute position of the rotor, is commonly used for PMSM drives. On the other hand, since the vector control of induction motors does not require the absolute position of the rotor, an incremental encoder is usually used among digital devices.

Now we will explore the resolver and rotary encoder.

### 9.1.1 RESOLVER

A resolver is a type of rotary electrical transformer connected to the rotating shaft. The resolver produces signals that vary sinusoidally as the shaft rotates. It is commonly used for measuring the absolute position of the rotor. Fig. 9.1

Electric Motor Control. DOI: http://dx.doi.org/10.1016/B978-0-12-812138-2.00009-X
© 2017 Elsevier Inc. All rights reserved.


Hesai Exhibit 1030, page 375

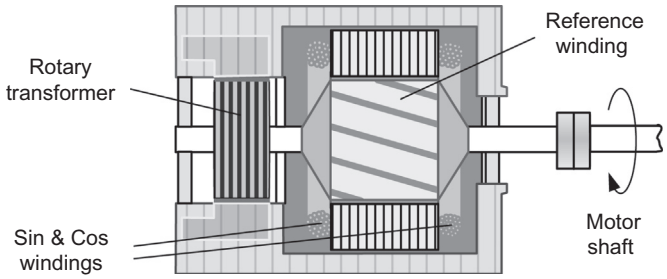



**FIGURE 9.1**

Resolver.

*Source:* http://www.amci.com/tutorials/tutorials-what-is-resolver.asp

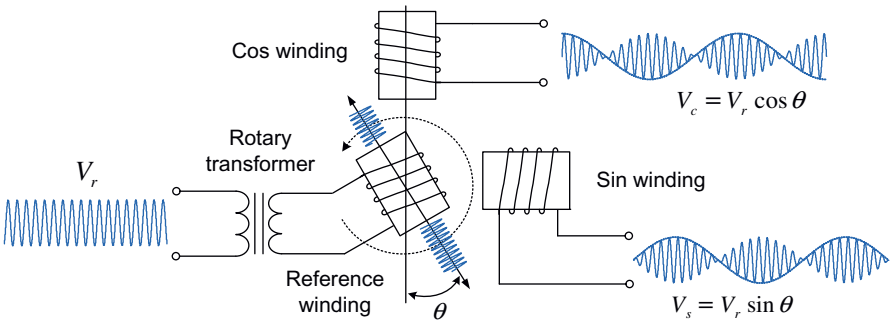



**FIGURE 9.2**

Resolver windings and their signals.

*Source:* http://www.amci.com/tutorials/tutorials-what-is-resolver.asp

depicts the configuration of a resolver, which consists of a stator, a rotor, and a rotary transformer [1].

The primary winding of a resolver, called reference winding, is located in the rotor and is excited through a rotary transformer. The two secondary windings, called SIN and COS Windings, are located in the stator and mechanically displaced 90° from each other. In the resolver operation, a shaft angle $\theta$ can be measured from signals induced in the secondary windings after injecting AC voltage signal into the primary winding as shown in Fig. 9.2.

When the primary winding is excited by an AC voltage $V_r$ through a rotary transformer, voltages in the secondary windings are induced differently depending on the angle $\theta$ of the rotor shaft. The induced voltages vary as sine or cosine of the rotor angle, respectively. From an arctangent function of these signals, we can know the absolute angle $\theta$ of the rotor connected to the shaft as

$$\theta = \tan^{-1}\left(\frac{V_c}{V_S}\right) = \tan^{-1}\left(\frac{V_r \sin\theta}{V_r \cos\theta}\right) \tag{9.1}$$

The resolver usually uses a resolver-to-digital converter to provide resolver excitation and convert angular analogue signals of the resolver into a digital form (a serial binary output or pulses equivalent to an incremental encoder) that can be more easily used by digital controllers. The resolver is a rugged device, which can provide a reliable performance in high temperatures, vibration, and contaminated environments. However, resolvers are costly and require complex excitation and signal processing circuits that are susceptible to noise. In practice, a periodical position error may exist due to amplitude imbalance, inductive harmonics, reference phase shift, excitation signal distortion, and disturbance signals [2]. The position error causes a torque ripple with twice the electrical frequency, and thus should be corrected by a compensation method [3].

### 9.1.2 ROTARY ENCODER

A rotary encoder is a sensor of mechanical motion that generates digital signals in response to the rotational motion of the shaft. There are two main types of rotary encoder according to output forms: the *absolute encoder*, which can provide the absolute value of the rotation angle, and the *incremental encoder*, which provides only the incremental value of the rotation. Incremental encoders are the most widely used for most adjustable motor drive systems because absolute encoders are much more complicated and expensive. There are two sensor types used in encoders to generate digital signals such as magnetic and optical. The latter is more commonly used.

The incremental encoder generates a series of pulses as its shaft moves. These pulses can be used to measure the position, speed, and direction. The resolution of an incremental encoder is frequently described in terms of *pulse per revolution* (PPR), which is the total number of output pulses per complete revolution of the encoder shaft. An encoder with 512 or 1024 PPR is popular in the motor drive systems. The rotary encoders come in two configurations as shown in Fig. 9.3: a *shaft type* that connects the shaft of a rotor with a coupling, and a *hollow type* into which the shaft of a rotor is inserted into.

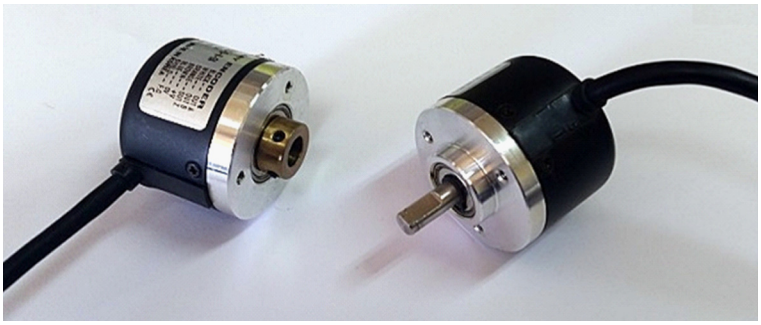


**FIGURE 9.3**

Incremental encoders.

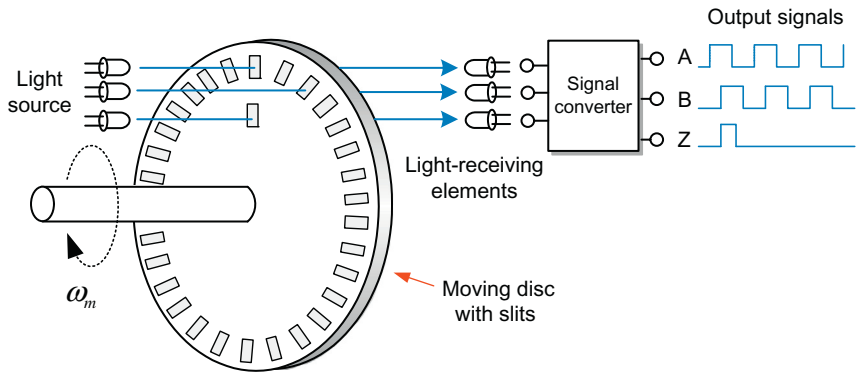



**FIGURE 9.4**

Simple configuration of an optical incremental encoder.

The encoders are a device that is sensitive to the surrounding environment such as temperature, shock, vibration, and contamination. To prevent noise from affecting encoder signals, it is preferable to use a shielded twisted pair cable for encoder output lines. Now we will explore how the incremental encoders work.

### 9.1.2.1 Operating principle of the optical incremental encoder

Fig. 9.4 shows the simple configuration of an optical incremental encoder, which consists of a moving disc mounted to the rotating shaft, light sources (LEDs), and light receivers (phototransistors). The moving disc has the same number of slits as PPR. The light of LEDs passing through the slits on the disc is transmitted to phototransistors, and in turn, is converted to square wave−shaped electric signals.

Commonly, the encoder has three outputs called A, B, and Z. The total number of A and B pulses per revolution is equal to PPR, with which the angular position and speed can be calculated. The A and B pulses are 90° out of phase, which allows the identification of the direction of rotation as shown in Fig. 9.5. For example, when rotating in the forward direction, pulse A is ahead of pulse B. There is another pulse Z known as the *index* or *reference pulse* besides pulses A and B. Pulse Z is generated once per revolution and can be used to set the reference position.

The absolute encoder is used when there is a need of an absolute position of the rotor. Since an absolute encoder generates a unique code (or multibit digital words) for each angular position of the rotor, we can find the actual position directly from the output signals. This output can be in binary code, binary coded decimal code, or gray code. The absolute encoder requires a complicated disc with many slits to generate the output code, resulting in a higher price.

Incremental encoders are the most widely used in motor drive applications. Since the incremental encoder produces a series of pulses as the rotor moves, we cannot measure the rotor speed directly from the encoders. Thus we will next discuss a method to estimate the speed from the output pulses of an encoder.

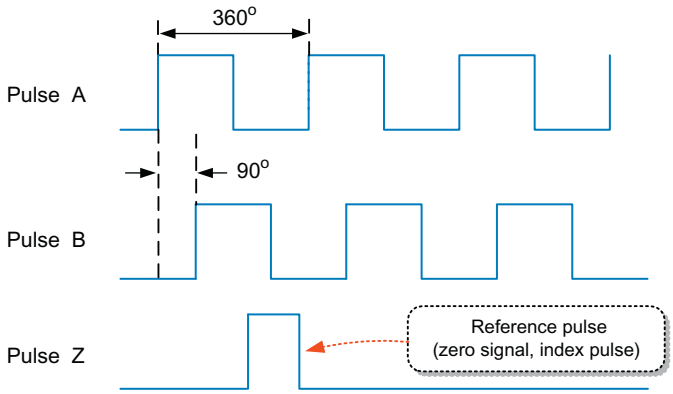



**FIGURE 9.5**

A, B, and Z pulses of incremental encoder.

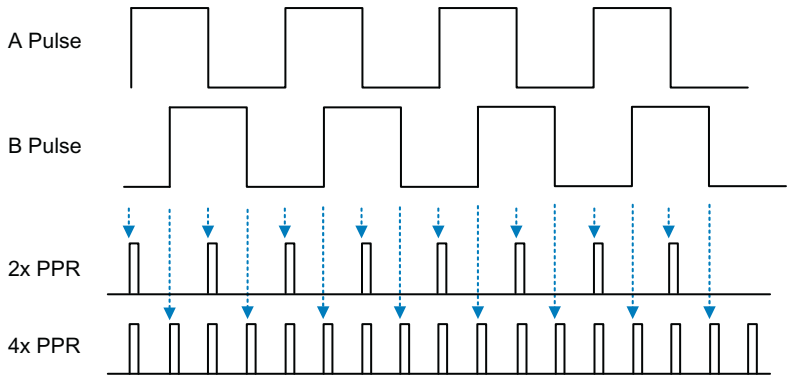



**FIGURE 9.6**

Pulse multiplication.

## 9.2 SPEED ESTIMATION USING AN INCREMENTAL ENCODER

We usually directly use the encoder pulses A or B themselves to calculate the speed. However, when more resolution is needed, we often increase the number of pulses by using a pulse multiplication. For a low-cost encoder with a low PPR, such multiplication can generate pulses more than the original pulse number, and thus results in a higher resolution. Fig. 9.6 shows that the PPR of an encoder can be doubled or quadrupled by counting the rising and falling edges of one or both pulses. In this way a 1000-PPR encoder can act like a 4000-PPR encoder by a 4× multiplication.

Now we will discuss how to calculate the speed of a rotor with pulses of an encoder mounted to the shaft of the rotor.

The angular velocity can be defined as the rate of change of the angular displacement $X$ rad over the time interval $T$ second as

$$\omega_m = \frac{X}{T} \quad (\text{rad/s}) \tag{9.2}$$

Here, the angular displacement $X$ is obtained by counting the pulses produced from the encoder. The angular velocity can be often expressed in terms of revolution per minute unit as

$$N = \left(\frac{60}{2\pi}\right)\frac{X}{T} \quad (\text{r/min}) \tag{9.3}$$

There are three typical methods to obtain the angular velocity from the encoder pulses: M method, T method, and M/T method. In the M method, the angular velocity is obtained by measuring the displacement for a constant time interval. In the T method, the angular velocity is obtained by measuring the time interval for a constant displacement. Now, we will examine these methods in detail as follows.

### 9.2.1 M METHOD

In this method, the angular velocity is obtained by counting the pulses produced from the encoder during the constant sampling time interval $T_c$ as shown in Fig. 9.7.

Assuming that the number of encoder pulses during the sampling time interval $T_c$ is $m$, the angular displacement $X$ over the $T_c$ is given as

$$X = \frac{m}{PPR} \cdot 2\pi \quad (\text{rad}) \tag{9.4}$$

Thus the angular velocity is given from Eqs. (9.2) and (9.3) as

$$\omega_m = \frac{X}{T_c} = \frac{2\pi}{T_c}\frac{m}{PPR} \quad (\text{rad/s}) \tag{9.5}$$

$$N_f = \frac{60}{2\pi} \cdot \omega_m = \frac{60}{T_c} \cdot \frac{m}{PPR} \quad (\text{r/min}) \tag{9.6}$$

For example, if an encoder with a resolution of 1024 PPR produces 2048 pulses for 0.1 s, then the angular velocity can be calculated as

$$N = \frac{60 \cdot 2048}{0.1 \cdot 1024} = 1200 \text{ r/min} \tag{9.7}$$

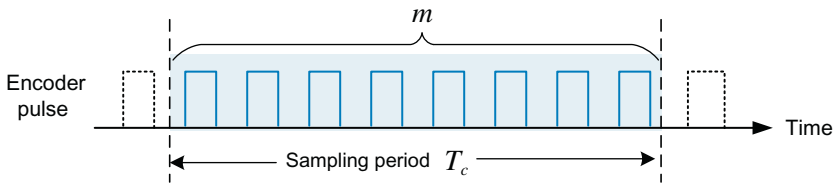



**FIGURE 9.7**

M method.

Since the M method is simple and easy to be implemented, it can be widely used in many applications where high precision in speed is not required. In addition, in this method, since the speed calculation time, i.e., the sampling time of the speed is constant, it is easy to design the speed controller where the speed is periodically controlled. The sampling period is commonly chosen within 1−3 ms according to the required control bandwidth. However, if the sampling time interval is not synchronous with pulses, as it is true in most cases, there exists a speed error. The maximum pulse error is one pulse, resulting in a maximum speed error of $60/(T_c \text{ PPR})$ (r/min). For example, for PPR = 2000, 4× multiplication, and $T_c = 1$ ms, the maximum speed error is $(60/(1 \text{ ms} \times 4 \times 2000)) = 7.5$ r/min. Thus in this case, it is impossible to identify a speed less than 7.5 r/min. In particular, this absolute pulse error of one pulse deteriorates the accuracy of the calculated speed in the low-speed region. It is because, in the low-speed region, the number of pulses becomes low as shown in Fig. 9.8. Thus this method is more effective in the high-speed region where there is are a large number of pulses. To reduce the speed error, it is necessary to use a large PPR or a long sampling time interval. However, a long time interval reduces the speed control bandwidth as we discussed in Chapter 2. Thus it is desirable to use an encoder with a large PPR, but it is an expensive solution.

### 9.2.2 T METHOD

In this method, the angular velocity is obtained by measuring the time interval $T_c$ between two consecutive pulses to eliminate the pulse error as shown in Fig. 9.9.

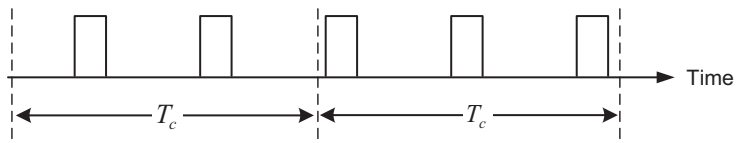



**FIGURE 9.8**

Pulse error in the low-speed region.

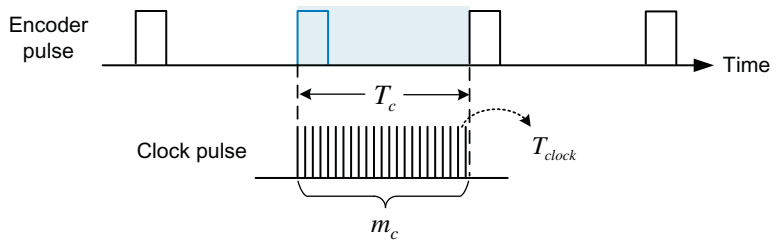



**FIGURE 9.9**

T method.

In the T method, the angular displacement $X$ is always fixed as

$$X = \frac{2\pi}{PPR} \quad \text{(rad)} \tag{9.8}$$

The time interval $T_c$ between two pulses is estimated by counting a reference clock, whose frequency is high enough compared to that of the encoder pulse. Assuming that the period of the reference clock is $T_{clock}$ and the number of the reference clock generated for the time between two pulses is $m_c$, then the time $T_c$ is given as

$$T_c = m_c \cdot T_{clock} \quad \text{(s)} \tag{9.9}$$

Thus the angular velocity is given as

$$\omega_m = \frac{X}{T} = \frac{2\pi}{PPR} \cdot \frac{1}{m_c T_{clock}} \quad \text{(rad/s)} \tag{9.10}$$

$$N = \frac{60}{2\pi} \cdot \omega_m = \frac{60}{PPR} \cdot \frac{60}{m_c \cdot T_{clock}} \quad \text{(r/min)} \tag{9.11}$$

Unlike the M method, the T method has an advantage of enabling an accurate calculation in the low-speed region because it has no pulse omitting. On the other hand, in the high-speed region, the frequency of the reference clock should be high enough to calculate the pulse period accurately. However, when such high-frequency reference clock is used, a clock counter with large bits is required for the operation in the low-speed region. Besides these, the calculation of Eq. (9.11) requires a division, which takes a long calculation time for a digital controller. Moreover, since the speed calculation time $T_c$ varies with the speed, this method is not preferable for use for a speed controller, which carries out the speed control at each constant time interval.

### 9.2.3 M/T METHOD

The M/T method combines the two methods explained previously, which improves the accuracy of the speed calculation. The M/T method is now widely used in many motor drive applications for obtaining the speed information with a high resolution.

In the M/T method, similar to the M method, the encoder pulses are first counted in the constant sampling time interval $T_c$. However, if the sampling time does not synchronize with the last pulse, the extra time $\Delta T$ to the last pulse is additionally measured to eliminate the pulse error by adopting the T method as shown in Fig. 9.10. Thus in this method, the angular velocity can be calculated accurately by measuring the total time $T(= T_c + \Delta T)$ for the encoder pulses $m_1$.

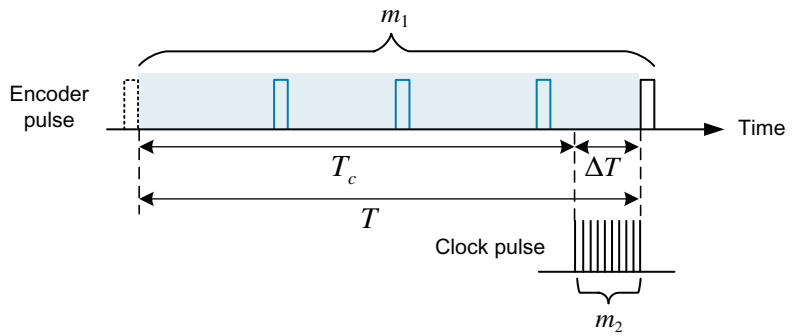



**FIGURE 9.10**

M/T method.

For the number of the encoder pulses $m_1$, the angular displacement $X$ is given as

$$X = \frac{2\pi}{PPR} m_1 \quad \text{(rad)} \tag{9.12}$$

If the period of the reference clock is $T_2$ and counts of the number of the clock pulses is $m_2$, the total duration time for the pulses $m_1$ is given as

$$T = T_c + \Delta T = T_c + T_2 m_2 \quad \text{(s)} \tag{9.13}$$

Then the angular velocity is given as

$$\omega_m = \frac{X}{T} = \frac{2\pi}{PPR} \cdot \frac{m_1}{T_c + m_2 T_2} \quad \text{(rad/s)} \tag{9.14}$$

$$N = \frac{60}{2\pi} \cdot \omega_m = \frac{60}{PPR} \cdot \frac{m_1}{T_c + m_2 T_2} \quad \text{(r/min)} \tag{9.15}$$

The speed calculation based on the M/T method is more accurate than the other two methods, but its implementation is quite difficult. The M/T method has a problem in the very low-speed region. Since, in the very low-speed region, the number of the encoder pulses is too small, the extra time $\Delta T$ may be larger than the sampling time interval $T_c$. Thus the period for the speed calculation can vary with the speed.

The speed estimation methods introduced above cannot inherently estimate the true instantaneous speed, but only a discrete average speed over the sample interval. Since the actual speed within the sampling period interval cannot be identified, the speed control cannot work properly for a system with a long sampling period. In addition, a system with a high bandwidth of speed control may become unstable in the low-speed region, where the speed detection delay time is long. To overcome this problem, we need to estimate the instantaneous speed by using a *position observer* or a *state filter* with the discrete average speed obtained from the encoder pulses [4,5].

## 9.3 SENSORLESS CONTROL OF ALTERNATING CURRENT MOTORS

The vector control of AC motors requires the position of the rotor flux. The knowledge of the rotor position is used for identifying the position of the rotor flux. For this purpose, a position sensor such as an encoder or a resolver is installed at the rotor shaft as shown in Fig. 9.11.

A resolver is usually used for PMSM drives that require an absolute position of the rotor for start-up and vector control. On the other hand, an incremental encoder to measure the angular displacement of the rotor is commonly used for induction motor drives. When an incremental encoder is used for PMSMs, the initial rotor position should be provided [6].

Such position sensors cause several problems. Above all, these sensors increase the cost of the whole motor drive system. These sensors are also sensitive to the surrounding environment. The DC power lines and interface lines for a sensor increase the complexity of the system and are susceptible to noise. This may degrade the system reliability. In addition, the sensor attached to the shaft of a motor increases its size and requires maintenance periodically.

To solve this problem, a control technology without any position sensor, referred as *sensorless control*, has emerged and become an important research subject in the field of AC motor drives. The vector control using a sensor can

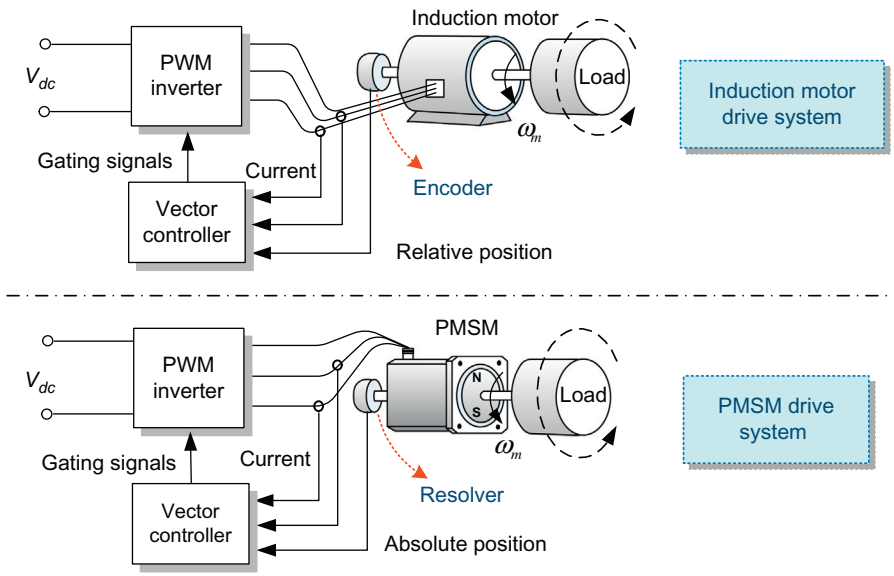



**FIGURE 9.11**

Position sensor for AC motor drive systems.

provide the speed accuracy of $\pm 0.01\%$ and the speed control range of 1:1000. These days, the sensorless vector control can provide a speed accuracy of $\pm 0.5\%$ and a speed control range of 1:150. The performance of the sensorless vector control exceeds that of the scalar control such as the *V/f* control, which has a speed accuracy of $\pm 1 \sim 2\%$. Nowadays, sensorless control techniques to achieve a performance comparable to that of the sensored vector control have been investigated continuously.

Understanding the sensorless control techniques requires a comprehensive knowledge of the motor control that was stated in the previous chapters 4–8. Now we will review briefly the sensorless control techniques of AC motors.

## 9.3.1 TYPES OF SENSORLESS CONTROL

For more than two decades, many efforts have been made to develop a sensorless drive of AC motors. These sensorless techniques are subdivided into two major groups according to their method of deriving the rotor position as shown in Fig. 9.12. One typical group is based on back-electromotive force (EMF) retaining information on the rotor speed [7–17]. The technique of this group is that the rotor position can be obtained through an estimator or observer using mathematical equations of a motor. Another group obtains the rotor position from the characteristics of a motor itself [18–24]. In this technique, a special signal to extract the rotor position-dependent characteristics from a motor is injected into the motor. High-frequency voltage is commonly used as the special signal.

### *9.3.1.1 Sensorless technique using the motor model*

The basic concept of this sensorless technique is to use the back-EMF retaining information on the rotor speed to obtain the rotor flux position [7–17]. This sensorless technique usually uses an estimator or observer to obtain the rotor flux

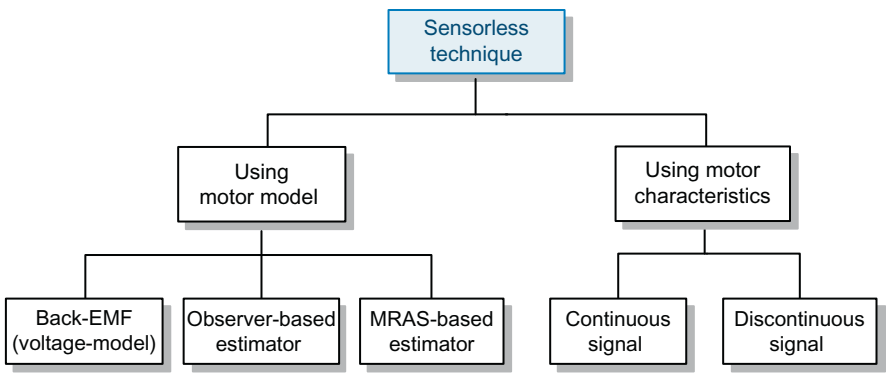



**FIGURE 9.12**

Different types of sensorless control methods.

position or the rotor flux linkage by using mathematical equations of a motor with its measured voltage and current.

We have already seen one example of the sensorless control of an induction motor based on this concept in Chapter 5. In the voltage model of Section 5.3.1, it was seen that the rotor flux angle could be estimated from the rotor flux linkage obtained by using the stator voltage equations. We will now review this process. The stator flux linkages are obtained first by the integral of back-EMFs, and in turn, the rotor flux linkages are estimated from the stator flux linkages as

$$\hat{\lambda}^s_{dqs} = \int (v^s_{dqs} - R_s i^s_{dqs})dt = \int e^s_{dqs}dt \rightarrow \hat{\lambda}^s_{dqr} = \frac{L_r}{L_m}(\hat{\lambda}^s_{dqs} - \sigma L_s i^s_{dqs}) \tag{9.16}$$

From the rotor flux linkages, the rotor flux angle $\hat{\theta}_e$ and the rotor speed $\hat{\omega}_r$ can be estimated as

$$\hat{\theta}_e = \tan^{-1}\left(\frac{\hat{\lambda}^s_{qr}}{\hat{\lambda}^s_{dr}}\right) \tag{9.17}$$

$$\hat{\omega}_e = \frac{d\hat{\theta}_e}{dt} = \frac{d}{dt}\left[\tan^{-1}\left(\frac{\hat{\lambda}^s_{qr}}{\hat{\lambda}^s_{dr}}\right)\right] \tag{9.18}$$

$$\hat{\omega}_r = \hat{\omega}_e - \omega_{sl} \tag{9.19}$$

Likewise, for a PMSM, the rotor flux angle $\hat{\theta}_r$ and the rotor speed $\hat{\omega}_r$ can be estimated by using the stator voltage and the stator flux linkage equations as

$$\begin{aligned}\hat{\lambda}^s_{dqs} &= \int (v^s_{dqs} - R_s i^s_{dqs})dt \\ &= \int e^s_{dqs}dt \quad (e^s_{dqs} = v^s_{dqs} - R_s i^s_{dqs})\end{aligned} \tag{9.20}$$

$$\hat{\theta}_r = \tan^{-1}\left(\frac{\hat{\lambda}^s_{qr}}{\hat{\lambda}^s_{dr}}\right) = \tan^{-1}\left(\frac{\hat{\lambda}^s_{qs} - L_s i^s_{qs}}{\hat{\lambda}^s_{ds} - L_s i^s_{ds}}\right) \tag{9.21}$$

$$\hat{\omega}_r = \frac{d\hat{\theta}_r}{dt} \tag{9.22}$$

As we can see, the sensorless control technique based on the motor model is simple compared to the other methods using the characteristics of a motor and is capable of providing a satisfactory estimating performance in the medium- to high-speed range. However, since it is based on the back-EMF proportional to a rotor speed, its performance is inevitably limited in the low-speed range. A satisfactory performance cannot be obtained 10% below the rated speed. Especially, at zero speed where the back-EMF is equal to zero (or at zero stator frequency for an induction motor), no information on the rotor flux can be acquired, so this technique will fail to control the motor. Therefore this sensorless control technique is not an easy task to improve the performance in the low-speed range and at zero speed.

Hesai Exhibit 1030, page 386

The accuracy of the estimation obtained from the sensorless control technique based on the motor model depends on the accuracy of motor parameters and input values used in the model as well as the accuracy of the model itself. The motor parameters can vary easily according to operating conditions such as winding temperature and flux level. The variation of parameters has influence on the accuracy of the estimation. For example, it can be readily seen that an accurate information on the stator resistance is required to estimate the stator flux linkage accurately from Eq. (9.16) or (9.20). Thus for an accurate sensorless control, an algorithm which provides real-time adaptation for motor parameters is necessary. The input values used in the model such as the current and voltage of the motor should also be measured precisely. Mostly, the motor currents are directly measured by using current sensors. However, since the voltages applied to the motor are generated as a pulse width modulation (PWM) waveform, it is hard to be directly measured. Thus voltage commands or output voltages calculated reversely by the switching pattern of an inverter are commonly used instead. In this case, as stated in Chapter 7, nonlinearity of an inverter due to a voltage drop on the switching devices and the dead time effect should be considered.

As a type of this sensorless control method for induction motors, the model reference adaptive control (MRAC) method, which estimates the rotor speed by comparing outputs of two models that estimate the rotor flux linkage, is a classic example [7,8]. Besides the MRAC, several techniques using the advanced control theory, such as the adaptive speed observer or Kalman filter, have been developed [9,10]. The stable operation region for such sensorless control methods is limited to 1−3 Hz due to insufficient back-EMF information in the low-speed range. However, some researches to further lower the available operating range have been proposed [11].

Several approaches used for induction motors are also adopted for the sensorless control of PMSMs such as a method estimating the rotor position from the flux obtained by an integral of back-EMF [13], a method adopting the MRAC using the error between outputs of two motor models [13,14], and a method using the advanced control theory such as the state observer or Kalman filter [15−17].

#### 9.3.1.2 Sensorless technique using the characteristics of a motor

Sensorless control methods using the motor model mentioned previously cannot inherently avoid performance degradation in the low-speed range and at zero speed due to their dependency on back-EMF. Thus sensorless control methods using a different concept have been researched. These methods derive information on the rotor position from secondary effects of a motor such as eccentricity of a rotor, magnetic saliency, and slot harmonics [18,19]. Since these characteristics appear regardless of the rotor speed, they can be exploited for sensorless control even in the low-speed range and at zero speed.

Most of these sensorless methods exploit spatial magnetic saliency, which indicates the spatial variation of the inductance according to the rotor position

[20–25]. In this case, a special signal is injected into the motor to extract the magnetic saliency. A discontinuous pulse signal or modified PWM signal can be used as the injected signal, but a continuous high-frequency signal of a sinusoidal waveform is mainly used. Voltage rather than current has been mainly used as a type of high-frequency injection signal. The high-frequency injection voltage is added to the output of the current controller. The rotor position can be estimated from the motor's response to the injected voltage signal because the motor's response varies according to the magnetic saliency. The high-frequency signal enables us to estimate the magnetic saliency for a surface-mounted permanent magnet synchronous motor or an induction motor without magnetic saliency on its rotor as well as an interior permanent magnet synchronous motor with magnetic saliency on its rotor.

Fig. 9.13 shows a block diagram of a typical sensorless drive based on the high-frequency signal injection. The sensorless drive system consists of three parts. First one is a high-frequency signal injection part, which injects a special signal continuously to obtain the saliency information of the motor. Another is a signal processing part, which decomposes the current induced by the injected voltage and extracts the rotor position-related value. Finally, there is a position observer part, which estimates the rotor position and speed from the extracted rotor position-related value.

In the high-frequency signal injection, it is known that the voltage signal injection into the *d*-axis of the estimated rotor reference frame can result in a simpler signal processing and a better performance, even though the signal can be injected into any reference frame. The signal processing part often requires low-pass filters to extract the fundamental current and band-pass filters to extract the injected frequency component current from the measured motor current. Time delay by these filters limits the control bandwidth of the sensorless drives. The bandwidth of the speed controller is usually only about several Hertz.

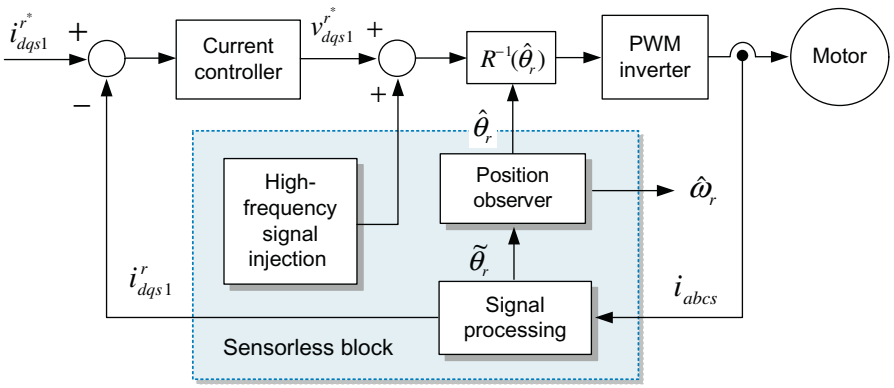



**FIGURE 9.13**

Typical sensorless drive system based on the high-frequency signal injection.

Recently, instead of the conventional sinusoidal-type signal injection, a square wave−type voltage injection has been proposed to eliminate the low-pass filters for the signal processing and enhance the control bandwidth of the sensorless drives. In these methods, the control bandwidth is very close to the value available in sensored drives [22−24].

The sensorless control methods using magnetic saliency and high-frequency voltage injection give a complex signal processing to estimate the rotor position information, requiring a high-performance microprocessor. In addition, the voltage injected to extract the rotor position produces an additional loss, acoustic noise, and torque ripple. Another problem is that there is a voltage shortage in the high-speed operation because an extra voltage is used to generate the injection signal. Thus this leads to a loss of high-speed operation. To overcome this problem, hybrid sensorless methods combing the two techniques mentioned above have been proposed for operation in the entire speed range [25]. The hybrid sensorless methods use the high-frequency signal injection technique at low-speed region and at zero speed but the back-EMF technique at a higher speed region, in which sufficient back-EMF information is available. In the hybrid methods, a transition between the two techniques is an important issue.

## REFERENCES


[1] <http://www.amci.com/tutorials/tutorials-what-is-resolver.asp>.

[2] D.C. Hanselman, Resolver signal requirement for high accuracy resolver-to-digital conversion, IEEE Trans. Ind. Electron. 37 (6) (Dec. 1990) 556−561.

[3] H.-S. Mok, S.-H. Kim, Y.-H. Cho, Torque ripple reduction of PMSM caused by position sensor error for EPS application, Electron. Lett. 43 (11) (2007) 646−647.

[4] H.W. Kim, S.K. Sul, A new motor speed estimator using Kalman filter in low-speed range, IEEE Trans. Ind. Electron. 43 (4) (Aug. 1996) 498−504.

[5] R.D. Lorenz, K.V. Patten, High-resolution velocity estimation for all-digital AC servo drives, IEEE Trans. Ind. Appl. 27 (4) (Aug. 1991) 701−705.

[6] N.-C. Park, Y.-K. Lee, S.-H. Kim, Initial rotor position estimation for an interior permanent-magnet synchronous motor using inductance saturation, Trans. Korean Inst. Power Electron. 16 (4) (Aug. 2011) 374−381.

[7] C. Schauder, Adaptive speed identification for vector control of induction motors without rotational transducers, IEEE Trans. Ind. Appl. 28 (5) (Sep./Oct. 1992) 1054−1061.

[8] T. Ohtani, N. Takada, K. Tanaka, Vector control of induction motor without shaft encoder, IEEE Trans. Ind. Appl. 28 (1) (Jan./Feb., 1992) 157−164.

[9] H. Kubota, K. Matsuse, T. Nakano, DSP-based adaptive flux observer of induction motor, IEEE Trans. Ind. Appl. 29 (2) (Mar./Apr. 1993) 344−348.

[10] Y.R. Kim, S.K. Sul, M.H. Park, Speed sensorless vector control of induction motor using extended Kalman filter, IEEE Trans. Ind. Appl. 30 (5) (Sep./Oct. 1994) 1225−1233.

[11] J. Holtz, Sensorless control of induction motor drives, Proc. IEEE 90 (8) (Aug. 2002) 1359−1394.

[12] R. Wu, G.R. Slemon, A permanent magnet motor drive without a shaft sensor, IEEE Trans. Ind. Appl. 27 (5) (Sep./Oct. 1991) 1005–1011.
[13] N. Matsui, M. Shigyo, Brushless DC motor control without position and speed sensor, IEEE Trans. Ind. Appl. 28 (1) (1992) 120–127.
[14] N. Matsui, T. Takeshita, K. Yasuda, A new sensorless drive of brushless DC motor, in: Proc. 1992 Int. Conf. IECON, 1992, pp. 430–435.
[15] L.A. Jones, J.H. Lang, A state observer for the permanent-magnet synchronous motor, IEEE Trans. Ind. Electron. 36 (3) (1989) 374–382.
[16] Z. Chen, M. Tomita, S. Doki, S. Okuma, An extended electromotive force model for sensorless control of interior permanent magnet synchronous motors, IEEE Trans. Ind. Appl. 38 (2) (2003) 288–295.
[17] S. Bolognani, R. Oboe, M. Zigliotto, Sensorless full-digital PMSM drive with EMF estimation of speed and rotor position, IEEE Trans. Ind. Electron. 46 (2) (1999) 240–247.
[18] R. Blasco-Gimenez, G.M. Asher, M. Sumner, K.J. Bradley, Performance of FFT-rotor slot harmonic speed detector for sensorless induction motor drives, IEE Proc. Elect. Power Appl. 143 (3) (May 1996) 258–268.
[19] M. Schroedl, Sensorless control of AC machines at low speed and standstill based on "INFORM" method, in: Conf. Rec. IEEE IAS Annu. Meeting, 1996, pp. 270–277.
[20] J.-I. Ha, S.-K. Sul, Sensorless field-orientation control of an induction, IEEE Trans. Ind. Appl. 35 (1) (Jan./Feb. 1999) 45–51.
[21] J. Holtz, Sensorless control of induction machines-with or without signal injection?, IEEE Trans. Ind. Electron. 53 (1) (2006) 7–30.
[22] Y.-D. Yoon, S.-K. Sul, S. Morimoto, K. Ide, High-bandwidth sensorless algorithm for AC machines based on square-wave-type voltage injection, IEEE Trans. Ind. Appl. 47 (3) (2011) 1361–1370.
[23] S.-M. Kim, J.-I. Ha, S.-K. Sul, PWM switching frequency signal injection sensorless method in IPMSM, IEEE Trans. Ind. Appl. 48 (5) (2012) 1576–1586.
[24] N. Park, S.-H. Kim, A simple sensorless algorithm for IPMSMs based on high-frequency voltage injection method, IET Elect. Power Appl. 8 (2) (2014) 68–75.
[25] K. Ide, J.-I. Ha, M. Sawamura, A hybrid speed estimator of flux observer for induction motor drives, IEEE Trans. Ind. Electron. 53 (1) (2006) 130–137.

CHAPTER

# Brushless direct current motors

# 10

As explained in Chapter 2, direct current (DC) motors need mechanical commutation devices consisting of brushes and commutators that change the direction of the current of conductors to produce an average torque for continuous rotation as shown in Fig. 10.1. However, this mechanical commutation causes an electromagnetic and acoustic noise. The commutators and brushes also need a periodical maintenance and replacement due to wear-out and flashover. Small DC motors with a radius of $\phi 25-\phi 34$ can operate about 1000 hours, whereas ones with a radius of $\phi 37-\phi 60$ can operate about 2000 hours. Specially designed DC motors are capable of operating about 3000 hours.

DC motors have been widely used for speed or position control applications because of their control simplicity when compared with alternating current (AC) motors. However, since they require periodic maintenance of brushes and commutators, their utilization has been reduced in many motor drive applications, which require continuous running and enhanced system reliability.

To overcome this problem of DC motors, a motor called *brushless direct current (BLDC) motor* was developed in 1962 [1]. This motor has similar electrical characteristics to a DC motor, but it has an enhanced reliability by replacing mechanical commutation with electronic commutation. To implement the electronic commutation, BLDC motors use sensors and driving circuits. The sensors detect the position of magnets on the rotor. By using the detected magnet position, the driving circuits excite a specific winding for continuous rotation.

In BLDC motors, to eliminate the brushes of DC motors, the armature windings are placed on the stator side and the magnets are placed on the rotor side. As a result, BLDC motors have a different configuration from that of DC motors. Since there is a degree of freedom in the motor configuration when designing to eliminate brushes, various BLDC motor designs to fit a wide application needs such as a smaller or thinner configuration are possible. The BLDC motors have many merits such as high efficiency, high-power density, high torque-to-inertia ratio, high-speed operation capability, simple drive method, and low cost. Thus, nowadays, they are widely used for cost-effective solution in many small and medium motor drive applications such as home appliances, industrial, office products, and light vehicles.

In this chapter, we will discuss the configuration, driving principle, mathematical model, speed and current control, and sensorless techniques of BLDC motors.

**Electric Motor Control. DOI:** http://dx.doi.org/10.1016/B978-0-12-812138-2.00010-6
© 2017 Elsevier Inc. All rights reserved.



Hesai Exhibit 1030, page 391

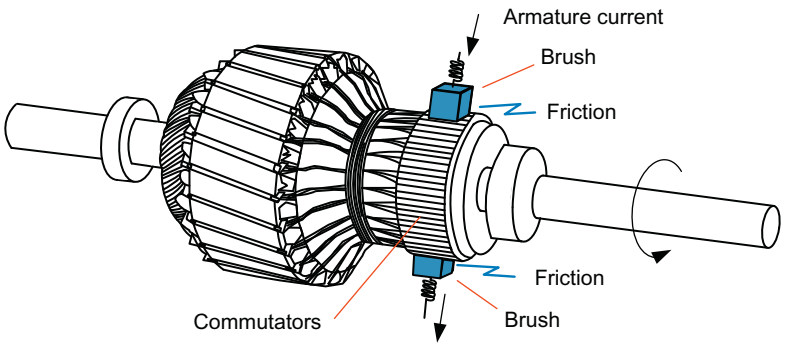



**FIGURE 10.1**

Mechanical commutation devices of a DC motor.

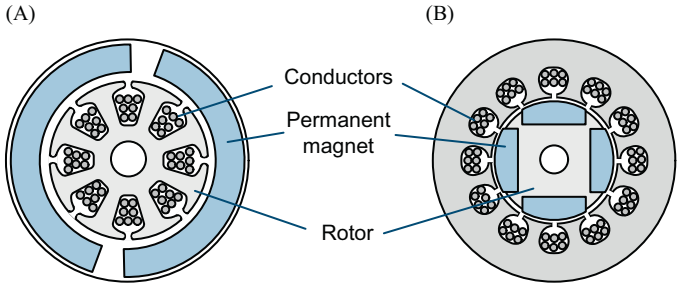



**FIGURE 10.2**

Configurations of (A) DC motor and (B) BLDC motor.

## 10.1 CONFIGURATION OF BRUSHLESS DIRECT CURRENT MOTORS

### 10.1.1 COMPARISON BETWEEN BRUSHLESS DIRECT CURRENT MOTORS AND DIRECT CURRENT MOTORS

BLDC motors do not have the crucial weakness of DC motors because the function of brushes and commutators is replaced with semiconductor switches operating based on the information from the rotor position. As a result of this replacement, the configuration of a BLDC motor becomes different from that of a DC motor, but similar to the configuration of a permanent magnet synchronous motor (PMSM). As shown in Fig. 10.2B, the BLDC motor has a configuration in which the windings are placed on the stator side and the magnets on the rotor side. This results in the reversed configuration of a DC motor as shown in Fig. 10.2A. Instead, its configuration resembles that of a PMSM, shown in Fig. 4.8.

However, similar to the current flowing in armature windings of a DC motor, the current flowing in the windings of a BLDC motor is a quasi-square waveform.

Such configuration of BLDC motors has the following merits over DC motors. Compared to the heavy rotor of DC motors consisting of many conductors, BLDC motors have a low inertia rotor. Thus BLDC motors can provide a rapid speed response. Moreover, windings placed on the stator side can easily dissipate heat, allowing BLDC motors to have a better attainable peak torque capability compared to DC motors whose maximum current is limited to avoid the demagnetization of magnets. In addition, BLDC motors can operate at a higher speed because of nonmechanical commutation devices.

### 10.1.2 COMPARISON BETWEEN BRUSHLESS DIRECT CURRENT MOTORS AND PERMANENT MAGNET SYNCHRONOUS MOTORS

Due to their structural similarity, BLDC motors are often confused with PMSMs. Commonly, BLDC motors can be distinguished from PMSMs by their shape of back-electromotive force (back-EMF). A BLDC motor is designed to develop a trapezoidal back-EMF waveform as shown in Fig. 10.3A. Thus the amplitude of the magnetic flux density generated by the rotor magnets remains constant along the air gap. This can be achieved by using magnets with parallel magnetization.

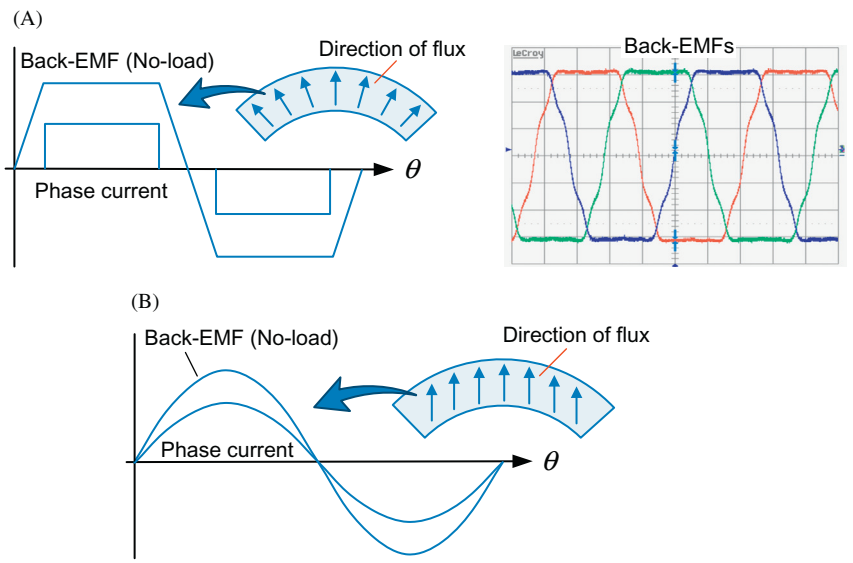



**FIGURE 10.3**

Comparison between (A) BLDC motors and (B) PMSMs.

When a BLDC motor with a trapezoidal back-EMF waveform is fed with a rectangular stator current, a constant torque can be developed. On the other hand, a PMSM is a type of AC motor with a sinusoidal back-EMF waveform, and thus its current should be a sinusoidal waveform for constant torque generation as shown in Fig. 10.3B.

A sinusoidal back-EMF waveform requires the magnetic flux density generated by the rotor magnets to be distributed sinusoidally along the air gap [2]. A PMSM is often referred to as *BLAC motor*, in contrast to BLDC motors.

Power density of a BLDC motor with a trapezoidal back-EMF waveform is 15% higher than that of a PMSM [3]. This is because the trapezoidal waveform has a higher fundamental component than the sinusoidal waveform, even though they have the same peak value. Besides the back-EMF waveform, there are several differences between BLDC motors and PMSMs. The comparison is listed in Table 10.1.

As shown in Fig. 10.4, a BLDC motor commonly uses concentrated stator windings, and quasi-square waveform current flows into them. In contrast, a PMSM usually uses distributed stator windings, into which the sinusoidal waveform current flows as shown in Chapter 3. However, recently, PMSMs often use concentrated windings due to their short end windings and simple structure suitable for automated manufacturing.

There is a clear difference in drive methods for these two motors. In the excitation of a three-phase BLDC motor, the phase currents flow only in two of the three-phase windings at a time and thus, each switch of the inverter always operates for a 120° conduction interval per fundamental operating cycle. By contrast, as described in Chapter 7, in a three-phase PMSM, the phase currents flow in all three-phase windings at a time and thus, each switch of the inverter always operates for a 180° conduction interval per fundamental operating cycle.

**Table 10.1** Comparison Between BLDC Motors and PMSMs

| | BLDC Motor | PMSM |
|---|---|---|
| Back-EMF | Trapezoidal waveform | Sinusoidal waveform |
| Stator winding | Concentrated winding | Distributed winding |
| Stator current | Quasi-square waveform | Sinusoidal waveform |
| Driving circuit | Inverter (120° conduction) | Three-phase inverter (180° conduction) |
| Drive method | Simple, using low-cost Hall effect sensors | Complex (using high-resolution position sensor such as an encoder or a resolver) |
| Torque ripple | Significant torque ripple | Nearly constant torque |
| System cost | Low cost | High cost |

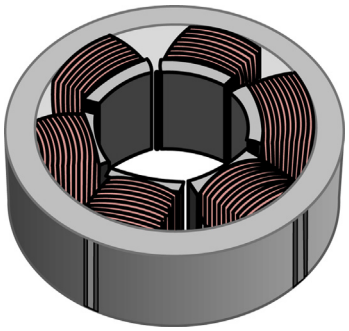


**FIGURE 10.4**

Concentrated stator windings of BLDC motors.

The BLDC motor drive is simple and inexpensive compared with the PMSM drive, which requires a complex method of the vector control as described in Chapter 5. However, the BLDC motors have a significant torque ripple during the phase commutation of changing an active switch, which will be explained later.

### 10.1.3 CONSTRUCTION OF BRUSHLESS DIRECT CURRENT MOTORS

BLDC motors can be categorized according to their number of stator windings: single-phase, two-phase, three-phase, and multi-phase.

Single-phase BLDC motors are widely used for appliances and small machines due to their simple structure, simple driving circuit, and low cost. However, such motors can rotate only in one direction. Furthermore, since they have a detent point where there is no starting torque, a motor design including an ancillary part is necessary for start-up. A reluctance torque is usually used as the starting torque, resulting in a large cogging torque. Single-phase BLDC motors are beneficial to small power applications below 10 W such as fans and blowers that require a low starting torque.

Multi-phase BLDC motors above four-phase can be mainly applied to aerospace and military applications requiring high reliability due to increased power density and fault-tolerance capability. Three-phase BLDC motors are the most widely used and our discussion will be limited to these motors in this book.

There are two BLDC motor designs which are classified in terms of magnetic flux direction: *radial-flux type*, where the flux from the rotor magnet crosses the air gap in a radial direction and *axial-flux type*, where the flux crosses the air gap in an axial direction as shown in Fig. 10.5.

Traditionally the radial-flux motors have been used almost exclusively. This type of motor can be either an *inner rotor type* or an *outer rotor type* as shown in Fig. 10.5A and B. As the most common type, the inner rotor design has an advantage of higher heat dissipating capacity, high torque-to-inertia ratio, and lower rotor inertia. Its common application is servo drives requiring a quick dynamic response.

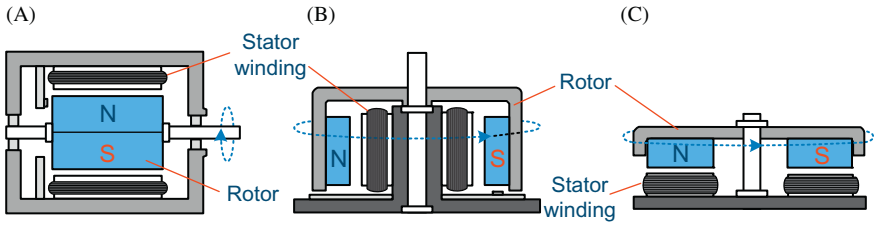



**FIGURE 10.5**

Classification of BLDC motors. (A) Radial-flux (inner rotor), (B) radial-flux (outer rotor), and (C) axial-flux.

Since the rotor is cylindrical in shape with a shaft on which the bearings are mounted, this type of motor can produce less vibration and acoustic noise. Outer rotor motors shown in Fig. 10.5B, in which the rotor magnets rotate around the stator windings located in the iron core of the motor, have relatively high rotor inertia. Thus this motor is favorable for systems requiring constant speed operation. The magnets affixed inside the yoke are beneficial to high-speed operation. The outer rotor motor can use more magnetic material than the inner rotor device, which means it is capable of more flux even though lower energy product magnets are used. These days, this type of motor is increasingly being used in many applications such as computer disk drives, cooling fans, and washing machines.

In the axial-flux motors shown in Fig. 10.5C, a disc rotor with magnets whose flux is in an axial direction rotates facing the stator. Permanent magnets are glued to the surface of the rotor. In this design topology small motors often have coreless stator windings mounted to a nonmagnetic substrate or slotless stator windings mounted to an iron core without slots. The primary advantage of such a technology is that it has a very low ripple torque and acoustic noise since the cogging torque associated with typical iron core motors can be eliminated due to no variations in reluctance. Their relatively high rotor inertia is favorable to constant speed operation. However, due to increased effective air gap, the available flux is somewhat low. Common applications are VCR and CD player drives. This axial-flux motor with a slimmer structure of shorter axial length is very suitable for applications in which the axial length of the motor is the limiting design parameter, or the motor is directly coupled to the driven load. Such applications include electrical vehicles in-wheel motors and elevator motors.

## 10.2 DRIVING PRINCIPLE OF BRUSHLESS DIRECT CURRENT MOTORS

The basic driving principle of the BLDC motor is to change the phase windings, which should be excited according to the position of permanent magnet on the

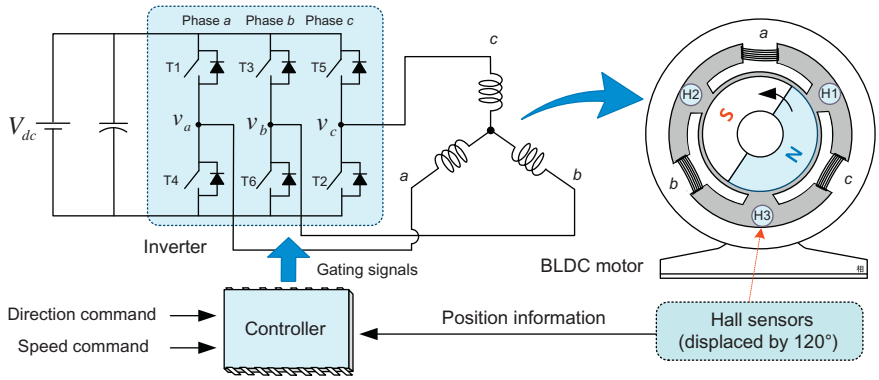



**FIGURE 10.6**

BLDC motor drive system.

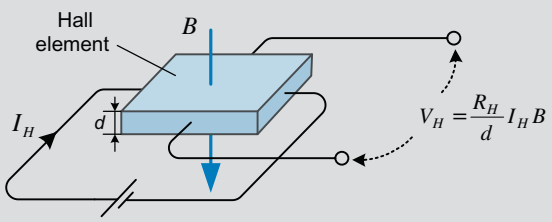
rotor for producing a continuous torque. To implement this function, information on the rotor magnet position is indispensable. The position sensing is commonly achieved with Hall effect sensors.

A two-pole three-phase Y-connected BLDC motor drive system is shown in Fig. 10.6. Three Hall effect sensors are displaced from each other by 120 electrical degrees on the stator to detect the magnetic field flux produced from the rotor magnets. Three output signals of Hall effect sensors enable us to recognize the rotor position divided into six different sections. Accordingly, a basic drive (often called *six-step drive*) to complete one electrical cycle consists of six different sections.

## HALL EFFECT SENSOR

The Hall effect sensor is a device that can detect magnetic field by making use of the Hall effect on the semiconductor material. As shown in the following figure, when a current $I_H$ is flowing through the plate of semiconductor material (called Hall element) and a magnetic field density $B$ passes through the plate, a voltage $V_H$ is generated in response to the magnetic field by the Hall effect as

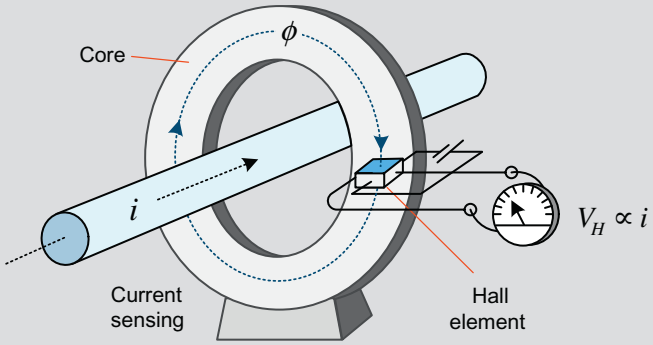
$$V_H = \frac{R_H}{d} I_H B \text{ (V)} \quad (R_H\text{: Hall constant}, d\text{: width of an element})$$




(*Continued*)

## HALL EFFECT SENSOR (CONTINUED)

From measuring the voltage $V_H$, the position and polarity of a magnetic field can be detected. Thus the Hall effect sensors are used to detect the rotor position of permanent magnet motors such as BLDC motors and PMSMs. They are also used for current sensors as shown in the following figure. From measuring the output voltage of the Hall effect sensor, the magnitude and the direction of the current, which produces the magnetic field, can be detected.




The switching sequence for the six-step drive is illustrated in Fig. 10.7. In the BLDC motor drive, only two of the three-phase windings are excited, while the other winding is left unexcited. This is the difference from the inverter drive method for AC motors, which is mentioned in Chapter 7. Rotor position feedback signals can be used to determine which two of the three-phase windings should be excited to produce the continuous torque at each instant. As a driving circuit, a three-phase inverter is used to flow the current into the required two-phase windings. In the inverter for a BLDCM drive as shown in Fig. 10.7, switching devices of only two phases work at any given instant. Accordingly, each switching device has a 120° conduction interval. In the six-step drive, a changeover of an active switch is done to the switch of the other phase, and thus a dead time is not required for short-circuit protection in the inverter.

Fig. 10.8 illustrates Hall effect sensor signals ($H_1$, $H_2$, $H_3$) with respect to back-EMFs of stator windings in the six-step drive as shown in Fig. 10.7, and the relationship between the sensor signals and the phase currents. Here, assume that each sensor outputs a digital high level for the north pole, whereas it outputs a low level for the south pole. From the sensor signals, the excited phase winding, i.e., an active phase winding, should be changed every 60 electrical degrees of rotation for producing a continuous torque. The transition of an active phase winding is called *commutation*. For the reverse rotation, the switching sequence with respect to Hall effect sensor signals should be altered.

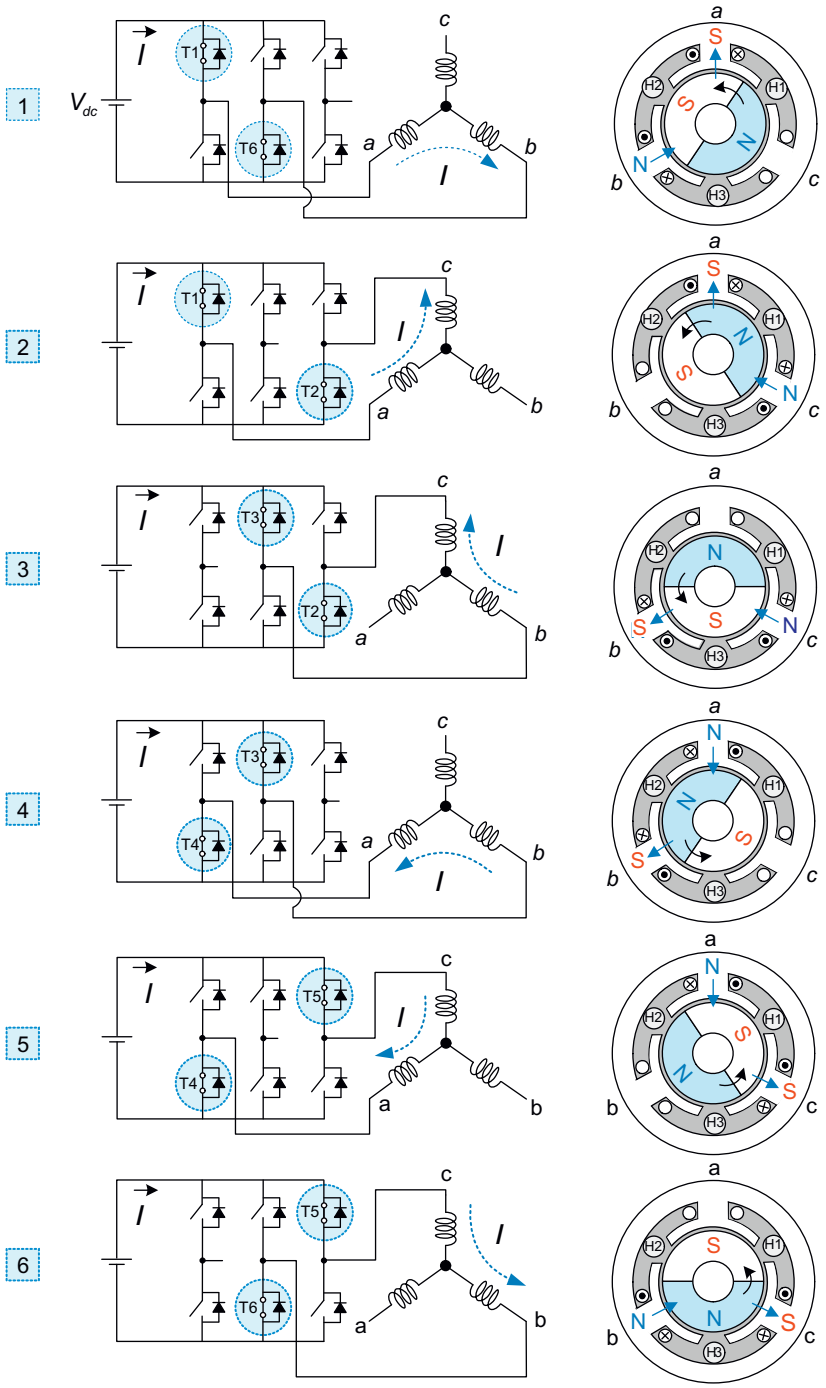



**FIGURE 10.7**

Switching sequence for two-pole three-phase BLDC motor.

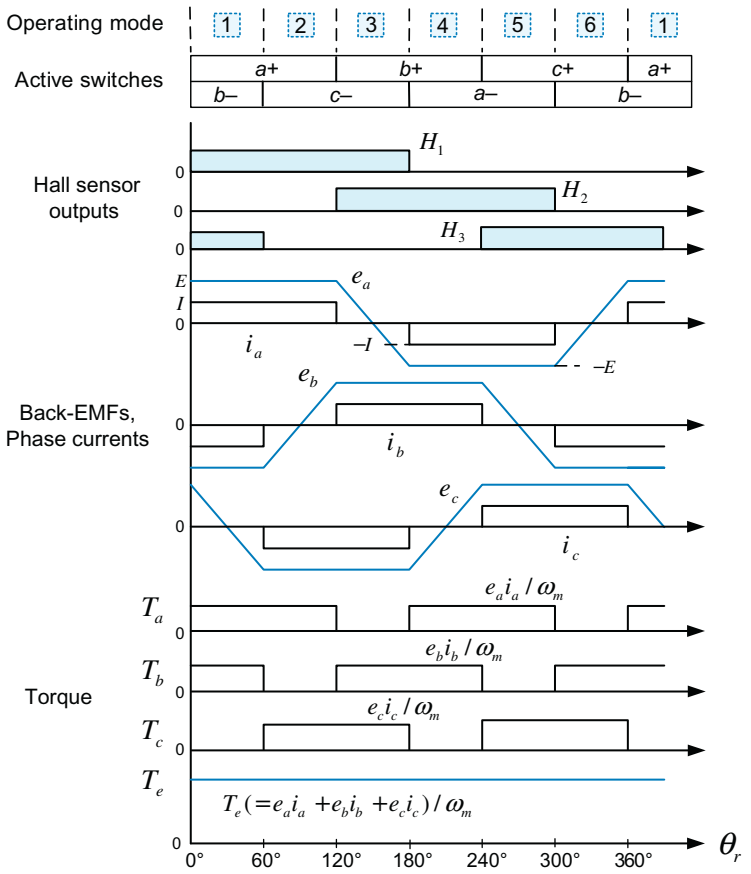



**FIGURE 10.8**

Driving principle of three-phase BLDC motor.

## 10.3 MODELING OF BRUSHLESS DIRECT CURRENT MOTORS

In this section, we will derive the mathematical model of a three-phase BLDC motor [3]. The model of a BLDC motor is similar to that of a PMSM due to their structural similarity.

### 10.3.1 VOLTAGE EQUATIONS

Let us consider a two-pole three-phase BLDC motor as shown in Fig. 10.9. Similar to AC motors examined in Chapter 4, the voltage equation for the stator windings of a BLDC motor can be expressed as

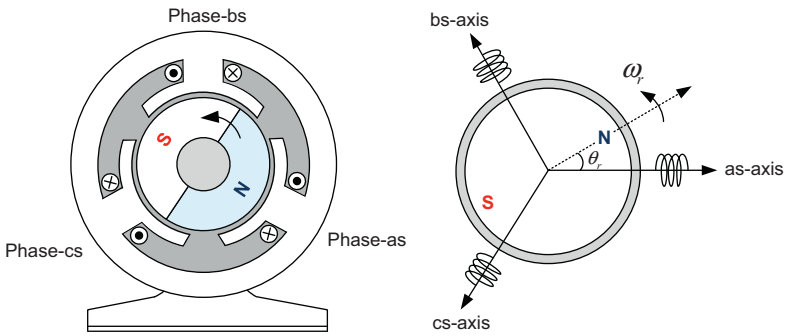



**FIGURE 10.9**

Windings of a two-pole three-phase BLDC motor.

$$\boldsymbol{v}_{abcs} = \boldsymbol{R}_s \boldsymbol{i}_{abcs} + \frac{d\boldsymbol{\lambda}_{abcs}}{dt} \tag{10.1}$$

where the stator voltage $\boldsymbol{v}_{abcs} = [v_{as} v_{bs} v_{cs}]^T$, the stator current $\boldsymbol{i}_{abcs} = [i_{as} i_{bs} i_{cs}]^T$, the stator flux linkage $\boldsymbol{\lambda}_{abcs} = [\lambda_{as} \lambda_{bs} \lambda_{cs}]^T$, and the stator resistance $\boldsymbol{R}_s = \begin{bmatrix} R_s & 0 & 0 \\ 0 & R_s & 0 \\ 0 & 0 & R_s \end{bmatrix}$.

The flux linkage $\boldsymbol{\lambda}_{abcs}$ of the stator windings consists of $\boldsymbol{\lambda}_{abcs(s)}$ due to the stator currents $\boldsymbol{i}_{abcs}$ and $\boldsymbol{\lambda}_{abcs(f)}$ due to the permanent magnet as

$$\boldsymbol{\lambda}_{abcs} = \boldsymbol{\lambda}_{abcs(s)} + \boldsymbol{\lambda}_{abcs(f)} \tag{10.2}$$

Substituting Eq. (10.2) into Eq. (10.1) gives the following stator voltage equation.

$$\boldsymbol{v}_{abcs} = \boldsymbol{R}_s \boldsymbol{i}_{abcs} + \frac{d\boldsymbol{\lambda}_{abcs}}{dt} = \boldsymbol{R}_s \boldsymbol{i}_{abcs} + \frac{d\boldsymbol{\lambda}_{abc(s)}}{dt} + \boldsymbol{e}_{abcs} \tag{10.3}$$

where the back-EMF due to the magnet flux is expressed as $\boldsymbol{e}_{abcs} = d\boldsymbol{\lambda}_{abc(f)}/dt$ and is also given as

$$\boldsymbol{e}_{abcs} = \begin{bmatrix} e_{as} \\ e_{bs} \\ e_{ac} \end{bmatrix} = \omega_m \begin{bmatrix} \lambda_{asf} \\ \lambda_{bsf} \\ \lambda_{csf} \end{bmatrix} = \omega_m \lambda_f \begin{bmatrix} f(\theta_r) \\ f(\theta_r - 120^\circ) \\ f(\theta_r - 240^\circ) \end{bmatrix} \tag{10.4}$$

where $\lambda_f (= N\phi_f)$ is the amount of the magnet flux $\phi_f$ linking $N$ turns of the stator windings, $f(\theta_r)$ is a unit function representing the waveform of the back-EMF and $\theta_r$ is the rotor position.

The unit function for the trapezoidal back-EMF waveform of a BLDC motor can be expressed as

$$f(\theta_r)=\begin{cases}6\theta_r/\pi & (0\le\theta_r<\pi/6)\\ 1 & (0\le\theta_r<\pi/6)\\ -6\theta_r/\pi & (0\le\theta_r<\pi/6)\\ -1 & (0\le\theta_r<\pi/6)\\ 6\theta_r/\pi-12 & (0\le\theta_r<\pi/6)\end{cases} \tag{10.5}$$

The stator flux linkage $\boldsymbol{\lambda}_{abcs(s)}$ due to the stator currents is given by

$$\boldsymbol{\lambda}_{abcs(s)}=\boldsymbol{L}_s\boldsymbol{i}_{abcs}=\begin{bmatrix}L_{aa} & L_{ab} & L_{ac}\\ L_{ba} & L_{bb} & L_{bc}\\ L_{ca} & L_{cb} & L_{cc}\end{bmatrix}\begin{bmatrix}i_{as}\\ i_{bs}\\ i_{cs}\end{bmatrix} \tag{10.6}$$

As can be seen in Section 4.1.1, for symmetry three-phase windings, the self-inductances are all the same and the mutual-inductances are all the same as in the following

$$L_{aa}=L_{bb}=L_{cc}=L_s=L_{ls}+L_m \tag{10.7}$$

$$L_{ab}=L_{ac}=L_{ba}=L_{bc}=L_{ca}=L_{cb}=-\frac{1}{2}L_m=M \tag{10.8}$$

where $L_{\alpha\beta}(=\lambda/i_\beta)$ expresses the winding inductance, which is the ratio of the flux linkage $\lambda$ of the winding $\alpha$ to the current $i_\beta$ that produces the flux. Here, the values of leakage inductance $L_{ls}$ and magnetizing inductance $L_m$ are the same as those of a PMSM described in Chapter 4.

From Eqs. (10.6)–(10.8), the stator voltage equation is rewritten as

$$\boldsymbol{v}_{abcs}=\boldsymbol{R}_s\boldsymbol{i}_{abcs}+\boldsymbol{L}_{abcs}\frac{d\boldsymbol{i}_{abc(s)}}{dt}+\boldsymbol{e}_{abcs} \tag{10.9}$$

$$\begin{bmatrix}v_{as}\\ v_{bs}\\ v_{cs}\end{bmatrix}=\begin{bmatrix}R_s & 0 & 0\\ 0 & R_s & 0\\ 0 & 0 & R_s\end{bmatrix}\begin{bmatrix}i_{as}\\ i_{bs}\\ i_{cs}\end{bmatrix}+\begin{bmatrix}L_s & M & M\\ M & L_s & M\\ M & M & L_s\end{bmatrix}\frac{d}{dt}\begin{bmatrix}i_{as}\\ i_{bs}\\ i_{cs}\end{bmatrix}+\begin{bmatrix}e_{as}\\ e_{bs}\\ e_{cs}\end{bmatrix} \tag{10.10}$$

here, since $i_{as}+i_{bs}+i_{cs}=0$, the mid-term of Eq. (10.10) is reduced as

$$\frac{d}{dt}[L_si_{as}+Mi_{bs}+Mi_{cs}]=\frac{d}{dt}[L_si_{as}-Mi_{as}] \tag{10.11}$$

Thus Eq. (10.10) becomes the following voltage equations.

$$\begin{bmatrix}v_{as}\\ v_{bs}\\ v_{cs}\end{bmatrix}=\begin{bmatrix}R_s & 0 & 0\\ 0 & R_s & 0\\ 0 & 0 & R_s\end{bmatrix}\begin{bmatrix}i_{as}\\ i_{bs}\\ i_{cs}\end{bmatrix}+\begin{bmatrix}L_s-M & 0 & 0\\ 0 & L_s-M & 0\\ 0 & 0 & L_s-M\end{bmatrix}\frac{d}{dt}\begin{bmatrix}i_{as}\\ i_{bs}\\ i_{cs}\end{bmatrix}+\begin{bmatrix}e_{as}\\ e_{bs}\\ e_{cs}\end{bmatrix} \tag{10.12}$$

**Voltage Equations of a Brushless Direct Current Motor**

$$v_{as} = R_s i_{as} + (L_s - M)\frac{di_{as}}{dt} + e_{as} \tag{10.13}$$

$$v_{bs} = R_s i_{bs} + (L_s - M)\frac{di_{bs}}{dt} + e_{bs} \tag{10.14}$$

$$v_{cs} = R_s i_{cs} + (L_s - M)\frac{di_{cs}}{dt} + e_{cs} \tag{10.15}$$

Unlike AC motors that use the $d-q$ axes reference frame to facilitate their control, BLDC motors directly use three-phase $abc$ quantities for their control. The $d-q$ transformation is necessary for the sinusoidal quantities. Since currents, flux, and back-EMFs of a BLDC motor are nonsinusoidal quantities, the $d-q$ transformation on the BLDC motor is meaningless.

### 10.3.2 TORQUE EQUATION

The output torque $T_e$ of a three-phase motor is generally calculated from the output power $P_e$ and the mechanical angular velocity $\omega_m$ as

$$P_e = e_{as} i_{as} + e_{bs} i_{bs} + e_{cs} i_{cs} \tag{10.16}$$

$$T_e = \frac{P_e}{\omega_m} = \frac{e_{as} i_{as} + e_{bs} i_{bs} + e_{cs} i_{cs}}{\omega_m} \tag{10.17}$$

here, the mechanical angular velocity $\omega_m = \omega_r / P$. In addition, $\omega_r$ is the electrical angular velocity and $P$ is the number of pole.

From this torque equation, we can readily see that the phase current is needed to be in phase with the back-EMF to produce the maximum torque. The drive shown in Fig. 10.8 satisfies this requirement for maximum torque production.

Now we will discuss the output torque of a three-phase BLDC motor driven by the 120° conduction method. In a BLDC motor, the currents of two-phase windings are the same in magnitude but flow in the reverse direction except during the commutation interval. As an example, consider Section 1 shown in Fig. 10.8. In that section, $i_{as} = I$, $i_{bs} = -I$, $i_{cs} = 0$ and $e_{as} = E$, $e_{bs} = -E$. Since the phase current is in phase with the back-EMF, the torque of Eq. (10.17) can be simply expressed as the product of the magnitudes of the phase current and back-EMF as

$$T_e = \frac{e_{as} i_{as} + e_{bs} i_{bs} + e_{cs} i_{cs}}{\omega_m} = 2\frac{EI}{\omega_m} \tag{10.18}$$

For the remaining sections, we can obtain the same result.

If $I$ and $E$ are constant values, the output torque of Eq. (10.18) becomes a constant value. However, if the back-EMF is not an ideal trapezoidal waveform,

there is a torque ripple even though the BLDC motor is fed with constant stator currents. For a BLDC motor having arbitrary back-EMF waveforms of Eq. (10.4), the output torque can be expressed as

$$T_e = \lambda_f[i_{as}f(\theta) + i_{as}f(\theta - 240^\circ) + i_{as}f(\theta - 120^\circ)] \tag{10.19}$$

### 10.3.2.1 Torque ripple during the commutation

Even though the back-EMF is an ideal trapezoidal waveform, a torque ripple may occur due to the current ripple introduced during the commutation of phase currents [4–8]. This torque ripple may be a major obstacle in applying a BLDC motor for high-performance motor drives. Below is a description on the causes of the torque ripple during the commutation of phase currents.

Consider the commutation of the phase current from Section 2 to Section 3 in Fig. 10.10. The stator current during the commutation is assumed to be constant and equal to $I$. The magnitude of back-EMF is also supposed to remain as a constant value $E$.

In Section 2, the stator current $I$ flows from phase $as$ to phase $cs$, while in Section 3, the current $I$ flows from phase $bs$ to phase $cs$. Thus the current is commutated from phase $as$ to phase $bs$ during the transition from Section 2 to Section 3. In this case the phase $as$ current $i_{as}$ decreases to zero, while the phase $bs$ current increases to its final value $I$. Meanwhile, the phase $cs$ current $i_{cs}$, i.e.,

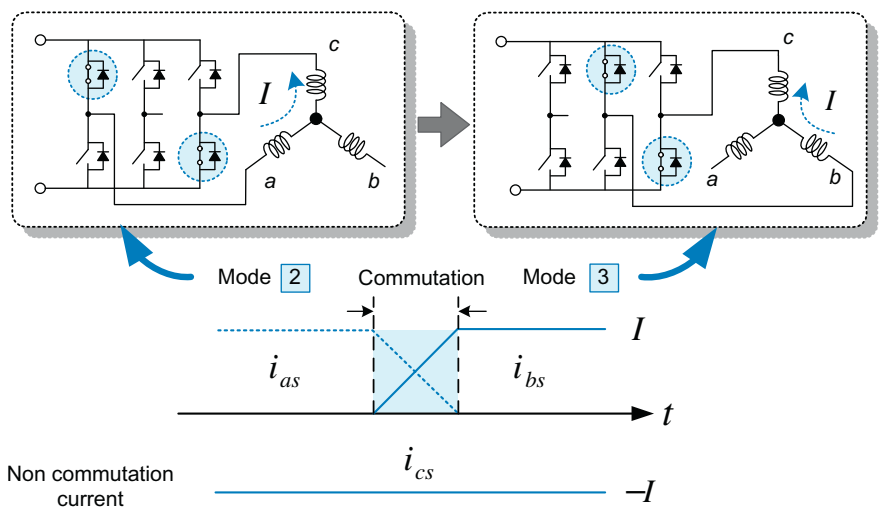



**FIGURE 10.10**

Commutation of phase currents.

noncommutation current, remains unchanged. During the transition from Section 2 to Section 3, $e_{as} = e_{bs} = E$, $e_{cs} = -E$. Thus the output torque of Eq. (10.18) can be expressed as

$$T_e = \frac{e_{as}i_{as} + e_{bs}i_{bs} + e_{cs}i_{cs}}{\omega_m} = \frac{E(i_{as} + i_{bs}) - Ei_{cs}}{\omega_m} = -\frac{2E}{\omega_m}i_{cs} \tag{10.20}$$

From Eq. (10.20), it can be readily seen that, during the commutation, the torque is proportional to the noncommutation current $i_{cs}$. If the noncommutation current $i_{cs}$ remains a constant value during the commutation, then the torque also becomes a constant value.

During the commutation, it takes time to change the current due to the winding inductance. If the decreasing rate of the phase *as* current is equal to the increasing rate of the phase *bs* current, then $i_{as} + i_{bs} = I$, so the phase *cs* current $i_{cs}$ remains at a constant value, $-I$. However, in practice, these two rates of change are usually not equal to each other due to the back-EMF, DC-link voltage, time constant of windings, etc. Accordingly, the noncommutation current cannot remain as a constant value, resulting in a torque ripple. For example, Fig. 10.11 shows that the rate of change of the current varies according to the back-EMF and DC-link voltage [4].

Fig. 10.11A shows that the phase *bs* current reaches the final value $I$ before the phase *as* current reduces to zero. Hence, the noncommutation current, the phase *cs* current $i_{cs}$, becomes larger than $I$, resulting in an increase in the torque. On the other hand, Fig. 10.11C shows that the phase *as* current reduces to zero before the phase *bs* current reaches the final value, $I$. In this case the noncommutation current, phase *cs* current $i_{cs}$, becomes smaller than $I$, resulting in a decrease in the torque. Fig. 10.11B shows an ideal case where the phase *as* current reduces

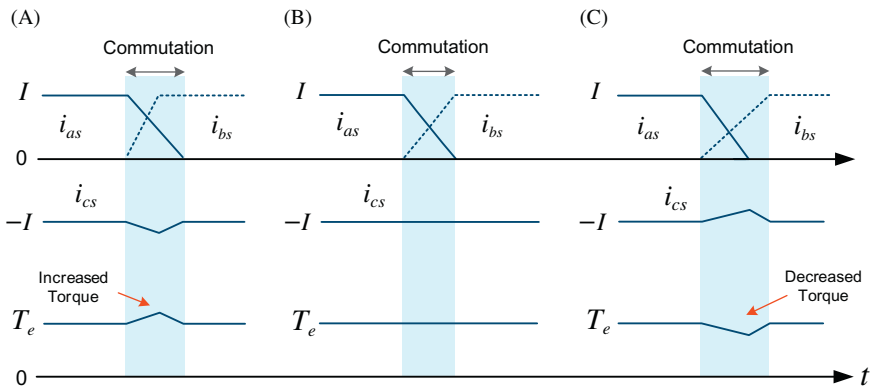



**FIGURE 10.11**

Phase currents during commutation in different cases. (A) low-speed ($V_{dc} > 4E$), (B) mid-speed ($V_{dc} = 4E$), and (C) high-speed ($V_{dc} < 4E$).

to zero at the same time the phase *bs* current reaches the final value *I*. In this case the noncommutation current remains constant, and thus results in the constant torque.

For this reason, whenever the winding current is commutated from one phase to another, a ripple in the output torque is generated. Thus this ripple of the torque occurs six times per cycle. The magnitude of the torque ripple depends on the operating current level and the operating speed. This is also different according to the pulse width modulation (PWM) techniques used in a driving inverter. Fig. 10.12A and B shows output torque and phase currents for the case shown in Fig. 10.11C. Commutation torque ripples produce noise and degrade speed control characteristics especially at low speeds. Thus many methods to reduce this torque ripple have been developed [4–8]. As an example, Fig. 10.12C shows that the ripple of the phase currents (thus, torque) is eliminated by using a commutation ripple compensation in which the motor input voltage is adjusted to equalize the rate of change of the current during the commutation [8]

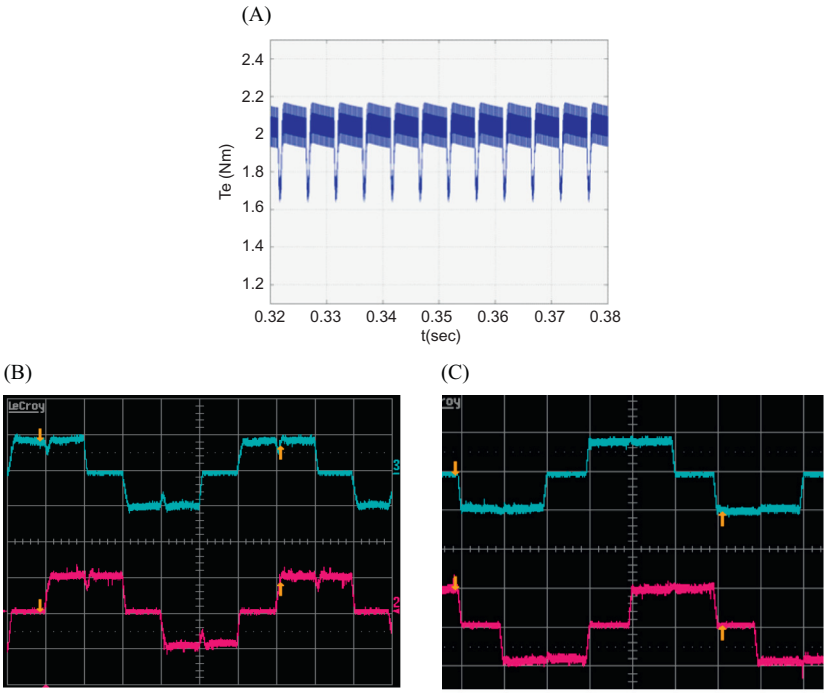


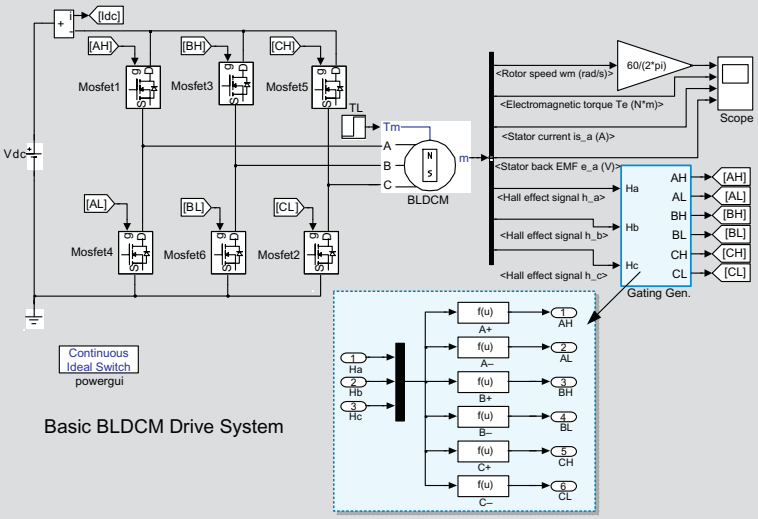

**FIGURE 10.12**

Ripple of output torque and phase currents. (A) output torque, (B) phase current (without compensation), and (C) with compensation.

## MATLAB/SIMULINK SIMULATION: BRUSHLESS DIRECT CURRENT MOTOR

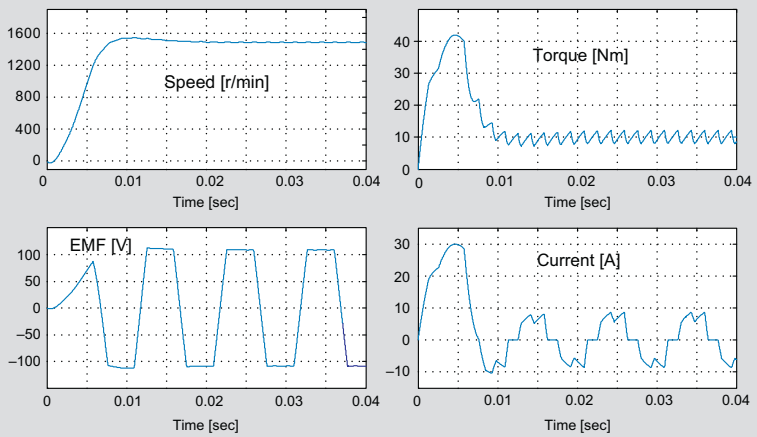
The six-step drive for 4-pole, 300-V BLDC motor is simulated by using a permanent magnet synchronous machine block in SimPowerSystems/Machines library and Mosfet blocks in SimPowerSystems/Power Electronics library.

- Overall diagram for simulation




Basic BLDCM Drive System

- Simulation results



## 10.4 CONTROL OF BRUSHLESS DIRECT CURRENT MOTORS

As can be seen in the Section 10.2, we can operate a BLDC motor easily by a proper commutation of phase currents based on the information of the rotor position. Similar to a DC motor, the operating speed of a BLDC motor is proportional to the voltage applied to the motor, and thus its speed can be controlled by adjusting the applied voltage.

### 10.4.1 SPEED CONTROL

The simplest speed control system to control the speed of a BLDC motor is shown in Fig. 10.13. A proportional−integral (PI) controller as mentioned in Chapter 2, is commonly used for the speed control. This PI speed controller outputs the motor voltage reference (or PWM duty) as

$$V^* = \left(K_P + \frac{K_i}{s}\right) \cdot (\omega_m^* - \omega_m) \tag{10.21}$$

where $K_P$ and $K_i$ are the proportional and integral gains of the PI speed controller, respectively.

This reference voltage is generated by a PWM technique and then applied to the BLDC motor. This speed control system is simple but has a big problem. In this method, the motor current is hard to control within a proper range. This is because when a speed command is changed, the voltage reference may be changed largely. Thus we cannot expect to obtain a good dynamic response of the speed control. Moreover, this may incur a large transient current more than the rated current, which may lead to a shutdown of the drive system.

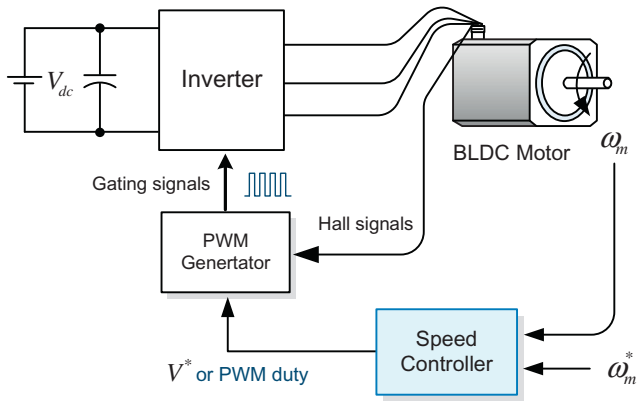



**FIGURE 10.13**

Speed control system of a BLDC motor.

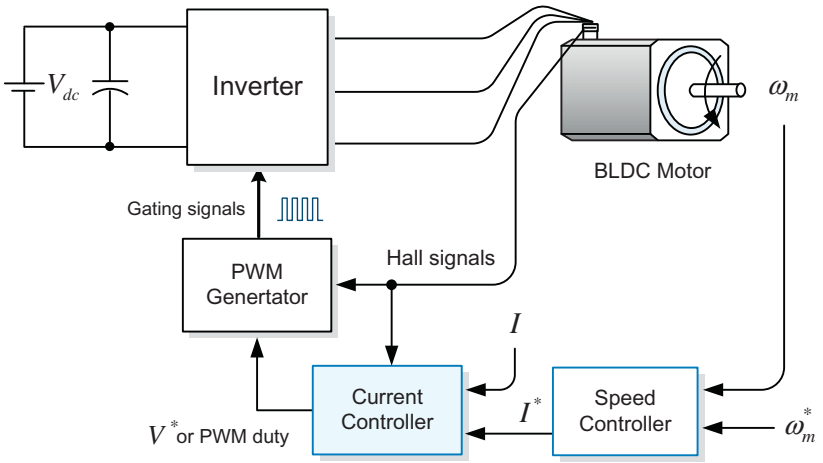



**FIGURE 10.14**

Speed control system based on the motor current.

To obtain a better dynamic response of the speed control, it is necessary to control the speed by controlling the torque or current of the BLDC motor. An enhanced speed control system based on the current control is shown in Fig. 10.14. Compared to the previous system of Fig. 10.13, this system includes a current controller to control the speed by regulating the current (thus, torque). In this case, the output of the PI speed controller becomes the motor current reference and a current sensor is needed to measure the actual motor current for the current control.

For AC motor drives, both the amplitude and phase of three-phase currents are instantaneously regulated to control the torque. However, for the BLDC motor drive, only the amplitude of phase currents needs to be regulated. This is because, as we can see in Eq. (10.18), the developed torque is proportional to the amplitude of the phase current. In addition, when controlling the amplitude of the current, we may regulate three-phase currents individually like in the current control of AC motors. However, since the amplitude of the phase current of a BLDC motor is proportional to the DC-link side current $I_{dc}$, the amplitude of the phase current is commonly controlled by regulating $I_{dc}$. In this case, the drive system needs only one current sensor at the DC-link side, and thus is more cost-effective.

Fig. 10.15 shows the speed control system using the regulation of the DC-link current. In this system, the speed controller produces the DC-link current reference as

$$I_{dc}^* = \left(K_{ps} + \frac{K_{is}}{s}\right) \cdot (\omega_m^* - \omega_m) \tag{10.22}$$

here, $K_{ps}$ and $K_{is}$ are the proportional and integral gains of the PI speed controller, respectively. These values can be determined from the gains selection procedure of a PI speed controller that was explained in Section 2.7.

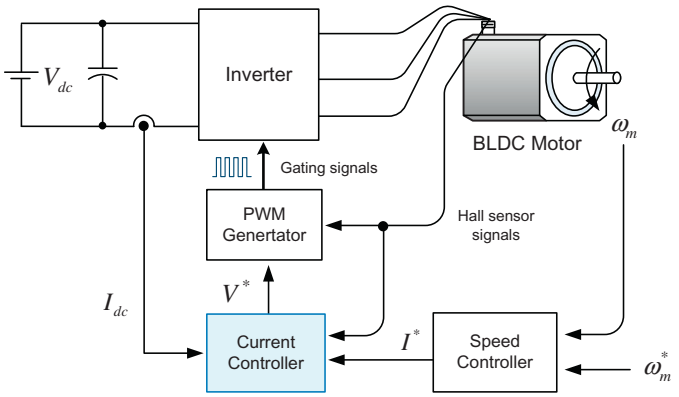



**FIGURE 10.15**

Speed control system using the regulation of the DC-link current.

To achieve the DC-link current reference $I_{dc}^*$ produced by the speed controller, switching signals for an inverter are usually generated by a hysteresis regulation technique or a PWM technique.

## 10.4.2 CURRENT CONTROL

As can be seen from Chapter 6, the hysteresis technique is simply implemented and gives an excellent transient response because it directly determines the switching states from the current error. However, the hysteresis technique has a major drawback of varying the switching frequency with operating conditions, such as the back-EMF, load condition, etc. Thus, to have a constant switching frequency, a PWM technique is commonly used, but it is inferior to the hysteresis technique in performance.

In the case of using a PWM technique, a motor voltage reference (or PWM duty) is generated by the PI current controller from an error between the current command $I_{dc}^*$ and the actual current as

$$V^* = \left(K_{pc} + \frac{K_{ic}}{s}\right) \cdot (I_{dc}^* - I_{dc}) \tag{10.23}$$

here, $K_{pc}$ and $K_{ic}$ are the proportional and integral gains of the current controller, respectively. These values can also be determined from the gains selection procedure of a PI current controller that was explained in Chapter 2.

Finally, the actual active switches are determined by combining the PWM switching signals with the operating mode signal decoded by using Hall effect sensor signals.

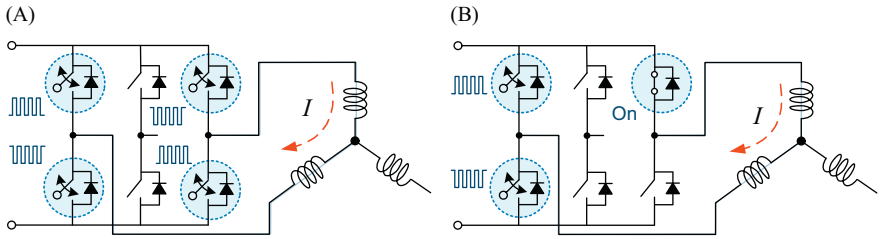



**FIGURE 10.16**

PWM techniques. (A) bipolar switching and (B) unipolar switching.

## 10.5 PULSE WIDTH MODULATION TECHNIQUES

In BLDC motor drives, there are two conventional PWM techniques for generating a motor applied voltage the as shown in Fig. 10.6: *bipolar switching method* and *unipolar switching method* [9−10]. These are similar to the PWM techniques of the H-bridge circuit for DC motor drives in Section 2.8. This similarity is due to the facts that switches of only two phases are being driven in the three-phase inverter for BLDC motor drives. However, there are several variations for the unipolar switching method. Now let us examine these PWM techniques.

### 10.5.1 BIPOLAR SWITCHING METHOD

In the bipolar switching method, a PWM signal is applied to all switches of two phases as shown in Fig. 10.16A. By contrast, in the unipolar switching method as shown in Fig. 10.16B, a PWM signal is applied to the switches of only one phase while one switch of the other phase is kept at an on-state. The bipolar method is simple and can give a better transient response because $+V_{dc}$ or $-V_{dc}$ is applied across the phase winding. However, the current ripple (thus, torque ripple) and switching losses are greater than those of the unipolar switching method. The PWM gating signals by the bipolar switching method are shown in Fig. 10.17.

### 10.5.2 UNIPOLAR SWITCHING METHOD

In the unipolar switching method, switching losses can be reduced because the PWM signal is applied to the switches of only one phase. In addition, since the applied voltage to the phase windings is 0 and $+V_{dc}$ or 0 and $-V_{dc}$, the current ripple is half of that of the bipolar switching method. Due to these advantages, the unipolar switching method is more widely used for BLDC motor drives. However, this method is complicated and has a slower response than the bipolar switching method. In addition, circulating currents may occur in the inactive phase windings. Thus this method is less favorable for precision servo drives.

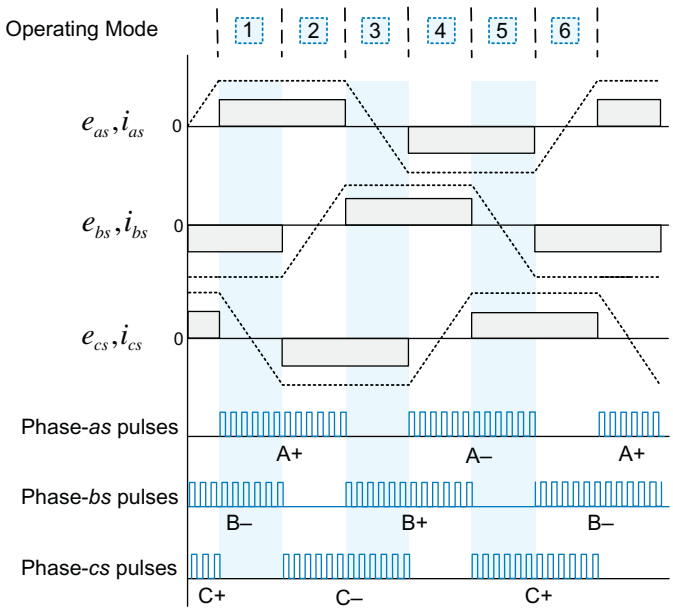



**FIGURE 10.17**

Bipolar switching method.

The unipolar switching method is also divided into several schemes according to the executing switch. In the *upper switch PWM scheme* in Fig. 10.18A, the PWM signal is applied to the upper switch only while the lower switch is kept at an on-state. On the other hand, in the *lower switch PWM scheme* in Fig. 10.18B, the PWM signal is applied to the lower switch only while the upper switch is kept at an on-state. In these two schemes, however, the utilization of switches and switching losses are biased because only one specific switch makes a continuous switching.

As types of improved schemes through uniform switching, there are *on-going PWM scheme* and *off-going PWM scheme* [9]. In the on-going PWM scheme shown in Fig. 10.18C, the PWM signal is applied to each switch during the front 60° part of the 120° conduction interval. In the off-going PWM scheme shown in Fig. 10.18D, the PWM signal is applied to each switch during the latter 60° part of the 120° conduction interval.

These unipolar PWM schemes have a disadvantage of having an increased ripple torque and a lowered efficiency because of ripple current, which occurs in the inactive phase windings due to diode freewheeling. The magnitude and direction of the ripple current depends on the PWM schemes. We can see, from Fig. 10.19, the ripple current during the inactive interval for unipolar PWM schemes that were explained above. In addition, the bipolar switching method has no ripple current due to no diode freewheeling. The PWM scheme, which is called

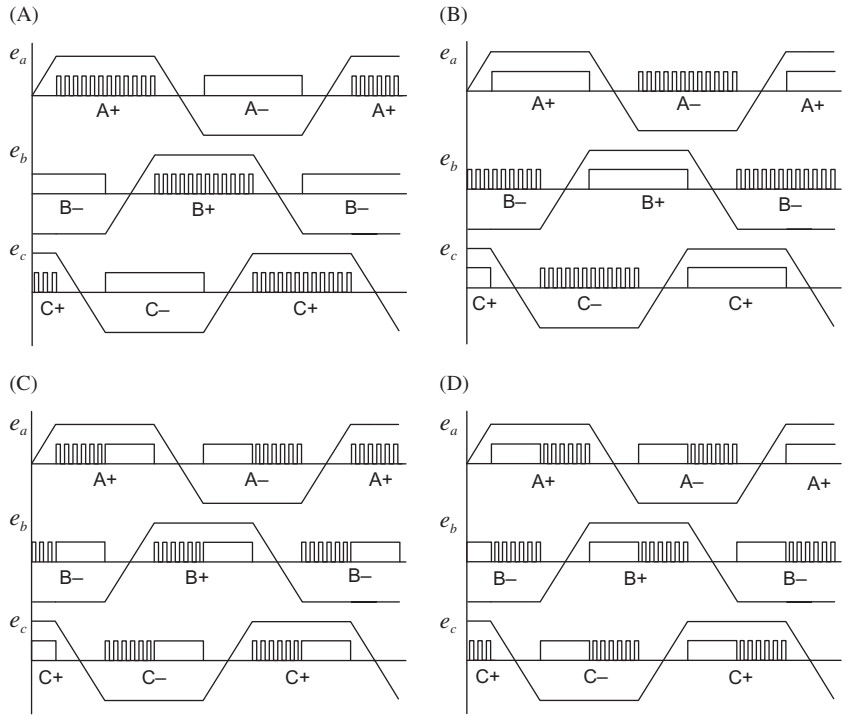



**FIGURE 10.18**

Different schemes of the unipolar switching method. (A) upper switch PWM, (B) lower switch PWM, (C) on-going PWM, and (D) off-going PWM.

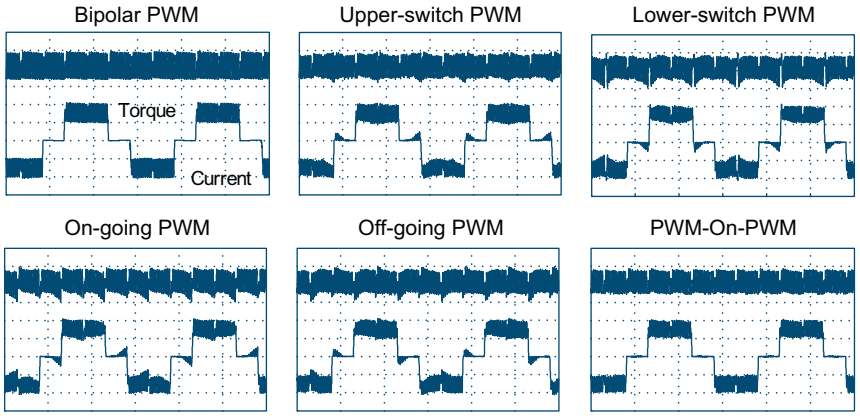



**FIGURE 10.19**

Comparison of phase and torque for PWM schemes.

*PWM_ON_PWM scheme*, to eliminate diode freewheeling in the inactive phase has been developed [10]. In this scheme the switches are in PWM mode in the beginning 30° and the last 30° zones, and in continuous on-state in the middle 60° zone of the 120° conduction interval.

As it can be seen from above, characteristics such as ripple torque during commutation, switching losses, and sensorless control performance vary according to different unipolar PWM schemes. The torque ripple comparison of PWM schemes is shown in Fig. 10.19.

## 10.6 SENSORLESS CONTROL OF BRUSHLESS DIRECT CURRENT MOTORS

As described in the Section 10.2, Hall effect sensors for obtaining the rotor position are indispensable for BLDC motor drives. However, since the position sensors increase the cost and size of the motor and reduce the reliability of a drive system, a BLDC motor drive without position or speed sensors is becoming more popular.

Various sensorless methods for BLDC motors have been seen in the literature [11–15]. One well-known method is the back-EMF-based method [11]. There is also a method based on the current of the freewheeling diodes of the noncommutation phase [13] and a method based on a flux observer. Among these, we will explore the back-EMF-based method, which is the most widely used for low-cost applications such as fan, pump, and compressor drives due to its easy principle and implementation.

### 10.6.1 SENSORLESS CONTROL BASED ON THE BACK-ELECTROMOTIVE FORCE

The back-EMF of a motor includes information on the magnetic flux. Thus the rotor position can be obtained by detecting the back-EMF. It is hard to measure the back-EMF of AC motors because all three windings are excited at all times. On the other hand, in three-phase BLDC motor drives, since only two of the three-phase windings are conducting at a time, the back-EMF appears in the open winding of the nonconducting phase. Thus the back-EMF can be detected by sensing the voltage of the nonconducting phase. In BLDC motors, we can consider that the nonconducting phase winding plays the role of a sensor to detect the position.

In this case, there is no need to detect the whole waveform of the back-EMF. Instead, the commutation instants can be identified by detecting only the zero crossing point (ZCP) of the back-EMF. From Fig. 10.20, we can easily see that the back-EMFs of a nonconducting phase always pass through zero (see the parts arrows are indicating). For example, in Section 2 where phase *as* and *cs* are conducting and phase *bs* is nonconducting, we can identify that the back-EMF of

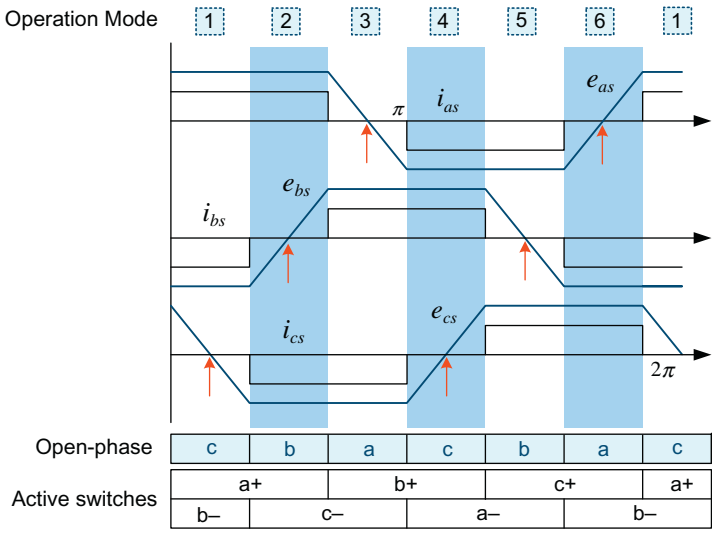



**FIGURE 10.20**

ZCPs of the back-EMF.

phase *bs* passes through zero. In addition, it can be seen that the commutations happen 30 electrical degrees after the ZCPs of the back-EMFs.

Therefore, without any position sensor, the phase commutation is made possible by detecting the ZCPs of the back-EMFs.

For three-phase Y-connected windings, the back-EMF across a phase can be obtained directly from measuring the phase terminal voltage referred to the neutral point of windings as shown in Fig. 10.21. However, in most cases, the neutral point of windings is not accessible. Thus the most commonly used method is to create a virtual neutral point by using the three-phase terminal voltages.

The back-EMF-based methods have the following problems. When measuring the terminal voltage, a large amount of electrical noise is induced on the sensed terminal voltage due to PWM switching signals driving the motor. Low-pass filters are usually used to remove unwanted switching noise, but the phase delay of the low-pass filter causes a commutation delay at high speeds. In addition, attenuation by a voltage divider will be required to lower the level of the sensed signal to an acceptable range of the control circuit. This lowers the signal-to-noise ratio at low speeds, resulting in degradation of low-speed operation performance. Moreover, the commutation happens 30 electrical degrees after the ZCPs of the back-EMFs. It is hard to obtain commutation instants precisely when the operating speed is changing. To improve these problems, the back-EMF integration the third harmonic voltage integration, and the method detecting the conducting current of the freewheeling diodes in the unexcited phase have been presented [13–14]. However, they still have a low accuracy problem at low speeds.

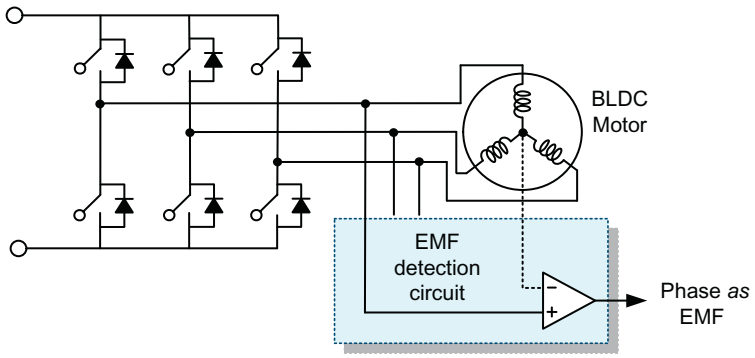



**FIGURE 10.21**

Back-EMF detection circuit.

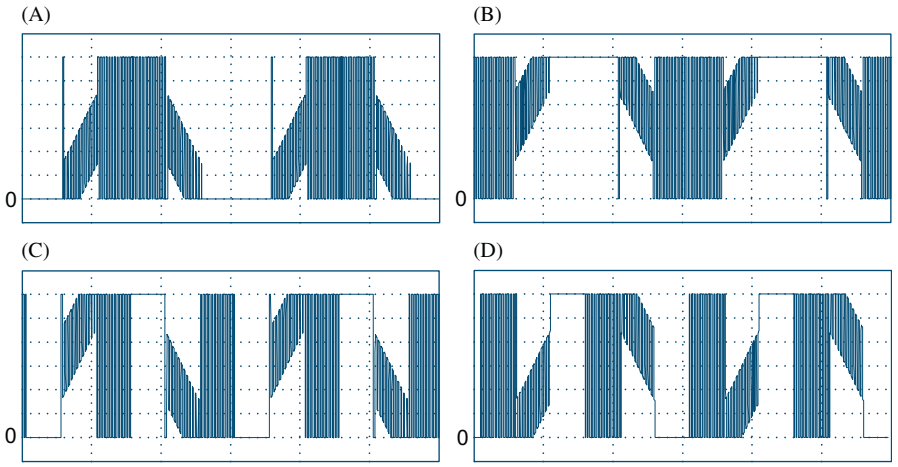



**FIGURE 10.22**

Back-EMFs according to unipolar PWM techniques: (A) upper switch PWM, (B) lower switch PWM, (C) on-going PWM, and (D) off-going PWM.

We have just now discussed the ZCPs of the back-EMF waveforms for a six-step drive in Fig. 10.20. However, BLDC motors are usually driven by using a PWM technique. In this case, PWM signals are superimposed on the back-EMF waveforms, as can be seen in Fig. 10.22. Thus, The ZPSs are obscured by the PWM signals. Several improved back-EMF sensing methods linked to PWM techniques, which require neither a virtual neutral voltage nor a great amount of filtering, have been introduced [14].

However, these back-EMF-based methods have intrinsic restrictions on low-speed operations where the back-EMF becomes insufficient. In addition, since there is no information on the back-EMF at start-up, an additional method for start-up is needed. Commonly, a sensorless BLDC motor is first started using initial rotor position detection method and brought up to a certain speed by an open-loop operation. When the motor reaches a speed where the back-EMF is sufficient to be sensed, the operation is transferred to the sensorless control.

## REFERENCES


[1] G. Bauerlein, A brushless DC motor with solid-state commutation, IRE Natl. Conv. Rec. (1962) 184–190.

[2] T.M. Jahns, W.L. Soong, Pulsating torque minimization technique for permanent magnet AC motor drives—a review, IEEE Trans. Ind. Electron. 43 (2) (Apr. 1996) 321–330.

[3] P. Pillay, R. Krishnan, Modeling, simulation, and analysis of permanent-magnet motor drives, Part II. The brushless DC motor drive, IEEE Trans. Ind. Appl. 25 (2) (Mar./Apr. 1989) 274–279.

[4] R. Carlson, M. L-Mazenc, J. Fagundes, Analysis of torque ripple due to phase commutation in brushless DC machines, IEEE Trans. Ind. Appl. 28 (3) (1992) 441–450.

[5] C. Berendsen, G. Champenois, A. Bolopion, Commutation strategies for brushless DC motors: influence on instant torque, IEEE Trans. Power Electron. 8 (2) (1993) 231–236.

[6] K-W Lee, et al., Current control algorithm to reduce torque ripple in brushless DC motors, in: Conf. Rec. ICPE'98, vol. 1, Seoul, Korea, October 1998, pp. 380–385.

[7] J.H. Song, I. Choy, Commutation torque ripple reduction in brushless DC motor drives using a single DC current sensor, IEEE Trans. Power Electron. 19 (2) (Mar., 2004) 312–319.

[8] K.-J. Kwun, S.-H. Kim, A current control strategy for torque ripple reduction on brushless DC motor during commutation, Trans. Korean Inst. Power Electron. 9 (4) (Jun. 2002) 195–202.

[9] Z. Xiangjun. C. Boshi, The different influences of four PWM modes on the commutation torque ripples in sensorless brushless DC motors control system, in: Proc. the Fifth International Conference Electrical Machines and Systems, vol. 1, 2001, pp. 575–578.

[10] U. Vinatha, S. Pola, K.P. Vittal, A novel PWM scheme to eliminate the diode freewheeling in the inactive in BLDC motor, in: Conf. Rec. IEEE PESC'2004, pp. 2282–2286.

[11] K. Iizuka, et al., Microcomputer control for sensorless brushless motor, IEEE Trans. Ind. Appl. 27 (May/Jun., 1985) 595–601.

[12] P.P. Acarnley, J.F. Watson, Review of position-sensorless operation of brushless permanent-magnet machines, IEEE Trans. Ind. Electron. 53 (2) (Apr. 2006) 321–330.

[13] T. Kim, H.-W. Lee, M. Ehsani, Position sensorless brushless DC motor/generator drives: review and future trends, IET Electr. Power, Appl. 1 (4) (2007) 557–564.

[14] S. Ogasawara, H. Akagi, An approach to position sensorless drive for brushless DC motors, IEEE Trans. Ind. Appl. 27 (5) (Sep./Oct., 1991) 928–933.
[15] Y.-S. Lai, Y.-K. Linl, A unified approach to back-emf detection for brushless dc motor drives without current and hall sensors, in Conf. Rec. IEEE IECON 2006, pp. 1293–1298.

# Index

*Note*: Page number followed by "*f*," "*t*," and "*b*" refer to figures, tables, and boxes, respectively.

## A


Absolute encoder, 375−376
Active voltage vector, 301−304, 310
Actual efficiency and ideal efficiency, 120*f*
Air-gap flux−oriented (AFO) control, 212
Air-gap power, 114
  distribution of, 115*f*
Alnico magnets, 167
Alternating current (AC) motors, 1, 2*f*, 4−7, 6*f*, 36, 39, 95
  AC motor drive applications, 266
  AC power supply applications, 266−267
  induction motors, 95−142
    characteristics of, 112−122
    determining equivalent circuit parameters for, 128−131
    effect of rotor resistance, 124−127
    equivalent circuit of, 104−112
    fundamentals of, 99−104
    operating modes of, 123−124
    operation regions of, 139−142
    speed control of, 131−138
    structure of, 96−99
  position sensors, 373−376
    resolver, 373−375
    rotary encoder, 375−376
  sensorless control of, 382−387
  speed estimation using incremental encoder, 377−381
    M method, 378−379
    M/T method, 380−381
    T method, 379−380
  synchronous motors, 143−152
    cylindrical rotor synchronous motors, 144−148
    salient pole rotor synchronous motors, 148−151
    starting of, 151−152
Alternating current (AC) motors, current regulator of, 247
  complex vector current regulator, 263−264
  feedforward control, 259−262
    for induction motors, 261
    for permanent magnet synchronous motors, 261−262
  hysteresis regulator, 248−250
  ramp comparison current regulator, 250−251
  stationary reference frame $d-q$ current regulator, 252−254
  synchronous frame PI current regulator, gain selection of, 256−259
  synchronous reference frame $d-q$ PI current regulator, 255−256
Alternating current (AC) motors, high-speed operation of, 341
  field-weakening control for induction motors, 343−357
    classic field-weakening control method, 344
    maximum torque, producing, 347−357
    voltage- and current-limit conditions, 344−347
  permanent magnet synchronous motor, 357−370
    high-speed operation of, 360−366
    surface-mounted permanent magnet synchronous motor, 366−370
Alternating current (AC) motors, vector control of, 203
  conditions for instantaneous torque control of motors, 204−206
  induction motor, 206−234
    combined flux estimation method, 230−232
    detuning in the indirect vector control, 223−225
    direct vector control based on the rotor flux, 212−220
    indirect vector control based on the rotor flux, 220−223
    instantaneous torque control, 207−212
    proportional−integral flux controller, 233−234
    rotor flux linkages estimation based on rotor voltage equations, 228−230
    rotor flux linkages estimation based on stator voltage equations, 226−228
  permanent magnet synchronous motors, 234−245
    Interior Permanent Magnet Synchronous Motor, vector control of, 238−245
    Surface-Mounted Permanent Magnet Synchronous Motor, vector control of, 236−238
Alternating current (AC) motors modeling and reference frame theory, 153
  $d-q$ axes model of an induction motor, 188−197




Hesai Exhibit 1030, page 419

Alternating current (AC) motors modeling and reference frame theory (*Continued*)
flux linkage equations in, 190–193
torque equation in, 193–197
voltage equations in, 189–190
*d*–*q* axes model of permanent magnet synchronous motor, 197–201
flux linkage equations in, 198–200
torque equation in, 200–201
voltage equations in, 198
inductance between stator and rotor windings, 160–163
permanent magnet synchronous motor, modeling of, 163–174
model of, 169–174
structure of, 164–169
reference frame transformation, 174–188
by complex vector, 185–188
*d*–*q* reference frame, types of, 175–176
by matrix equations, 176–184
rotor windings, 158–159
stator windings, 157–158
Anti-windup control, 73–74
Anti-windup controller, 73–74, 90, 262
proportional–integral current controller, gains selection procedure of, 74
Arago's Disk, 95–96, 96*f*
Armature circuit, 42
Armature voltage control, 45–46, 46*f*
Armature winding, 39, 41–42, 42*f*, 143–144
Asynchronous motor, 6, 95
Average torque control technique, 203
Axial-flux type BLDC motor, 393–394
Axial-flux type PMSMs, 165–166

## B

Back calculation method, anti-windup control by, 73*f*, 74*f*
Back-electromotive force (back-EMF), 13*b*, 42–43, 342–343, 345–346, 383
sensorless control based on, 412–415
Bandwidth, 65*b*, 72
of speed control, 77
Base speed, 140, 142, 341, 350–351
Bipolar switching method, 83, 84*f*, 409, 409*f*, 410*f*
Blanking time. *See* Dead time
Blocked rotor test, 130–131, 130*f*
Breakdown torque region, 116–117, 139, 142, 142*f*
Brushless direct current (BLDC) motors, 1, 389
configuration of, 390–394
construction of, 393–394
control of, 406–408
current control, 408
speed control, 406–408
versus direct current motors, 390–391
driving principle of, 394–397
Matlab/Simulink simulation, 405*b*
modeling of, 398–405
torque equation, 401–405
voltage equations, 398–401
versus permanent magnet synchronous motors, 391–393
pulse width modulation techniques, 409–412
bipolar switching method, 409
unipolar switching method, 409–412
sensorless control of, 412–415
based on back-electromotive force, 412–415
Butterworth filter, 231, 231*b*

## C

Carrier wave, 292*b*
Clark's transformation, 178
Classification of electric motors, 1, 2*f*
Closed-loop control, 58–60, 58*f*
feedback control, 58–60
integral controller (I controller), 59, 59*f*
proportional controller (P controller), 58, 58*f*
proportional–integral controller, 59, 60*f*
feedforward control, 60–61, 61*f*
Closed-loop frequency response, 65, 71*f*
Closed-loop transfer function, 52*b*, 70, 78
Commutation, 396
of phase currents, 402*f*
torque ripple during, 402–405
Complex vector current regulator, 263–264
Complex vector synchronous frame current regulator, 263–264, 264*f*
Compound motor, 39
Configuration of electric motors, 3–4, 3*f*
Constant power region, 48–50, 140–142, 141*f*, 350–352, 361–366, 368–370
Constant torque region, 48, 139
operation characteristics in, 140*f*, 349–350, 349*f*, 360–361
Constant voltage constant frequency (CVCF) inverter, 266–267
Constant volts per Hertz control, 134–136
Continuous modulation, 310–311
Continuous pulse width modulation (CPWM) methods, 311
Critical damping, 54
Current model, 226, 228–230
Current source inverter (CSI), 265, 266*f*
Cylindrical motors, 26
Cylindrical rotor configuration, 23, 23*f*

Cylindrical rotor synchronous motors, 144–148
output power and torque for, 148*f*
per phase equivalent circuit of, 146*f*
torque of, 147–148
Cylindrical stator and rotor configurations, 23*f*, 96

## D

Damping ratio, system responses according to, 53–54, 54*f*
Dead time, 269–270, 331–338
compensation, 336–338
negative current, 337–338
positive current, 336–337
effect, 333–336
Decoupling control. *See* Feedforward control
Deep-bar rotor, 125–126
effective resistance and output torque in, 126*f*
versus normal rotor, 125*f*
Detuning effects, 224, 224*f*
reference frame error due to, 225*f*
Digital controllers, 37
Direct current (DC) motors, 1, 2*f*, 4–5, 5*f*, 25, 36, 39
block diagram for, 51*f*
and brushless direct current motors, 390–391
capability curve of, 49*f*
closed-loop control, 58–60, 58*f*
feedback control, 58–60
feedforward control, 60–61, 61*f*
configuration, 39–42, 40*f*
control system, configuration of, 56
control system, design consideration of, 61–66
gain margin and phase margin, 63–64
response time/speed of response, 64–65
stability, 62–64
steady-state error, 65–66
current controller design for, 66–74
anti-windup controller, 73–74
PI controller, 66
proportional–integral current controller, 69–72
current control system, 68*f*
direct current motor drive system, simulation of, 86–92
direct current motor modeling, 86–87
four-quadrant chopper modeling, 91–92
mechanical system modeling, 87–89
proportional–integral current controller modeling, 89
proportional–integral speed controller modeling, 90
equivalent circuit of, 43*f*
modeling of, 42–44
armature circuit, 42
back-electromotive force, 42–43
mechanical load system, 44
torque, 43–44
open-loop control, 57–58, 57*f*
operation regions of, 48–50
constant power region, 48–50
constant torque region, 48
power electronic converter for, 82–85
four-quadrant chopper, 82
switching schemes, 83–85
simple driving circuit for, 82*f*
speed controller design, 75–81, 75*f*
integral-proportional controller, 79–81
proportional–integral speed controller, 75–79
steady-state characteristics of, 45–50
armature voltage control, 46, 46*f*
field flux control, 47–48, 47*f*
transient response characteristics of, 50–55
Direct current (DC) power, 36, 95
Discontinuous modulation, 310–311
Discontinuous PWM techniques, 311–317
30-degree, 313–317
60-degree, 311–312
60-degree ( ± 30-degree), 312
± 120-degree, 312–313
Distributed winding, 97–98, 100–101, 164, 164*f*
Double sampling, 338
Double-cage rotor, 126, 127*f*
Doubly fed machine, 20, 21*f*, 25*f*
*d–q* axes current regulators, 252–259
stationary reference frame *d–q* current regulator, 252–254
synchronous frame PI current regulator, gain selection of, 256–259
for induction motors, 257–258
for permanent magnet synchronous motors, 258–259
synchronous reference frame *d–q* PI current regulator, 255–256
*d–q* axes model
of induction motor, 188–197
flux linkage equations, 190–193
torque equation, 193–197
voltage equations, 189–190
of permanent magnet synchronous motor, 197–201
flux linkage equations, 198–200
torque equation, 200–201
voltage equations, 198
*d–q* transformation, 174
Dynamic braking, 33

Dynamic equation of motion, 27–32
gears/pulleys, system with, 31–32
translational motion and rotational motion, combination system of, 30–31
Dynamic overmodulation methods, 325–327
minimum-magnitude-error pulse width modulation method, 326
minimum-phase-error pulse width modulation method, 325–326
overmodulation method considering the direction of current, 327

## E

Efficiency, defined, 119
Electric and magnetic parts of electric motors, 3*f*
Electric drive system, 35–37, 56*f*
configuration of, 35*f*
digital controllers, 37
electric motors, 36
power electronic converters, 36–37
power supply, 36
sensors and other ancillary circuits, 37
Electromagnetic induction, 1, 6, 95
Electromechanical energy conversion, 7, 7*f*
Electromotive force (EMF), 95–96

## F

Faraday's law, 13*b*, 99, 107–108
Feedback control, 58–60
integral controller, 59, 59*f*
proportional controller, 58, 58*f*
proportional–integral controller, 59, 60*f*
Feedforward compensation technique, 336
Feedforward control, 60–61, 61*f*, 259–262
for induction motors, 261
for permanent magnet synchronous motors, 261–262
Feedforward field-oriented control, 223
Feedforward field-weakening control method, 355–357
Ferrite (or ceramic) magnets, 167
Ferromagnetic materials, 8, 96
Field flux control, 45, 47–48, 47*f*
Field winding, 39, 143–144
Field-oriented control, 203–204, 209–210
Field-weakening control for induction motors, 343–357
classic field-weakening control method, 344
feedback method, 343
feedforward method, 343
maximum torque, producing, 347–357
constant torque region, 349–350
field-weakening region I, 350–352
field-weakening region II, 352–357
voltage- and current-limit conditions, 344–347
current-limit condition, 346–347
voltage-limit condition, 344–346, 346*f*
Field-weakening region, 48–50, 139
Final value theorem, 65
Flux angle, 210–212
Flux estimation method, combined, 230–232
Flux linkage equations, in $d-q$ axes, 190–193, 198–200
Flux–current characteristic, 9*f*
magnetic energy in, 13*f*
Flux-producing current, 207–209, 214
Flux-weakening operation, 364–365
concept of, 358*f*
onset of, 364*f*
optimal currents in, 365*f*
optimal current vector in, 365*f*
Flux-weakening region, optimal current trajectory in, 366*f*
Force for a current carrying conductor, 44*f*
Force on a conductor, 40*f*
Forward braking (generating) mode, 35
Forward motoring mode, 34
Four-quadrant chopper, 82, 91–92
Four-quadrant operation modes, 33–34, 33*f*
in elevator drive, 34*f*
Fractional-pitch winding, 108
Frequency modulation index, 295
Frequency response, 61*b*
closed-loop, 71*f*
open-loop, 70*f*, 75–76
Full-bridge inverter, 275, 275*f*

## G

Gain margin, 62–64, 63*f*
Gate turn-off (GTO) thyristor, 36–37, 268
Gears/pulleys, system with, 31–32
Generalized rotating transformation, 176
Generating mode, 32–33

## H

Hall effect sensors, 37, 217–220, 226, 395–396, 395*b*, 408, 412
Harmonic distortion factor (HDF), 313–315, 314*f*
H-bridge circuit, 82, 83*f*
Hysteresis regulator, 248–250
operation principle of, 249*f*

## I


Ideal efficiency, 120–122, 120*f*
Incremental encoder, 236, 375–376, 375*f*
  speed estimation using, 377–381
Induced voltage, 13*b*, 106, 109
  for a moving conductor, 252*f*
Inductance of the coil, 10*f*
Induction motor, 5–6, 26, 95–142
  back-electromotive force of, 140
  capability curve of, 143*f*
  characteristics of, 112–122
    efficiency, 119–122
    input power factor, 113
    output torque, 113–117
    stable operating point, 117–119
    stator current, 112–113
  combined flux estimation method, 230–232
  determining equivalent circuit parameters for, 128–131
    blocked rotor test, 130–131
    measurement of stator resistance, 128–129
    no-load test, 129–130
  detuning in indirect vector control, 223–225
  direct vector control based on rotor flux, 212–220
    induction motor drive system by the direct vector control, 215–220
    relation between *d*-axis stator current and rotor flux linkage, 213–214
    relationship between *q*-axis stator current and output torque, 214–215
  *d*–*q* axes model of, 188–197
    flux linkage equations in, 190–193
    torque equation in, 193–197
    voltage equations in, 189–190
  effect of rotor resistance, 124–127
  equivalent circuit of, 104–112
    rotor circuit, 109–112
    stator circuit, 105–108
  feedforward control for, 261
  field-weakening control for, 343–357
    classic field-weakening control method, 344
    maximum torque, producing, 347–357
    voltage- and current-limit conditions, 344–347
  flux controller of, 232–234
    proportional–integral flux controller, 233–234
  fundamentals of, 99–104
    rotating magnetic field, 100–104
  generation mode, 123
  indirect vector control based on rotor flux, 220–223
  instantaneous torque control, 207–212
    flux angle, 210–212
  instantaneous torque control method of, 210*f*
  modeling of, 154–163
    inductance between stator and rotor windings, 160–163
    rotor windings, 158–159
    stator windings, 157–158
  motoring mode, 123
  operating modes of, 123–124
  operation regions of, 139–142, 139*f*
    breakdown torque region, 142
    constant power region, 140–141
    constant torque region, 139
  plugging mode, 124
  power-flow diagram in, 114*f*
  proportional–integral gains for, 257–258
  regenerative braking, 123–124
  rotor flux linkages estimation
    based on rotor voltage equations, 228–230
    based on stator voltage equations, 226–228
  speed control of, 131–138
    closed-loop speed control, 136–138
    slip control, 131–133
    synchronous speed control, 133–136
  stator and rotor windings of, 154*f*, 155*f*
  structure of, 96–99, 97*f*
    rotor, 98–99
    stator, 97–98
Inner rotor type, 167–169, 393–394
Instantaneous torque control, 203–204
  of induction motor, 207–212
Insulated gate bipolar transistor (IGBT), 36–37, 268
  switching characteristics of, 332*f*
Integral controller, 59, 59*f*
Integral windup, 73
Integral-proportional (IP) controller, 79–81
Integrated gate-commutated thyristor (IGCT), 36–37, 268
Interior permanent magnet synchronous motor (IPMSM), 166–167, 169–170, 357–358, 360, 362
  high-speed operation of, 360–366
    constant power region, 361–366
    constant torque region, 360–361
  rotor and its equivalent of, 170*f*
  rotor configurations of, 167*f*
  self-inductance of, 171
  surface-mounted permanent magnet synchronous motor, 366–370
    constant power region, 368–370
International Electrotechnical Commission (IEC), 127

Inverters, 265–288
basic circuit, 267*f*
single-phase full-bridge inverters, 275–277
single-phase half-bridge inverters, 271–274
switching devices for, 268*f*
three-phase inverter using switching functions, 283–288
three-phase square wave inverter (six-step inverter), 277–283
voltage source inverters, 267–271
output voltage of basic circuit, 269–271

## K

Kramer drive system, 133

## L

Leakage flux, 105
Lenz's law, 13*b*, 100
Linear modulation range, 293
Linear motion device, 13–17, 14*f*
Linear region, 9
Line-to-line voltages, 278, 279*f*, 282
Load torque, 29, 30*b*
Lorentz force, 95–96
Lower switch PWM scheme, 410, 411*f*, 414*f*

## M

M method, 378–379, 378*f*
M/T method, 380–381, 381*f*
Magnetic energy, 8–13
in the flux–current characteristic, 13*f*
Magnetic field energy increment, 21
Magnetic flux, 3–4, 8–9, 11*b*
Magnetic system, 7, 11*f*
Magnetization curve, 9
Magnetizing flux, 105, 145, 157–158
Magnetomotive force (mmf), 10, 11*b*
Magnitude invariance transformation, 178
MATLAB/Simulink, 86–92, 195*b*, 219*b*, 244*b*
direct current motor modeling, 86–87
four-quadrant chopper modeling, 91–92
mechanical system modeling, 87–89
proportional–integral current controller modeling, 89
proportional–integral speed controller modeling, 90
Maximum torque per ampere (MTPA), 237, 348*f*, 349, 360
control, 238–239
current-limit circle and MTPA trajectory, 363*f*
*d*–*q* Axes current commands for, 360*f*
Maximum torque per voltage (MTPV), 352, 364–365
Mechanical load system, 27–35, 44, 87*f*
dynamic equation of motion, 27–32
gears/pulleys, system with, 31–32
translational motion and rotational motion, combination system of, 30–31
operation modes of electric motor, 32–35
Mechanical system, 7, 87–89
Metal oxide semiconductor field effect transistor (MOSFET), 268
Minimum-magnitude-error pulse width modulation method, 326, 326*f*
Minimum-phase-error pulse width modulation method, 325–326, 325*f*
Model reference adaptive control (MRAC) method, 385
Modulating wave, 292*b*
Modulation index (MI), 290
Moment of inertia, 28, 28*b*
Motor characteristics according to speed, 342*f*, 343*f*
Motor control system, configuration of, 57*f*
Movable part, movement of, 14, 14*f*
Multilevel inverter, 268
Mutual-inductance, 19*b*, 153
between stator as winding and the rotor *ar* winding, 160*f*
between stator winding and magnet, 173*f*

## N

National Electrical Manufacture's Association (NEMA), 127
Naturally sampled PWM, 297
Neodymium magnet, 165
Neodymium–iron–boron (NdFeB) magnets, 168
Neutral voltage, in Y-connected three-phase load, 282–283, 283*f*
Neutral-point clamped inverter, 268
Newton's second law of motion, 27
No-load test, 129–130, 129*f*
Nonfeedback control. *See* Open-loop control
*N*-turn coil, flux linkage of, 9

## O

Off-going PWM scheme, 410, 411*f*, 414*f*
"$1/\omega_r$" method, 354
On-going PWM scheme, 410, 411*f*, 414*f*
Open-loop control, 57–58, 57*f*
Open-loop frequency response, 69–70, 70*f*, 75–76
Open-loop transfer function, 69, 75
Operating principle of electric motors, 3–7

alternating current motor, 5–7, 6*f*
configuration of electric motors, 3–4, 3*f*
direct current motor, 5, 5*f*
Operation modes of electric motor, 32–35, 33*f*
Optical incremental encoder, operating principle of, 376, 376*f*
Optimal PWM, 291
Outer rotor type, 164, 393–394
Output torque of three-phase BLDC motor, 401–405
torque ripple during the commutation, 402–405
Output voltage control of an inverter, 289*f*
Output voltage of basic circuit, 269–271
Overdamping, 54
Overmodulation, 323–331
considering the direction of current, 327
dynamic overmodulation methods, 325–327
minimum-magnitude-error pulse width modulation method, 326
minimum-phase-error pulse width modulation method, 325–326
overmodulation method considering the direction of current, 327
steady-state overmodulation methods, 327–331

## P

Park's transformation, 176, 180
Permanent magnet synchronous motor (PMSM), 34, 143, 152, 163, 225, 234–245, 258–259, 373, 382, 390
and brushless direct current motors, 391–393
configurations, 166*f*
different structures for the stator and rotor of, 164*f*
*d*–*q* axes model of, 197–201
flux linkage equations in, 198–200
torque equation in, 200–201
voltage equations in, 198
feedforward control for, 261–262
flux-weakening control for, 357–370
modeling of, 163–174
rotor, 165–169
stator, 164–165
structure of, 164–169
operation region of, 358, 358*f*
output power according to speed regions of, 359*f*
proportional–integral gains for, 258–259
rotor of, 165
rotor topologies of, 166*f*
speed regions of, 359
vector control of Interior Permanent Magnet Synchronous Motor, 238–245
vector control of Surface-Mounted Permanent Magnet Synchronous Motor, 236–238
Permanent magnets, 167*b*
temperature effects on, 168
Phase margin, 62–64, 63*f*
Pole voltage, 268
and phase voltage, 281*t*
Fourier series, 272*b*
of three-phase inverter, 278*f*
Pole-zero cancellation, 69, 256–257, 263
Position observer, 381
Position sensors, 373–376
resolver, 373–375
rotary encoder, 375–376
optical incremental encoder, operating principle of, 376
Power bipolar junction transistor (BJT), 36–37
Power electronic converter for DC motors, 36–37, 82–85
four-quadrant chopper, 82
switching schemes, 83–85
bipolar switching scheme, 83
unipolar switching scheme, 83–85, 85*f*
Power invariance transformation, 178
Power metal oxide semiconductor field effect transistor (MOSFET), 36–37
Power supply, 36
Powering mode, 271
Prime mover, 1
Programmed PWM technique, 290–291
Proportional controller, 58
Proportional–integral current controller, 59, 60*f*, 66, 69–72, 231
gains selection procedure of, 74
modeling, 89
selection of the bandwidth for current control, 71–72
Proportional–integral flux controller, 233–234
Proportional–integral speed controller, 75–79
drawback of, 78–79
gains selection procedure of, 77
selection of the bandwidth of speed control, 77
Proportional–integral speed controller modeling, 90
Pull-out torque, 116–117, 147–148
Pulse per revolution (PPR), 375
Pulse width modulation (PWM) inverters, 265, 288–310
current measurement, 338–339
dead time, 331–338
compensation, 336–338
effect, 333–336
discontinuous PWM techniques, 311–317
30-degree, 313–317

Pulse width modulation (PWM) inverters (*Continued*)
60-degree, 311−312
60-degree ( ± 30-degree), 312
± 120-degree, 312−313
inverters, 265−288
basic circuit of, 267*f*
single-phase full-bridge inverters, 275−277
single-phase half-bridge inverters, 271−274
switching devices for, 268*f*
three-phase inverter using switching functions, 283−288
three-phase square wave inverter (six-step inverter), 277−283
voltage source inverter, 267−271
overmodulation, 323−331
dynamic overmodulation methods, 325−327
steady-state overmodulation methods, 327−331
programmed PWM technique, 290−291
PWM technique based on offset voltage, 317−323
space vector PWM technique implementation, 319−323
sinusoidal PWM technique, 291−297
space vector PWM technique, 300−310
principle of, 302−304
symmetrical space vector pulse width modulation technique, 304−310
third harmonic injection PWM technique, 298−300
Pulse width modulation (PWM) technique, 82, 344−345
Pulse width modulation (PWM) waveform, 227, 385
Pulse-based compensation technique, 336
PWM_ON_PWM scheme, 410−412

## R

Radial-flux type BLDC motor designs, 393−394
Radial-flux type PMSMs, 165−166
Ramp comparison current regulator, 250−251, 251*f*
Rare-earth magnets, 167−168
Reference frame transformation, 153−154, 174−188
by complex vector, 185−188
*d*−*q* reference frame, types of, 175−176
by matrix equations, 176−184
transformation between reference frames, 179−184
transformation of *abc* variables into *dqn* variables in the stationary reference frame, 178−179
Reference winding, 374
Regeneration mode, 271
Regenerative braking, 33, 123−124
Regular-sampled PWM, 297, 297*f*
Reluctance, 10, 17
Reluctance motor, 4, 18, 26
Reluctance torque, 18, 238
Remanence, 168
Residual flux density, 168
Resolver, 373−375, 374*f*
Reverse braking (generating) mode, 35
Reverse motoring mode, 35
Rotary encoder, 375−376
Rotating machine, 18−26, 18*f*
direct current motor, 25
induction motor, 26
synchronous motor, 26
Rotating magnetic field, 100−104, 111*f*
Rotating reference frame, 175−176
Rotation of electric motors, 4, 4*f*
Rotor, 3
Rotor equivalent circuit, 110, 110*f*
Rotor flux angle, 212*f*, 213, 216−220, 223
Rotor flux linkage, 21, 212, 214
Rotor flux linkage vector, 212
Rotor flux−oriented (RFO) control, 212
Rotor reference frame, 176
Rotor voltage equations, rotor flux linkages estimation based on, 228−230
Rotor windings, 99, 104, 111−112, 143−144
inductance of, 158−159

## S

Salient pole rotor synchronous motors, 144, 148−151
equivalent circuit of, 150*f*
phasor diagram of, 150*f*
torque of, 149−151
Samarium−cobalt (SmCo) magnets, 167−168
Saturation region, 9
Scalar control method, 203
Scherbius drive system, 133
Self-excited DC motor, 39
Self-inductance, 19, 19*b*, 19*f*, 153
Sensorless control, 223
of AC motors, 382−387
of brushless DC motors, 412−415
Sensorless techniques
using characteristics of motor, 385−387
using motor model, 383−385
Sensors and other ancillary circuits, 37
Separately excited DC motor, 39, 204, 205*f*, 206
Series motor, 39

Shaft type rotary encoders, 375
Shoot-through condition, 269, 269*f*
Short-pitch winding, 108
Shunt motor, 39
Silicon carbide, 36–37
Simulink block diagram of mechanical load system, 87*f*
Single-phase full-bridge inverters, 275–277, 275*f*
  load voltage, 276*f*
  operation, 276*f*
Single-phase half-bridge inverter, 271–274, 271*f*
Single-phase or three-phase AC voltage sources, 36
Sinusoidal PWM (SPWM), 289, 291–297, 344–345
  line-to-line voltage for, 296*f*
  overmodulation on, 298*f*
  pole voltage for, 295*f*
  voltage modulation range for, 293*f*
Six-step inverter, 279–280
  MATLAB/Simulink simulation, 287*b*
  phase voltage of, 290*f*
Slip energy, 133
Slip energy recovery system, 133
Slip frequency, 110, 136–138
Slip speed, 109
Space vector PWM (SVPWM) technique, 290, 300–310, 344–345
  principle of, 302–304
  symmetrical space vector pulse width modulation technique, 304–310
Speed control, selection of the bandwidth of, 77
Speed controller design, 75–81, 75*f*
  integral-proportional controller, 79–81
  proportional–integral speed controller, 75–79
    drawback of, 78–79
    gains selection procedure of, 77
    speed control bandwidth, selection of, 77
Speed estimation using incremental encoder, 377–381
  M method, 378–379
  M/T method, 380–381
  T method, 379–380
Speed voltages, 189, 255
Speed–torque characteristic of a DC motor in the steady-state, 45*f*
Square wave inverter, 267, 271, 277–278
Squirrel-cage induction motors, 124–125
Squirrel-cage rotor, 98–99, 98*f*
State feedback decoupling control, 262–264, 263*f*
State filter, 381
Stationary reference frame, 175, 178–179
  $d$–$q$ current regulator, 252–254
Stator, 3
Stator and rotor windings, 104
  inductance between, 21, 160–163
Stator flux linkage, 21, 105, 144
Stator flux-oriented (SFO) control, 212
Stator phase winding, 98*f*
Stator voltage equations, 170
  rotor flux linkages estimation based on, 226–228
Stator windings, 97, 97*f*
  equivalent circuit of, 106*f*
  inductance of, 157–158, 159*f*
Steady-state overmodulation methods, 325, 327–331
Step speed command, transient response to, 50, 51*f*
Stray-load loss, 119
Surface-mounted permanent magnet synchronous motor (SPMSM), 165–166, 169, 357–358
  high-speed operation of, 366–370
Switching schemes, 83–85
  bipolar switching scheme, 83, 84*f*
  unipolar switching scheme, 83–85, 85*f*
Switching sequence in two-phase modulation, 310*f*
Symmetrical space vector pulse width modulation technique, 304–310
Synchronous frame current regulator, 255*f*, 256
  and stationary frame regulators, 256*f*
Synchronous frame PI current regulator, gain selection of, 256–259
  proportional–integral gains
    for induction motors, 257–258
    for permanent magnet synchronous motors, 258–259
Synchronous motors, 5–6, 26, 95, 143–152
  categories of, 164*f*
  cylindrical rotor synchronous motors, 144–148
  phasor diagram for, 148*f*
  salient pole rotor synchronous motors, 148–151
  starting of, 151–152
  synchronization in, 152*f*
Synchronous reference frame $d$–$q$ PI current regulator, 255–256
Synchronous reluctance motor, 20
Synchronous speed, 6, 20, 104
Synchronously rotating reference, 176

## T

T method, 379–380, 379*f*
Third harmonic injection PWM (THIPWM), 297–300, 299*f*
Three-level inverter, 268
  basic circuit used in, 269*f*
Three-phase AC voltage source, 36, 99

Three-phase inverter, 278*f*, 283*f*
pole voltages of, 278*f*
using switching functions, 283–288
Three-phase load, 247, 252–253, 253*f*
current control of, 248*f*
Three-phase modulation, 310
Three-phase square wave inverter (six-step inverter), 277–283
Three-phase windings, 102–104, 102*f*
Torque control system of a DC motor, 206*f*
Torque production, continuous, 7–26
linear motion device, 13–17
magnetic energy, 8–13
rotating machine, 18–26
direct current motor, 25
induction motor, 26
synchronous motor, 26
Torque production in the motor, 204*f*
Torque-producing current, 214–215
Total harmonic distortion (THD), 273–274
Traction drives, 341
Translational motion and rotational motion, combination system of, 30–31
Two-level inverter, 268
Two-phase modulation, 310, 310*f*

## U

Underdamping, 54
Unipolar switching method, 409–412, 409*f*
Unipolar switching scheme, 83–85, 85*f*
Unit feedback system, 65, 65*f*
Unsaturated region, 9
Unstable system, 64*f*
Upper switch PWM scheme, 410, 411*f*, 414*f*

## V

Variable Voltage Variable Frequency (VVVF) inverter, 138, 266
Vector control, 138, 204, 217
of Interior Permanent Magnet Synchronous Motor, 238–245
of Surface-Mounted Permanent Magnet Synchronous Motor, 236–238
Voltage equation
in *d*–*q* axes, 189–190, 198
for a motor, 153
Voltage model, 226–228
Voltage source inverter (VSI), 265, 266*f*
basic circuit configuration of, 267–271
Voltage source inverter, 267–271
output voltage of basic circuit, 269–271
Voltage vector, rotation of, 302*f*
Voltage-limit condition, 344–346, 346*f*, 364–365

## W

Wound rotor, 99, 99*f*
Wound-rotor type induction motors, 99, 132–133

## Z

Zero voltage vector, 301, 305
Ziegler–Nichols method, 69